LITHOFACIES AND PETROPHYSICAL CHARACTERIZATION OF THE LATE ORDOVICIAN SARAH FORMATION, RUB' AL-KHALI BASIN, SAUDI ARABIA

BY

ABDULLAH ALQUBALEE

A Thesis Presented to the
DEANSHIP OF GRADUATE STUDIES

KING FAHD UNIVERSITY OF PETROLEUM & MINERALS

DHAHRAN, SAUDI ARABIA

In Partial Fulfillment of the
Requirements for the Degree of

MASTER OF SCIENCE

In

GEOLOGY

March 2017

KING FAHD UNIVERSITY OF PETROLEUM & MINERALS
DHAHRAN- 31261, SAUDI ARABIA
DEANSHIP OF GRADUATE STUDIES

This thesis, written by **ABDULLAH MOHAMMED SALEH ALQUBALEE** under the direction his thesis advisor and approved by his thesis committee, has been presented and accepted by the Dean of Graduate Studies, in partial fulfillment of the requirements for the degree of **MASTER OF SCIENCE IN GEOLOGY.**

Dr. Abdulaziz M. Al-Shaibani
Department Chairman

Dr. Salam A. Zummo
Dean of Graduate Studies

1/5/17

Date

Dr. Osman M. Abdullatif
(Advisor)

Dr. Lamidi O. Babalola
(Member)

Dr. Mohammad H. Makkawi
(Member)

To

my parents,

my brothers and sisters,

my wife and sons, Mohammed and Saleh,

my uncles and cousins,

and to the soul of my professor, Dr. Ali Sahin (Allah’s mercy on him).

ACKNOWLEDGMENTS

All praise and glory are due to Almighty Allah (Subḥānahu wa ta'alā) for his limitless blessings and guidance and may Allah bestow his peace on the prophet, Muhammad (Peace be upon him).

I sincerely acknowledge the support provided by King Fahd University of Petroleum and Minerals (KFUPM). This work was conducted under the NSTIP Project# 14-OIL468-04 supported by King Abdulaziz City for Science and Technology (KACST). Samples were provided by the Ministry of Energy, Industry and Mineral Resources (MEIMR), Saudi Arabia. Support from these organizations at every stage of the study is duly acknowledged. The petrographic thin section study, porosity, and permeability measurements were conducted at Center for Integrative Petroleum Research laboratories. The XRD and SEM/EDX are performed at Engineering Research Center laboratories. The XRF data were acquired at Geosciences Department laboratories. All managers and operators of these laboratories are highly appreciated.

I would like also to express my deepest appreciation to my thesis advisor, Dr. Osman Abdullatif, for his great effort and guidance and to my committee members, Dr. Lamidi Babalola and Dr. Mohammad Makkawi, for their guidance and sincere advice throughout my thesis work. Dr. Ali Sahin (Allah's Mercy on him) was the power and motivator of this study and his enormous effort will not be forgotten. Prof. Gabor Korvin was one of my committee members before he left the university and Dr. Abdulaziz Al-Laboun is the project's consultant, the efforts of these professors are highly appreciated.

I would like also to thank our chairman, Dr. Abdulaziz Al-Shaibani, faculty members of Geosciences Department, and my colleagues for their supports and encouragements. Special thanks to my brother, Saleh Alqubalee, and uncle, Abdullah Alqubalee for the support and encouragements and to Mr. Mohammed Benaafi, Mr. Ammar Adam, Mr. Waleed Ejaz, Mr. Mohammed Yaqot, Mr. Abdullatif Albassair and Mr. Mohammed Al-Asali for their help during my thesis work. Acknowledgments are also extended to Dr. Neil Craigie, Dr. Briner, Dr. Andrew, Mr. Nawaf, Mr. Mohannad, Mr. Mohammed Mujawar and Mr. Mohammed Al-Ghamdi.

TABLE OF CONTENTS

LIST OF TABLES

LIST OF FIGURES

ABSTRACT

Full Name	:	Abdullah Mohammed Saleh Alqubalee
Thesis Title	:	Lithofacies and Petrophysical Characterization of the Late Ordovician Sarah Formation, Rub' Al-Khali Basin, Saudi Arabia
Major Field	:	Geology
Date of Degree	:	March 2017

The Late Ordovician Sarah Formation is considered as a potential tight gas sand reservoir in Rub' Al-Khali Basin, Saudi Arabia. Exploration work carried out in the basin revealed the existence of challenges that are related to lithofacies, paleoenvironmental, and paleogeographic heterogeneity of the Formation. In order to enrich the existing knowledge and to tackle these challenges from the subsurface, this study investigates lithofacies, petrographical, geochemical and petrophysical characteristics of the Sarah Formation based on core samples retrieved from six exploratory wells drilled in the Rub Al-Khali Basin. Detailed facies, thin section petrographical, XRD, SEM/EDX, and XRF analyses were carried out on the cores. Porosity and permeability measurements were acquired from the cores. Each core interval has been divided into several lithofacies. The lithofacies are assembled to represent four lithofacies associations including massive bioturbated sandstone, grayish massive sandstone, diamictites, and partially deformed, graded to massive sandstone. Based on the lithofacies associations, four depositional environments comprising a nearshore lake, glaciolacustrine delta, subglacial tillite, and glaciofluvial outwash environments were interpreted. The nearshore environment is characterized by subarkoze sandstone with porosity ranging from 4.5% to 13.5% and permeability ranging from 0.04 mD to 17.46 mD. This environment shows relatively high reservoir quality enhanced by fractures and feldspar dissolutions. The glaciofluvial environment is characterized by sublitharenite sandstone with porosity ranging from 0.7% to 6.4% and permeability ranging from 0.03 mD to 4.21mD. It exhibits relatively moderate reservoir quality which is controlled by grains compaction, poor sorting, and silica overgrowth. Both the nearshore and the glaciofluvial environments show no significant variation observed in their geochemical characteristics. The glaciolacustrine and subglacial environments are quartzarenite to sublitharenite sandstones. The permeability of these environments is less than 0.1 mD while the porosity is variable. Natural fractures and feldspar dissolutions enhanced their reservoir quality while matrix content, compaction, and cementation diminished the reservoir quality of diamictite lithofacies. Both the glaciolacustrine and subglacial environments exhibit significant variation in their geochemical characteristics. This attributed to a variation in their mineralogical composition. The lithofacies heterogeneity of the formation is expected to impact reservoir quality and architecture. Identifying lithofacies and diagenetic characteristics in the Sarah Formation is crucial to understand the reservoir heterogeneity and to facilitate reservoir evaluation of tight sand reservoir for future exploration and development.

ملخص الرسالة

الاسم الكامل: عبدالله محمد صالح القبالي

عنوان الرسالة : دراسة السحنات الرسوبية والبتروفيزيائية لمتكون صارة الأردوفيشي في حوض الربع الخالي, المملكة العربية السعودية

التخصص: جيولوجيا

تاريخ الدرجة العلمية: مارس 2017

يعتبر متكون صارة ذو العمر الأردوفيشي المتأخر كمكمن محتمل للغاز المتواجد في الصخور الرملية المحكمة في حوض الربع الخالي, المملكة العربية السعودية. كشفت أعمال التنقيب في حوض الربع الخالي عن وجود تحديات متعلقة بالسحنات الرسوبية و بالبيئات الترسيبية والجغرافية القديمة في هذا المكمن. لإثراء المعرفة ولمعالجة هذه التحديات، يهدف هذا البحث إلى دراسة السحنات الرسوبية، والبتروجرافية، والجيوكيميائية, والبتروفيزيائية لمتكون صارة باستخدام عينات صخرية أخذت من ستة آبار استكشافية حفرت في حوض الربع الخالي. في هذه الدراسة تم إجراء وصف تفصيلي للسحنات الرسوبية من خلال الوصف المباشر للعينات الصخرية. ومن ثم تم اجراء عدة أختبارات على عينات صخرية صغيرة. تشمل هذه الاختبارات: التحليل البتروجرافي, و اختبار المسامية والنفاذية , واختبار الانكسار و الوميض للأشعة السينية وكذلك ايضاً تم استخدام المجهر الإلكتروني. من خلال دمج السحنات الرسوبية, تم تشكيل اربع مجموعات سحنية رسوبية تشمل حجر رملي حيوي ، وحجر رمادي رملي كتلي، و رواسب جليدية، و حجر رملي مشوه جزئيا متدرج و كتلي. أربع بيئات ترسيبيه تم تفسيرها لهذه المجموعات الرسوبية والتي تضم بيئة شاطئية لبحيرة، و بيئة دلتا بحيرية جليدية، وبيئة جليدية، وبيئة جليدية نهرية. تتميز البيئة الشاطئية ذات الحجر الرملي الشبه اركوزي بمسامية تتراوح بين 4.5 إلى 13.5 بالمائة و بنفاذية تترواح بين 0.04 إلى 17.46 ملي دارسي و بخصائص مكمنية افضل من بين البيئات الرسوبية المدروسة الآخرى. وقد لوحظ أن الكسور و الانحلالات الجزئية والكليه للفلسبار تعمل على تحسين جودة الرواسب المكمنية لهذه البيئة الرسوبية. أما رواسب البيئة الجليدية النهرية ذات الحجر الرملي الصخري فتتميز بمسامية تتراوح بين 0.7 الى 6.4 بالمائة وبنفاذية تترواح بين 0.03 الى 4.21 ملي دارسي و بخصائص مكمنية متوسطة نسبياً. في هذه البيئة, لوحظ وجود عدة عوامل تعمل على تقليل الجودة المكمنية لهذه الرواسب منها

كبس الحبيبات، و التسميت، و نمو الكوارتز و الفرز الرديء للحبيبات. في كلا من البيئة الشاطئية والبيئة الجليدية النهريه لوحظ أنه لايوجد عدم تجانس جيوكيميائي هام. أما البيئات الآخرى والتي تشمل كلا من البيئة الجليدية والدلتا الجليدية البحيرية ذوات الحجر الرملي المرو و الحجر الرملي الصخري فتتميز بمسامية متغيرة و بنفاذية أقل من 0.1 ملي دارسي وبخصائص مكمنية رديئة. تعمل كلا من الكسور الطبيعية وانحلال الفلسبار على تحسين جودة هذه الرواسب بينما كبس الحبيبات والتسميت والرواسب الارضية فإنها تعمل على تقليل جودة الرواسب المكمنية. في رواسب هاتين البيئتين لوحظ وجود عدم تجانس كيميائي والذي تم تفسيره بوجود عدم تجانس في التركيب المعدني لهذه الرواسب. من المتوقع أن يؤثر عدم تجانس السحنات الرسوبية على نوعية المكمن وأسلوب بناءة. لذلك تحديد خصائص السحنات الرسوبية وكذلك تحديد تغيرات النشأة المتأخرة في متكون صارة أمر بالغ الأهمية حيث يساعد في تسهيل تقييمه في المراحل القادمة من التنقيب والتطوير كأحد المكامن المهمة في الصخور الرملية المحكمة.

CHAPTER 1

INTRODUCTION

1.1 Introductory Statement

According to the report published by the U.S. Energy Information Administration (EIA, 2016), worldwide consumption of natural gas is expected to be 203 trillion cubic feet (Tcf) in 2040. This will amount to an increase of 59% from what it was (120 Tcf) in 2012. Following this report, the natural gas demand in the Middle East may rise more than any region. In the region, the demand is expected to increase from ~15 Tcf in 2012 to ~30 Tcf in 2040. Thus, additional resources for conventional and unconventional natural gas are required for energy security. The difference between the conventional and unconventional resources is explained in the hydrocarbon resources triangle (Figure 1.1). The conventional resources have small volumes and are easy to develop whilst the unconventional resources are large in volumes but are difficult to develop. In other words, the term unconventional implies that the traditional extraction and development techniques cannot be practiced with unconventional resources (Rogner, 1997). Costly technologies are required to develop and produce from this type of resources.

Tight sand and shale gas targets in the Paleozoic siliciclastic succession of Saudi Arabia have been intensively studied for unconventional resources (Sahin, 2013). Potential tight gas in Saudi Arabia was previously recognized in south Ghawar and the Rub’ Al-Khali Basin and regionally developed in northwestern Saudi Arabia (Hayton et al., 2010). The Late Ordovician Sarah Formation characterized by low porosity and low permeability is considered as a tight gas sand reservoir (Sahin, 2013). Geological characterization of tight sand reservoirs is essential for drilling, evaluation, completion and stimulation activities (Holditch, 2006). Therefore, this study investigates the sedimentological, petrographical, petrophysical and geochemical characteristics of the lithofacies and the depositional environments of the Sarah Formation from the subsurface of the Rub' Al-Khali Basin, Saudi Arabia. This study aims at contributing significant information to the reservoir evaluation of tight gas sand reservoir of the Sarah Formation.

Core description and laboratory analyses are performed on 147.3 ft (44.9 m) of core samples retrieved from six wells drilled in the basin. The results have been analyzed, integrated, and interpreted to achieve the research objectives. This thesis consists of eight chapters. Chapter one introduces the study area and discusses the scope and objectives of the research followed by a summary of the previous studies conducted on the Formation. The reviewed literature includes the geological setting of the studied area, elaborated discussion on the previous studies conducted on the formation, tight gas sand and reservoir description and quality are pointed out in chapter two. The dataset and methods applied in this study are discussed in chapter three and followed by the facies analysis in chapter four. Subsequently, the petrographical analysis is illustrated in chapter five. Chapter six discusses the geochemical characterization while chapter seven illustrates the petrophysical characteristics of the studied cores. The research is generally summarized and concluded in chapter eight.

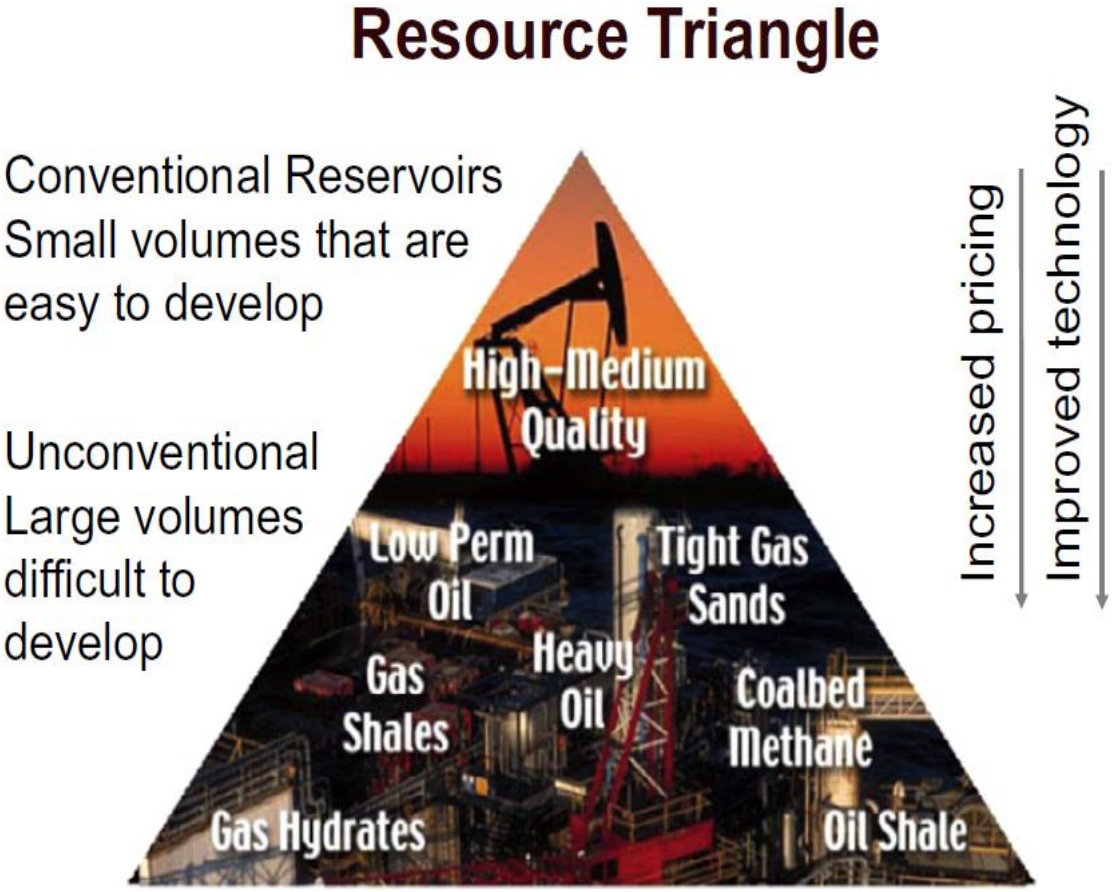

Figure 1.1: Hydrocarbon resources triangle. Tight gas sand is one of the unconventional resources that have large volumes but difficult to be developed unless costly technologies are used.

1.2 Study Area

The study area is situated in the northern part of the Rub’ Al-Khali Basin and southwest of the largest oilfield in the world, the Ghawar field, Saudi Arabia. Core samples retrieved from six wells that penetrated the Late Ordovician glaciogenic Sarah Formation in the basin were used to investigate several challenges encountered during hydrocarbon exploration. This formation is considered as a tight gas reservoir in the study area and elsewhere in Saudi Arabia. The location map of the study area showing the location of the studied wells is illustrated in Figure 1.2. The core samples of the Sarah Formation were retrieved from different depths. The deepest core interval is located at a graben-like structure in the basement depth map of Konert et al. (2001) (Figure 1.3). The Sarah Formation among the Paleozoic stratigraphic column of central Saudi Arabia is underlain by Qasim Formation and overlain by Qalibah “Formation” (Figure 1.4).

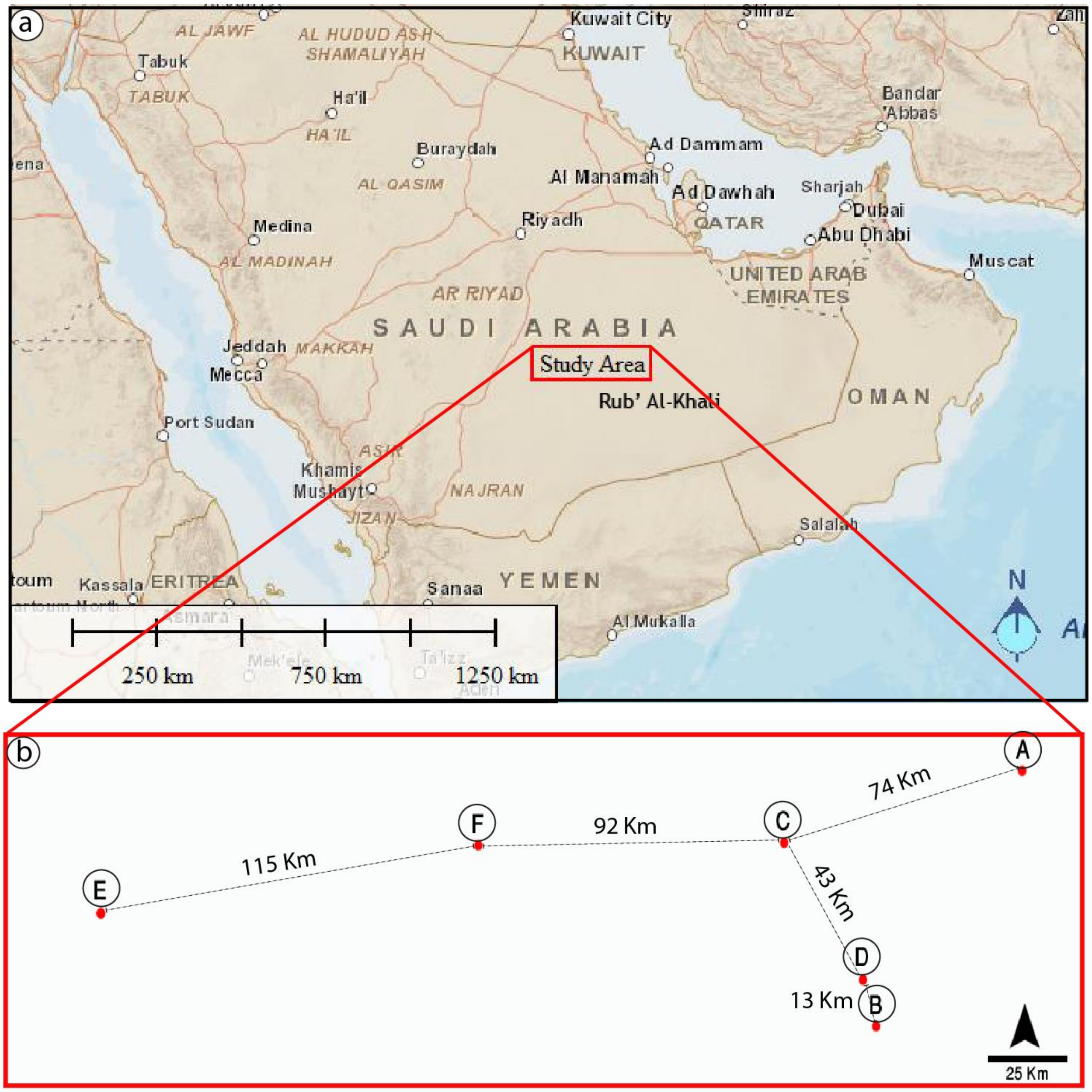

Figure 1.2: (a) Map of Saudi Arabia showing the study area location map and (b) Studied Wells locations map. The study area is located in the Rub' Al-Khali Basin, Saudi Arabia.

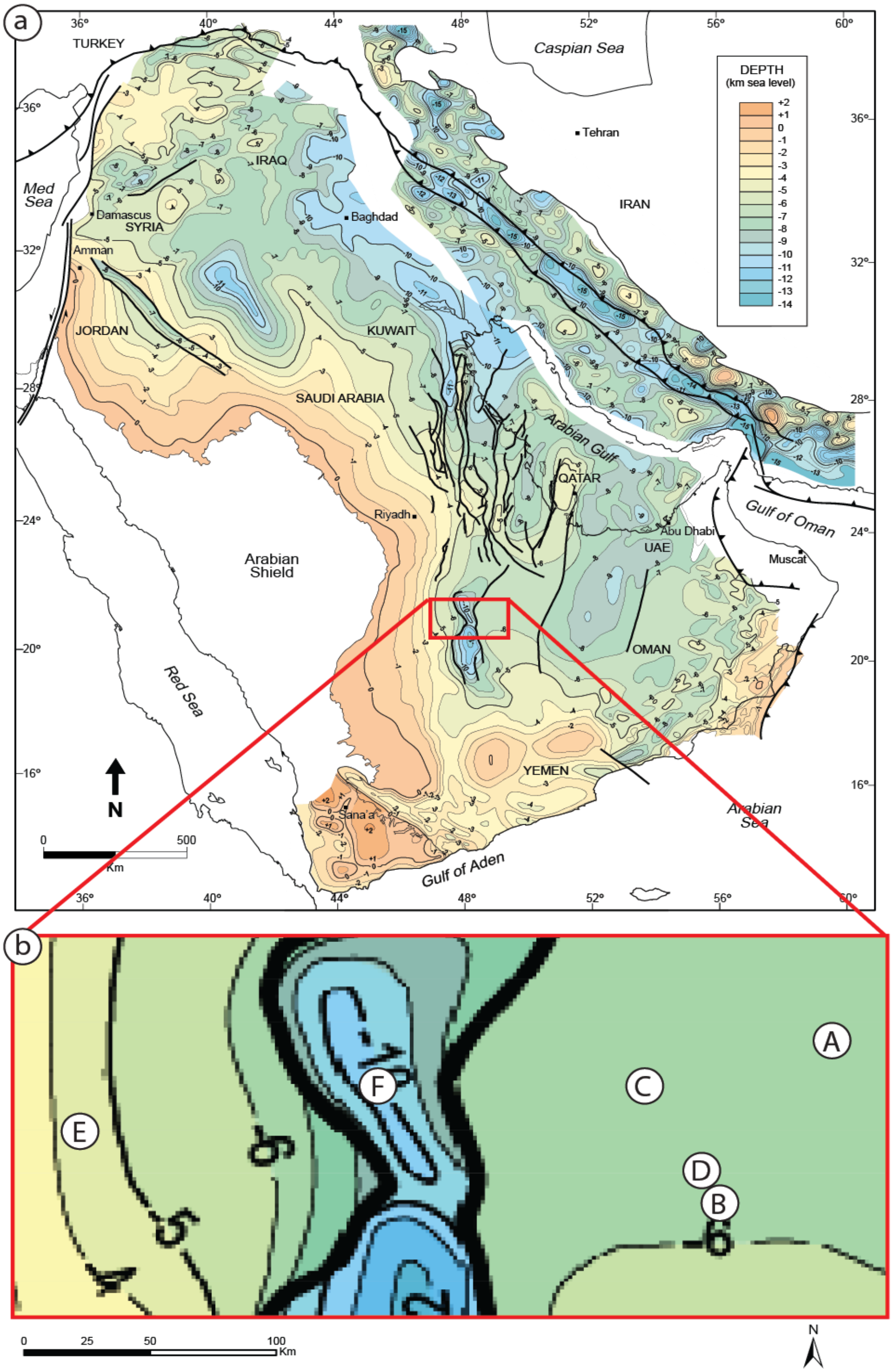

Figure 1.3: The study area shown on the basement depth map of the Arabian basin. (a) Basement depth map, (b) Isopach contour map showing the well locations. Modified after Konert et al. (2001)

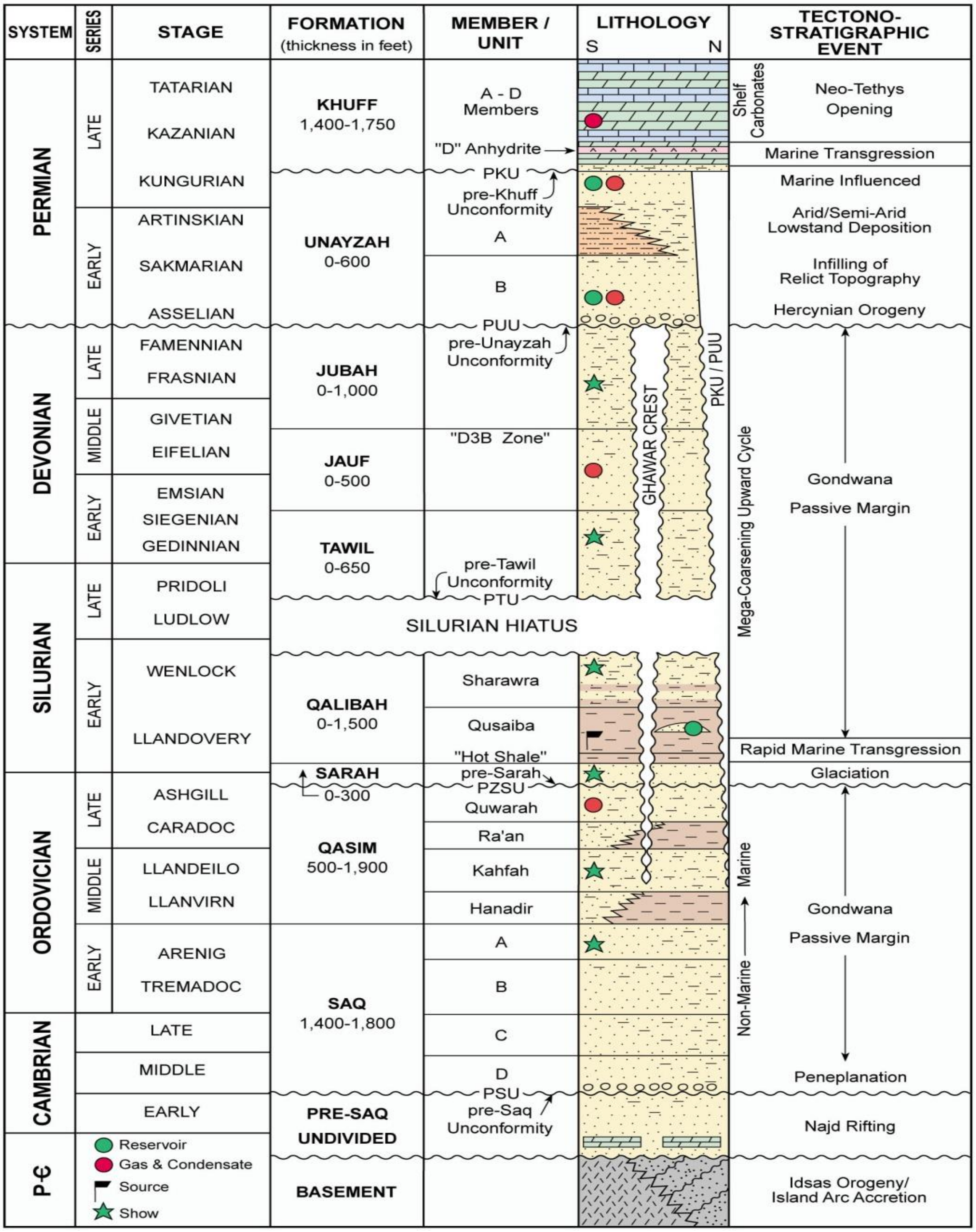

Figure 1.4: The Paleozoic stratigraphic column of Saudi Arabia. Sarah Formation was deposited during the period between the Late Ordovician and the Early Silurian. After Abu-Ali et al. (1999)

1.3 Scope and Objectives

Worldwide energy demands require that more attention needs to be given to the tight sand reservoirs which provide considerable opportunities for oil and gas companies to extract a natural gas (Beretta, 2009). It is difficult to produce from a tight sand reservoir unless hydraulic fracturing or horizontal drilling is used (Holditch, 2006). Hence it is important to first understand its geological and reservoir properties to facilitate hydraulic fracturing and stimulation (Holditch, 2006). Sarah Formation is a potential primary tight sand reservoir in Saudi Arabia (Briner et al., 2010). The formation has been described as a heterogeneous reservoir (Briner et al., 2010; El-Deek et al., 2014; Razzaq et al., 2014). Geological characterization of the tight sand reservoir is the key to understanding reservoir heterogeneity and quality. To establish the essential tools to evaluate the tight sand of Sarah reservoir, the study was intended to:

- Determine the lithofacies and their depositional environment.
- Characterize the identified lithofacies in terms of their petrographical, petrophysical and geochemical characteristics.
- Identify reservoir heterogeneity and quality, and define sweet spots.

1.4 Previous Studies

In this section, a brief discussion about the previous studies on the Sarah Formation is provided. Unfortunately, most of the reviewed literature were conducted on different outcrops in various locations in Saudi Arabia. McClure (1978), Clark-Lowes (1980, 2005), Williams et al. (1986), Vaslet et al. (1987), Vaslet (1990), and Senalp and Al-Laboun (2000) studied and mapped the paleovalleys of the Late Ordovician in central Saudi Arabia. The Zarqa-Sarah incised paleovalley was recognized from a seismic section by McGillivray and Husseini (1992). The provenance of the Sarah paleovalleys deposits was studied by Al-Harbi and Khan (2011) whilst the petrophysical characterization of these deposits was conducted using different approaches by El-Deek (2014) and Razzaq (2013). Briner et al. (2010) and Moscariello et al. (2008) integrated outcrop with subsurface investigations on the Late Ordovician Formations in the Rub' Al-Khali Basin and Wajid area, respectively. Michael et al. (2015) investigated the characteristics of the depositional environments of the filling deposits of the Sarah paleovalley in Tayma area, northwestern Saudi Arabia. Craigie and Rees (2016) applied a chemostratigraphic study on Sarah Formation based geochemical data extracted from four wells. Babiker (2015) studied the relationship between the lithological and geomechanical characteristics of the Sarah Formation based on an outcrop study while Ejaz (2016) integrated the geomechanical properties of the formation with electro-facies using well-log data and core plug samples. The latter used the same core samples of this study. The above-mentioned literature is further discussed in chapter 2 (see section 2.3).

CHAPTER 2

LITERATURE REVIEW

2.1 Introduction

The literature review of this study consists of four parts. The first part focuses on the geological setting of the study area from the Infracambrian to the Late Ordovician glaciations. The second part reviews several studies conducted on Sarah Formation. The third part encompasses the tight sand definition and potential tight gas in Saudi Arabia. The fourth part illustrates sandstone reservoir description and quality.

2.2 Geological Setting

Subsiding rift of the Rub' Al-Khali Basin was formed during the Infracambrian and Early Cambrian (Pollastro, 2003). The outcrops of the Paleozoic rocks in Saudi Arabia are located in three areas including (1) Tabuk, NW of Saudi Arabia (2) Hail and Qasim, central Saudi Arabia, and (3) Wajid, SW of Saudi Arabia (Vaslet, 1990). During the Late Ordovician, the Arabian Plate was located in the southern latitude; about 55º S (Figure 2.1) (Konert et al., 2001). The evidence of the Ordovician glaciations in central Saudi Arabia was first recognized by McClure (1978) who suggested that a part of the Gondwana ice caps extended eastward. It supports the hypothesis of ice pole in central Africa (Vaslet, 1990). The Late Ordovician Hirnantian glaciations affected the intracratonic basins of Saudi Arabia, Libya, Algeria, Morocco and Mauritania (Le Heron et al., 2009). The Gondwana paleogeographic reconstruction of the Late Ordovician indicates that the ice flow in the Arabian Plate was directed eastward (Figure 2.2). However, the extent of Hirnantian ice sheets into the Arabian basin remains unknown (Le Heron et al., 2009). Moscariello et al. (2008) illustrated glacial evidence in southwestern Saudi Arabia in Sanamah Formation of the Wajid Group. The Late Ordovician glaciogenic formations in Saudi Arabia including Zarqa (Vaslet et al., 1987), Sarah (Williams et al., 1986) and Hawban (Saudi Stratigraphic Committee, 2012) formations can be correlated stratigraphically with the Sanamah Formation of the Wajid Group.

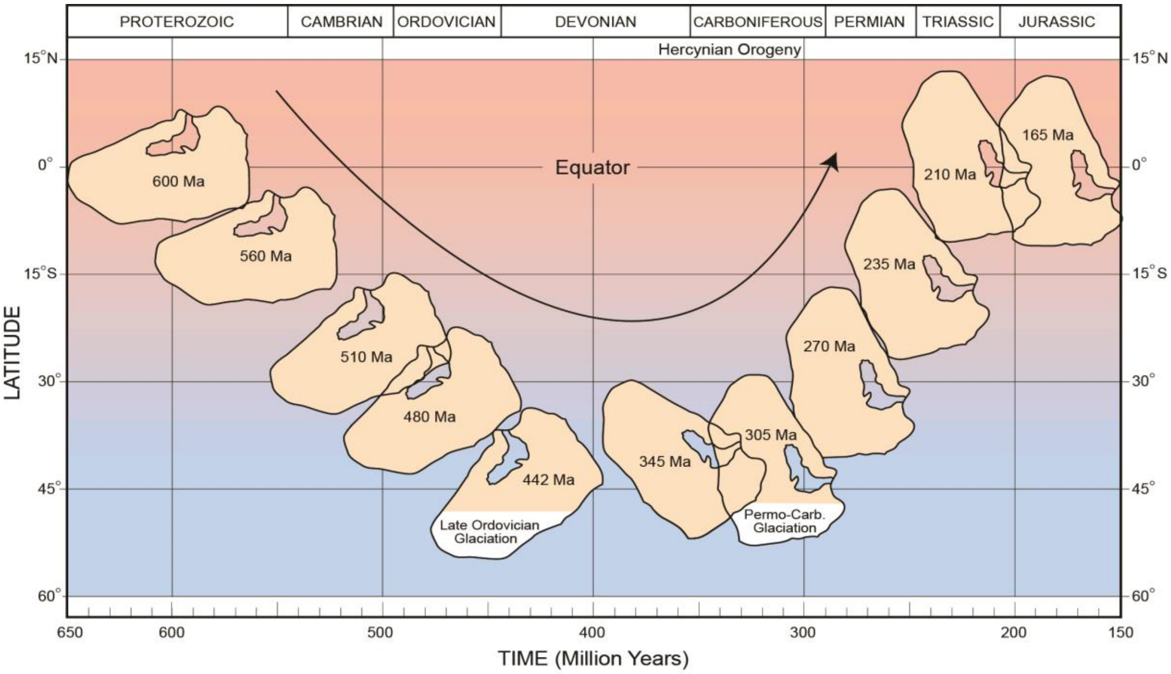

Figure 2.1: Paleolatitude positions of the Arabian Plate show that the Late Ordovician glaciation period affected the northern part of the Arabian Plate. After Konert et al. (2001).

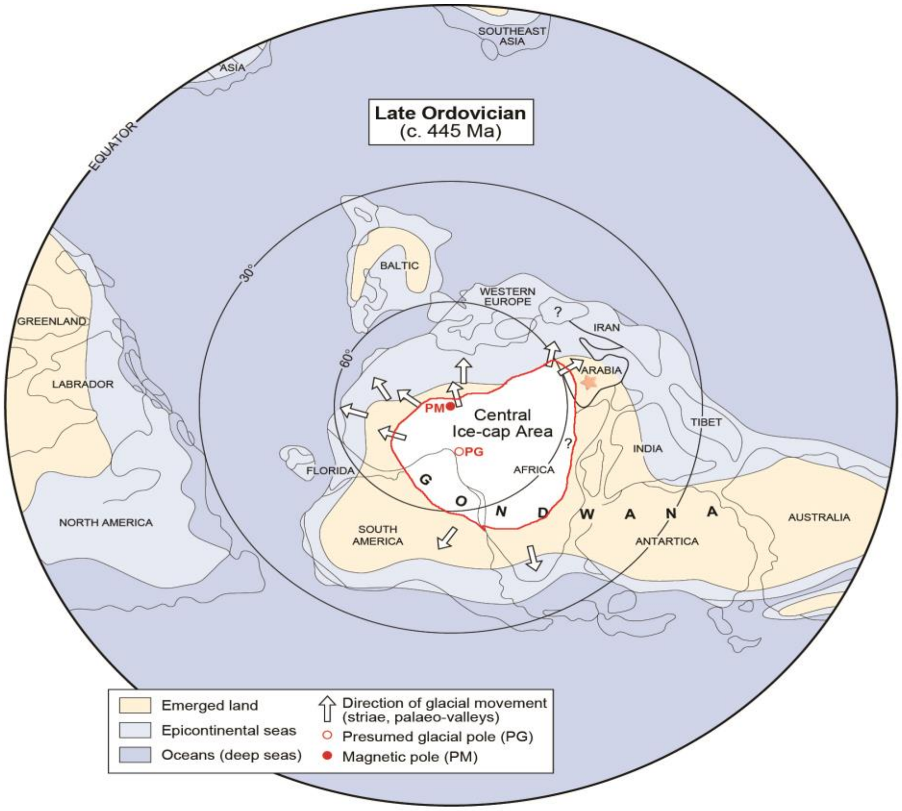

Figure 2.2: Paleo-tectonic reconstruction of Gondwana during the Late Ordovician glaciations. After Vaslet (1990); modified by Sharland et al. (2001)

2.3 Sarah Formation

The name of Sarah was first suggested by Clark-Lowes (1980) as Sarah Member of the Tabuk Formation and was subsequently elevated to a formation by Williams et al. (1986). The Late Ordovician glaciogenic formations in central Saudi Arabia (Table 2.1) are considered to be equivalent to the Sanamah Formation of Wajid Sandstone Group (Figure 2.4) in southwestern Saudi Arabia (Moscariello et al., 2008). Sarah Formation was deposited on second glacial erosional surface cutting deeply into Zarqa, Qasim, and

Saq formations (Williams et al., 1986; Vaslet et al., 1987). The glaciofluvial Sarah Formation displays a range of grain sizes and colors in the outcrop (Clark-Lowes, 2005). In the subsurface, the grains become finer eastward and several structures indicate fluviomarine facies (Senalp and Al-Laboun, 2000). The Sarah Sandstones were derived from complex granite, metasedimentary and older sedimentary rocks (Al-Harbi and Khan, 2011). Sarah Formation is a heterogeneous reservoir (Briner et al., 2010; El-Deek et al., 2014; Razzaq et al., 2014). The channel filled sediments of the Sarah Formation mainly consist of sandstone, fine-medium grained, moderately to well sorted, quartz arenite with minor feldspar and rare to trace lithic fragment contents (El-Deek et al., 2014).

Table 2.1: The Late Ordovician formations in central Saudi Arabia. Note that the dashed lines indicate unconformities (Senalp and Al-Laboun, 2000) while TSM stands for tectonostratigraphic megasequence following Sharland et al. (2001).

Era	System	Group	Formation	Type locality	TSM
Paleozoic	**Late Ordovician**	Tabuk (Janjou et al., 1996)	Hawban (Saudi Stratigraphic Committee, 2012)	Baq'a	AP3 (Sharland et al., 2001)
			Sarah (Williams et al., 1986) -------------------	Sarah ridge, Jabal Habashi quadrangle	
			Zarqa' (Vaslet et al., 1987) -------------------	East of Wadi U'aywij, near Jal az Zarqa'	

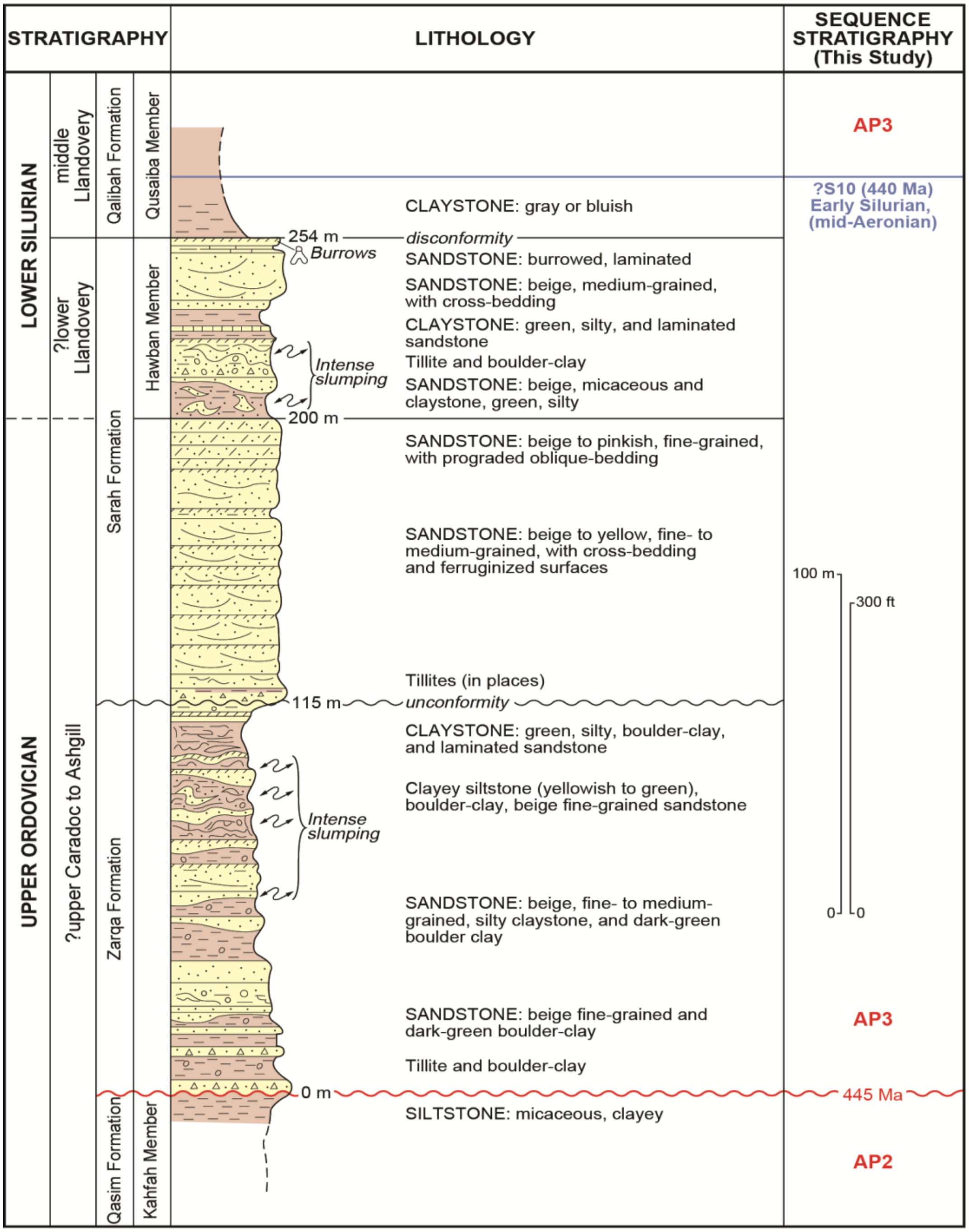

Figure 2.3: The Upper Ordovician-Lower Silurian lithostratigraphy of central Saudi Arabia. After Vaslet et al. (1987); modified by Sharland et al. (2001).

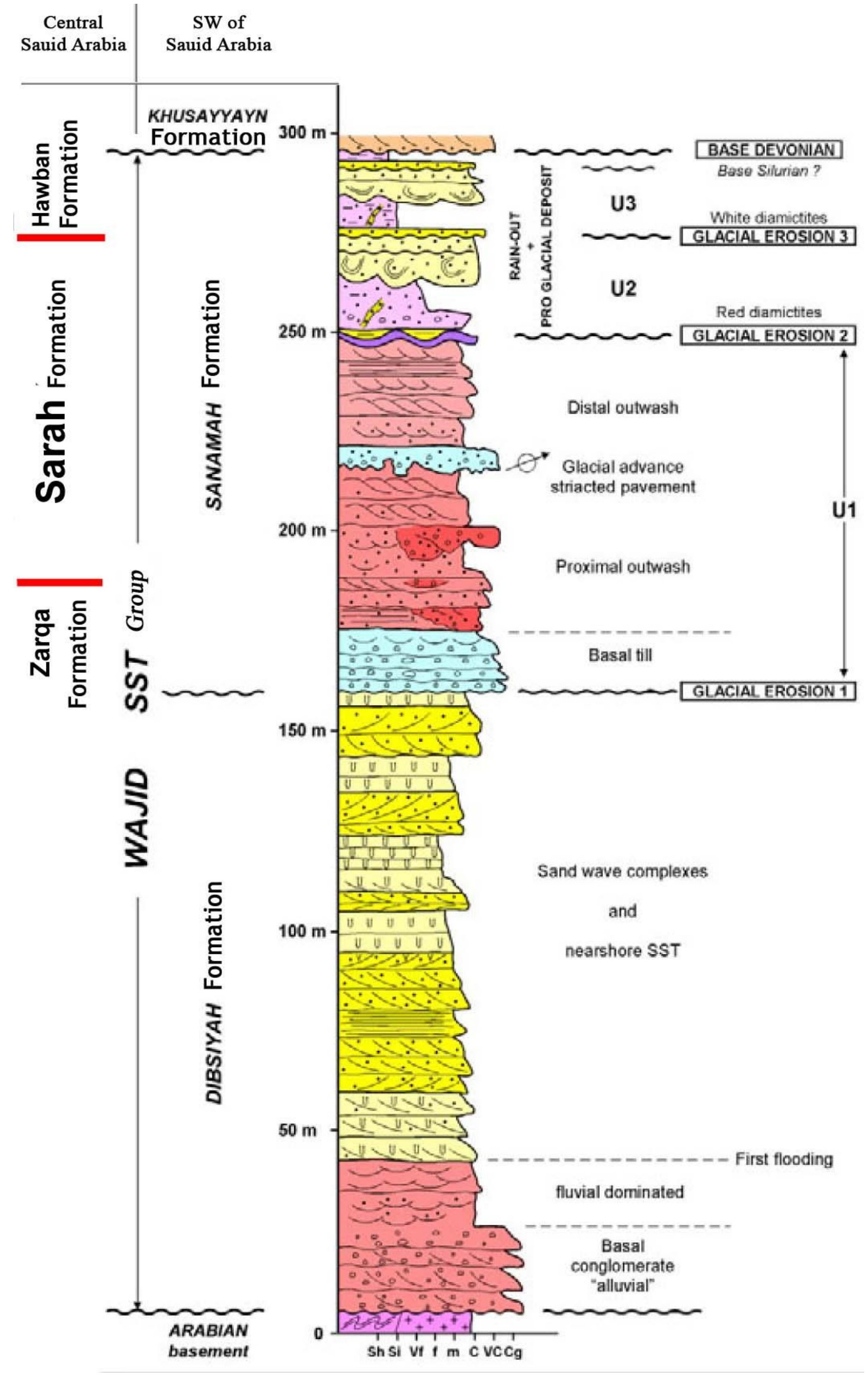

Figure 2.4: The Lower stratigraphic succession of Wajid Group, SW of Saudi Arabia. The Sanamah Formation in the southwestern Saudi Arabia is equivalent to Zarqa, Sarah and Hawban Formation in central Saudi Arabia. After Moscariello et al. (2008).

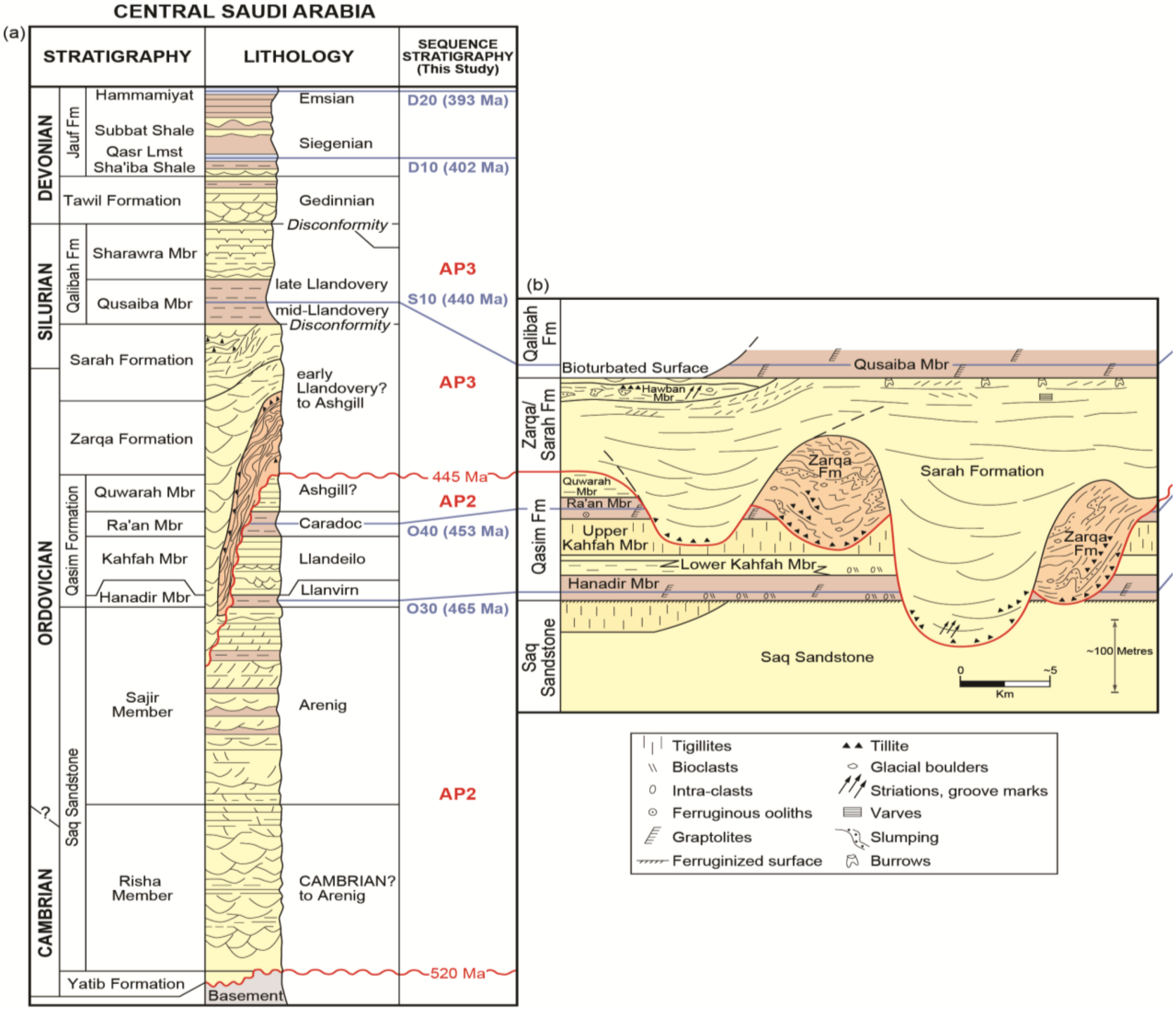

Figure 2.5: Surface and subsurface expression of the Late Ordovician glaciogenic channel fill. (a) Early Paleozoic succession of central Saudi Arabia. (b) Stratigraphic relationships of the early Paleozoic sub-glacial deposits in outcrops of central Saudi Arabia. After Vaslet (1990); modified by Sharland et al. (2001).

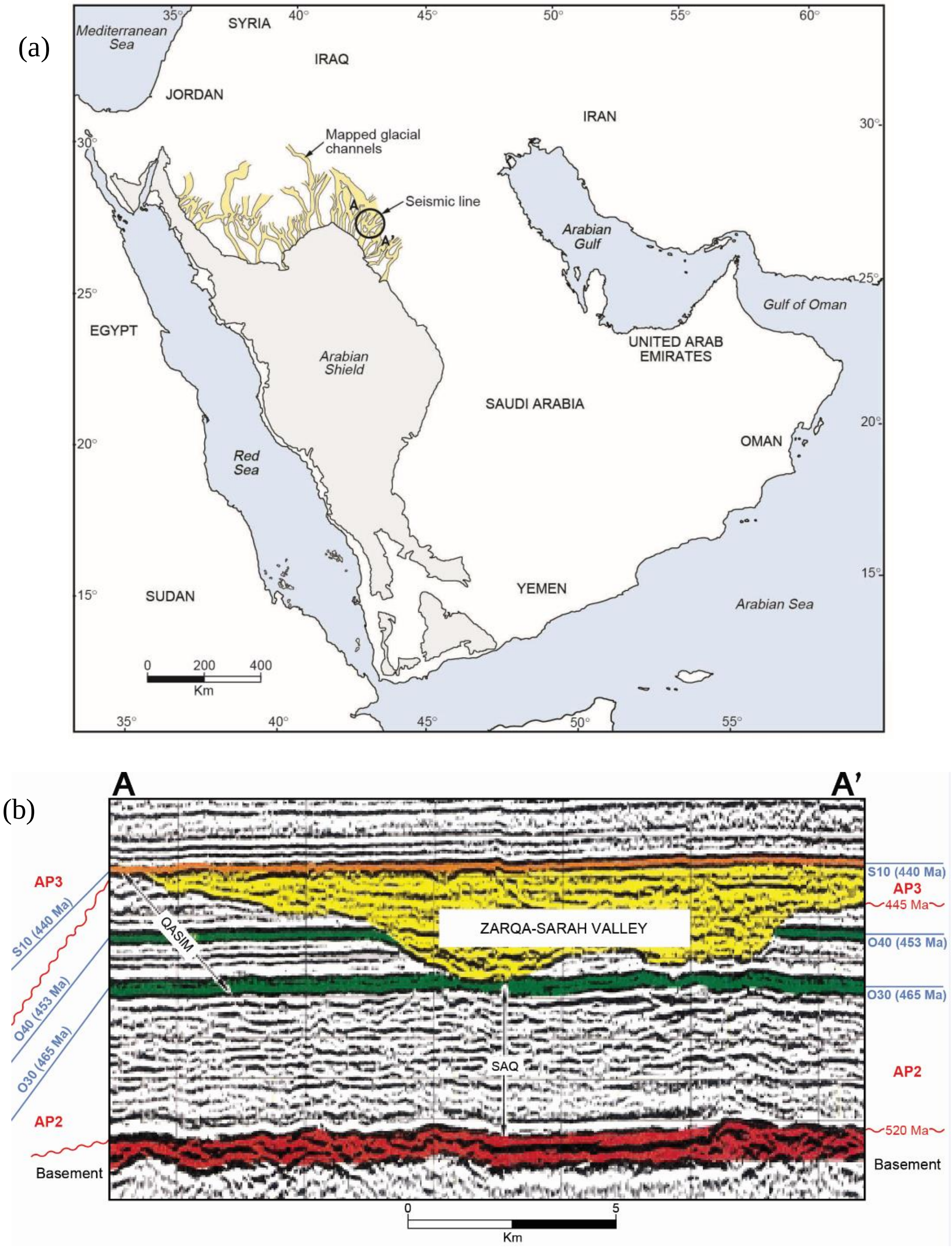

Figure 2.6: Zarqa-Sarah incised valley in the subsurface. (a) Location map of a seismic line. (b) Zarqa-Sarah incised valley in a seismic section. After McGillivray and Husseini (1992); modified by Sharland et al. (2001).

Sarah paleovalleys were mapped in central Saudi Arabia by Williams et al. (1986), Vaslet et al. (1987) (Figure 2.3), and Vaslet (1990) (Figure 2.5), while the Sanamah glacial paleovalley in southwestern Saudi Arabia was studied by Moscariello et al. (2008). McGillivray and Husseini (1992) recognized Zarqa-Sarah incised valley in the subsurface of central Saudi Arabia using seismic data (Figure 2.6). The Ordovician glacial deposits were accumulated by advancing and retreating ice sheets (Vaslet, 1990).

2.4 Tight Gas Sand

The unconventional gas resources include tight gas, shale gas, gas hydrate, coal bed methane (Figure 1.1) (Holditch, 2006), geo-pressured gas, and depth earth gas (Kawata and Fujita, 2001). Among them, tight gas sand and shale gas are the only resources that are present in huge amounts in Saudi Arabia (Sahin, 2013). About 3370 Tcf of tight gas and shale gas were estimated in the Middle East and North Africa (Rogner, 1997; Sahin, 2013) and about 24.42% (823 Tcf) of these resources was estimated for the tight gas alone in this region (Kawata and Fujita, 2001; Sahin, 2013). According to EIA (2014) and Islam (2015), about 291 Tcf of natural gas reserves was proved in Saudi Arabia.

By the definition and according to Saudi Aramco's standard drilling and completion procedures, a reservoir which does not flow at commercial rates and has a porosity less than 12% with permeability <1 millidarcy is considered as a tight gas reservoir (Hayton et al., 2010). Several authors such as Forsyth et al. (2011), Aguilera et al. (2008) and Sahin (2013) defined the tight reservoir within permeability less than 0.1 millidarcy. Holditch (2006) suggested that the tight gas reservoirs can be defined as reservoirs that cannot produce at economic flow rates, nor recover economic volume unless hydraulic fracturing is applied or multilateral or horizontal wellbores are drilled through them. Tight gas reservoirs can be found in deep or shallow environments, high pressure or low pressure and high or low-temperature zones and they occur as a blanket or lenticular, homogeneous or naturally fractured bodies, and can contain a single layer or multiple layers (Holditch, 2006). Characterizing tight gas reservoirs is crucial for research and development. Such studies would increase our understanding of tight reservoir complexity and their resource potentials. According to Al-Mahmoud and Al-Ghamdi (2010), the tight gas reservoirs in Saudi Arabia are found mainly in clastic rocks ranging from Cambrian to Permian. Potential tight gas reservoir in Saudi Arabia was previously recognized in South Ghawar and the Rub' Al-Khali Basin and regionally developed in Northwestern Saudi Arabia (Hayton et al., 2010). Four Lower Paleozoic formations including the Late Ordovician Sarah, Silurian Qalibah, Devonian Jauf and Permian Unayzah Formations are the main targets for unconventional natural gas in Saudi Arabia (Sahin, 2013).

2.5 Reservoir Description and Quality

Rushing et al. (2008) suggested a workflow for tight sand rock typing. The authors classified the tight gas sand rock types into depositional, petrographic and hydraulic rock types. The depositional type is based on lithofacies description having similar depositional energy, environment, and morphology. The petrographical type is based on the description of pore-scale microscopic imaging. The hydraulic type is based on pore scale measurements of the rock flow and storage properties at current condition. Based on controlling factors, Khalil (2012) classified the reservoir sweet spots in the Arabian

Basins to tectonic, sedimentologic and diagenetic sweet spots. Hippler et al. (2013) discussed the importance of using microscopic tools to identify pore types. They suggested that the integration of core analysis and field observation leads to the classification of unconventional reservoirs into low, moderate and high quality. El Hajj et al. (2015) highlighted the significance of classifying clay minerals using advanced X-ray powder diffraction, X-ray fluorescence, and scanning electron microscopy techniques. Hardman et al. (2011) characterized and correlated the Unayzah-A reservoir by applying geochemical and statistical analyses. Zhang et al. (2015) conducted sedimentologic and petrographic studies on the tight sand strata in twenty-four core samples obtained from eight wells that penetrated the Lower Cretaceous Dalaoyefu Formation, northeast of China. Their study was aimed at understanding the diagenetic processes that affected the reservoir quality leading to sweet spots. This study adopts several concepts from the published literature as described in the methodology chapter (Chapter 3).

CHAPTER 3

DATASET AND METHODS

3.1 Introduction

The dataset used for this study was provided by Ministry of Energy, Industry, and Minerals Resources (MEIMR), Saudi Arabia. It consists of continuous core samples with a total thickness about 147.3 ft (44.9 m) (Table 3.1) retrieved from six wells in the block B of the Rub' Al-Khali Basin, and 140 core plugs with their thin sections (Table 3.2). In addition, another dataset was collected from laboratory investigations such as thin section petrographic, X-ray diffraction (XRD), X-ray fluorescence (XRF), Scanning Electron Microscopic and Energy-dispersive X-ray spectroscopic (SEM/EDX) analyses. Porosity and permeability measurements carried on plug samples were also part of the datasets used in this study. The study's methodology (Figure 3.1) was designed as follows: describing core samples to identify lithofacies and to define their depositional environments. The lithofacies were subsequently integrated with the laboratory results to achieve the study's objectives. The detailed research methods are discussed in details in the subsequent sections.

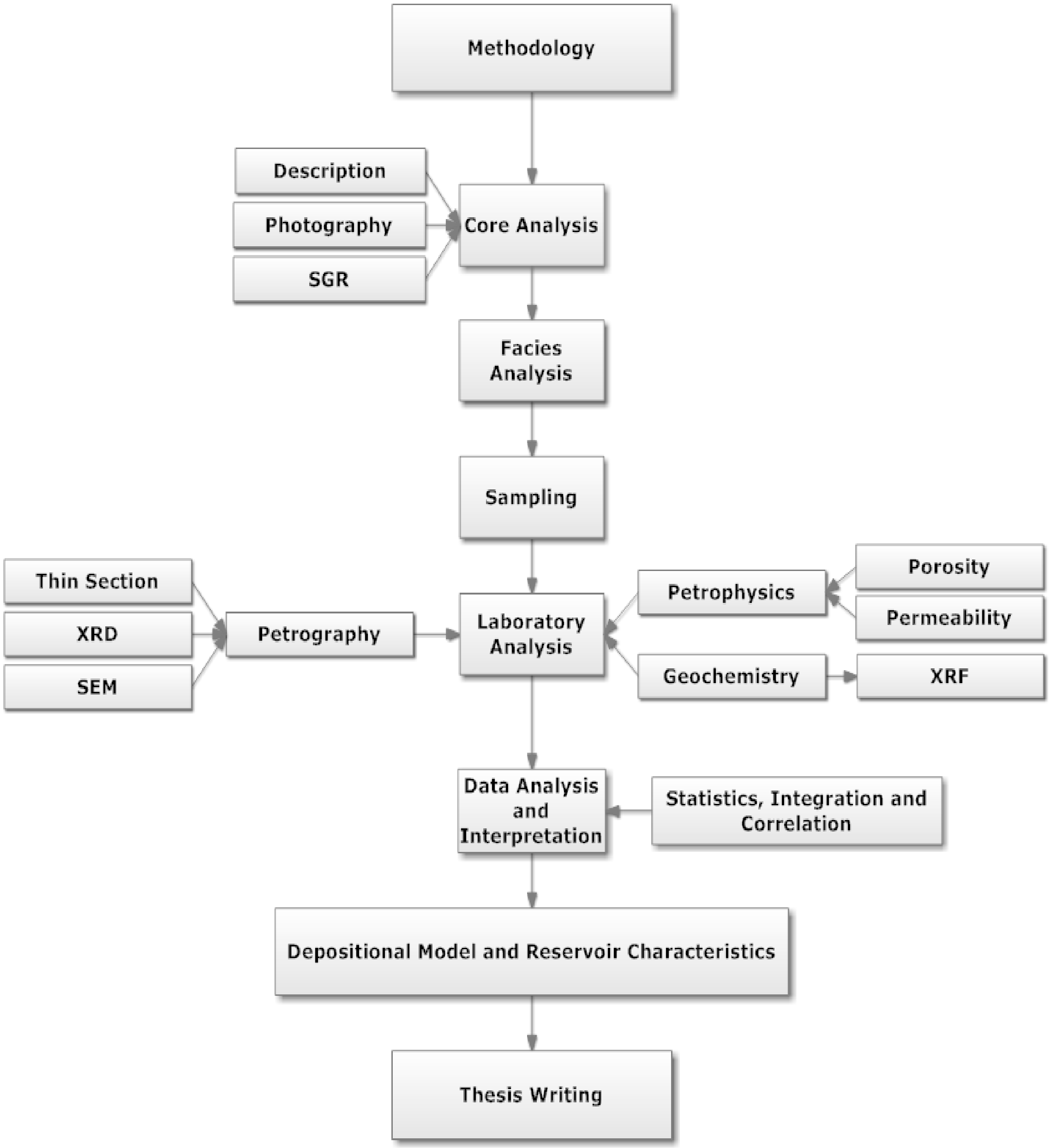

Figure 3.1: Research methodology starts with core description and ends with thesis writing.

3.2 Facies Analysis

The facies analysis represents the basic step for this study. Through this, the lithofacies identification and classification have been established. Following the idealized core description sheet suggested by Morton-Thompson and Woods (1993) with minor modifications, the salient features including sedimentary structures, color, and texture (grain size, sorting, sphericity, roundness, and grains contact) were acquired from the cores. The facies codes of Miall (2000) and Evan and Benn (2004) with few modifications were applied to facilitate facies description and interpretation.

3.3 Thin section Petrography

Petrographic thin section study has been conducted at Center for integrative Petroleum Research (CIPR) using Olympus petrographic microscope. A total number of 140 thin sections delivered by MEIMR have been studied in terms of mineralogical composition, grains texture (size, roundness, sphericity, sorting, contact and packing), matrix, and cement type. Following Gazzi-Dickinson point-counting method, about three-hundred points were counted for quartz, feldspar and lithic rock fragments (QFL) to facilitate sandstone classification and provenance interpretation. The sandstone provenance following Dickinson (Dickinson, 1985) and the sandstone classification using the Folk (1980) classification scheme have been established. The spreadsheet suggested by Zahid and Jr (2011) was used for sandstone and provenance classifications.

3.4 SGR, XRD, XRF, and SEM

Spectral Gamma Ray (SGR) was taken one reading point per inch using a high-resolution *SPECTRAL CORE GAMMA* tool. A total number of 49 samples were obtained from all the identified lithofacies and pulverized at Geosciences Department Laboratories (GDL) for X-ray powder diffraction (XRD) and X-ray fluorescence (XRF) analyses. In order to extract elemental compositions of the samples, the powdered samples were analyzed using *JSX-3400RII ELEMENTAL ANALYZER*. In this XRF technique, each grinded sample was cautiously prepared using especial cups and films and following device's manual instruction while running this instrument. The mineralogical composition of the samples, XRD data was also acquired at Engineering Research Center (ERC) using *Ultima IV X-ray Diffractometer*. Scanning Electron Microscope and Energy-dispersive X-ray spectroscopy (SEM/EDX) conducted at ERC are also used to identify pore filling, pore lining clay minerals, and their morphology.

3.5 Porosity and Permeability

Porosity and permeability measurements were acquired from all core plugs using *AP-608* automated permeameter porosimeter at CIPR. The data has been statistically analyzed to illustrate their distribution and heterogeneity. Fracture sweet spots or fractured permeability was differentiated using the box plot graph as they represent high value outliers. On the other hand, the outliers with low values are expected since we are dealing with tight sand samples. The relationship between porosity and permeability is defined by cross plotting their values. The petrophysical data is integrated with petrographical and geochemical data to investigate the reservoir quality controlling factors.

Table 3.1: The studied core intervals provided by MEIMR. Note that most of the cores represent the upper part of the Sarah Formation.

Well	**Core interval**	**Thickness (ft)**
A	Middle Sarah	29.1
B	Upper Sarah	29.1
C	Upper Sarah	36.8
D	Upper Sarah	13.7
E	Upper Sarah	30
F	Upper Sarah (Transition zone)	8.6
	Total Thickness (ft)	**147.3**

Table 3.2: The studied core plugs provided by MEIMR. A thin section of each plug was also provided.

Core plugs		**Average Dimension**	
		Length	**Diameter**
Well	Number	(in)	(in)
A	29	2.02	1.46
B	25	1.84	0.99
C	40	1.97	0.99
D	8	1.91	1.50
E	30	2.04	1.48
F	8	1.94	1.51
Total Plugs	**140**		

CHAPTER 4

FACIES ANALYSIS

4.1 Introduction

Lithofacies (F) is a rock unit recognized based on its distinctive lithological features including composition, grain size, bedding characteristics and sedimentary structures (Miall, 2000). A group of facies which is genetically related to a depositional environment is called facies association (FA) (Miall, 2000). Facies analysis illustrated in this chapter is divided into three sections. The first section (4.2) includes visual sedimentological descriptions, the second section (4.3) interprets and discusses all the recognized lithofacies associations in term of their inferred ancient depositional environments, and the third section (4.4) introduces the lithofacies and depositional models of this study. Besides, a general discussion for all lithofacies associations is provided in the fourth section (4.5).

4.2 Lithofacies Description and Analysis

The lithofacies were identified in all the core samples using several criteria such as lithology, grain size, sorting, and sedimentary structures. The facies codes of Miall (2000) and Evan and Benn (2004) with minor modification were applied to facilitate the lithofacies description (Table 4.1).

Table 4.1: Facies codes and their description and interpretation, modified after Miall (2000) and Evan and Benn (2004).

Facies codes	Description	Interpretation
Dmm	Matrix-supported, massive diamictite	Plastic Debris flow (Schultz, 1984; Isbell, 2010)
Dms	Matrix-supported stratified diamictite	Plastic Debris flow. Stratification due to winnowing out of fine grains associated with low sedimentation rate (Schultz, 1984; Isbell, 2010)
Dcm	Clast-supported, massive diamictite	Pseudoplastic debris flow (Schultz, 1984)
GRfu	Fining upward granules	Rapid deposition by highly concentrated, non-cohesive sediment gravity flows (Mulder & Alexander, 2001; Gani, 2004; cf. Lang et al., 2012)
GRh	Horizontally bedded granules	
Sm	Massive sandstone	Gravity flow deposits (Miall, 2000)
St	Trough cross-stratified sandstone	3D dunes deposited from turbulent, high-energy currents (Allen, 1984; cf. Lang et al., 2012)
Sd	Deformed sandstone	Deformation due to glacial movements or by reworking
Fm	Massive siltstone, claystone/shale	Deposited by suspension

4.2.1 Core Interval of Well-A

The Well-A thick core interval (29 ft) is divided into four lithofacies based on lithology, grain size, sorting and bioturbation (Figure 4.1A). The basal lithofacies (F1) is comprised of 0.3 ft thick dark gray claystone/shale with horizontal and inclined filled fractures. Lenses of siltstone with lenticular laminations are observed at the top of the lithofacies (Figure 4.1B, a). The overlying 10.6 ft thick lithofacies (F2) consists of off white, bioturbated, horizontally fractured, fine to medium-grained, occasionally coarse-grained, angular to rounded, well to moderately sorted, massive sandstone (Figure 4.1B,b,c). Disrupted mud drapes also observed in this lithofacies indicating a soft deformation in the bioturbated zones. F3 lithofacies is an 8.1 ft thick, bioturbated, fine to coarse-grained, poorly sorted, and occasionally moderately sorted massive sandstone (Figure 4.1B,d,e). Except for the grain size and sorting, this lithofacies is almost like F2. The uppermost lithofacies (F4) is nearly like F2 and F3; however, grain size, grain sorting, and thickness are different. This F4 lithofacies is 10.2 ft thick composed of fine to medium-grained, well to moderately sorted sandstone. Iron oxides healed horizontal fractures are observed in several intervals of the whole core but mostly in the upper part (i.e. Figure 4.1B,c).

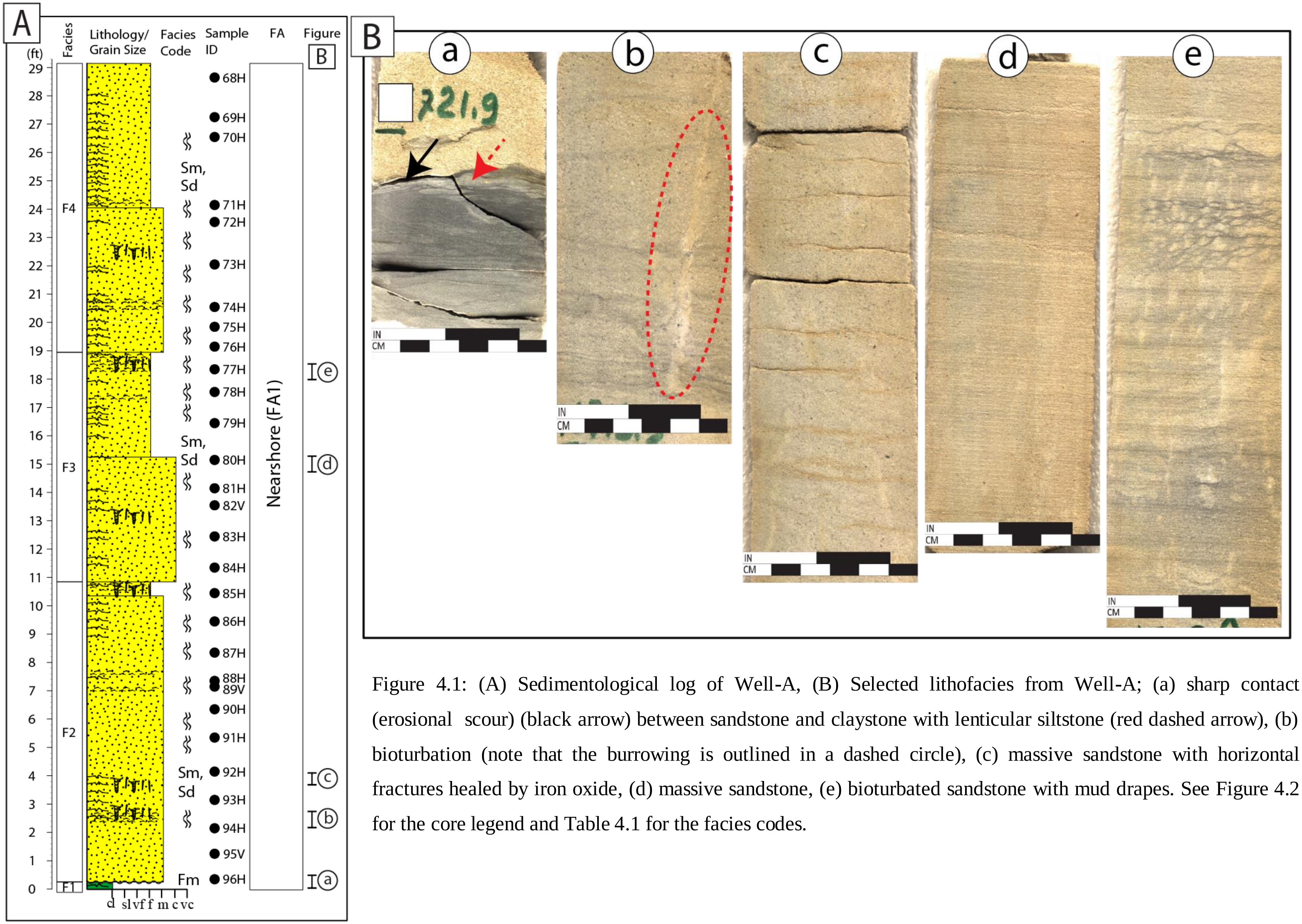

Figure 4.1: (A) Sedimentological log of Well-A, (B) Selected lithofacies from Well-A; (a) sharp contact (erosional scour) (black arrow) between sandstone and claystone with lenticular siltstone (red dashed arrow), (b) bioturbation (note that the burrowing is outlined in a dashed circle), (c) massive sandstone with horizontal fractures healed by iron oxide, (d) massive sandstone, (e) bioturbated sandstone with mud drapes. See Figure 4.2 for the core legend and Table 4.1 for the facies codes.

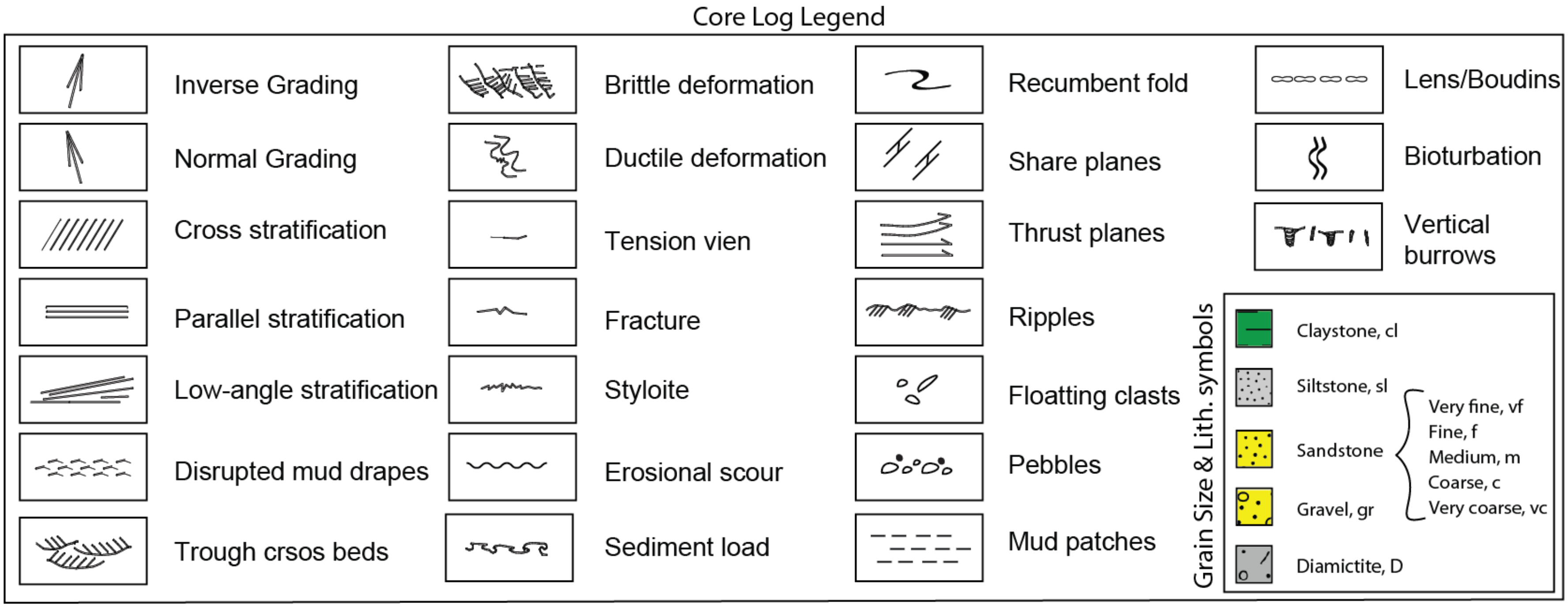

Figure 4.2: The legend for all sedimentological logs. (for the facies codes, see Table 4.2)

4.2.2 Core Interval of Well-B

The 29 ft thick core interval of Well-B is classified into eight lithofacies based on lithology, sedimentary structures, and deformation structures (Figure 4.3A). F1 lithofacies is a dark gray claystone/shale with rip-up clasts of light-gray siltstone. This 1.9 ft thick lithofacies is overlain by a 4.2 ft thick highly deformed, dark gray, fine to very fine-grained with minor medium-grained, angular to well-rounded argillaceous sandstone (F2). Deformed clasts of sandstone, veins, folded laminae (Figure 4.3B, a) and disrupted lenses of sandstone (Figure 4.3B,b) were observed in F2. Clay matrix decreases gradually towards F3 lithofacies which is a deformed, light gray to gray, subangular to well-rounded, moderately sorted, fine to medium-grained sandstone. This lithofacies, characterized by folded laminas, shear planes, disrupted clasts of siltstone, disturbed mud partings, and veins, is 8.3 ft thick. Inclined and horizontally fractures filled by mud were also observed in this interval. It is terminated by a 0.5 ft thick of massive clast-supported diamictite (Figure 4.3B,c) overlain by 3.2 ft thick, massive, sandy matrix-supported diamictite (F4). Irregular and disrupted mud partings and slump features (Figure 4.3B,d) were observed in F4. This lithofacies is overlain by F5 lithofacies which is a 3.9 ft thick, deformed, light gray to gray, off white (at the base), massive, sandy matrix-supported diamictite. This lithofacies is further characterized by dark gray, oriented floating intraformational clasts (Figure 4.3B,e), folded laminae, small recumbent fold (Figure 4.3B,f), filled fractures, disrupted mud partings and mud patches. F5 is capped by F6 which is one-foot thick, dark gray claystone with white rip-up clasts of siltstone (Figure 4.3B,g). A sharp contact separates lithofacies F6 from lithofacies F7 which is a 3.9 ft thick, gray to dark gray, fine to medium-grained, massive sandstone. It is characterized by intensive mud patches and horizontal filled fractures. Horizontal stylolites filled by mud separate F7 from F8 lithofacies. The latter lithofacies is composed of light gray to gray, fine to medium-grained, subrounded to rounded, well sorted massive sandstone. Horizontal fractures and stylolites are also observed in this interval (Figure 4.3B,h).

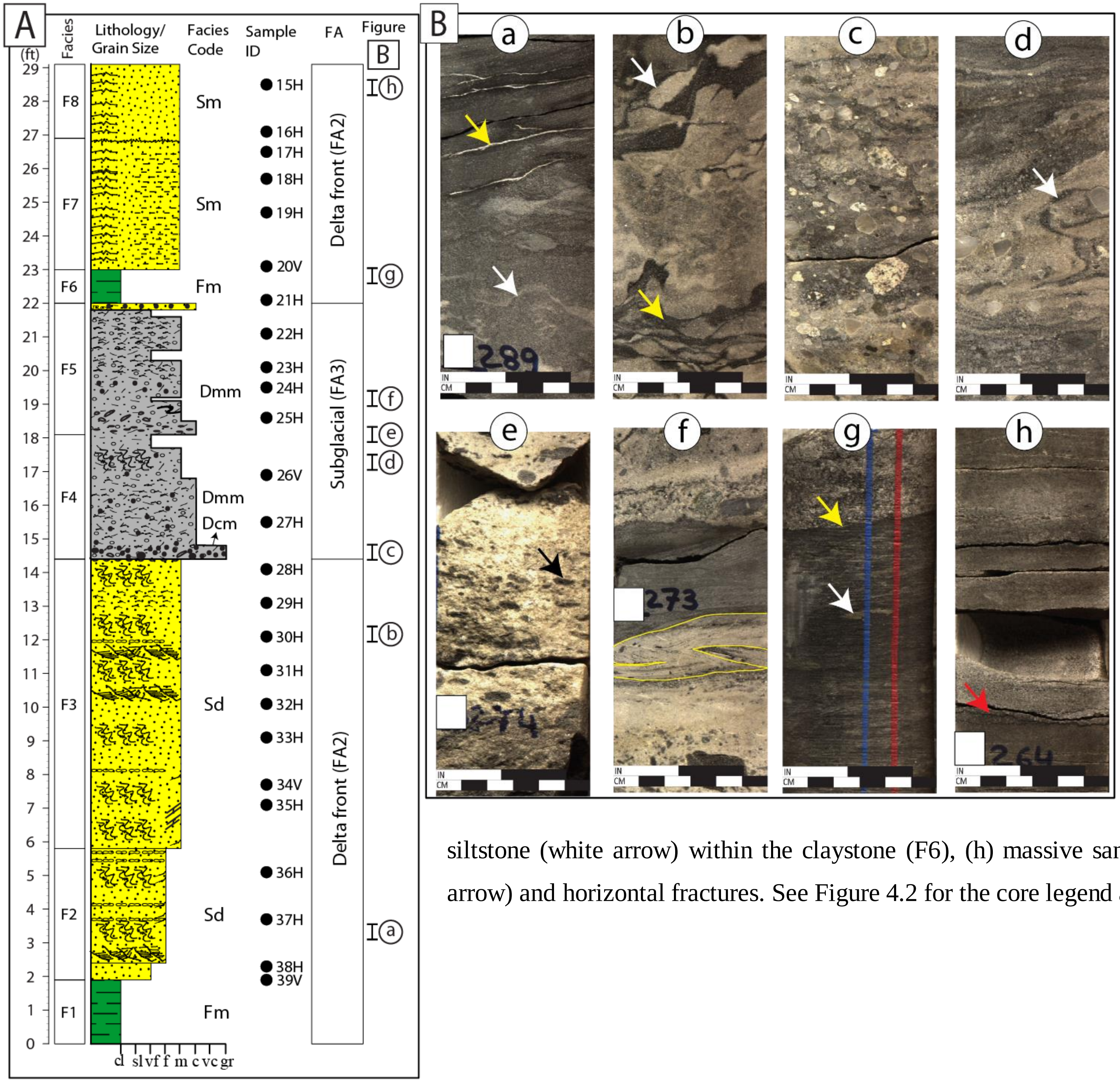

Figure 4.3: (A) Sedimentological log of Well-B, (B) Selected lithofacies from Well-B; (a) folded laminae (white arrow) and tension veins (yellow arrow), (b) brittle deformation generates fractures subsequently filled by mud (yellow arrow) and lenses or boudinage (white arrow), (c) clast-supported diamictite, (d) slump or folded laminae (white arrow) within diamictite, (e) oriented floating intraformational clasts (black arrow) within massive, sandy matrix-supported diamictite, (f) small recumbent fold (outlined in yellow), (g) sharp contact between F6 and F7 lithofacies (yellow arrow) and rip-up clast of siltstone (white arrow) within the claystone (F6), (h) massive sandstone associated with stylolite (red arrow) and horizontal fractures. See Figure 4.2 for the core legend and Table 4.1 for the facies codes.

4.2.3 Core Interval of Well-C

Core representing Well-C is divided into six lithofacies from bottom to top based on changes in color, grain size, and sorting (Figure 4.4A). F1 lithofacies comprises of 16.6 ft thick, gray to dark gray, subangular to subrounded, moderately sorted, fine to medium-grained, massive sandstone. It is occasionally intercalated with thin beds of fine-grained sandstone associated with mud drapes. Stylolite (Figure 4.4B, a,b), clasts of siltstone, and deformation bands (compaction) are observed in this lithofacies. F1 is overlain by a 10.7 ft thick, light gray to gray, subangular to subrounded, moderately sorted, fine to coarse-grained, massive sandstone (F2). Mud drapes, mud patches, floating intraformational clasts (Figure 4.4B,c), erosional scours (Figure 4.4B,d), and stylolites are observed in this interval. F3 is a 4 ft thick, light gray to gray, subrounded to rounded, moderately sorted, medium to coarse-grained, massive sandstone. The contact between this lithofacies and F2 is marked by an erosional scour. Mud patches and mud drapes (Figure 4.4B,e) are also observed in this interval. The actual thickness of F3 is unknown due to unavailability of 3 ft core interval. F4 is a completely broken core with 0.4 ft thickness resembling massive, light gray, subangular to rounded, moderately to poorly sorted, fine to coarse-grained calcareous sandstone. It is overlain by massive, gray, fine to coarse-grained, subangular to rounded, moderately to poorly sorted sandstone with a thickness of 4.2 ft (F5). Another broken core interval of 0.8 ft thickness towards the top of the core interval is classified as F6. This lithofacies is dark gray, massive, fine to medium-grained, occasionally coarse-grained, subangular to subrounded, moderately sorted sandstone.

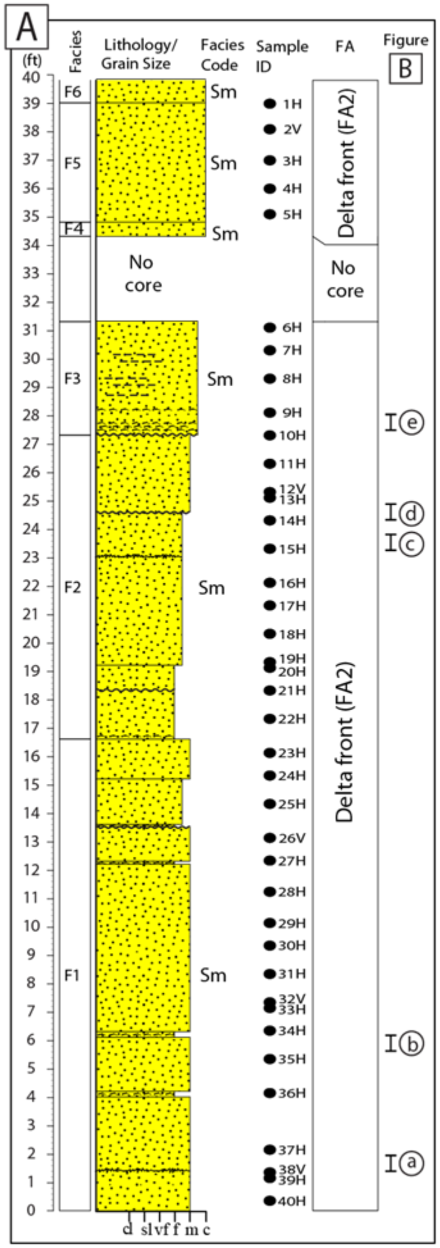

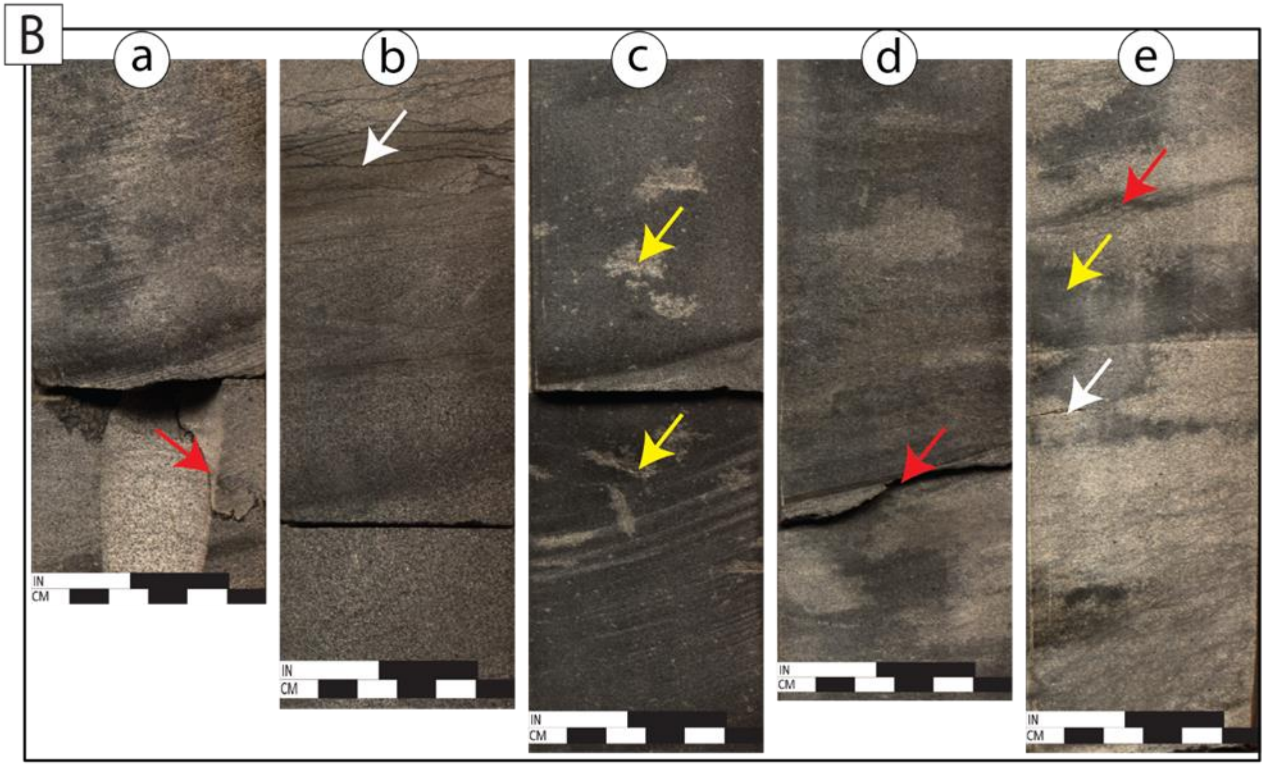

Figure 4.4: (A) Sedimentological log of Well-C, (B) Selected lithofacies from Well-C; (a and b) stylolites within massive sandstone (red and white arrows), (c) floating intraformational clast of sandstone (yellow arrows), (d) erosional scour (red arrow), (e) massive sandstone with mud patches (yellow arrow), mud drapes (red arrow) and horizontal fracture (white arrow). See Figure 4.2 for the core legend and Table 4.1 for the facies codes.

4.2.4 Core Interval of Well-D

The core interval of Well-D is divided into two lithofacies based on a change in lithology and grain size (Figure 4.5A). From bottom to top, the F1 lithofacies consists of 13.2 ft thick massive, matrix-supported, dark gray, horizontally fractured diamictite (Figure 4.5B, a,b). An abrupt change in lithology from F1 to the overlying F2 lithofacies is indicated by erosional scour filled by mud (Figure 4.5B,c). The F2 encompasses massive, pale yellow, light gray, fine to medium grained, subrounded to rounded, well-sorted argillaceous sandstone.

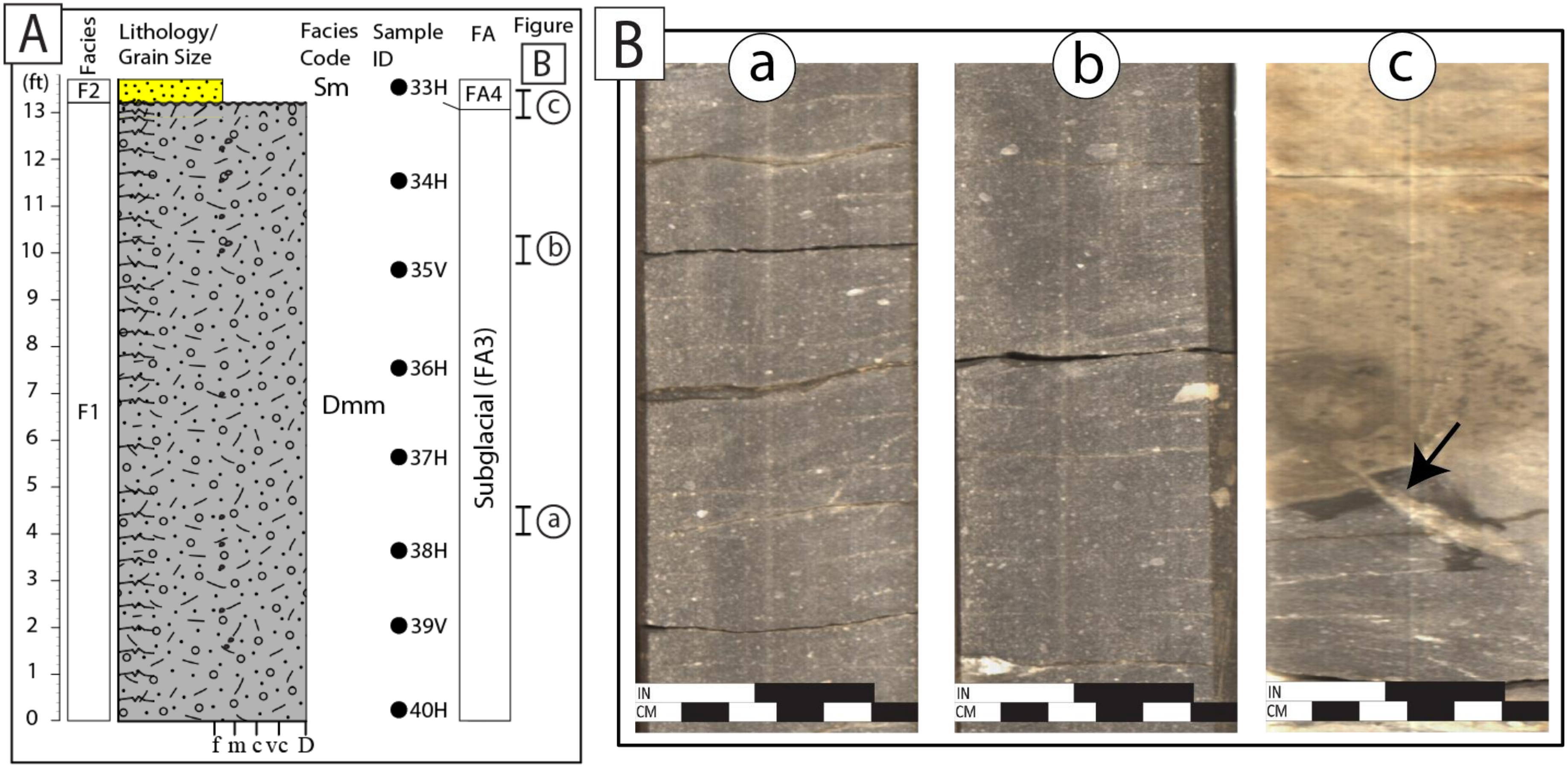

Figure 4.5: (A) Sedimentological log of Well-D, (B) Selected lithofacies from Well-D; (a,b) matrix-supported diamictite with horizontal fractures, (c) erosional scour filled by mud (black arrow) separates the only two lithofacies (F1 and F2) of this core interval. Note that the F1 lithofacies is interpreted as subglacial tillite while the F2 lithofacies is glaciofluvial deposits. See Figure 4.2 for the core legend and Table 4.1 for the facies codes.

4.2.5 Core Interval of Well-E

Based on salient changes in grain size, observable sedimentary, and deformation structures, the cores retrieved from Well-E were classified into eight lithofacies (Figure 4.6A). F1 lithofacies with a thickness of 2.6 ft is comprised of pale yellow, fine to coarse-grained, occasionally very coarse-grained, angular to subrounded, poorly sorted massive sandstone. It commences with horizontally bedded to massive, medium-grained sandstone at the base. Horizontal and inclined filled fractures are observed at the top of this lithofacies. F1 is overlain by a 10.8 ft thick, pale yellow to very light beige, fine to medium, occasionally coarse to very coarse-grained, angular to rounded, moderately to poorly sorted, deformed sandstone of F2 lithofacies (Figure 4.6B, a). Several structures such as irregular filled fractures, erosional scours (Figure 4.6B,b), planar, cross and low angle stratifications, shear planes and convoluted structures distinguish this lithofacies from the others. F2 is followed by a 2.5 ft thick massive, graded, light beige to pale yellow, fine to coarse occasionally very coarse-grained, subangular to rounded, poorly sorted sandstone (F3 lithofacies) (Figure 4.6B,c). F4 is a 2.9 ft thick cross stratified (Figure 4.6B,d), inversely graded (Figure 4.6B,e), light beige to pale yellow, angular to rounded, poorly sorted, medium to very coarse-grained sandstone. It is followed by a 3 ft thick massive, light beige, pale yellow, subangular to rounded, moderately to poorly sorted, fine to very coarse-grained sandstone (F5). F6 lithofacies is a 2.1 ft thick horizontally stratified to massive, deformed, pale yellow, subangular to rounded, moderately to poorly sorted, medium to coarse-grained sandstone. A sharp contact separates lithofacies F6 from lithofacies F7 (Figure 4.6B,f). The latter encompasses 2 ft thick, massive, light gray, pale yellow, subangular to rounded, and poorly sorted, medium to granular grained sandstone. F8 commences with 0.6 ft thick stratified pebbly sandstone (Figure 4.6B,g) overlain by 3.2 ft thick massive, light beige, pale yellow, light gray, subangular to rounded, poorly sorted, medium to coarse-grained sandstone.

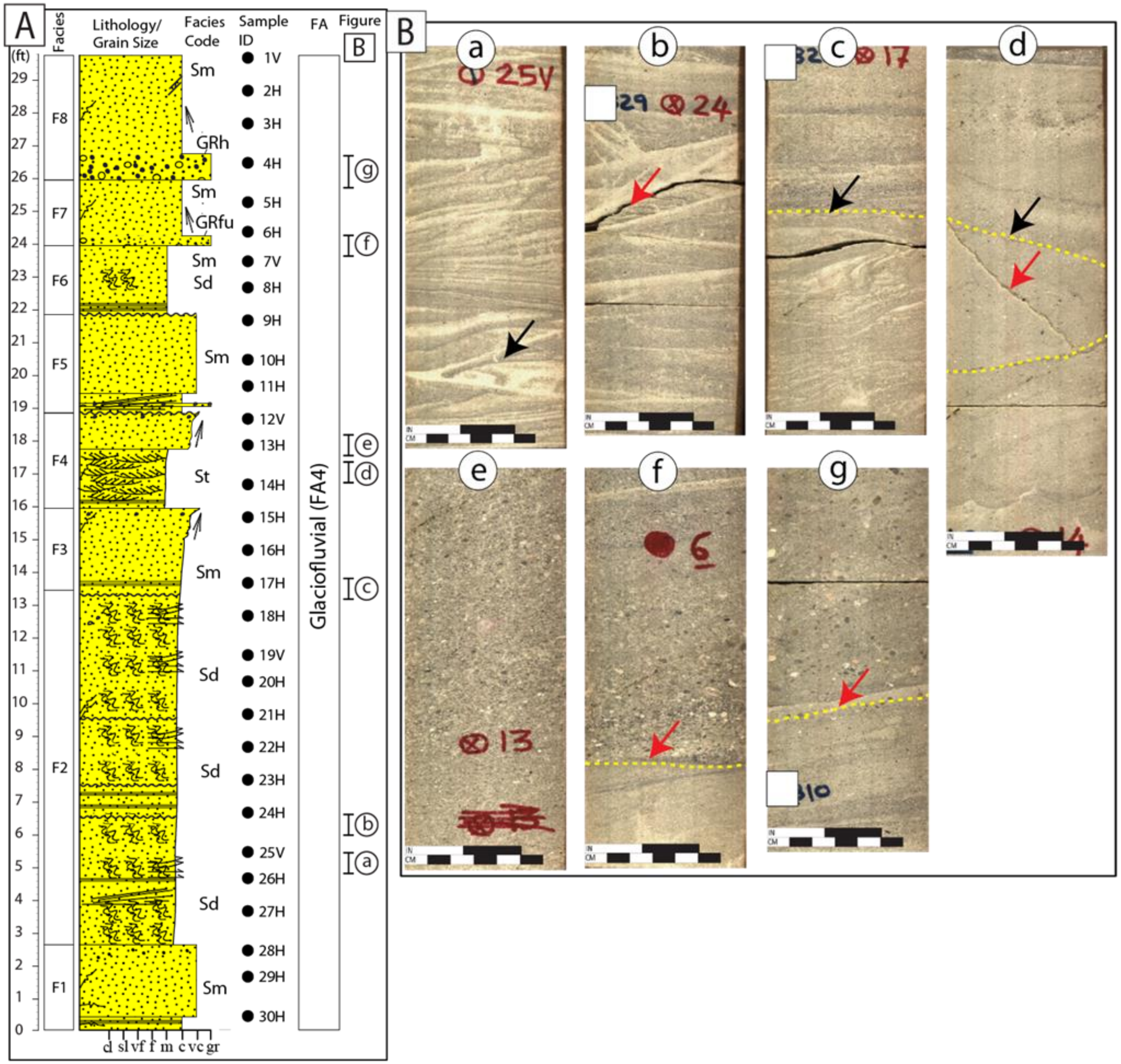

Figure 4.6: (A) Sedimentological log of Well-E, (B) Selected lithofacies from Well-E; (a) deformed lithofacies (convoluted structure is indicated by a black arrow), (b) another deformed lithofacies with erosional scour (red arrow), (c) sharp contact between deformed and undeformed lithofacies (black arrow), (d) cross stratification (black arrow) with an inclined fracture (red arrow), (e) inversely graded lithofacies, (f) channel base surface (red arrow) between massive and graded sandstone, (g) another channel base surface of pebbly sandstone lithofacies. See Figure 4.2 for the core legend and Table 4.1 for the facies codes.

4.2.6 Core Interval of Well-F

Based on the changes in lithology and sedimentary structures, the core interval of Well-F is classified into four lithofacies from bottom to top (Figure 4.7A). F1 lithofacies comprises of a 3.5 ft thick, dark gray, massive, matrix-supported diamictite (Figure 4.7B, a). It is followed by a 1.9 ft thick, dark gray, fissile shale interbedded with gray, stratified diamictite (F2) (Figure 4.7B,b). The latter is overlain by 1.3 ft thick dark gray, massive, matrix-supported diamictite of F3 lithofacies. The F3 is in turn followed by 1.9 ft thick of dark gray, horizontally fractured, fissile shale intercalated at the base with thin beds of dark-gray, stratified diamictite (F4) (Figure 4.7B,c,d).

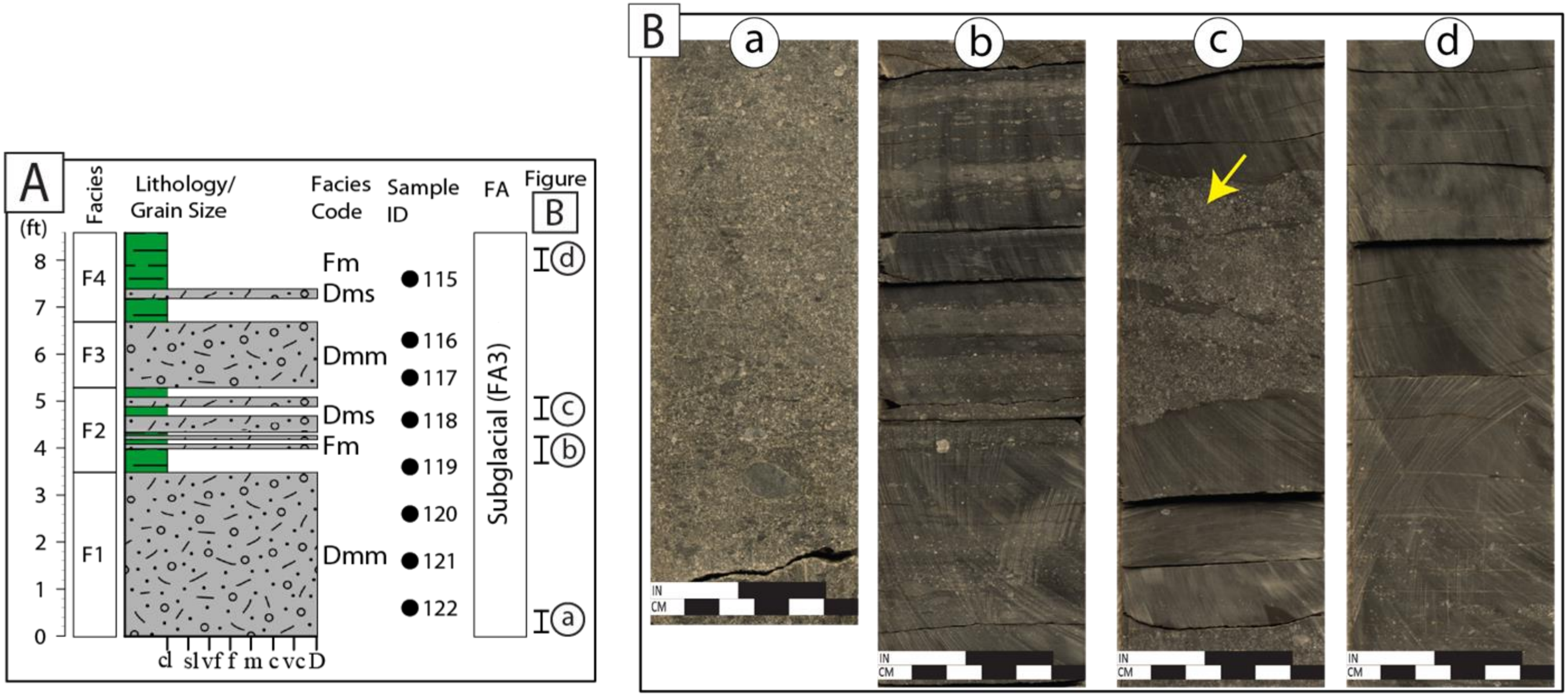

Figure 4.7: (A) Sedimentological log of Well-F, (B) Selected lithofacies from Well-F; (a) matrix supported-diamictite, (b) stratified, matrix-supported diamictite with horizontal fractures, (c) fissile shale intercalated with matrix-supported diamictite (yellow arrow), (d) fissile shale with horizontal fractures. Note: in the sedimentological log (A), F2 and F3 can be considered as a transition zone between Sarah and Qusaiba Formations. See Figure 4.2 for the core legend and Table 4.1 for the facies codes.

4.3 Lithofacies Association Interpretation

A group of facies which is genetically related to a depositional environment is called facies association (Miall, 2000). This detailed study revealed four lithofacies associations (FA) including massive bioturbated sandstone (FA1), grayish massive sandstone (FA2), glaciogenic diamictites (FA3), and partially deformed, graded to massive sandstone (FA4). These lithofacies associations have been interpreted as deposits of nearshore, glaciolacustrine delta, subglacial tillite, and glaciofluvial environments, respectively.

4.3.1 Bioturbated Massive Sandstone (FA1)

FA1 is dominantly comprised of bioturbated massive sandstone (Well-A: F2 to F4). It sharply overlies a thin claystone bed (Well-A: F1) and it is characterized by bioturbation and soft sediment deformation. The coarsening upward sequence from claystone to sandstone indicates a progradational sequence formed during a period of regression. Soft sediment deformation is probably caused by the bioturbation. From thin section study and geochemical analysis, zones of biogenic silica are observed (Figure 4.8e and Figure 6.8). Therefore, the bioturbation, progradational sequence and biogenic silica may suggest the affiliation of this lithofacies association to a nearshore environment. As mentioned earlier, the Sarah Formation is described as a sediment fill deposited in paleovalleys cutting deeply into the older formations (i.e. Zarqa, Qasim and Saq Formations) (Williams et al., 1986; Vaslet et al., 1987; McGillivray and Husseini, 1992). The core interval of Well-A retrieved from the middle part of Sarah Formation (Table 3.1) exhibits bioturbation rather than glacial lithofacies. In other words, no glacial evidence is observed in this core. Pre-Sarah Formations (i.e. Qasim Formation) contains the former lithofacies. Thus, this core interval might be pre-Sarah Formation rather than Sarah Formation and the core might be retrieved from one of the valley margins. However, in the subsequent characterizations of this study, we considered it as Sarah Formation following MEIMR.

4.3.2 Grayish Massive Sandstone (FA2)

The F1 to F3 and F6 to F8 of Well-B represent two coarsening upward sequences. They are interpreted to represent two progradational sequences. The first sequence is highly affected by deformation observed as brittle and ductile deformations. The second sequence is an undeformed interval, but it is dominated by horizontal fractures and mud patches. The sandstone of each sequence is interpreted as deposits of a glaciolacustrine delta front while the claystone was deposited by suspension deposited in a prodelta. However, the prodelta can be included within delta front (Reading and Collinson, 1996). A delta prograded over fine sediments due to large loads of sediments or quick fall into a lake level (Reading and Collinson, 1996). All lithofacies of Well-C are also interpreted as a glaciolacustrine delta front environment. The massive sandstones of both wells, Well-B and Well-C, indicate that the sediments were deposited by gravity flow (Miall, 2000).

4.3.3 Diamictites (FA3)

Diamictite is a non-genetic term used for lithified, unsorted, matrix-supported sediments while tillite, on the contrary, is a genetic term for the glacial environment (Miller, 1996). Another definition for the diamictite was suggested by Bates and Jackson (1980) who defined the diamictite as poorly sorted sediments having a wide range of grain sizes in a relatively fine matrix (cf. Melvin, 2015). Different processes in both polar and temperate glaciomarine settings usually generate massive and stratified diamictite (Isbell, 2010). The former is produced by melting out glacier's basal debris while the latter is formed by winnowing out of fine grains where the rate of sediments is low (Domack et al., 1999; cf. Isbell, 2010).

The F1 of the Well-D and F1, F2, and F3 of Well-F are interpreted as subglacial melt out tillites. Since the core interval of Well-F is extracted from a transition zone between Sarah and Qusaiba Formations (Table 3.1), the F4 lithofacies of this well is expected to be Qusaiba Formation and the underlying stratified diamictite intercalated with shale (F2 and F3) is expected to be a transition zone between these formations.

At the base of F4 in the Well-B core is 0.5 ft thick, clast-supported diamictite. Although Miller (1996) suggested that the term of diamictite should be restricted to the matrix-supported diamictite based on the original definition of the diamictite, the term of clast-supported diamictite was used by several authors such as Schultz (1984) and Eyles et al. (1983). This study follows the latter authors since they differentiated several types of diamictites. The massive, clast-supported diamictite of Well-B (F4) is overlain by massive, sandy matrix-supported diamictite. The former might have been deposited rapidly due to the influence of the gravity during the early stage of the deglaciation from pseudoplastic debris flow while the latter were likely been produced from plastic debris flow (Schultz, 1984). F5 of Well-B is also massive sandy matrix-supported diamictite with floating clasts at the base. However, floating clasts are indicative of cohesive debris flow (Johnson, 1984; Shultz, 1984; cf. Sohn et al., 2002). The slump and small recumbent fold observed at the top of F4 and F5, respectively, are indicative of glacial movement where they might be formed during the late stage of deglaciation. F4 and F5 of Well-B are interpreted as subglacial tillite/moraine which commonly experienced post-depositional deformation due to ice melt and ice motion (Edwards, 1986; cf. Clark-Lowes, 2005).

4.3.4 Partially Deformed Graded to Massive Sandstone (FA4)

FA4 represents all the lithofacies from Well-E which encompasses massive undeformed sandstone overlain by deformed and disrupted sandstone lithofacies followed by graded to massive sandstone. The massive sandstone is interpreted as gravity flow deposits while the graded sandstone is expected to have been deposited from pseudoplastic debris flow (Miall, 2000). Glacial processes are commonly superimposed upon other environments’ processes (Miller, 1996); therefore, the glacial motion might have disrupted the pre-existing lithofacies observed in the deformed interval of FA4. The evidence of the glacial deformation observed in the lithofacies includes shear planes, thrust planes, and convoluted structures. The undeformed inversely graded lithofacies which overlie the disrupted interval of FA4 are interpreted as longitudinal bars. The overlaying normal graded intervals likely represent stacked channels.

4.4 Lithofacies and Depositional Models

As an attempt to correlate the interpreted depositional environments throughout the basin, a correlation model for lithofacies associations is proposed for similar depositional environments (Figure 4.8). However, Well-A core interval representing the nearshore environment exhibits no correlation with the other cores. The diamictites lithofacies of Well-B representing subglacial environment is correlated with the other diamictites lithofacies observed in Well-D and Well-F. The massive grayish sandstones lithofacies in Well-B and Well-C have been correlated to each other. Both wells are interpreted as glaciolacustrine delta deposits. The sandstone lithofacies of Well-E is correlated with the sandstone lithofacies of Well-D as they represent a glaciofluvial environment.

Based on the observation collected from the facies analysis of core samples, following several published studies on the Sarah Formation (see sections 1.4 and 2.3) and the gravity map produced by Saudi Geological Survey (Figure 4.9g), a conceptual depositional model for the identified lithofacies associations is proposed (Figure 4.10). This model illustrates different depositional environments including glaciofluvial (FA4), glaciolacustrine delta (FA2), subglacial (FA3) and nearshore (FA1) environments for the Sarah Formation.

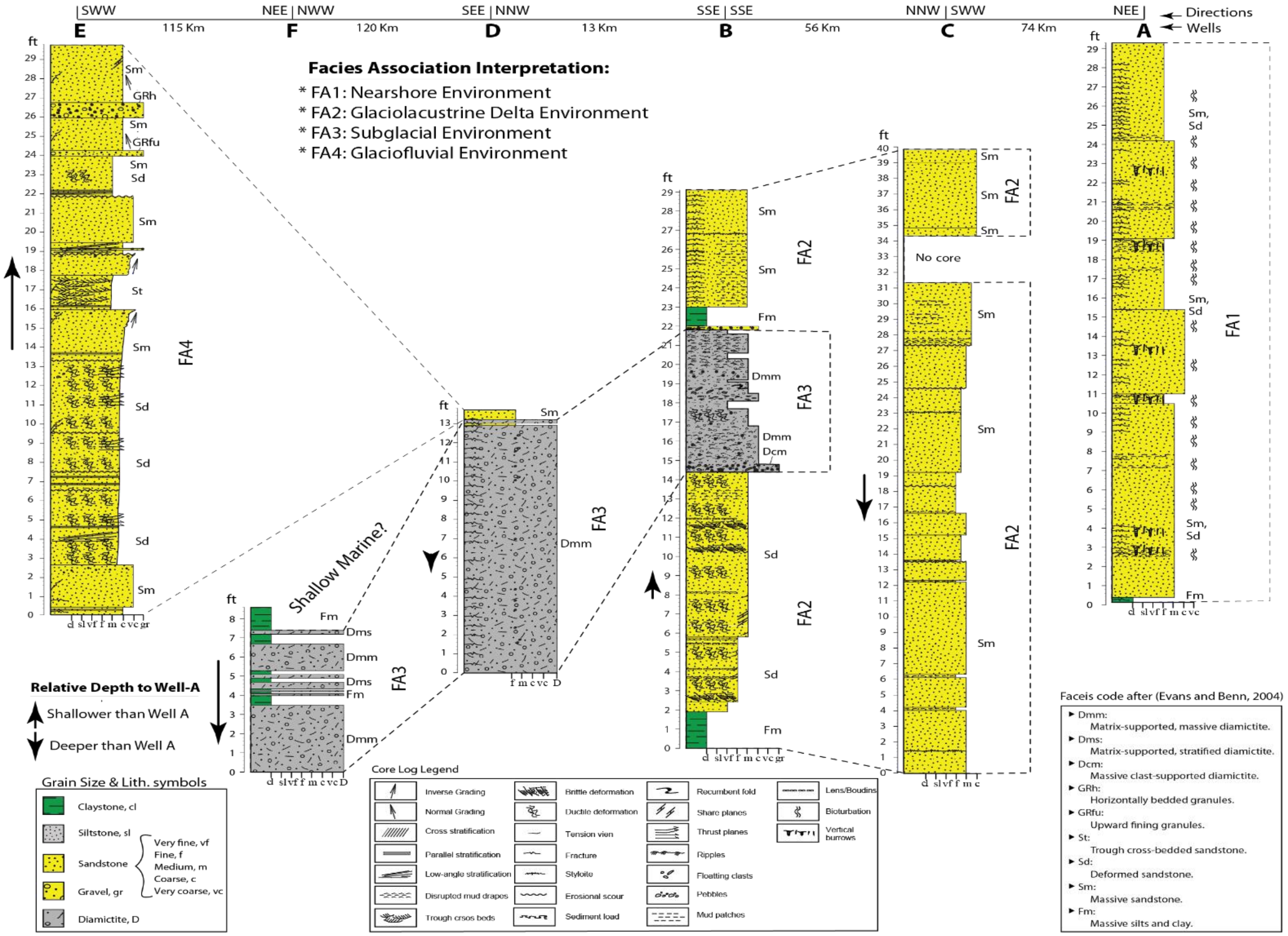

Figure 4.8: Lithofacies association correlation model. This model is designed based on the similarity of depositional environments. For instance, the diamictites lithofacies of Well-B is correlated with the other diamictites lithofacies of Well-D and Well-F. The shale overlying the diamictite of Well-F is expected to be the Qusaiba shallow marine deposits. The nearshore is not correlatable with the others and is expected to be Sarah or pre-Sarah Formation (i.e. Qasim Formation).

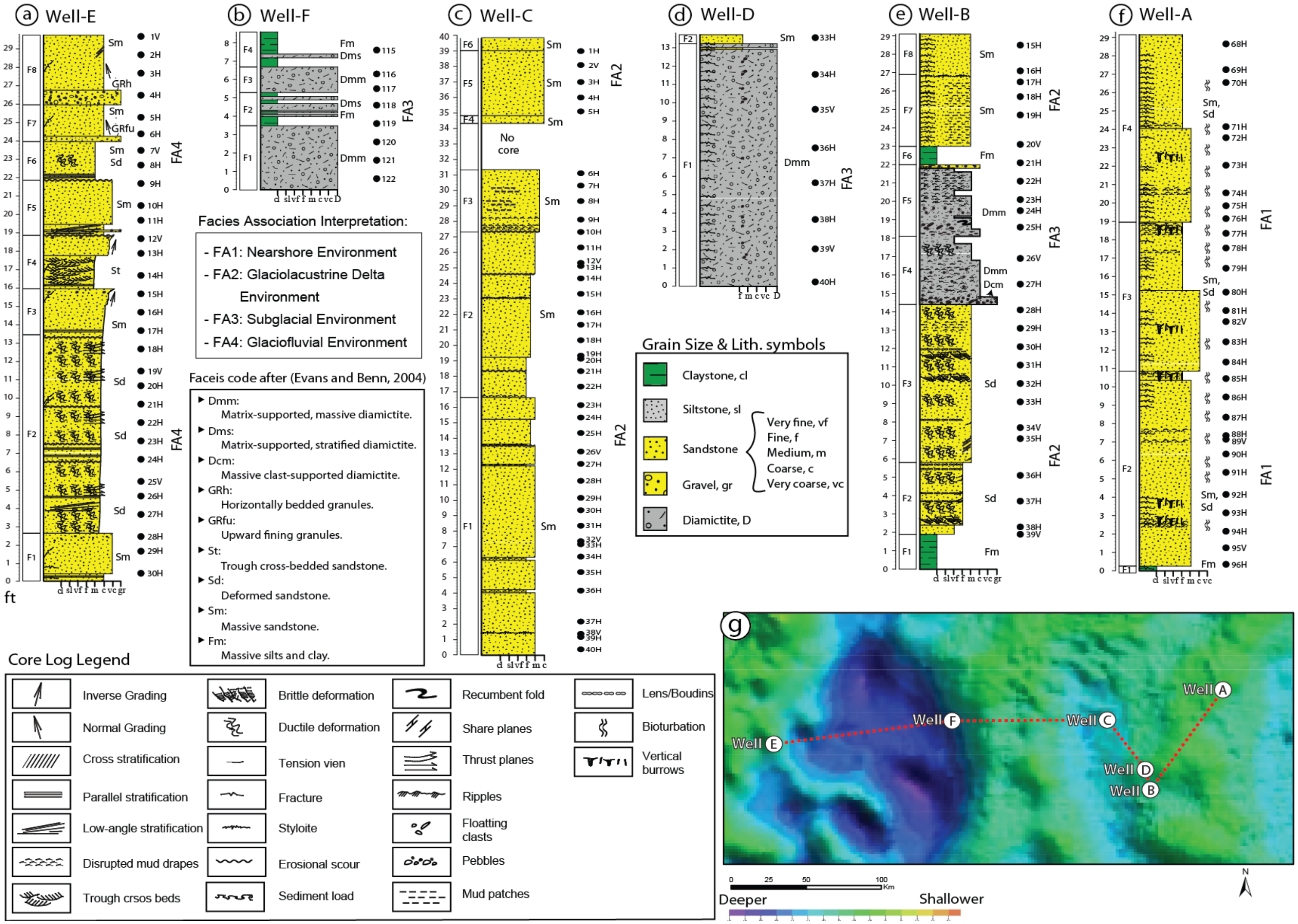

Figure 4.9: Sedimentological logs of all wells with gravity map and selected samples. (a-f) sedimentological logs of the wells, (g) gravity map of the study area after Saudi Geological Survey. Note that dark blue color in the gravity map indicates basement depression while the green color indicates basement high.

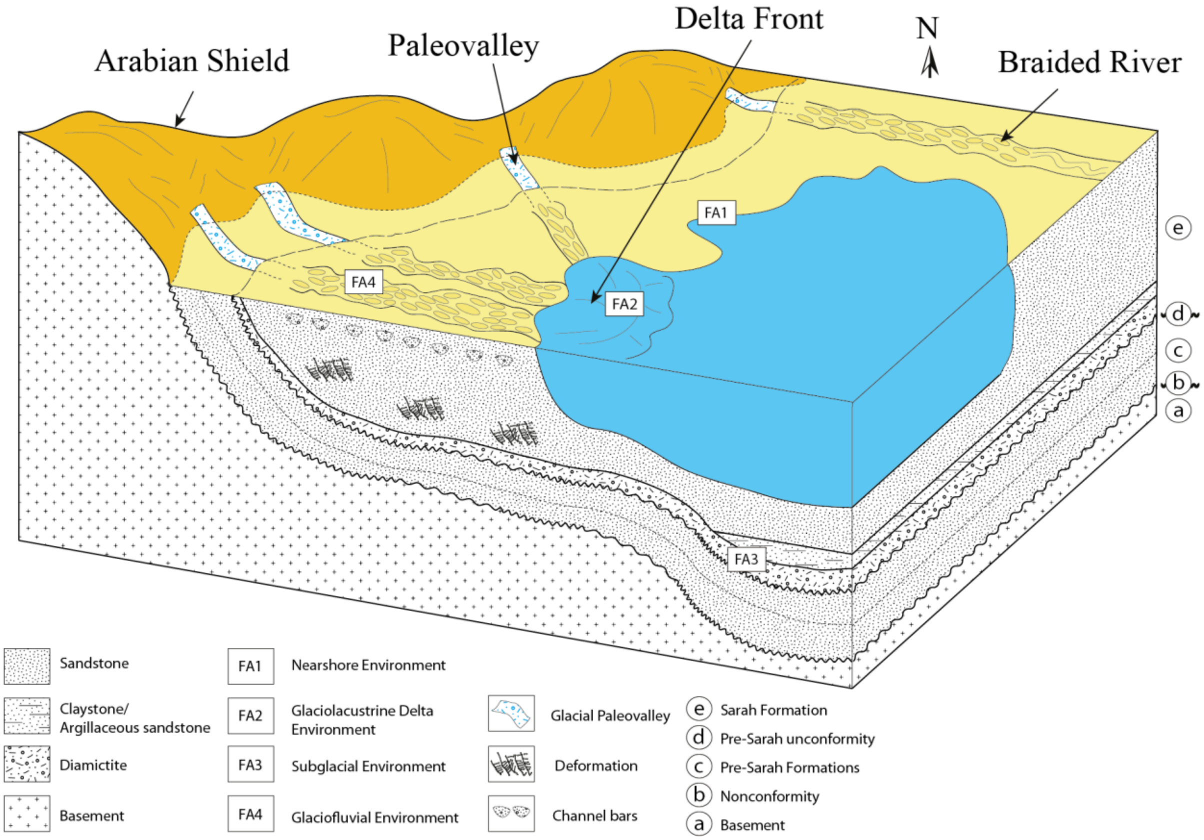

Figure 4.10: A conceptual depositional model for the Late Ordovician glaciogenic Sarah Formation in the northern part of the Rub' Al-Khali basin and its surrounded areas. This model is constructed based on the observation collected from the facies analysis of the core samples and following previous studies published in the southwestern part of Saudi Arabia.

4.5 Discussion

According to the MEIMR, the whole core intervals of this study, except Well-A core samples, were retrieved from the upper part of the Sarah Formation in the Rub' Al-Khali Basin (see Table 3.1). The Well-A core interval was obtained from the middle part of the Sarah Formation. This is a limitation where the cores do not represent the whole formation. Despite the long distance between the wells (Figure 1.2b), the difficulty with the core description and interpretation cannot be compared with the outcrop studies (Le Heron et al., 2009; Miall, 2015). However, the interpretation of the studied cores is based on our observations associated with several examples for the same lithofacies published literature. The interpreted depositional environments of these cores vary from the glaciofluvial environment (Well-E; close to the Arabian Shield) to the glaciolacustrine and subglacial environments (Well-B, Well-C, Well-D, and Well-F; near the basin center), to the nearshore environment (Well-A; eastward) (Figure 1.2b). Several published studies on the subsurface of Saudi Arabia indicated that the Late Ordovician Sarah Formation is characterized by various facies ranging from periglacial to proglacial facies (glaciofluvial and glaciomarine) (Senalp and Al-Laboun, 1996, 2000; Craigie and Rees, 2016; Craigie et al., 2016).

The glaciofluvial environment is almost characterized by the same facies of the non-glacial braided fluvial system (Miller, 1996). Multiple erosion and deposition, scours and channels suggested a high energy environment (Melvin and Sprague, 2006). The observed deformed facies such as shear zones, thrust planes, and folds are a result of glacial movements (Le Heron et al., 2009). From the subsurface, these disrupted facies were observed in the Lower Unayzah (Unayzah C) and interpreted as glaciofluvial deposits (Senalp and Al-Duaiji, 2001; Melvin and Sprague, 2006).

During the glaciation, the ice moved toward a depression to be deposited in a glaciolacustrine setting (Le Heron et al., 2009). Based on the gravity map of SGS, the study area lies on two basement depressions (grabens-like). The deepest one is located below the Well-F whilst the other one is beneath the Well-C, Well-D, and Well-B. The former was recognized and described as intrashelf depression by Konert et al. (2001). In this study, the subglacial and glaciolacustrine environment are identified in these depressions. The main criteria for recognition of the subglacial environment are the diamictites observed in various characteristics including massive matrix-supported diamictite, stratified matrix-supported diamictite, massive clast-supported diamictite, and massive sandy matrix-supported diamictite. Comparable features for stratified diamictite were published by Isabel (2010) from the outcrop of the Lower Permian Metschel Tillite, southern Victoria Land, Antarctica. Briner et al. (2010) also reported massive matrix-supported diamictites from Hawban “member” in the southern part of the Rub’ Al-Khali Basin that is similar to the diamictites of Well-D. From the Qusaiba-1 borehole core, Melvin (2015) stated that the stratified diamictite of the Baq’a Shale Member (Sarah Formation, Central Saudi Arabia) indicates a retreat of the Hirnantian glaciations. The extension of these glaciations into the Arabia remains unknown (Le Heron et al., 2009). However, the diamictites of the Well-F, Well-B, and Well-D, are considered as Hirnantian glaciations deposits.

In the glaciolacustrine delta environment (i.e. Well-B), two progradational sequences are observed. These sequences are separated by the intervening diamictite which was likely deposited during the glaciation period. Each of sequences consists of sandstone overlain claystone. The sandstone is interpreted as delta front deposits (also called the distal bar or delta platform (Scholle and Spearing, 1982)) while the claystone is interpreted as prodelta deposits. They can be considered as a delta front (Reading and Collinson, 1996). Several structures such as a small recumbent fold, folded laminae, and low angle bed indicate that these lithofacies were deposited on a slope. The core interval of Well-C is also interpreted as glaciolacustrine delta front deposits because it shows similar delta front facies of the Well-B.

At the eastern margin of the study area, the core sample of Well-A is characterized by massive bioturbated sandstone overlying claystone. This progradational lithofacies sequence differs from the progradational sequence of the delta. The former is interpreted as a nearshore. The bioturbation, biogenic silica, and progradational sequence are the main criteria for recognizing this environment.

CHAPTER 5

PETROGRAPHICAL CHARACTERIZATION

5.1 Introduction

A total number of 140 thin sections provided by MEIMR were studied under a petrographic microscope. These thin sections were taken from the end of each, approximately per foot vertical spacing. By this study, additional thin sections were prepared for missing intervals. For the petrographic characterization, this chapter contains several sections. Section 5.2 illustrates the quantitative mineralogy and texture for all samples and provides a modal composition for each well. The data of Quartz, feldspar and lithic rock fragments (QFL) was determined under a petrographic microscope following Gazzi-Dickinson method with three-hundred point-counting. The sandstone provenance following Dickinson (Dickinson, 1985) and sandstone classification following Folk (1980) are established using the spreadsheet suggested by Zahid and Jr (2011) and illustrated in section 5.3. Further analysis on selected samples taken based on facies change was conducted using XRD and SEM/EDX. The former is used to identify mineralogical composition (section 5.4) and the latter is utilized to identify clay minerals, their morphology and define the pore filling minerals (section 5.5). The diagenetic facies observed in the thin section study are highlighted in section 5.6. However, their effects on reservoir quality of the studied core intervals are discussed in more details in the petrophysical characterization chapter (see section 7.6). Finally, the whole petrographic results from this study are discussed in section 5.7.

5.2 Quantitative Mineralogy and Texture

Petrographically, the Well-A core interval (nearshore lithofacies) is characterized by $Q_{93}F_{6.6}L_{0.4}$ and grain size ranging from very fine to medium, angular to rounded, loose to compacted and moderately to poorly sorted grains. The grain contacts are mainly point to long, but also, they show concavo-convex and sutured contacts in several samples (Figure 5.3 and Table 5.1).

The Well-B core interval has been divided into two parts, glaciolacustrine and subglacial lithofacies. The former is characterized by $Q_{94}F_2L_4$ and by poorly sorted, occasionally moderately sorted, angular to rounded, and very fine to coarse grains with average 20% matrix content (claystone and siltstone). The grains are mainly loose with floating, point, and long contacts. However, compacted grains are common showing concavo-convex and sutured contacts. The latter is characterized by $Q_{91}F_{1.5}L_{7.5}$ and by fine to very coarse, very poorly sorted, and angular to rounded grains with average 30% matrix content. Most of the grains are loose and floated, but there are common point and long contacted grains (Figure 5.4 and Table 5.2).

The Well-C core interval (glaciolacustrine lithofacies) contains $Q_{97}F_2L_1$ and grain size ranging from very fine to coarse, angular to rounded, and moderately to poorly sorted grains. Few samples in this core are matrix-rich reaching up to 25%. The packing of the grains is varied from loose to compacted and the grain contacts are dominated by point and long contacts; however, concavo-convex and sutured contacts were also observed in several samples (Figure 5.5 and Table 5.3).

In the core interval of Well-D (glaciofluvial lithofacies), only one sample was taken from the available small core and is characterized $Q_{95}F_1L_4$ and fine-grained, subangular to rounded and poorly sorted sandstone. The contacts between grains are point and long while the packing of the grains is mainly loose. The rest of the samples of this core is for subglacial environments. They consist of $Q_{94}F_1L_5$ and grain size ranging from very fine to very coarse grained, subangular to rounded, moderately to poorly sorted. Floating and point contacts between grains are dominant while their packing is loose (Figure 5.6 and Table 5.4).

The core interval of Well-E (glaciofluvial lithofacies) is characterized by $Q_{92}F_1L_7$ and fine to very coarse grained, poorly to very poorly sorted, occasionally moderately sorted, and angular to rounded sandstone. Point and long grains contacts are dominant and they are commonly associated with concavo-convex and sutured contacts (Figure 5.7 and Table 5.5).

In Well-F core interval (subglacial lithofacies), the samples contain $Q_{89}F_3L_8$ and are poorly sorted, very fine to very coarse grained, angular to rounded grains with ~40% matrix contents. However, they are dominated by floating and point contacts (Figure 5.8 and Table 5.6).

5.3 Sandstone Classification and Provenance

The Well-A core interval (nearshore lithofacies) has been classified as subarkose derived from craton interior. While the glaciolacustrine delta of Well-B core is mainly quartzarenite to sublitharenite originated from craton interior and recycled orogen, the subglacial lithofacies of this core is sublitharenite sourced from recycled orogen. However, the core interval of Well-C (glaciolacustrine lithofacies) is characterized by quartzarenite derived from craton interior. The glaciofluvial lithofacies of Well-D is quartzarenite to sublitharenite originated from craton interior and recycled orogen whilst the diamictites lithofacies (subglacial facies) of this well is sublitharenite originated from recycled orogen. The Well-E core interval (glaciofluvial lithofacies) is classified as sublitharenite sourced from recycled orogen whilst the core interval of Well-F (subglacial lithofacies) is classified as sublitharenite with minor samples of subarkose originated from recycled orogen. Based on the depositional environments, the sandstone classifications of all cores are illustrated in Figure 5.1 whilst the provenance is illustrated in Figure 5.2.

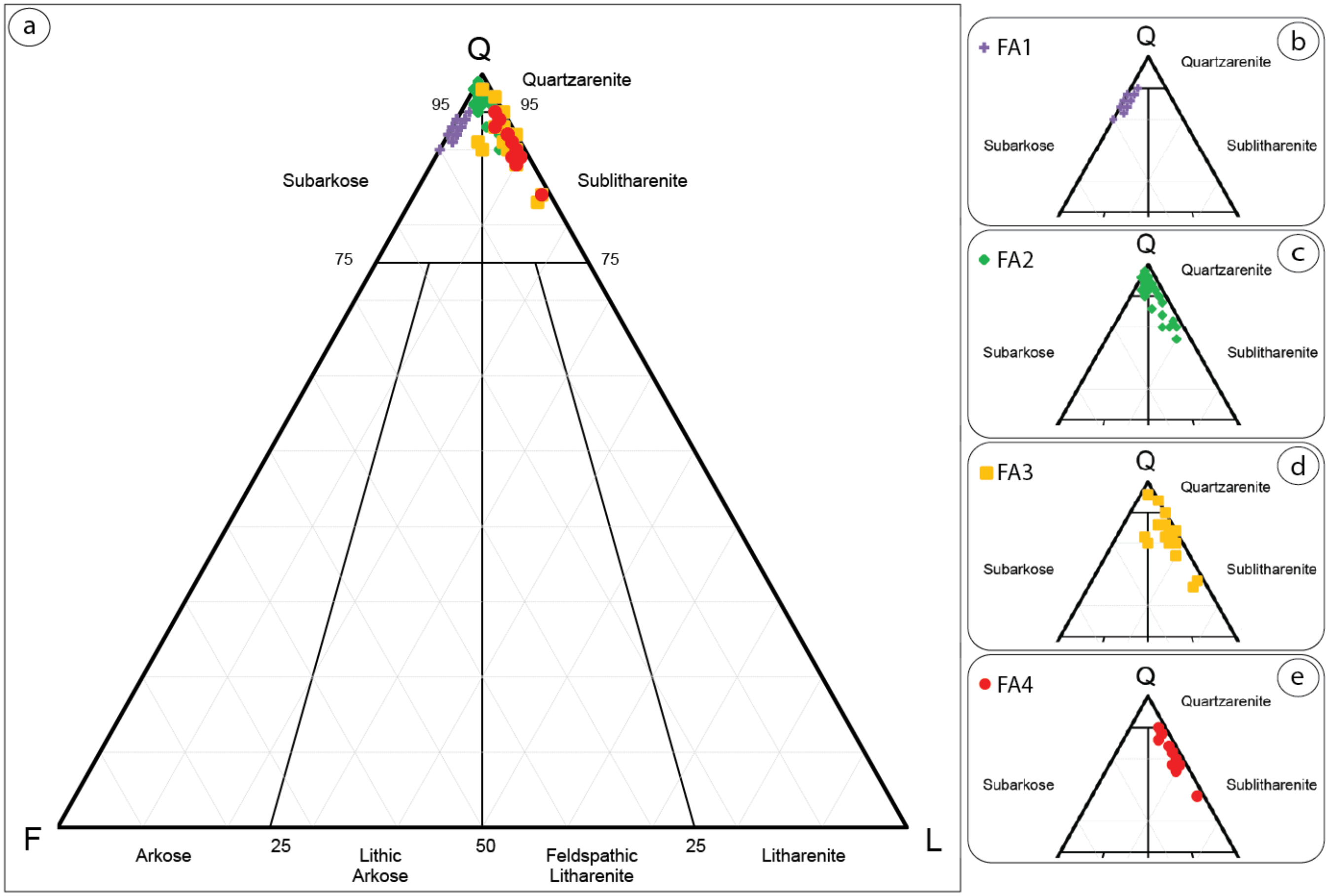

Figure 5.1: Sandstone classification of the studied environments based on Folk (1980) classification. (a) showing the sandstone types of all environments ranging between subarkose, quartzarenite and sublitharenite, (b) nearshore (FA1) is subarkose, (c) glaciolacustrine delta (FA2) ranges from sublitharenite to quartzarenite, (d) subglacial (FA3) is mainly sublitharenite, and (e) glaciofluvial (FA4) is sublitharenite. Q: quartz, F: feldspar, L: lithic rock fragments.

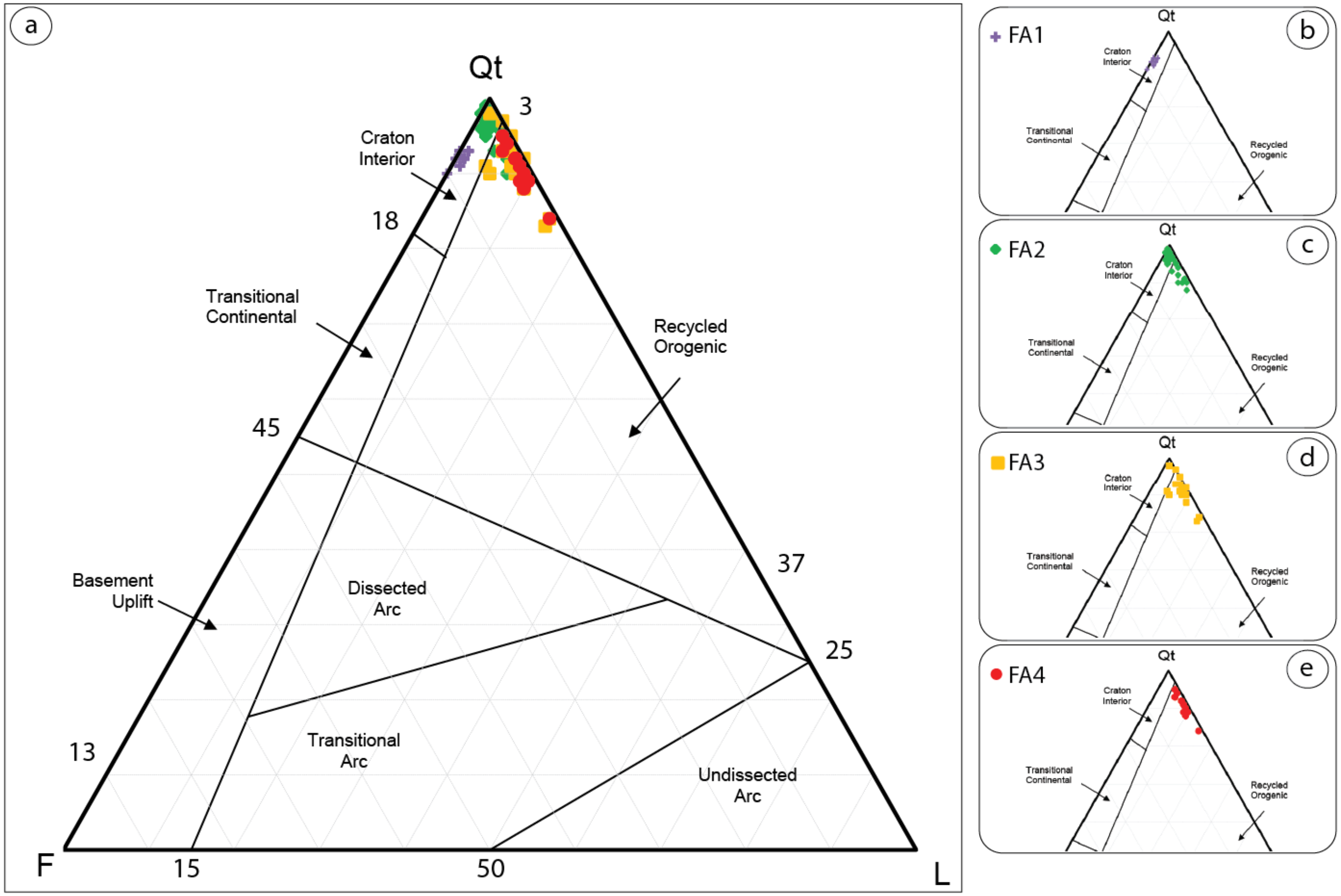

Figure 5.2: Sandstone provenance of the studied environments based on Dickinson (Dickinson, 1985) classification. (a) provenance of all environments ranges between carton interior and recycled orogen, (b) nearshore (FA1) was derived from craton interior, (c) glaciolacustrine delta (FA2) was originated from craton interior and recycled orogen, (d) subglacial (FA3), and (e) glaciofluvial (FA4) were mainly derived from recycled orogen. Q: quartz, F: feldspar, L: lithic rock fragments.

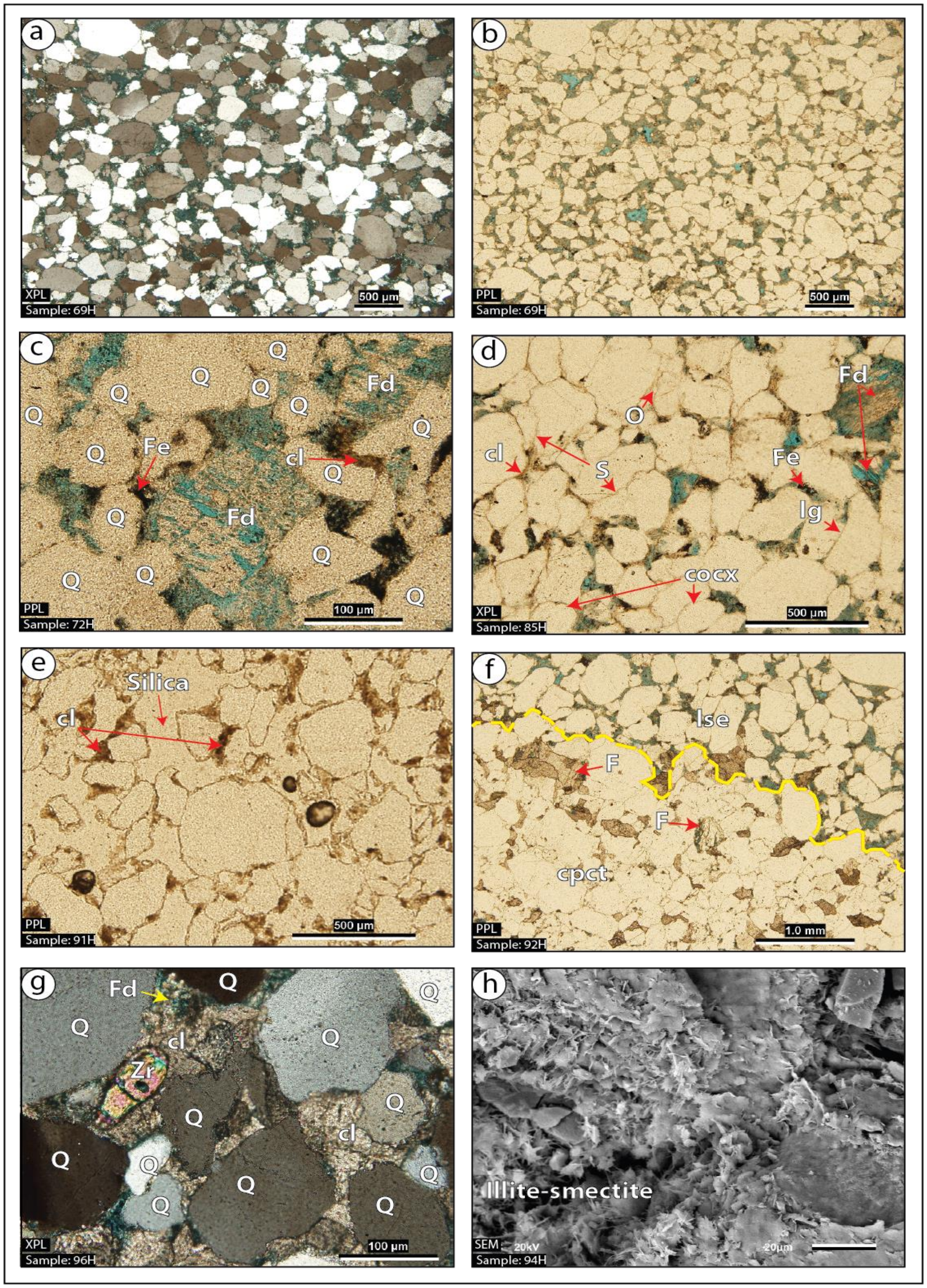

Figure 5.3: Selected photomicrographs from Well-A; (a,b) intergranular porosity, (c) feldspar dissolution (Fd), (d) grains contacts, (e) silica cement, (f) heterogeneity, (g) clay (cl), (h) illite-smectite. Q: quartz, S: sutured, cocx: concavo-convex, lg: long, O: quartz overgrowth, Fe: iron oxide, cpct: compacted, lse: loose, Zr: zircon.

Table 5.1: Modal composition of the Well-A core interval. The classification is based on Folk (1980) while the provenance is based on Dickinson (Dickinson, 1985). The sweet spots are based on the absent or present of each type (For the abbreviation see Table 5.4)

Wells	FA	Sample ID	Texture						Minerals %			Matrix %	Cement %	Cement type	Visual Porosity %	Classification	Provenance	Sweet Spots		
			Grain Size ≥ 20%	Sorting	Roundness	Sphericity	Grains contact	Packing	Quartz	Feldspar	Lithic							Frac.	Diag.	Depo.
A	1	68H	vf-m	mod-prly	ang-rnd	H	lg, cocx,s	cpct	94	5	1	-	3	Clay	3	sb-ark	ctn-int		■	■
A	1	69H	f-m	mod-prly	ang-sb-rnd	H	pnt, lg, cocx	cpct	95	4	1	-	5	Clay, Fe	5	qz-ar	ctn-int		■	■
A	1	70H	vf-m	mod-prly	ang-rnd	H	pnt, lg, s	lse, cpct	93	6	1	-	5	Fe, Clay	7	sb-ark	ctn-int		■	■
A	1	71H	f-m	mod	ang-rnd	H	pnt, lg, cocx	cpct	94	6		-	3	Fe, Clay, Silica	5	sb-ark	ctn-int		■	
A	1	72H	f-m	mod	ang-rnd	L-H	pnt, lg, cocx	cpct	92	8		-	3	Clay, Fe	7	sb-ark	ctn-int		■	
A	1	73H	f	mod	ang-sb-rnd	L-H	pnt, lg, cocx	cpct,lse	93	6	1	-	3	Clay, Fe	7	sb-ark	ctn-int		■	
A	1	74H	f	mod	ang-sb-rnd	L-H	pnt, lg	cpct,lse	94	6		-	5	Clay, Fe, Silica	7	sb-ark	ctn-int		■	
A	1	75H	f-m	mod	ang-sb-rnd	L-H	pnt, lg	cpct,lse	94	6		-	3	Clay, Fe	10	sb-ark	ctn-int		■	
A	1	76H	f-m	mod	ang-sb-rnd	L	pnt, lg	cpct	93	7		-	3	Clay, Fe	7	sb-ark	ctn-int		■	
A	1	77H	f-m	mod	ang-sb-rnd	L	pnt, lg, cocx, s	cpct,lse	93	7		-	3	Clay, Fe	7	sb-ark	ctn-int		■	
A	1	78H	f-m	mod	ang-sb-rnd	L-H	pnt, lg	cpct,lse	92	8		-	2	Clay, Fe	7	sb-ark	ctn-int		■	
A	1	79H	vf-f	mod	ang-sb-rnd	L-H	pnt, lg, cocx	cpct,lse	93	7		-	5	Clay, Fe	10	sb-ark	ctn-int	■	■	
A	1	80H	vf-f	mod	ang-sb-rnd	L	pnt, lg	cpct,lse	93	7		-	3	Clay, Fe	10	sb-ark	ctn-int		■	
A	1	81H	vf-f	mod-prly	ang-rnd	L	pnt, lg	cpct,lse	92	7	1	-	2	Clay, Fe, Silica	10	sb-ark	ctn-int		■	
A	1	82V	m	prly	sb-ang-rnd	L-H	pnt, lg	lse	92	7	1	-	2	Clay, Fe	7	sb-ark	ctn-int		■	
A	1	83H	f-m	mod	ang-rnd	L	pnt, lg	lse	90	10		-	7	Clay, Fe	12	sb-ark	ctn-int		■	
A	1	84H	f-m	prly	ang-rnd	L-H	pnt, lg	cpct,lse	93	6	1	-	5	Clay, Fe	10	sb-ark	ctn-int		■	
A	1	85H	vf-f	mod	ang-rnd	L-H	pnt, lg, cocx	lse	93	6	1	-	3	Clay	15	sb-ark	ctn-int		■	
A	1	86H	f-m	mod	ang-rnd	L-H	pnt, lg	lse	92	7	1	-	3	Clay	10	sb-ark	ctn-int		■	
A	1	87H	vf-f	mod	ang-rnd	L-H	pnt, lg	lse	92	7	1	-	3	Clay, Fe	10	sb-ark	ctn-int		■	
A	1	88H	vf-f	mod	ang-rnd	L	pnt, lg	lse	94	5	1	-	20	Silica, Fe	2	sb-ark	ctn-int		■	
A	1	89V	vf-f	mod	ang-rnd	L-H	pnt, lg	lse	91	8	1	-	3	Clay	7	sb-ark	ctn-int		■	
A	1	90H	f-m	mod	ang-rnd	L-H	pnt, lg	lse	91	8	1	-	2	Clay, Silica	10	sb-ark	ctn-int		■	
A	1	91H	f-m	mod-prly	ang-rnd	L-H	pnt, lg	cpct,lse	91	8	1	-	2	Clay, Fe	10	sb-ark	ctn-int		■	
A	1	92H	f-m	mod-prly	ang-rnd	L-H	pnt, lg	cpct,lse	94	5	1	-	2	Clay	7	sb-ark	ctn-int		■	
A	1	93H	f-m	mod	ang-rnd	L-H	pnt, lg	lse	94	5	1	-	2	Clay	10	sb-ark	ctn-int		■	
A	1	94H	f-m	mod-prly	ang-wl-rnd	L-H	pnt, lg	cpct,lse	93	6	1	-	4	Clay, Fe	10	sb-ark	ctn-int		■	
A	1	95V	f-m	mod-prly	ang-wl-rnd	L-H	pnt, lg	lse	92	7	1	-	3	Clay, Fe	15	sb-ark	ctn-int		■	
A	1	96H	f-m	mod-prly	ang-wl-rnd	L-H	pnt, lg	lse	92	7	1	-	4	Clay, Fe, Silica	5	sb-ark	ctn-int		■	

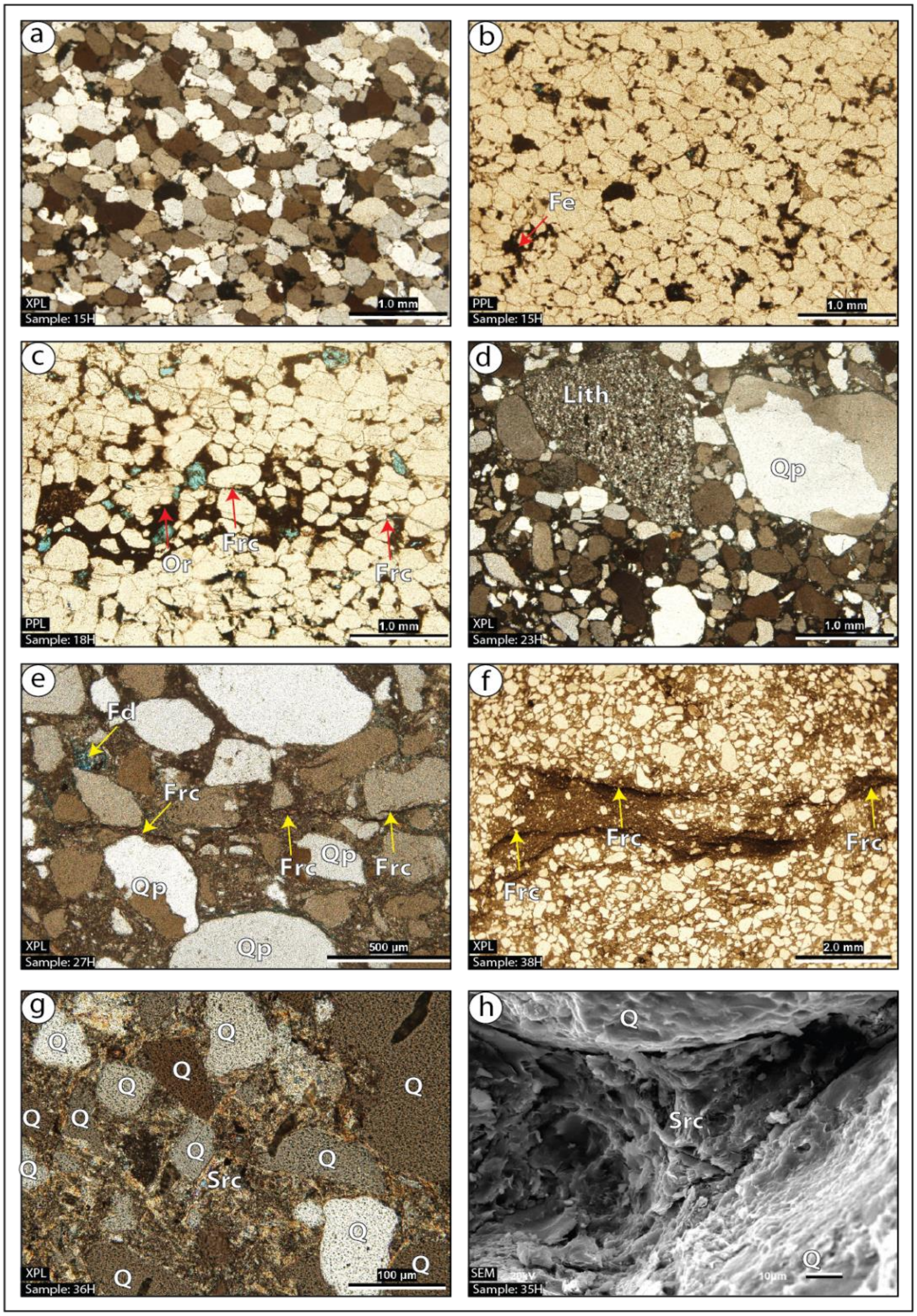

Figure 5.4: Selected photomicrographs from Well-B; (a,b) compaction, (c) organic matters (Or) fill pores, (d) poor sorting, (e) fractures (Frc), (f) deformation produces fractures, (g,h) sericite (Src) fills pores. Q: quartz, Qp: polycrystalline quartz, Fe: iron oxide, lith: lithic grain.

Table 5.2: Modal composition of the Well-B core interval. The classification is based on Folk (1980) while the provenance is based on Dickinson (Dickinson, 1985). The sweet spots are based on the absent or present of each type (For the abbreviation see Table 5.4)

Wells	**FA**	**Sample ID**	**Texture**						**Minerals %**			**Matrix %**	**Cement %**	**Cement type**	**Visual Porosity %**	**Classification**	**Provenance**	**Sweet Spots**		
			Grain Size ≥ 20%	Sorting	Roundness	Sphericity	Grains contact	Packing	Quartz	Feldspar	Lithic							Frac.	Diag.	Depo.
B	2	15H	f-m	mod-wl	ang-sb-rnd	L	lg, cocx	cpct	97	1	2	-	5	Fe	3	qz-ar	ctn-int		■	
B	2	16H	cl, m-crs	mod	ang-rnd	L-H	lg, cocx	cpct	96	1	3	-	5	Fe, Clay	5	qz-ar	ctn-int	■	■	
B	2	17H	cl, m-crs	mod-prly	ang-wl-rnd	L-H	pnt, lg	cpct, lse	95	1	4	-	15	Fe, Clay	5	qz-ar	rcl-orgn	■	■	
B	2	18H	cl, m	mod-prly	ang-wl-rnd	L-H	lg, cocx, s	cpct, lse	95	1	4	-	7	Fe, Clay	10	qz-ar	rcl-orgn	■	■	
B	2	19H	cl, f-m	mod-prly	ang-rnd	L-H	pnt, lg, cocx	cpct, lse	94	1	5	-	15	Fe, Clay	5	sb-lth	rcl-orgn	■	■	
B	2	20V	cl, f-m	mod-prly	ang-rnd	L-H	pnt, lg, cocx	cpct, lse	90	2	8	-	10	Fe, Clay	5	sb-lth	rcl-orgn		■	
B	2	21H	cl	vprly	ang-sb-rnd	L	fltg, pnt	lse	90	1	9	55	10	Fe, Clay	2	sb-lth	rcl-orgn		■	
B	3	22H	cl, m	mod-prly	ang-rnd	L-H	pnt, lg	lse	93	1	6	15	5	Fe, Clay	2	sb-lth	rcl-orgn		■	
B	3	23H	cl, m-crs	prly-vprly	ang-rnd	L-H	fltg, pnt, lg	lse	92	1	7	10	10	Fe, Clay	1	sb-lth	rcl-orgn	■	■	
B	3	24H	cl, m-crs	prly-vprly	ang-rnd	L-H	fltg, pnt, lg	lse	90	1	9	10	10	Fe, Clay	2	sb-lth	rcl-orgn		■	
B	3	25H	cl, f-m	mod-prly	ang-rnd	L-H	pnt, lg	cpct, lse	90	2	8	15	5	Fe, Clay	3	sb-lth	rcl-orgn	■	■	
B	3	26V	cl, crs-vcrs	prly-vprly	vang-wl-rnd	L-H	fltg	lse	88	2	10	15	5	Fe, Clay	5	sb-lth	rcl-orgn	■	■	
B	3	27H	cl, crs-vcrs	prly-vprly	vang-wl-rnd	L-H	fltg	lse	93	1	6	15	5	Fe, Clay	1	sb-lth	rcl-orgn		■	
B	2	28H	cl, f-m	prly-vprly	ang-rnd	L-H	fltg	lse	92	2	6	5	15	Fe, Clay	0	sb-lth	rcl-orgn			
B	2	29H	cl, f-m	prly-vprly	ang-rnd	L-H	fltg, pnt, lg	lse	95	1	4	5	15	Fe, Clay	2	qz-ar	rcl-orgn		■	
B	2	30H	cl, f-m	prly-vprly	ang-sb-rnd	L	fltg, pnt, lg	lse	92	2	6	2	15	Fe, Clay	2	sb-lth	rcl-orgn		■	
B	2	31H	cl, f-m	prly-vprly	ang-wl-rnd	L-H	fltg, pnt, lg	lse	96	1	3	2	15	Fe, Clay	1	qz-ar	ctn-int		■	
B	2	32H	cl, f	mod-prly	vang-rnd	L-H	fltg	lse	91	1	8	15	5	Fe, Clay	3	sb-lth	rcl-orgn	■	■	
B	2	33H	cl, f-m	prly-vprly	vang-sb-rnd	L	fltg, pnt	lse	88	2	10	15	5	Fe, Clay	0	sb-lth	rcl-orgn			
B	2	34V	cl, f-m	mod-prly	ang-rnd	L-H	fltg, pnt	lse	90	3	7	5	15	Fe, Clay	2	sb-lth	rcl-orgn		■	
B	2	35H	cl, f-m	prly-vprly	ang-rnd	L	fltg, pnt, lg	lse	95	3	2	7	7	Fe, Clay	1	qz-ar	ctn-int		■	
B	2	36H	cl, f-m	prly-vprly	ang-rnd	L-H	fltg	lse	95	3	2	65	5	Fe, Clay	3	qz-ar	ctn-int		■	
B	2	37H	cl, f	prly-vprly	ang-rnd	L-H	fltg	lse	95	3	2	40	5	Fe, Clay	1	qz-ar	ctn-int	■		
B	2	38H	cl, vf-f	prly-vprly	ang-rnd	L-H	fltg, pnt	lse	93	3	4	50	5	Fe, Clay	1	sb-lth	rcl-orgn	■		
B	2	39V	cl, f	mod-prly	ang-rnd	L-H	fltg	lse	95	3	2	40	5	Fe, Clay	0	qz-ar	ctn-int			

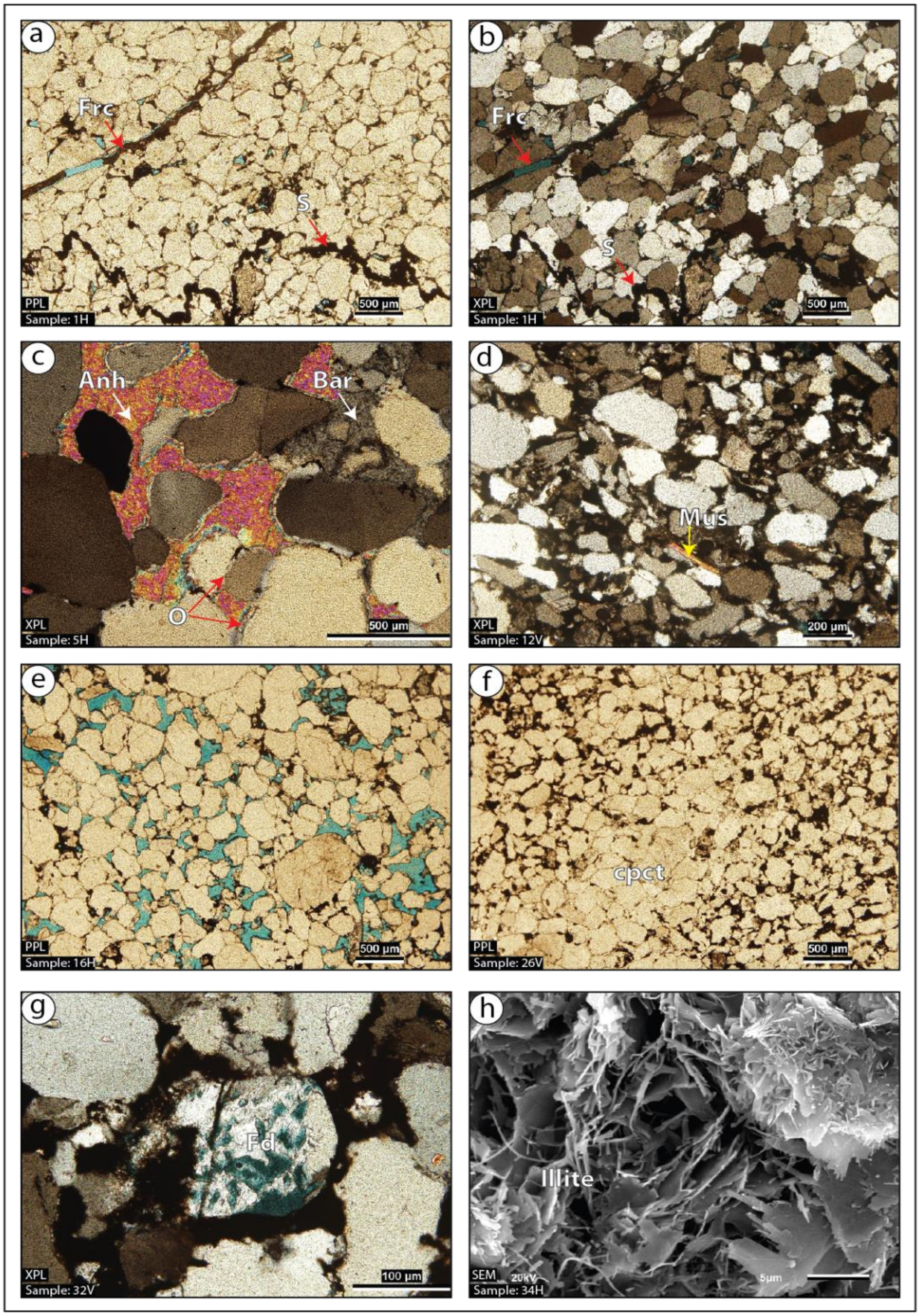

Figure 5.5: Selected photomicrographs from Well-C; (a,b) stylolite (S) and fracture (Frc), (c) anhydrite (Anh) and barite (Bar), (d) muscovite (Mus), (e) intergranular porosity, (f) compacted band (cpct), (g) feldspar dissolution (Fd), (h) illite.

Table 5.3: Modal composition of the Well-C core interval. The classification is based on Folk (1980) while the provenance is based on Dickinson (Dickinson, 1985). The sweet spots are based on the absent or present of each type (For the abbreviation see Table 5.4)

Wells	FA	Sample ID	Texture						Minerals %			Matrix %	Cement %	Cement type	Visual Porosity %	Classification	Provenance	Sweet Spots		
			Grain Size ≥ 20%	Sorting	Roundness	Sphericity	Grains contact	Packing	Quartz	Feldspar	Lithic							Frac.	Diag.	Depo.
C	2	1H	m	prly	ang-rnd	L-H	pnt, lg, cocx, s	cpct	99	1		-	10	Fe, Clay	10	qz-ar	ctn-int	■	■	
C	2	2V	m	prly	ang-rnd	L-H	pnt, lg, cocx, s	cpct	99	1		-	7	Fe, Clay	7	qz-ar	ctn-int		■	
C	2	3H	m	mod-prly	ang-rnd	L-H	pnt, lg, cocx, s	cpct	98	1	1	-	7	Fe, Clay	10	qz-ar	ctn-int		■	
C	2	4H	m	prly	ang-rnd	L-H	pnt, lg, cocx, s	cpct	98	1	1	-	15	Anh., Calc	0	qz-ar	ctn-int			
C	2	5H	cl, m-crs	prly-vprly	ang-rnd	L-H	pnt, lg	lse	98	2		-	20	Anh., Calc	0	qz-ar	ctn-int			
C	2	6H	cl, m-crs	prly	ang-rnd	L-H	pnt, lg	lse	98	1	1	-	20	Anh., Calc	0	qz-ar	ctn-int			
C	2	7H	cl, m-crs	prly	ang-rnd	L-H	pnt, lg	lse	98	1	1	-	10	Anh., Calc	0	qz-ar	ctn-int			
C	2	8H	cl, m-crs	prly	ang-wl-rnd	L-H	pnt, lg, cocx	cpct, lse	97	2	1	-	10	Fe, Clay, Anh.	0	qz-ar	ctn-int			
C	2	9H	f-m	mod-prly	ang-rnd	L-H	lg, cocx, s	cpct	98	2		-	3	Fe, Clay, Anh.	1	qz-ar	ctn-int		■	
C	2	10H	vf-f	mod-wl	ang-rnd	L	pnt, lg, cocx	cpct, lse	98	2		-	10	Fe	1	qz-ar	ctn-int			
C	2	11H	vf-f	mod	ang-rnd	L	pnt, lg, cocx, s	cpct, lse	98	2		-	10	Fe	0	qz-ar	ctn-int			
C	2	12V	sl-vf	prly	ang-rnd	L-H	pnt, lg	lse	98	2		-	15	Fe	3	qz-ar	ctn-int		■	
C	2	13H	f-m	prly	ang-sb-rnd	L	pnt, lg. cocx	cpct, lse	97	2	1	-	15	Fe	1	qz-ar	ctn-int		■	
C	2	14H	f-m	prly	ang-rnd	L-H	pnt, lg	cpct, lse	96	2	2	-	5	Fe	1	qz-ar	ctn-int		■	
C	2	15H	f-m	prly	ang-rnd	L-H	pnt, lg	cpct	97	2	1	-	10	Fe, Calc	5	qz-ar	ctn-int		■	
C	2	16H	f-m	prly	ang-rnd	L-H	pnt, lg. cocx, s	cpct, lse	97	1	2	-	10	Fe	7	qz-ar	ctn-int		■	■
C	2	17H	f-m	prly	ang-wl-rnd	L-H	pnt, lg. cocx	cpct, lse	96	2	2	-	7	Fe	20	qz-ar	ctn-int		■	■
C	2	18H	f-m	prly	ang-wl-rnd	L-H	pnt, lg. cocx	cpct	97	2	1	-	7	Fe	0	qz-ar	ctn-int			
C	2	19H	vf-f	mod	ang-rnd	L-H	pnt	lse	96	3	1	-	20	Fe	5	qz-ar	ctn-int		■	
C	2	20H	sl, vf-f	mod	ang-rnd	L-H	pnt	lse	97	2	1	-	15	Fe	10	qz-ar	ctn-int		■	
C	2	21H	f-m	mod-prly	ang-sb-rnd	L-H	pnt, lg	cpct, lse	96	2	2	-	5	Fe	1	qz-ar	ctn-int		■	
C	2	22H	vf-f	mod-prly	ang-sb-rnd	L-H	pnt, lg	lse	96	3	1	-	10	Fe	3	qz-ar	ctn-int		■	
C	2	23H	vf-m	prly	ang-sb-rnd	L-H	pnt, lg	lse	96	2	2	-	10	Fe	2	qz-ar	ctn-int		■	
C	2	24H	vf-m	prly	ang-rnd	L-H	pnt, lg	lse	96	2	2	-	10	Fe	5	qz-ar	ctn-int		■	
C	2	25H	vf-f	mod	ang-sb-rnd	L-H	pnt, lg	lse	97	2	1	-	15	Fe	2	qz-ar	ctn-int		■	
C	2	26V	vf-f	prly	ang-rnd	L-H	pnt, lg, cocx	cpct, lse	96	2	2	-	10	Fe	0	qz-ar	ctn-int			
C	2	27H	cl, vf-f	mod	ang-rnd	L-H	pnt, lg	cpct, lse	96	3	1	-	25	Fe, Clay	0	qz-ar	ctn-int	■		
C	2	28H	vf-m	prly	ang-rnd	L-H	pnt, lg	lse	96	2	2	-	20	Fe	5	qz-ar	ctn-int		■	
C	2	29H	vf-f	prly	ang-rnd	L-H	pnt, lg, cocx, s	cpct, lse	96	3	1	-	15	Fe	3	qz-ar	ctn-int		■	
C	2	30H	vf-f	prly	ang-rnd	L-H	pnt, lg	lse	97	2	1	-	15	Fe	5	qz-ar	ctn-int		■	
C	2	31H	vf-f	prly	ang-rnd	L-H	pnt, lg	lse	96	2	2	-	15	Fe	3	qz-ar	ctn-int		■	
C	2	32V	vf-f	prly	ang-rnd	L-H	pnt, lg	lse	96	2	2	-	17	Fe	2	qz-ar	ctn-int		■	
C	2	33H	vf-f	prly	ang-sb-rnd	L-H	pnt, lg	lse	97	2	1	-	20	Fe	3	qz-ar	ctn-int		■	
C	2	34H	vf-f	prly	ang-sb-rnd	L-H	pnt, lg	lse	98	2		-	15	Fe, Clay	0	qz-ar	ctn-int	■		
C	2	35H	f-m	prly	ang-rnd	L-H	pnt, lg, cocx, s	cpct, lse	97	2	1	-	15	Fe	2	qz-ar	ctn-int		■	
C	2	36H	f-m	prly	ang-wl-rnd	L-H	pnt, lg	lse	96	3	1	-	25	Fe, Clay	0	qz-ar	ctn-int	■		
C	2	37H	f-m	mod-prly	ang-rnd	L-H	pnt, lg, cocx	cpct	97	2	1	-	10	Fe, Clay, Barite	10	qz-ar	ctn-int		■	■
C	2	38V	f-m	mod-prly	ang-rnd	L-H	pnt, lg, cocx	cpct	97	2	1	-	7	Fe, Clay	5	qz-ar	ctn-int		■	
C	2	39H	f-m	prly	ang-rnd	L-H	pnt, lg, cocx	cpct	98	1	1	-	7	Fe, Clay	7	qz-ar	ctn-int		■	
C	2	40H	vf-m	mod-prly	ang-rnd	L-H	pnt, lg, cocx	cpct	97	2	1	-	7	Fe, Clay	10	qz-ar	ctn-int		■	

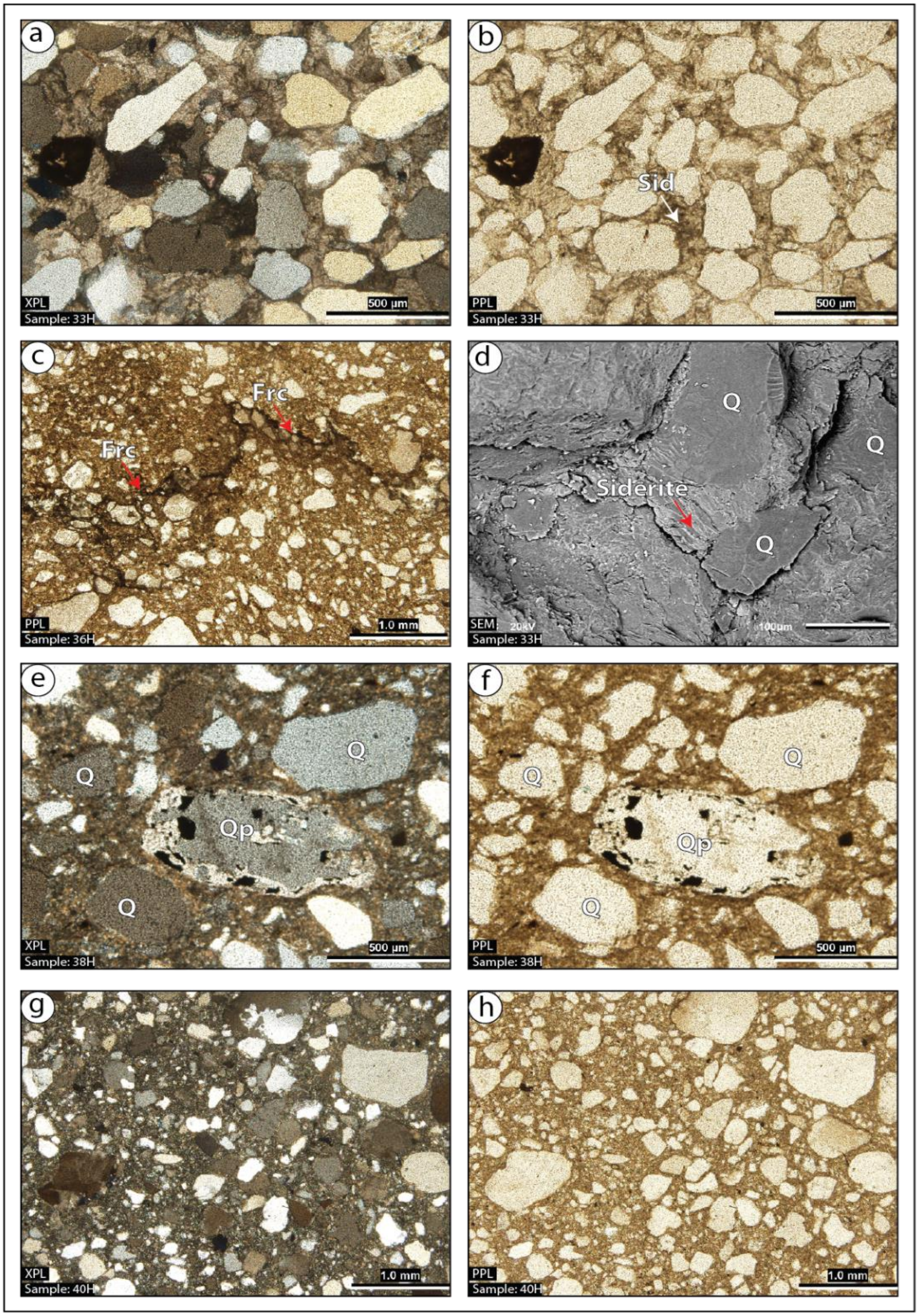

Figure 5.6: Selected photomicrographs from Well-D; (a,b) siderite cement (Sid), (c) deformation produces fractures (Frc), (d) siderite fills pores, (e,f) Monocrystalline (Q) and polycrystalline quartz (Qp), (g,h) matrix.

Table 5.4: Modal composition of the Well-D core interval. The classification is based on Folk (1980) while the provenance is based on Dickinson (Dickinson, 1985). The sweet spots types are based on the absence or presence of each type. Note: the abbreviated terms used in this study for all modals are: For Grain Size (vf: very fine, f: fine, m: medium, crs: coarse, vcrs: very coarse grains), Sorting (wl: well, mod: moderately, prly: poorly, vprly: very poorly sorted), Roundness (vang: very angluar, ang: angluar, sb-ang: subangluar, sb-rnd: subrounded, rnd: rounded, wl-rnd: well rounded), Sphericity (L: low, H: high), Grain contact (fltg: floating, pnt: point, lg: long, cocx: concavo-convex, s: sutured), Packing (cpct: compacted, lse: loose), Cement type (Fe: iron oxides, Anh.: anhydrite, Calc: calcite), Sandstone Classification (qz-ar: quartzarenite, sb-lth: sublitharenite, sb-ark: subarkose), Sandstone Provenance (ctn-int: craton interior, rcl-orgn: recycled orogen), and Sweet Spots (Frac.: fracture, Diag.: diagenetic, Depo.: depositional, each observed sweet spot type is heighted in black box).

Wells	**FA**	**Sample ID**	**Texture**						**Minerals %**			**Matrix %**	**Cement %**	**Cement type**	**Visual Porosity %**	**Classification**	**Provenance**	**Sweet spots**		
			Grain Size ≥ 20%	Sorting	Roundness	Sphericity	Grains contact	Packing	Quartz	Feldspar	Lithic							Frac.	Diag.	Depo.
D	4	33H	f	mod	sb-ang- rnd	L	pnt, fltg	lse	95	1	4	5	35	Siderite, Clay	0	qz-ar	rcl-orgn		■	
D	3	34H	f-m	prly	ang-rnd	L-H	fltg	lse	93	1	6	68	2	Fe, Clay	0	sb-lth	rcl-orgn	■		
D	3	35V	vf-f	prly	ang-rnd	L-H	fltg	lse	92	1	7	68	2	Fe, Clay	0	sb-lth	rcl-orgn			
D	3	36H	vf-f	prly	ang-rnd	L-H	fltg	lse	91	1	8	68	2	Fe, Clay	0	sb-lth	rcl-orgn			
D	3	37H	vf-f	prly	ang-rnd	L-H	fltg	lse	92	0	8	68	2	Fe, Clay	0	sb-lth	rcl-orgn			
D	3	38H	vf-f	prly	ang-rnd	L-H	fltg	lse	95	0	5	68	2	Fe, Clay	0	qz-ar	rcl-orgn			
D	3	39V	vf-f	prly	ang-rnd	L-H	fltg	lse	98	1	1	68	2	Fe, Clay	0	qz-ar	ctn-int			
D	3	40H	vf-f	prly	ang-rnd	L-H	fltg	lse	97	0	3	68	2	Fe, Clay	0	qz-ar	ctn-int			

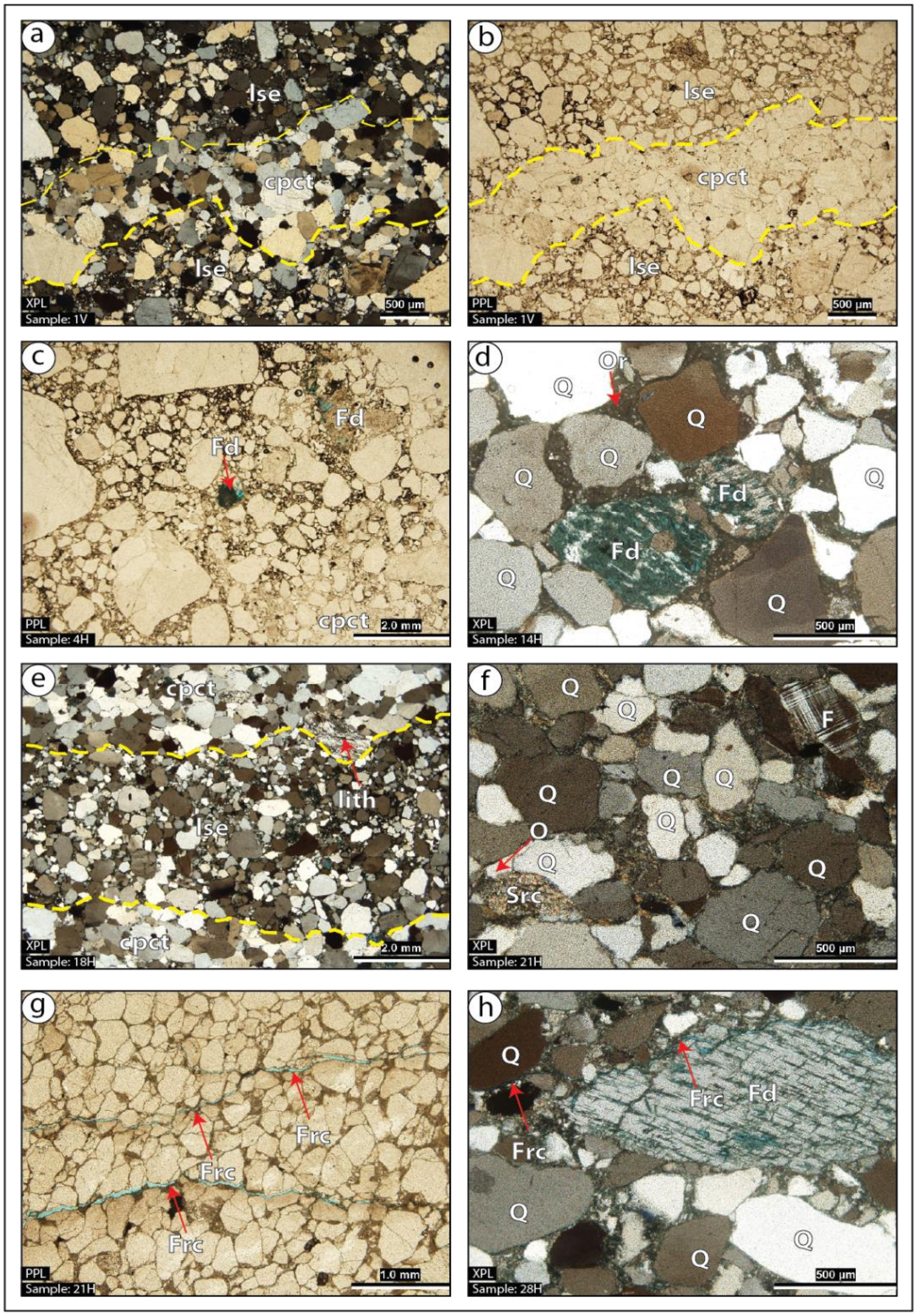

Figure 5.7: Selected photomicrographs from Well-E; (a,b) compacted (cpct) and loose (lse) grains, (c) poor sorting and feldspar dissolution (Fd), (d) feldspar dissolution, (e) heterogeneity, (f) sericite (Src), (g) fractures (Frc), (h) dissolution. Q: quartz, F: feldspar (microcline), lith: lithic grain.

Table 5.5: Modal composition of the Well-E core interval. The classification is based on Folk (1980) while the provenance is based on Dickinson (Dickinson, 1985). The sweet spots are based on the absent or present of each type (For the abbreviation see Table 5.4)

Wells	**FA**	**Sample ID**	**Texture**						**Minerals %**			**Matrix %**	**Cement %**	**Cement type**	**Visual Porosity %**	**Classification**	**Provenance**	**Sweet Spots**		
			Grain Size ≥ 20%	Sorting	Roundness	Sphericity	Grains contact	Packing	Quartz	Feldspar	Lithic							Frac.	Diag.	Depo.
E	4	1V	f-m	mod-prly	ang-sb-rnd	L-H	pnt, lg, s	cpct,lse	93	2	5	6	4	Clay, Fe, Silica	1	sb-lth	rcl-orgn		■	
E	4	2H	f-m	mod-prly	ang-rnd	L	pnt, lg, cocx	cpct,lse	94	1	5	7	3	Clay, Fe, Silica	2	sb-lth	rcl-orgn		■	
E	4	3H	m	mod-prly	ang-rnd	L-H	pnt, lg, cocx	cpct,lse	95	1	4	5	2	Clay	1	qz-ar	rcl-orgn		■	
E	4	4H	cl, m	prly-vprly	ang-rnd	L-H	pnt	lse	93	2	5	5	6	Clay, Fe	2	sb-lth	rcl-orgn		■	
E	4	5H	f-m	mod-prly	ang-rnd	L-H	pnt, lg, cocx	cpct,lse	94	1	5	7	6	Clay, Fe, Silica	3	sb-lth	rcl-orgn		■	
E	4	6H	m	mod-prly	ang-rnd	L-H	pnt, lg, cocx,s	cpct,lse	92	1	7	4	2	Clay, Fe, Silica	2	sb-lth	rcl-orgn		■	
E	4	7V	f-m	prly-vprly	ang-rnd	L-H	pnt, lg	lse	92	1	7	-	25	Clay, Fe, Silica	0	sb-lth	rcl-orgn		■	
E	4	8H	m	prly-vprly	ang-rnd	L-H	pnt, lg, cocx	cpct,lse	94	1	5	-	7	Clay, Fe	4	sb-lth	rcl-orgn		■	
E	4	9H	m	prly-vprly	ang-wl-rnd	L-H	pnt, lg, cocx	cpct,lse	92	1	7	-	10	Clay, Fe, Silica	4	sb-lth	rcl-orgn		■	
E	4	10H	m-crs	prly-vprly	ang-rnd	L	pnt, lg, cocx	cpct	90	1	9	-	10	Clay, Fe, Silica	0	sb-lth	rcl-orgn		■	
E	4	11H	m-crs	prly-vprly	ang-rnd	L-H	pnt, lg, cocx	cpct	89	1	10	-	10	Clay, Fe, Silica	2	sb-lth	rcl-orgn		■	
E	4	12V	m-crs	prly-vprly	ang-rnd	L	pnt, lg	lse	88	2	10	-	25	Clay, Fe, Silica	1	sb-lth	rcl-orgn		■	
E	4	13H	f-crs	prly-vprly	ang-sb-rnd	L-H	pnt, lg, cocx	cpct	88	2	10	-	7	Clay, Fe	3	sb-lth	rcl-orgn		■	
E	4	14H	f-m	prly-vprly	ang-rnd	L-H	pnt, lg, cocx	cpct,lse	89	2	9	-	10	Clay, Fe	5	sb-lth	rcl-orgn		■	
E	4	15H	f-crs	prly-vprly	ang-rnd	L-H	pnt, lg	lse	91	1	8	-	7	Clay, Fe	6	sb-lth	rcl-orgn		■	
E	4	16H	cl, m	prly-vprly	ang-rnd	L-H	pnt, lg, cocx	cpct,lse	91	1	8	-	6	Clay, Fe	3	sb-lth	rcl-orgn		■	
E	4	17H	cl, m-crs	prly-vprly	ang-rnd	L-H	pnt, lg, cocx	cpct,lse	90	1	9	-	5	Clay, Fe	3	sb-lth	rcl-orgn		■	
E	4	18H	m-crs	prly-vprly	ang-rnd	L-H	pnt, lg, cocx	cpct,lse	91	1	8	-	5	Clay, Fe	3	sb-lth	rcl-orgn		■	
E	4	19V	cl, m-crs	prly-vprly	ang-rnd	L-H	pnt, lg, cocx	cpct,lse	89	1	10	-	10	Clay, Fe	2	sb-lth	rcl-orgn		■	
E	4	20H	cl, f-m	prly-vprly	ang-rnd	L-H	pnt, lg, cocx, s	cpct,lse	92	1	7	-	7	Clay, Fe	2	sb-lth	rcl-orgn		■	
E	4	21H	f-m	prly-vprly	ang-sb-rnd	L-H	pnt, lg, s	cpct,lse	84	1	15	-	7	Clay, Fe	0	sb-lth	rcl-orgn		■	
E	4	22H	f-m	prly-vprly	ang-rnd	L-H	pnt, lg, s	cpct,lse	92	1	7	-	5	Clay, Fe	4	sb-lth	rcl-orgn	■	■	
E	4	23H	f-m	prly-vprly	ang-rnd	L-H	pnt, lg, cocx, s	cpct,lse	94	1	5	-	5	Clay, Fe	2	sb-lth	rcl-orgn		■	
E	4	24H	f-m	prly-vprly	ang-rnd	L-H	pnt, lg, cocx, s	cpct,lse	92	1	7	-	5	Clay, Fe	3	sb-lth	rcl-orgn		■	
E	4	25V	f-m	prly-vprly	ang-rnd	L-H	pnt, lg, cocx	cpct,lse	92	1	7	-	7	Clay, Fe	5	sb-lth	rcl-orgn		■	
E	4	26H	f-crs	mod-prly	ang-sb-rnd	L	pnt, lg, cocx, s	cpct	89	1	10	-	2	Clay, Fe	5	sb-lth	rcl-orgn		■	
E	4	27H	f-crs	mod-prly	ang-rnd	L-H	lg, cocx, s	cpct	91	1	8	-	1	Clay, Fe	1	sb-lth	rcl-orgn		■	
E	4	28H	f-m	prly-vprly	ang-rnd	L-H	pnt, lg, cocx	cpct,lse	92	1	7	-	5	Clay, Fe	1	sb-lth	rcl-orgn		■	
E	4	29H	m-crs	prly-vprly	ang-rnd	L-H	pnt, lg, cocx	cpct,lse	92	1	7	-	5	Clay, Fe	1	sb-lth	rcl-orgn		■	
E	4	30H	m-crs	prly-vprly	vang-rnd	L-H	pnt, lg	lse	89	1	10	-	5	Clay, Fe	2	sb-lth	rcl-orgn		■	

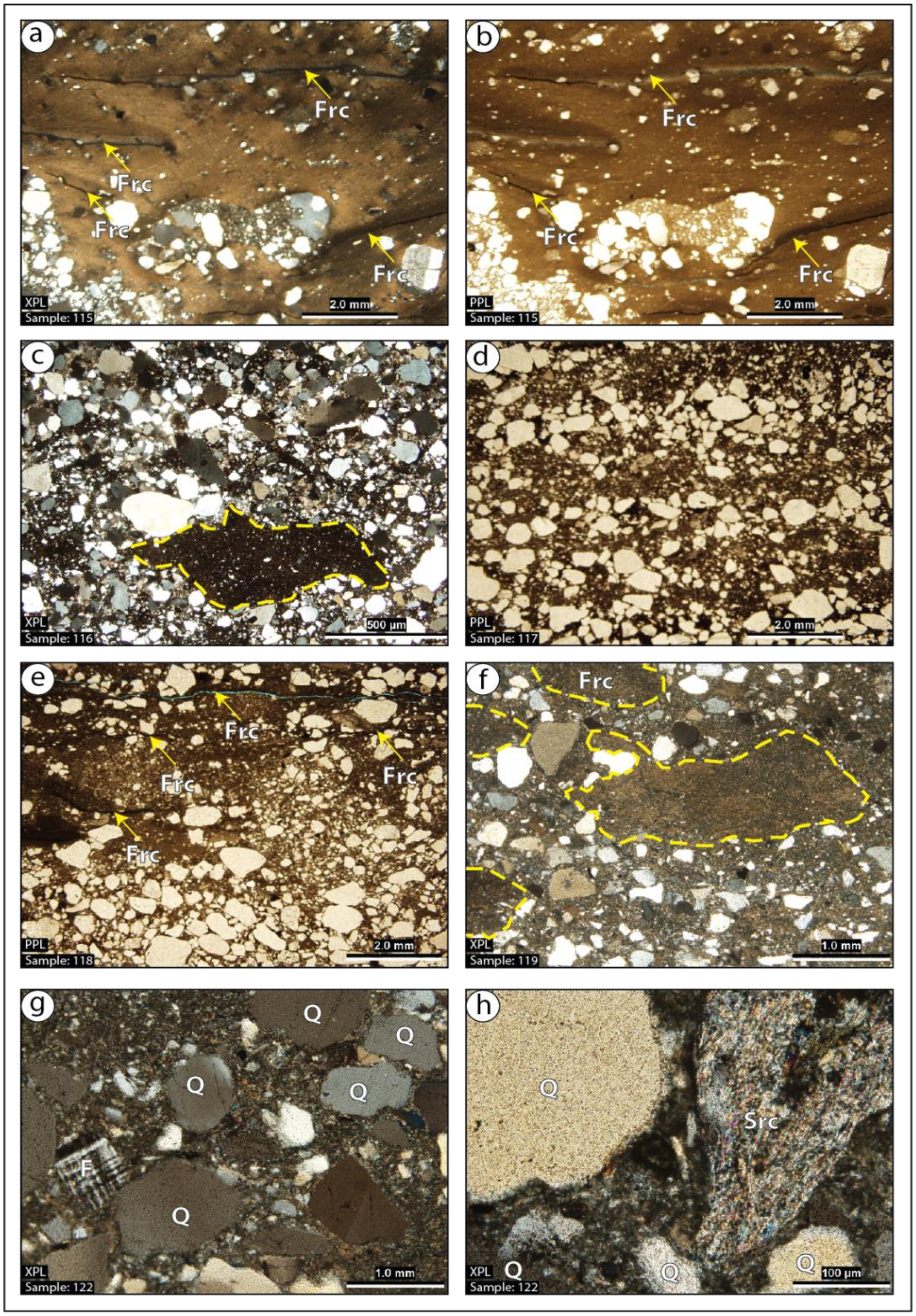

Figure 5.8: Selected photomicrographs from Well-F; (a,b) deformation produces fractures (Frc), (c) poor sorting and mud clast, (d) stratification, (e) fractures and matrix, (f) mud clasts are outlined in yellow dashed circles, (g) microcline (F) and quartz (Q), (h) sericite (Src).

Table 5.6: Modal composition of the Well-F core interval. The classification is based on Folk (1980) while the provenance is based on Dickinson (Dickinson, 1985). The sweet spots are based on the absent or present of each type. (For the abbreviation see Table 5.4)

Wells	**FA**	**Sample ID**	**Texture**						**Minerals %**			**Matrix %**	**Cement %**	**Cement type**	**Visual Porosity %**	**Classification**	**Provenance**	**Sweet Spots**		
			Grain Size ≥ 20%	Sorting	Roundness	Sphericity	Grains contact	Packing	Quartz	Feldspar	Lithic							Frac.	Diag.	Depo.
F	3	115	cl	prly	ang-rnd	L-H	fltg, pnt	lse	93	2	5	80	tr	Fe	0	sb-ark	rcl-orgn	■		
F	3	116	cl, m	prly	ang-rnd	L	fltg, pnt	lse	91	5	4	50	10	Fe	0	sb-ark	rcl-orgn			
F	3	117	cl, sl, vf	prly	ang-rnd	L-H	fltg, pnt	lse	93	2	5	55	7	Fe	0	sb-lth	rcl-orgn	■		
F	3	118	cl, sl	prly	ang-wl-rnd	L-H	fltg, pnt	lse	83	2	15	55	10	Fe	0	sb-lth	rcl-orgn	■		
F	3	119	cl, sl, m	prly	ang-rnd	L	fltg, pnt	lse	90	5	5	55	10	Fe	0	sb-ark	rcl-orgn	■		
F	3	120	cl, sl, m	prly	ang-rnd	L-H	fltg, pnt	lse	88	2	10	65	5	Fe	0	sb-lth	rcl-orgn	■		
F	3	121	cl, sl, m	prly	ang-rnd	L-H	fltg, pnt	lse	84	1	15	55	5	Fe	0	sb-lth	rcl-orgn			
F	3	122	cl, sl	prly	ang-wl-rnd	L-H	fltg, pnt	lse	91	2	7	55	5	Fe	0	sb-lth	rcl-orgn			

5.4 Mineralogical Composition Using XRD

The XRD data analysis revealed that Well-A core interval (nearshore lithofacies) is predominated by quartz. Minor minerals such as orthoclase, illite, and hematite were also detected (Figure 5.9). The core of Well-E (glaciofluvial lithofacies) is also predominated by quartz with a minor amount of K-feldspar content (orthoclase), and dolomite (Figure 5.13). All minor minerals in both wells appeared in very low intensity.

On the other hand, the other wells exhibit mineralogical variation. In the core of Well-B, the predominantly quartz mineralogy is associated with several minerals such as illite, muscovite, chlorite, orthoclase, magnesite, pyrite, hematite, and manganosite (Figure 5.10). Most of this variation is observed in the argillaceous sandstone (delta lithofacies) and the diamictite (subglacial lithofacies) of this core. The core of Well-C (delta front lithofacies) is mainly quartz with a minor amount of k-feldspar minerals observed with low peaks (Figure 5.11). The anhydrite and barite cement observed in thin section (Figure 5.5c) are also appeared in the XRD data analysis mostly in the samples from the upper part of the core. The diamictite of Well-D (subglacial lithofacies) is mainly characterized by quartz while the argillaceous sandstone (glaciofluvial lithofacies) shows clearly two peaks of siderite cement (Figure 5.12). Several peaks for minerals such as muscovite, chlorite or kaolinite, k-feldspars, dolomite, magnesite, and manganosite associated with prevailed quartz are observed in the Well-F core interval (subglacial lithofacies) (Figure 5.14).

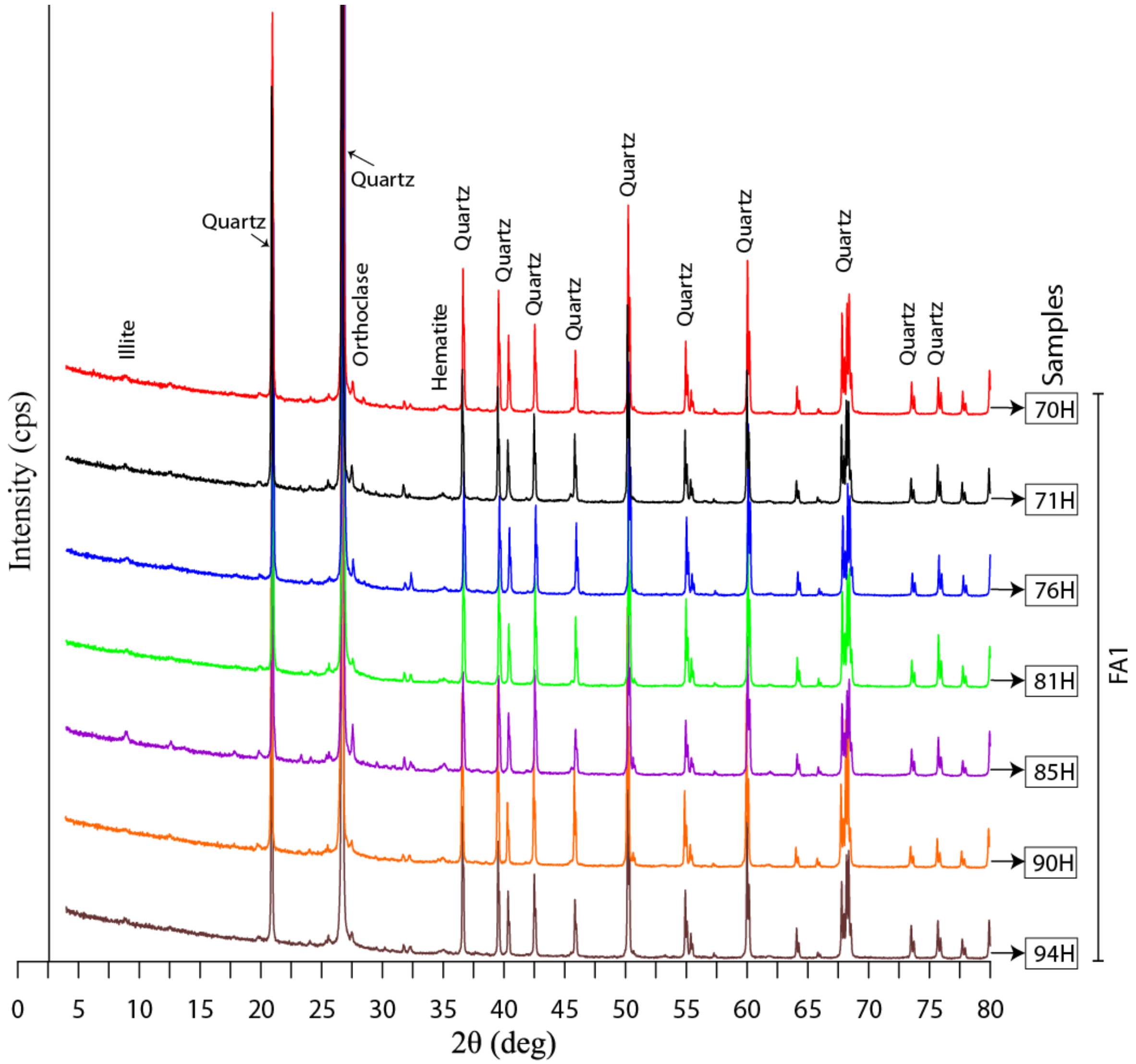

Figure 5.9: XRD analysis of Well-A. Note the abundance of quartz with minor very low peaks of illite, orthoclase, and hematite characterizes the nearshore environment (FA1). Samples are arranged according to their depth (94H is the deepest). In general, no significant variation is observed in this XRD results indicating clean sandstone.

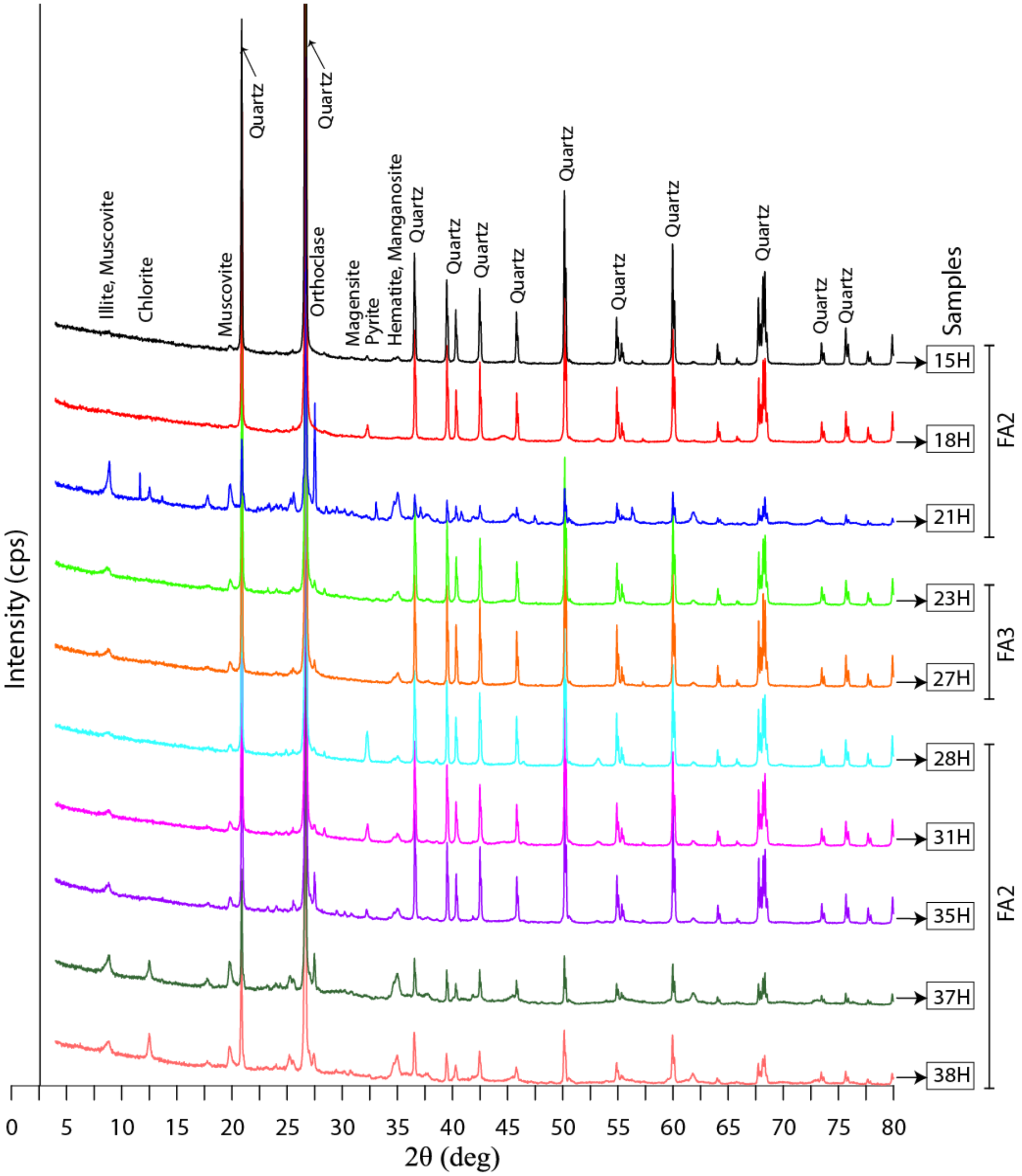

Figure 5.10: XRD analysis of Well-B. Note that the increased number of peaks in samples #21H, 37H and 38H reflect mineralogical variations. These variations are associated with claystone and argillaceous sandstone of the glaciolacustrine delta (FA2). Sample #15H shows clean sandstone. The subglacial environment (FA3) shows low mineralogical variation with comparing to #21H, 37H, and 38H of FA2. All samples are arranged according to their depth (38H is the deepest)

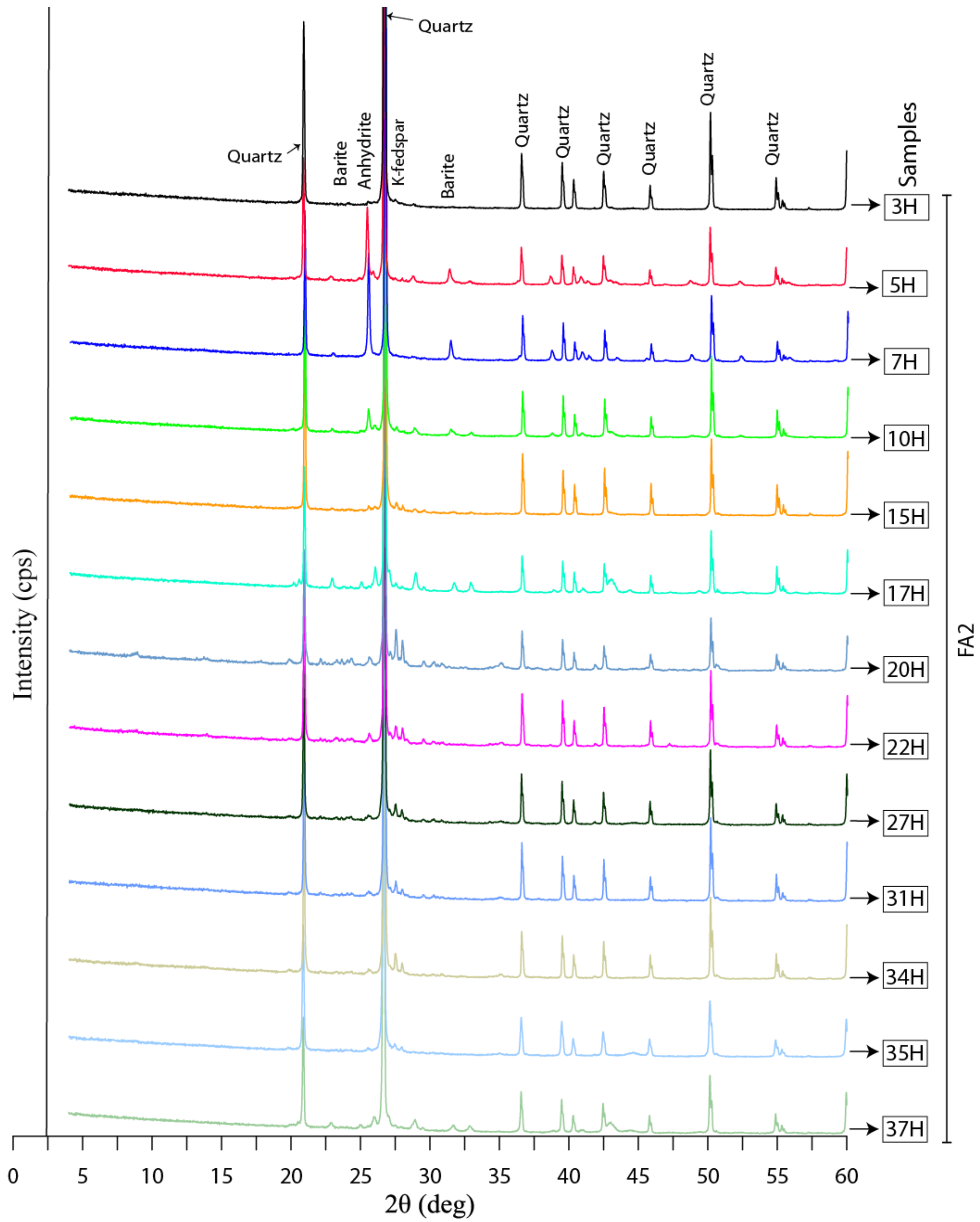

Figure 5.11: XRD analysis of Well-C, glaciolacustrine delta (FA2). Note the prominent peaks for anhydrite (5H, 7H, 10H), and for barite (5H, 7H, 17H). They indicate sulfate cement. All samples are arranged according to their depth (37H is the deepest).

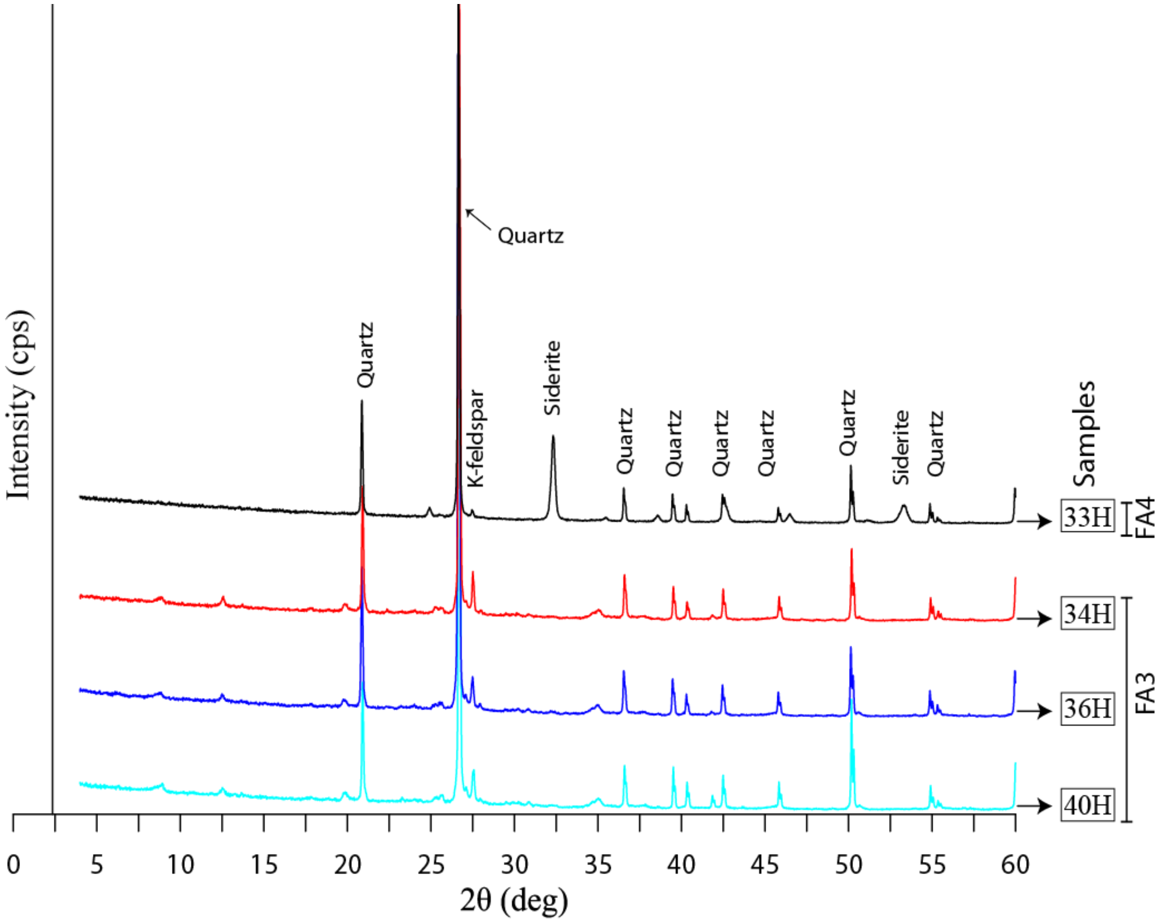

Figure 5.12: XRD analysis of Well-D. Note that the two peaks of siderite in sample #33H in the glaciofluvial environment (FA4) confirm siderite cement. The other peaks are for quartz in the diamictite lithofacies of the subglacial environment (FA3). All samples are arranged according to their depth (40H is the deepest).

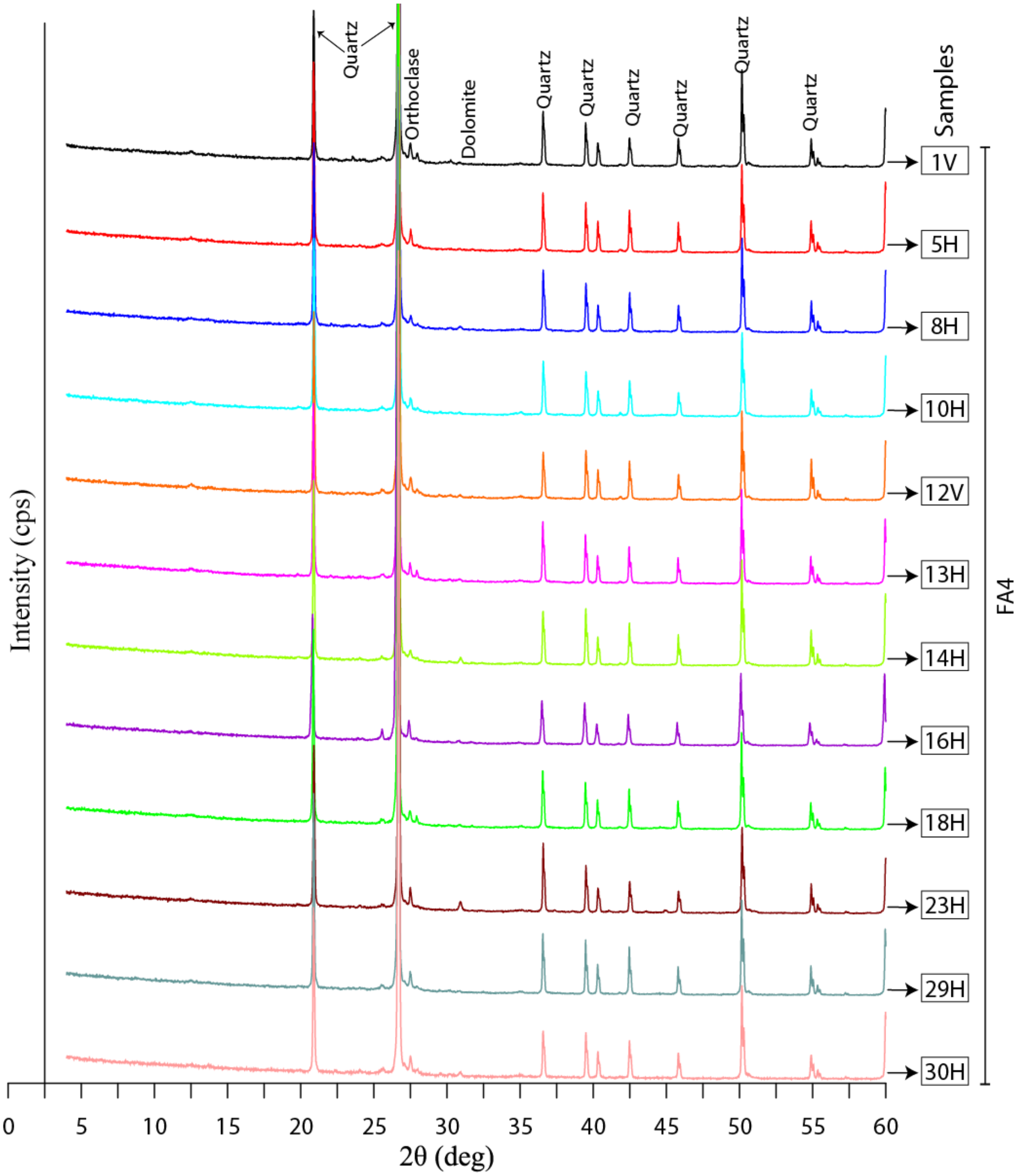

Figure 5.13: XRD analysis of Well-E. Note that the similarity of all peaks except sample# 23 which shows a very low peak of dolomite. The glaciofluvial environment (FA4) is also clean sandstone. All samples are arranged according to their depth (30H is the deepest).

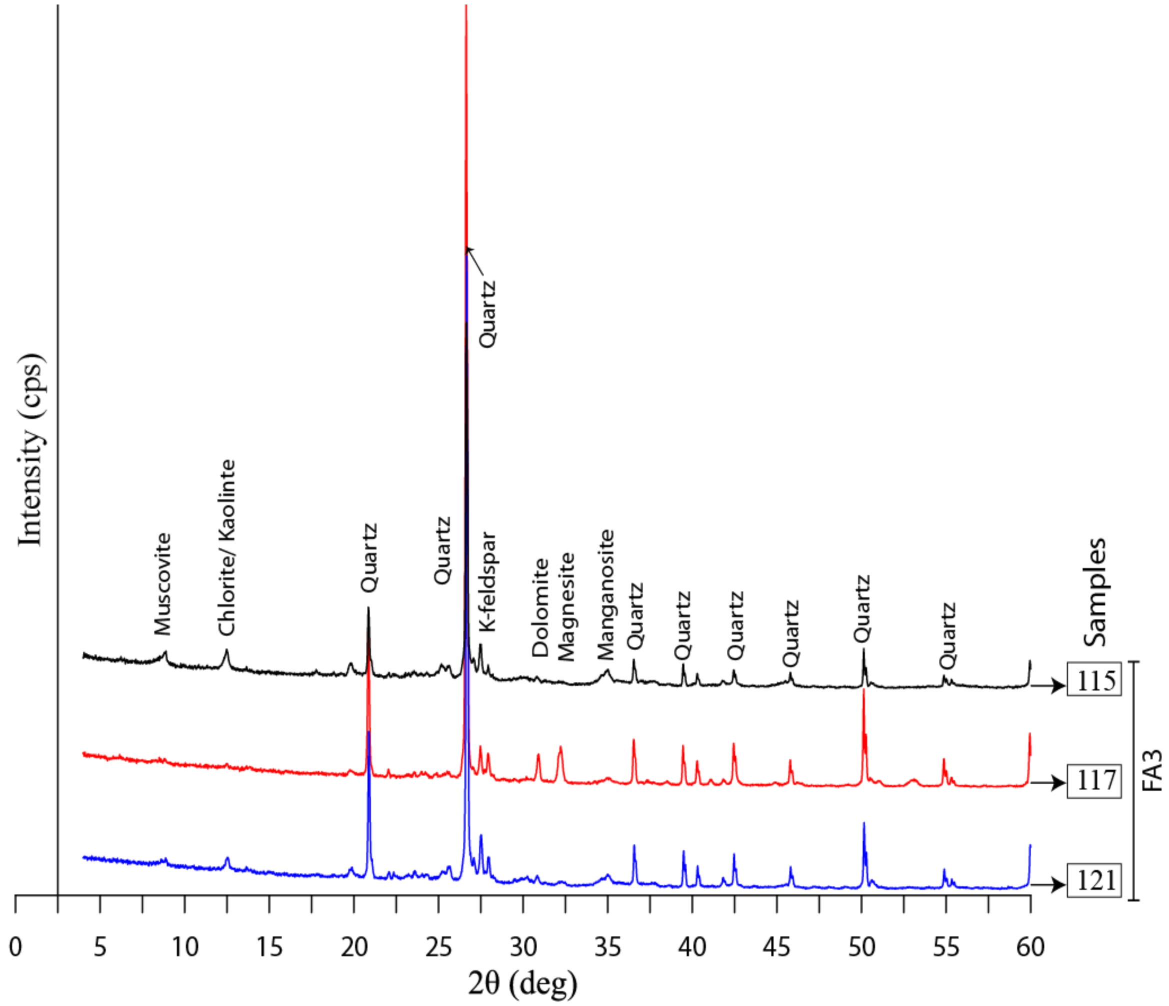

Figure 5.14: XRD analysis of Well-F. Note that the variability of the peaks indicates a variability within the mineralogical composition of the diamictite lithofacies of the subglacial environment (FA3). Samples are arranged according to their depth (121 is the deepest).

5.5 Pore Filling Minerals Under SEM/EDX

In order to define the pore filling minerals, several samples have been selected for SEM and EDX elemental analysis. The samples were taken from each core interval except the core interval of Well-F because it is totally filled by the matrix. In the nearshore environment (Well-A), the pores are filled by illite/smectite clay minerals (Figure 5.15c,e,d). The zircon (heavy mineral) is also observed in this environment (Figure 5.15a,b). Anhydrite (Figure 5.16a,b) and sericite (Figure 5.16d,e,f,g) are observed filling the pores in the Well-B (glaciolacustrine delta). The former is also observed in the upper part of the core interval of Well-C of the same environment (Figure 5.17a,b,c). The illite clay mineral (Figure 5.17d,e,f) is observed, but in the lower part of this core interval. In the glaciofluvial lithofacies of Well-D, siderite cement (Figure 5.18a,b,c) fills the pores. Remaining pieces of plants are observed in both argillaceous sandstone (glaciofluvial lithofacies) and the diamictite lithofacies (subglacial lithofacies) (Figure 5.18d). In the Well-E core interval (glaciofluvial lithofacies), resorbed alkali feldspar (Figure 5.19a,b,c) and illite/smectite mixed clay minerals (Figure 5.19d,e,f,g,h) are also observed.

The anhydrite cement in the glaciolacustrine delta in Well-C is confirmed by XRD (Figure 5.11, samples #5H,7H,10H) and thin section study (Figure 5.5c) while the siderite cement in the glaciofluvial lithofacies of Well-D is confirmed by XRD (Figure 5.12, samples #33H).

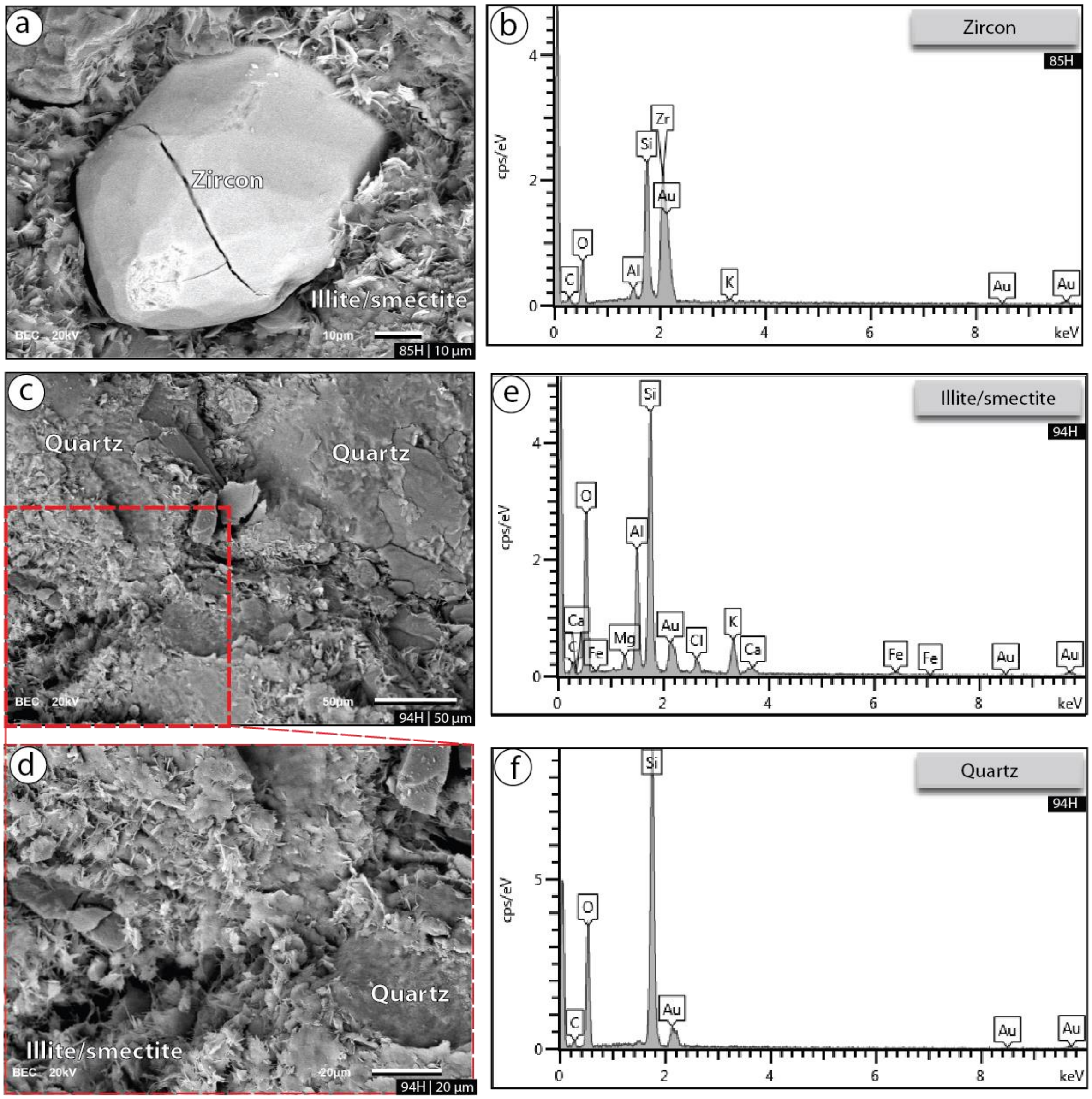

Figure 5.15: Selected SEM micrographs and EDX analysis from Well-A (nearshore lithofacies). (a) SEM photomicrograph for Zircon in the illite/smectite clay, (b) EDX shows Zr element affiliated to the zircon minerals, (c,d) SEM micrographs for pores filling and grains coating illite/smectite clay, (e) EDX shows the elemental composition of illite/smectite, (f) EDX shows Si element affiliated to quartz.

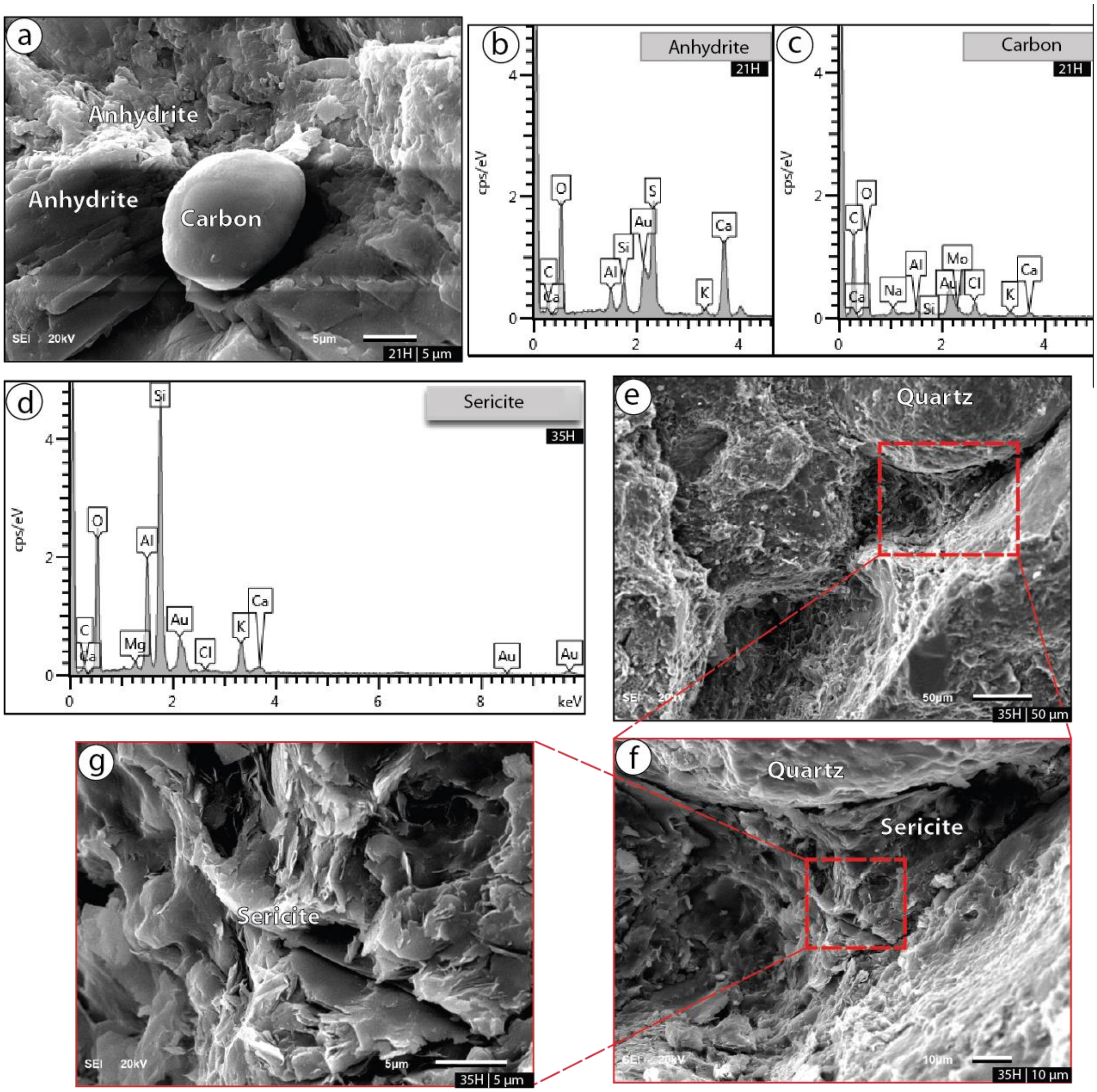

Figure 5.16: Selected SEM micrographs and EDX analysis from Well-B (glaciolacustrine delta). (a) SEM photomicrograph for anhydrite filling the pores and a grain of carbon, (b) EDX shows the major elements of the anhydrite (S,Ca), (c) EDX shows C element affiliated to the carbon grain, (d) EDX shows the elemental composition of sericite, (e,f,g) several SEM micrographs with different scale for the pore filling sericite.

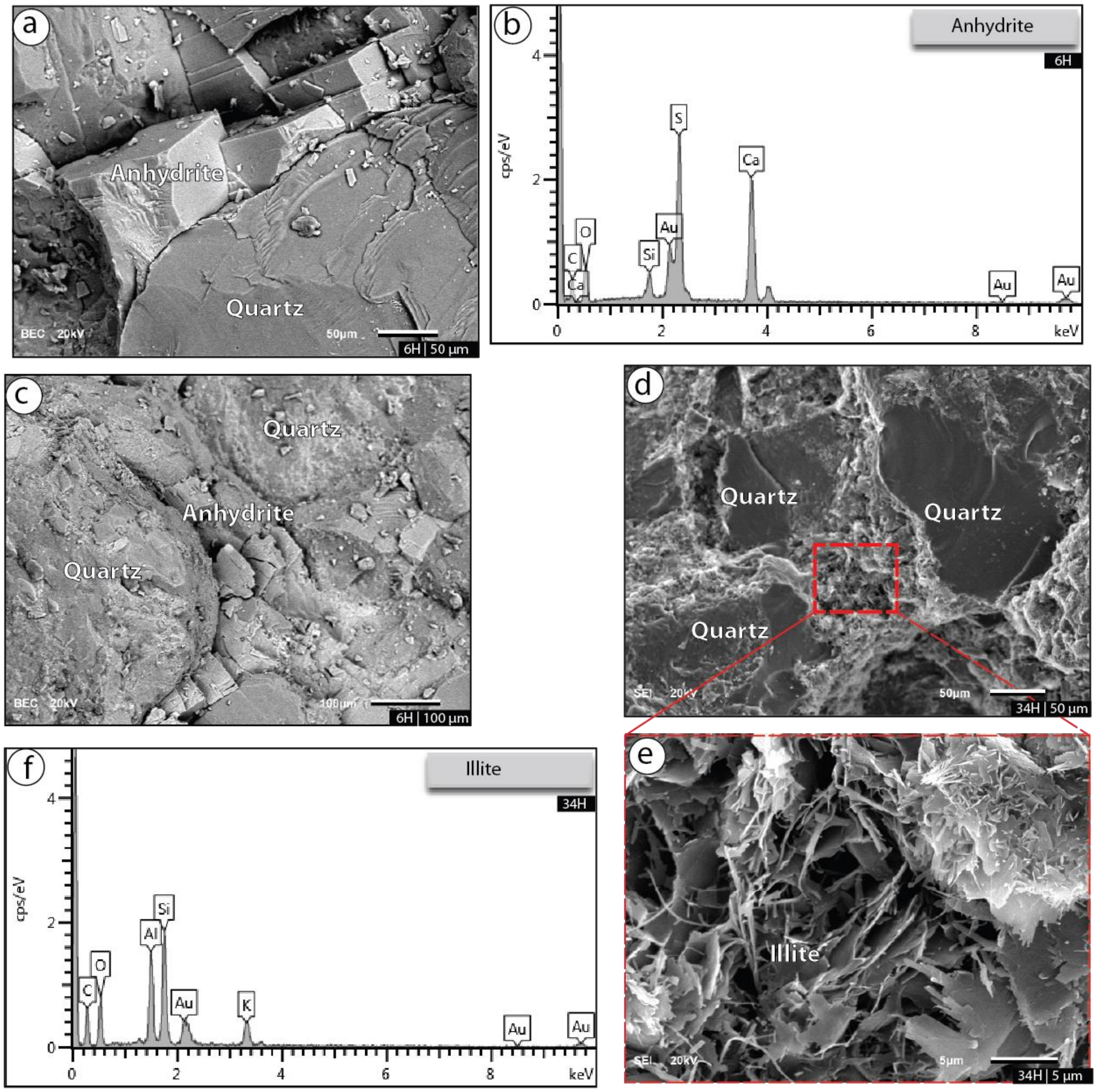

Figure 5.17: Selected SEM micrographs and EDX analysis from Well-C core interval (glaciolacustrine delta). (a,c) SEM micrographs with different scale for anhydrite filling the pores in the upper part of the core, (b) EDX shows the major elements of the anhydrite (S, Ca), (d,e) SEM micrographs with different scale for illite clay mineral filling the pores and coating the grains in the lower part of the core, (f) EDX shows the elemental composition of the illite clay mineral.

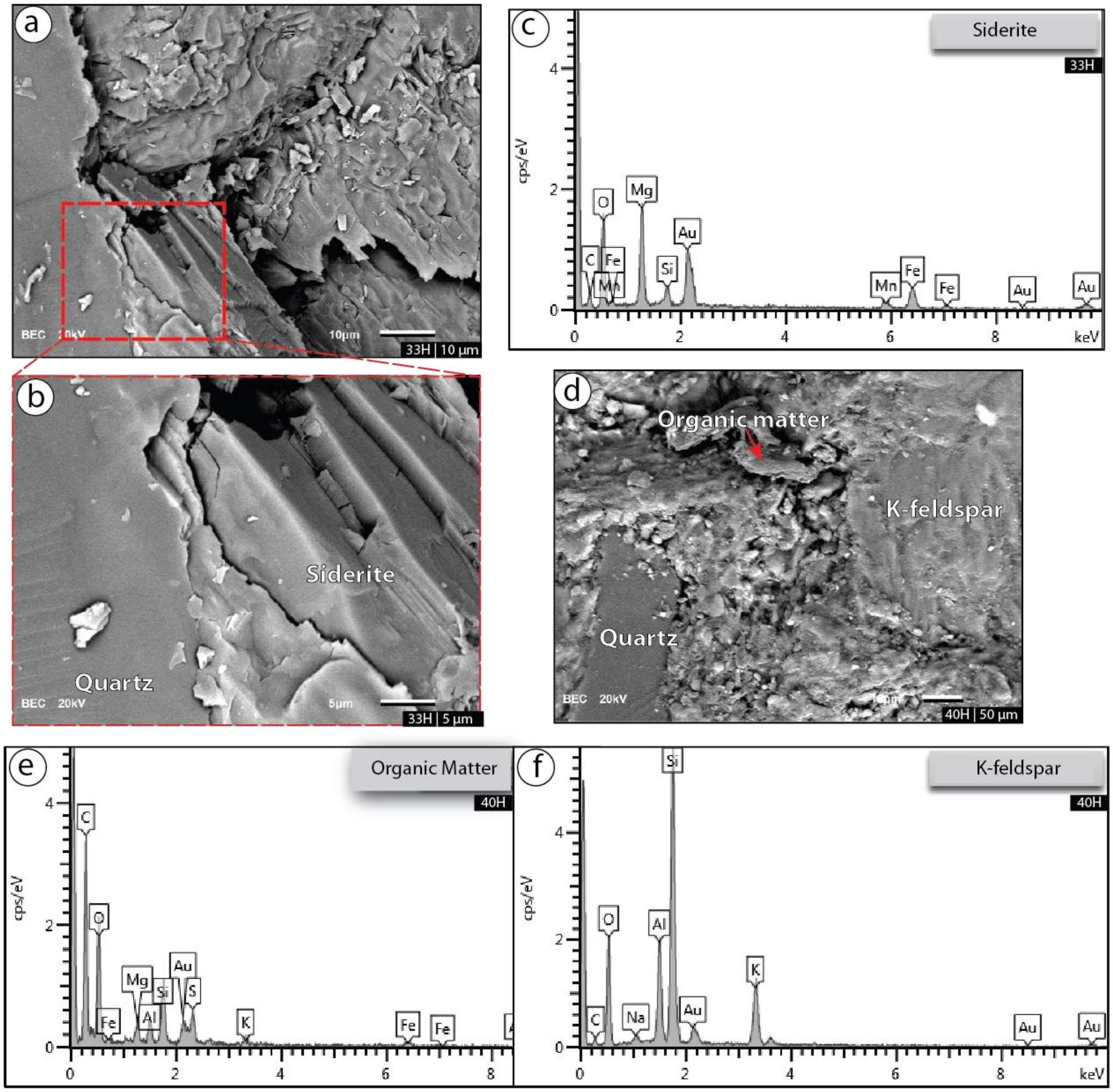

Figure 5.18: Selected SEM micrographs and EDX analysis from Well-D. (a,b) SEM micrographs with different scale for siderite cement filling the pores in the glaciofluvial lithofacies of this core, (c) EDX elemental analysis shows that the siderite is rich with Mg element, (d) SEM photomicrograph for the diamictite of this core (subglacial lithofacies) shows a piece of plant (organic matter), (e) EDX shows C element affiliate to the organic matter, (f) EDX shows the elemental composition of the alkali feldspar.

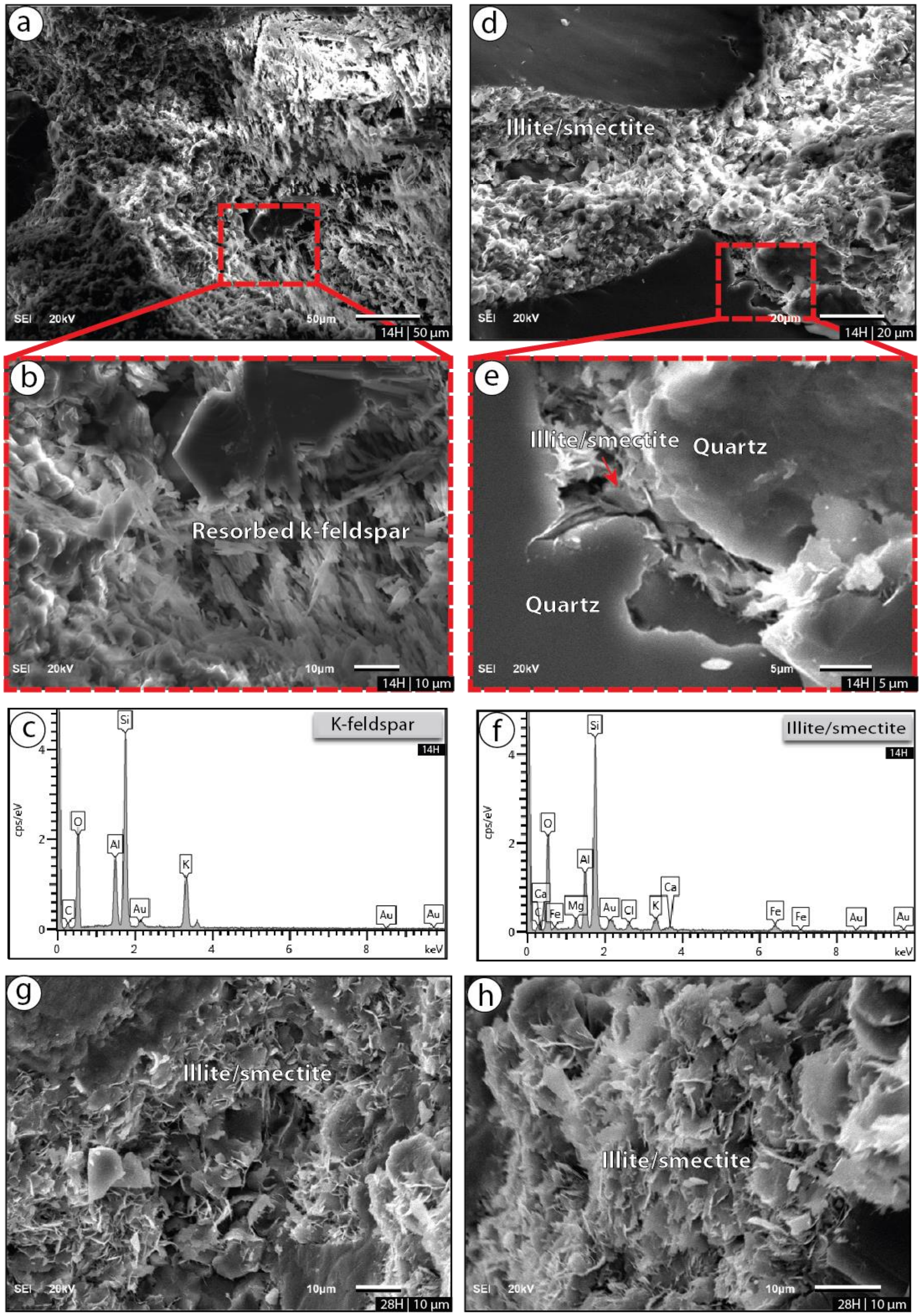

Figure 5.19: Selected SEM micrographs and EDX analysis from Well-E (glaciofluvial). (a,b) SEM micrographs with different scale for a resorbed alkali feldspar, (c) EDX shows the elemental composition of the alkali feldspar, (d,e) SEM micrographs with different scale for illite/smectite clay filling the pores and coating the grains, (g,h) SEM micrographs show the morphology of the pore filling and grains coating illite/smectite clay mineral.

5.6 Diagenesis

The “diagenesis” is a term that is used to described to all the phyico-chemical changes that affect sediments immediately after their deposition, but before metamorphism (Ali et al., 2010; Ulmer-Scholle et al., 2014). These effects are caused by physical, chemical and biological processes (Ali et al., 2010) which are responsible for the formation of sedimentary rocks from raw sediments (Worden and Burley, 2009). They comprise bioturbations, burials’ effects, chemical reactions, fluids and organic contents (Ali et al., 2010). However, the diagenetic processes are influenced by several environmental and sedimentary factors, the environmental factors include temperature, pressure, and chemical conditions whilst the sedimentary factors include grain size, mineralogical composition, fluid and organic contents (Krumbein, 1942). In the diagenetic processes, the grains might be subjected to compaction, cementation, recrystallization, replacement, differential solutions, and/or authigenesis (Ali et al., 2010; Burley and Worden, 2003; Morad et al., 2010).

The nearshore lithofacies exhibit compaction (Figure 5.3d), feldspar dissolution (Figure 5.3c) and cementation. Silica (Figure 5.3e), clay (Figure 5.3g, h) and iron oxides cement are observed. In the glaciolacustrine environment, the compaction is also observed in several zones of Well-B (Figure 5.4a, b) and Well-C (Figure 5.5a, b). The cementation in the former iron oxides, organic matter (Figure 5.4c) and sericite (Figure 5.4g) while in the latter is clay (Figure 5.5g), iron oxides, anhydrite and barite (Figure 5.5c). Feldspar dissolutions are also seen in these environments (see Figure 5.4e and Figure 5.5g). In the glaciofluvial environment of Well-D, neither compaction nor feldspar dissolution; however, the grains are cemented by siderite cement (Figure 5.6a, b,d). In

Well-E (glaciofluvial), compactions (Figure 5.7a,b,e,g) and feldspar dissolutions (Figure 5.7d,h) are observed. The cementation was also developed in this well as clay, sericite, and iron oxides. The subglacial environments of Well-B, Well-D, and Well-F are primary matrix-supported lithofacies. However, the observed diagenetic facies of all core intervals associated with porosity and permeability relationships are further discussed in details in the petrophysical characterization chapter (see chapter 7).

5.7 Interpretation and Discussion

Based on the classification of Folk (1980) for sandstone textural maturity and referring to Table 5.1 and Table 5.2, the nearshore and most of the glaciofluvial environments can be classified as mature sandstones. The glaciolacustrine sandstone of Well-C is totally mature (Table 5.3); however, in Well-B, the sandstones overlying the diamictites lithofacies can be classified as mature while the underlying argillaceous sandstone are immature (Table 5.2). All the subglacial deposits are immature (Table 5.4 and Table 5.6).

Based on outcrop studies, the sandstone of Sarah is quartzarenite derived from carton interior (Al-Harbi and Khan, 2011; Razzaq, 2013; El-Deek, 2014); however, the origin of all samples obtained from the Sarah Formation in the subsurface of Rub' Al-Khali Basin (Figure 5.2) ranges between craton interior and recycled orogen. The former is originated from low exposed granite and gneiss in a continental interior or a passive platform setting (Dickinson, 1985). The latter occurs in various tectonic settings including subduction complexes (oceanic and trench deposits), backarc thrust belts (sedimentary and metasedimentary) and suture belts (oceanic and continental rocks) (Dickinson, 1985).

Diagenetically, compaction, and cementation impact pores and pores connectivity of the grains and, therefore, alter reservoir volume and flow rate (Ali et al., 2010). Mechanical and chemical compactions (i.e. Figure 5.3d) were formed due to overburden loading and pressure-solution processes, respectively (Ali et al., 2010; Ulmer-Scholle et al., 2014). The compaction bands observed in several samples (i.e. Figure 5.7b) can be considered as porosity and permeability barriers in sandstone reservoirs. They have been reported as diminishing factors reducing the porosity to a few percent from 25% in the host (Mollema and Antonellini, 1996; cf. Fossen et al., 2007). The mechanism of such deformation bands depends on stress state, porosity, cementation, mineralogy, and grain texture (size, sorting, shape) (Fossen et al., 2007).

Various cement types are observed in this study including silica, anhydrite, barite, iron oxides, siderite, and clay cement. The silica cement (Figure 5.3e) might be a product of a dissolution from biogenic sources or from k-feldspars (Ulmer-Scholle et al., 2014). The anhydrite cement might be resulted from a circulation of sulfates-related pore water (Worden and Burley, 2009) while the barite cement might be resulted from drilling mud addititves. The siderite might be formed at a stage of precipitation through burial depth from basin brines originated from underlying marine formations (Worden and Burley, 2009; Morad et al.,1994). The sulfates and halides are commonly precipitated in playa lakes (Worden and Burley, 2009; Ulmer-Scholle et al., 2014). The clay minerals might be directly precipitated, or transformed from other clays, or resulted from an alteration of unstable silicates such as feldspar (Ulmer-Scholle et al., 2014).

CHAPTER 6

GEOCHEMICAL CHARACTERIZATION

6.1 Introduction

With the lack of biostratigraphic information, the geochemical analysis is one of the important tools for the reservoir evaluation. The analysis can be used to extract most information relating to the reservoir characteristics. In this study, forty-nine samples were selected for the geochemical analysis based on facies change observed in the studied core intervals of the Sarah Formation. Using the XRF technique, the acquired major elements are Si, Al, Fe, K, S, Ca, Ti, Mn, P and Mg, and the trace elements include Cr, Sr, V, Zn, Zr, Ni, and Ba. Other elements such as Th, U and K were acquired one reading point per inch using a high-resolution *SPECTRAL CORE GAMMA*.

Several applications are applied on the above-mentioned elements following published work on sandstone and associated sediments. Minerals such as quartz, feldspar, and clay are indicated by SiO_2, K_2O, and Al_2O_3, respectively. The mineralogical maturity reflecting the content of quartz versus other unstable detrital grains can be recognized from Harker diagram (Bhatia, 1983). Based on geochemical data, two sandstone classifications for terrigenous sandstone were established by Pettijohn et al. (Pettijohn et al., 1972, 1987) and Herron (1988). The former uses the relationship between $\log(Na_2O/K_2O)$ and $\log(SiO_2/Al_2O_3)$. The latter, so-called Sand Class system, uses the relationship between $\log(Fe_2O_3/K_2O)$ and $\log(SiO_2/Al_2O_3)$. Because of the lack of Na among the acquired oxides, The Sand Class system is used herein. The zones of biogenic silica can be recognized by the linear plotting of SiO_2 versus Zr; as a result, a negative trend indicates a biogenic source while a positive trend indicates a terrestrial input (Wright et al., 2010). The relationship between Th and K, so-called Th/K plot, has being used by Schlumberger for minerals identification, mainly clay minerals (Schlumberger, 2009). In the subsequent sections, several geochemical applications used in this study are discussed in more details.

6.2 Distribution of Elements

The analyzed major oxides and BaO in the comparative chart (Figure 6.1) show variability among the chemical composition of Well-B, Well-C, and Well-F reflecting a variation in mineralogical composition. Relatively, Well-A and Well-E have less variability. To perceive this heterogeneity, the data has been divided into four groups based on lithological characteristics of each well including; sandstone (G1), claystone and/or argillaceous sandstone (G2), calcareous and/or evaporitic sandstone (G3), and diamictite (G4).

The statistical summary of all analyzed major oxides and BaO for all groups in each well and environment are illustrated in Table 6.1. SiO_2 averages in the G1 range from 79% to 86% with coefficients of variations (CV) range from 2% to 4%. The other oxides such as Al_2O_3, Fe_2O_3, K_2O, SO_3 and CaO exhibit averages range from 0.7% to 7% and CV range from 14% to 72%. The rest of the oxides is less than 1% in their averages and up to 118% in their CV. In G2, SiO_2 averages range from 47% to 70% with CV range from 4% to 6%. Compared to G1, the concentrations of other oxides such as Al2O$_3$, Fe_2O_3 K_2O, and TiO_2 are higher in G2 than in G1. The averages of these oxides range from 3% to 16% while their CV ranges from 7% to 148%. In Well-D, this group is characterized by lower SiO_2 (average= 50%) and higher Fe_2O_3 (average=35%). BaO average in G2 of Well-C is 9.5%. The average of SiO2 is 57% (CV=19%) in G3. It decreases with increase of SO_3 (average= 14%) and CaO (average=18%). The averages of SiO_2 in the G4 range from 57% to 76%; however, the averages of the other oxides such as Al_2O_3, Fe_2O_3, K_2O, SO_3, and CaO range from 1% to 15% with CV ranges from 3% to 111%.

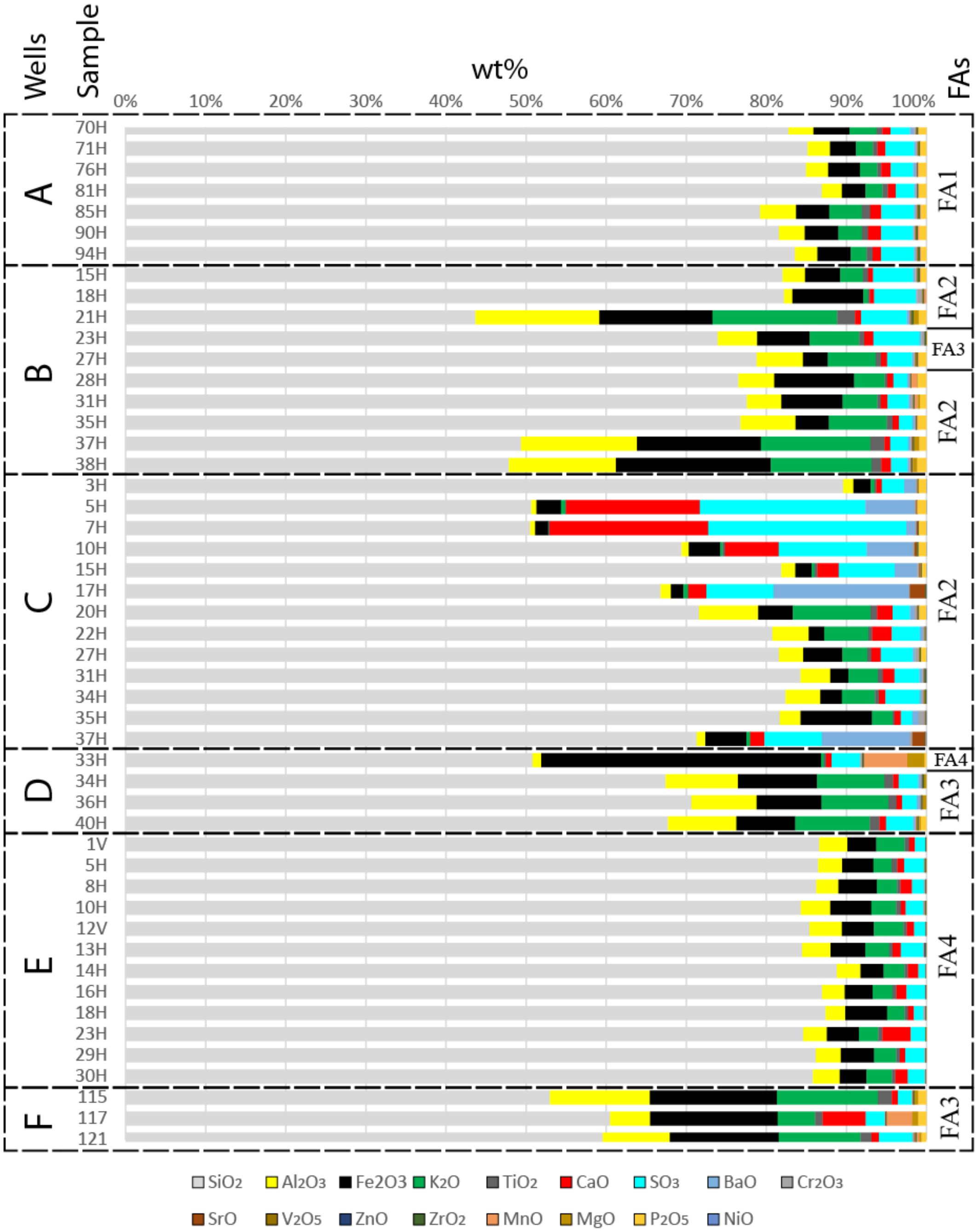

Figure 6.1: Comparative chart of the elemental oxides for the studied core samples. Note that the nearshore (FA1) and the glaciofluvial environments (FA4) are relatively characterized by low geochemical heterogeneity and are dominated by SiO_2 affiliated to quartz. This heterogeneity is relatively higher in the glaciolacustrine delta (FA2) and subglacial environments (FA3). It reflects the heterogeneity of the mineralogical composition within these environments.

Table 6.1: Statistical summary of all the analyzed oxides for the studied core intervals. Note that this table shows the elemental composition of the sandstone (G1) in the nearshore (FA1), glaciofluvial (FA4) and glaciolacustrine (FA2) environments, the clay/argillaceous sandstone (G3) in the FA2 and FA4, the calcareous/evaporitic sandstone (G3) in the FA2, and the diamictites (G4) of the subglacial environment (FA3).

Group	**Well**	**Stat.**	**SiO_2%**	**Al_2O_3%**	**Fe_2O_3%**	**K_2O%**	**SO_3%**	**CaO%**	**TiO_2%**	**MnO%**	**P_2O_5%**	**MgO%**	**BaO%**	**Samples**	**Facies**	**FAs**
G1	Well-A	**m**	83.47	3.10	3.88	2.68	3.32	1.18	0.71	0.10	0.82	-	0.27	70H, 71H, 76H, 81H, 85H, 90H, 94H	F2, F3, F4	FA1
		SD	2.55	0.66	0.56	0.81	0.80	0.23	0.18	0.07	0.15	-	0.13			
		CV	**3%**	**21%**	**14%**	**30%**	**24%**	**20%**	**25%**	**65%**	**18%**	**-**	**50%**			
	Well-B	**m**	79.03	3.90	7.02	3.75	3.25	0.72	0.47	0.32	0.90	0.13	0.22	15H, 18H, 28H, 31H, 35H	F3, F7, F8	FA2
		SD	2.85	2.16	2.61	2.40	1.73	0.12	0.23	0.27	0.16	0.10	0.06			
		CV	**4%**	**55%**	**37%**	**64%**	**53%**	**17%**	**49%**	**83%**	**18%**	**76%**	**26%**			
	Well-C	**m**	83.18	3.03	3.56	2.84	3.73	1.44	0.41	0.02	0.70	-	0.91	3H, 15H, 22H, 27H, 31H, 34H, 35H	F1, F2	
		SD	3.04	1.25	2.58	1.89	1.70	0.82	0.15	0.02	0.23	-	0.93			
		CV	**4%**	**41%**	**72%**	**67%**	**46%**	**57%**	**37%**	**102%**	**33%**	**-**	**102%**			
	Well-E	**m**	86.10	3.18	4.08	2.80	1.85	1.22	0.50	0.01	-	-	-	1V, 5H, 8H, 10H, 12V, 13H, 14H, 16H, 18H, 23H, 29H, 30H	F1-F8	FA4
		SD	1.33	0.45	0.72	0.49	0.60	0.80	0.10	0.01	-	-	-			
		CV	**2%**	**14%**	**18%**	**17%**	**32%**	**65%**	**21%**	**118%**	**-**	**-**	**-**			
G2	Well-B	**m**	46.99	14.44	16.31	13.93	3.35	0.89	1.74	0.02	0.99	0.60	0.30	21H, 37H, 38H	F2, F6	FA2
		SD	2.94	1.06	2.72	1.53	2.07	0.28	0.50	0.01	0.14	0.05	0.03			
		CV	**6%**	**7%**	**17%**	**11%**	**62%**	**32%**	**29%**	**38%**	**14%**	**9%**	**10%**			
	Well-C	**m**	69.92	3.25	3.68	3.58	5.90	2.00	0.82	0.02	0.87	-	9.49	17H, 20H, 37H	F2, F1	
		SD	2.68	3.61	1.86	5.28	3.28	0.25	-	0.02	-	-	8.30			
		CV	4%	111%	51%	148%	56%	12%	-	90%	-	-	88%			
	Well-D	**m**	**50.84**	**1.07**	**34.94**	**0.38**	**3.55**	**0.69**	**0.25**	**5.43**	**0.22**	**2.15**	**0.03**	33H	F2	FA4
G3	Well-C	**m**	56.88	0.72	2.88	0.30	18.80	14.41	0.22	0.00	1.00	-	4.32	5H, 7H, 10H	F3, F5	FA2
		SD	10.89	0.14	1.15	0.30	7.06	6.85	0.11	0.00	0.11	-	2.76			
		CV	**19%**	**19%**	**40%**	**101%**	**38%**	**48%**	**49%**	**12%**	**11%**	**-**	**64%**			
G4	Well-B	**m**	76.38	5.34	4.85	6.06	4.45	0.96	0.65	0.03	0.97	-	0.20	23H, 27H	F4, F5	FA3
		SD	3.45	0.59	2.41	0.16	1.89	0.30	0.05	0.04	-	-	0.03			
		CV	**5%**	**11%**	**50%**	**3%**	**42%**	**31%**	**7%**	**136%**	**-**	**-**	**16%**			
	Well-D	**m**	68.61	8.56	8.45	8.69	2.54	0.74	1.11	0.02	0.69	0.30	0.33	34H, 36H, 40H	F1	
		SD	1.77	0.43	1.30	0.54	0.79	0.07	0.09	0.03	-	0.12	0.06			
		CV	**3%**	**5%**	**15%**	**6%**	**31%**	**10%**	**8%**	**136%**	**-**	**40%**	**19%**			
	Well-F	**m**	57.70	8.61	15.14	9.15	2.76	2.35	1.36	1.15	0.87	0.50	-	115, 117, 121	F1, F3, F4	
		SD	4.11	3.74	1.33	4.08	1.25	2.62	0.38	1.76	0.22	0.24	-			
		CV	**7%**	**43%**	**9%**	**45%**	**45%**	**111%**	**28%**	**153%**	**25%**	**47%**	**-**			

6.3 Lithofacies Geochemical and Petrophysical logs

From Figure 6.2 to Figure 6.7 are integrated figures illustrating the lithofacies, SGR, XRF, porosity and permeability logs for each well. The SGR includes GR, Th, K and U whilst the XRF includes Si, Al, K, Ti, Fe, S, Ca, and Zr. The lithofacies of Well-A (nearshore environment) (Figure 6.2) and Well-E (glaciofluvial environment) (Figure 6.7) show very slight variation in their elemental composition. Petrographically, the former is classified as subarkose sandstone (Figure 5.1b) while the latter is classified as sublitharenite (Figure 5.1e) according to the sandstone classification of Folk (1980). In the claystone and argillaceous sandstone of the glaciolacustrine delta environment (Well-B) (Figure 6.3), the Si concentration decreases as those of Al, K, Ti, GR, Th, and U increase. In Well-B, the top of the subglacial environment (F5) is marked by the increase in Si, S and Ca concentrations and the decrease of Al, K, Ti and Fe concentrations while the bottom of this environment (F4) is marked by the increase in Mn and Fe. The difference between the subglacial lithofacies, F4 and F5, is that the former is characterized by lower concentrations of Fe, Mn, S, and Ca.

In the glaciolacustrine delta environment, the upper part of the Well-C core interval (Figure 6.4, F5) is characterized by a decrease of Si associated with an increase of S and Ca concentrations. This increase in S and Ca likely associated with the presence of anhydrite cement which is confirmed by XRD (Figure 5.11, sample #5H) and thin section analyses (Figure 5.5c). The Si concentration decreases in several zones with a corresponding increase of Ba and Sr. The latter elements are likely associated with the barite mineral confirmed by the XRD (Figure 5.11, i.e. sample #7H) and the thin section analyses (Figure 5.5c).

In the Well-D (Figure 6.5), the glaciofluvial argillaceous sandstone (F2) is distinguished from the subglacial diamictite lithofacies (F1) by its relatively higher concentrations of Fe, Mg, and Mn and lower concentrations of Si, Al, K, and Ti. The F2 samples from this core are characterized by siderite cement (Figure 5.12; sample #33H and Figure 5.6a,b). The gamma ray reading (GR) is higher in the subglacial environment (F1) than in the glaciofluvial environment (F1). It decreases in the lower part of the core. The porosity and permeability are enhanced by fractures in the F1.

The core interval from Well-F interpreted as subglacial environment (Figure 6.6) is characterized by very high GR, Th, K, and U values. These components which decrease within diamictite lithofacies are enriched in shale lithofacies. The elemental composition of the diamictite is variable reflecting the heterogeneity of its mineralogical composition. Porosity and permeability are only enhanced by fractures.

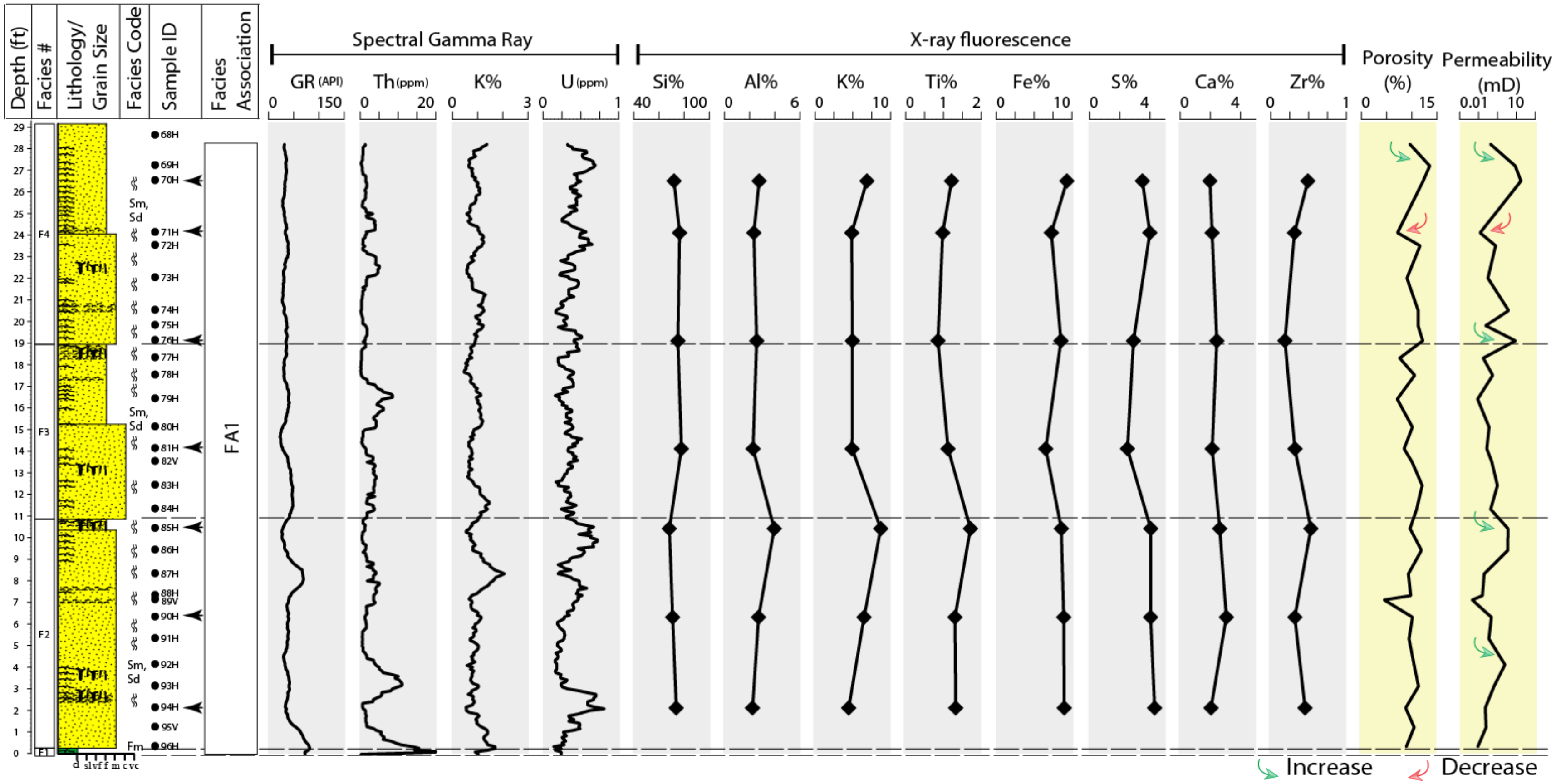

Figure 6.2: Integrated sedimentological, geochemical and petrophysical logs of Well-A. No significant geochemical variation is observed in the nearshore environment (FA1) except some SGR increases attributed to mud drapes. The porosity and permeability are enhanced by fractures (i.e. upper part of F4).

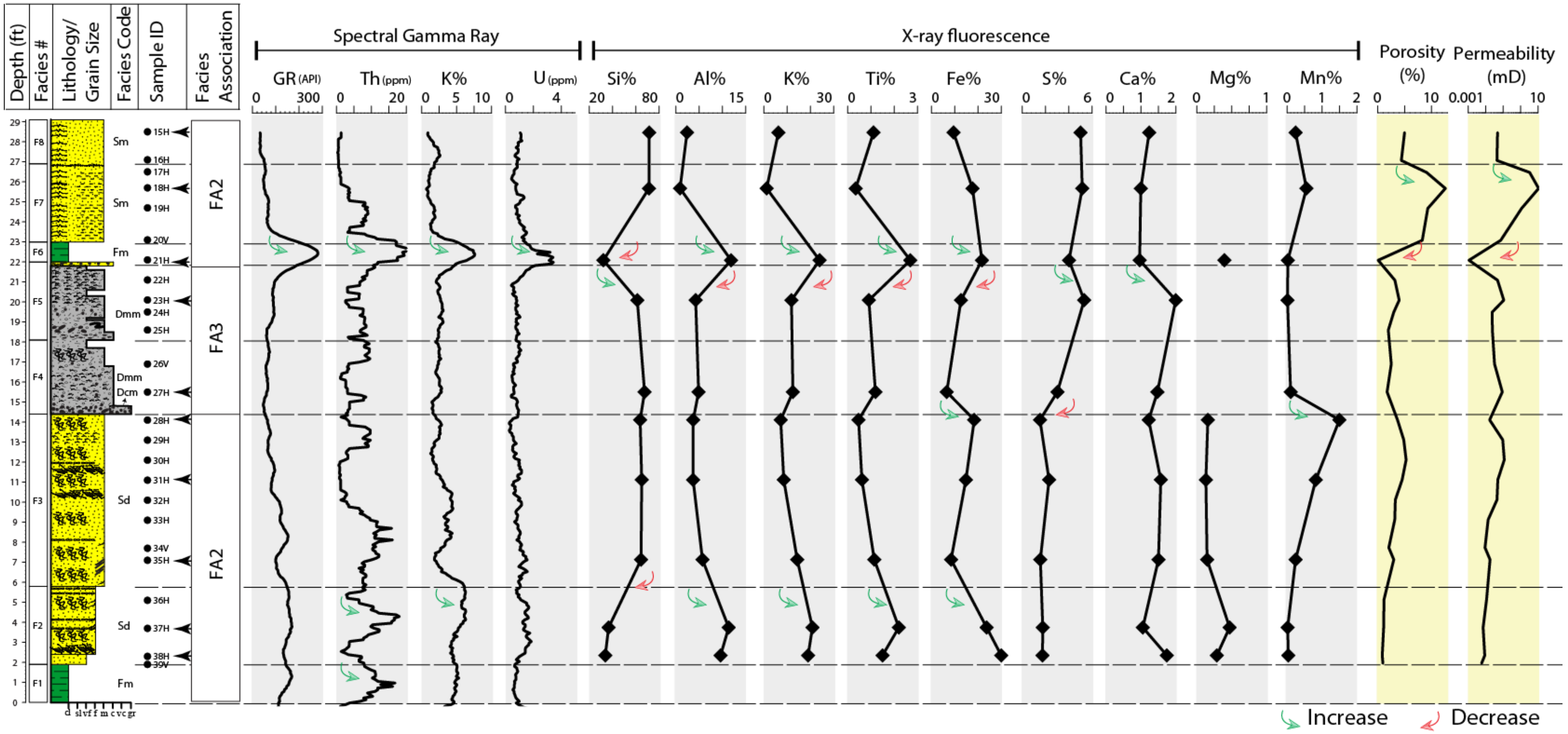

Figure 6.3: Integrated sedimentological, geochemical and petrophysical logs of Well-B. The GR, Th, K, U, Al, Ti, and Fe increases and Si decreases are associated with the claystone and/or argillaceous sandstone in the glaciolacustrine delta environment (FA2). The top of the subglacial lithofacies (FA3) is marked by the increase of S and Ca which might be affiliated to anhydrite while the bottom is marked by the increase of Mn. In F7, porosity and permeability increases are associated with the intensive fractured zone.

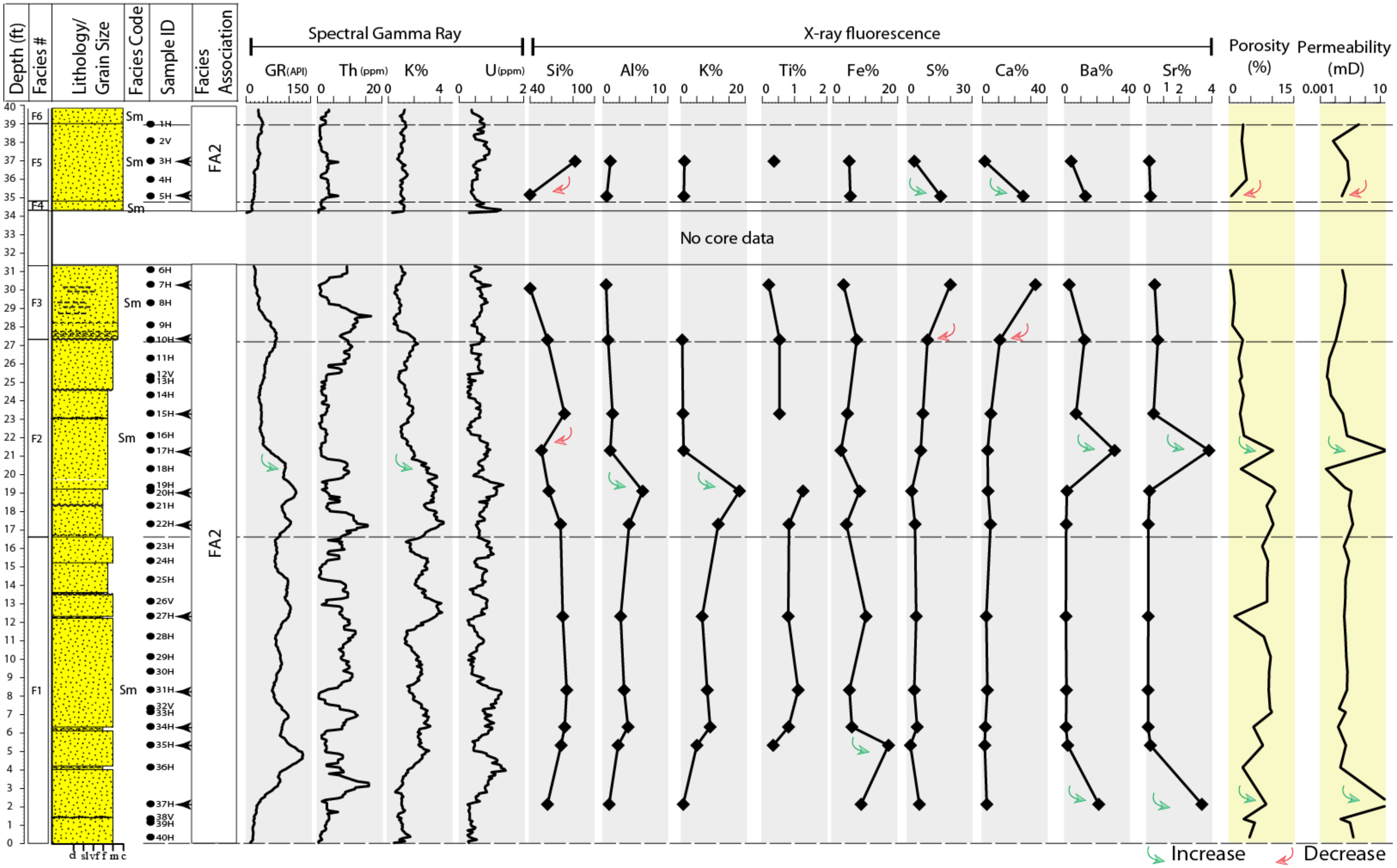

Figure 6.4: Integrated sedimentological, geochemical and petrophysical logs of Well-C, glaciolacustrine delta (FA2). In the upper part of the core (i.e. F5), S and Ca increase due to anhydrite cement. This increase can be a top marker for the Sarah Formation in this core. The increases of Ba and Sr are associated with barite mineral. The increase of Fe is affiliated to iron oxide cement. The sudden increases in porosity and permeability are related to fractures.

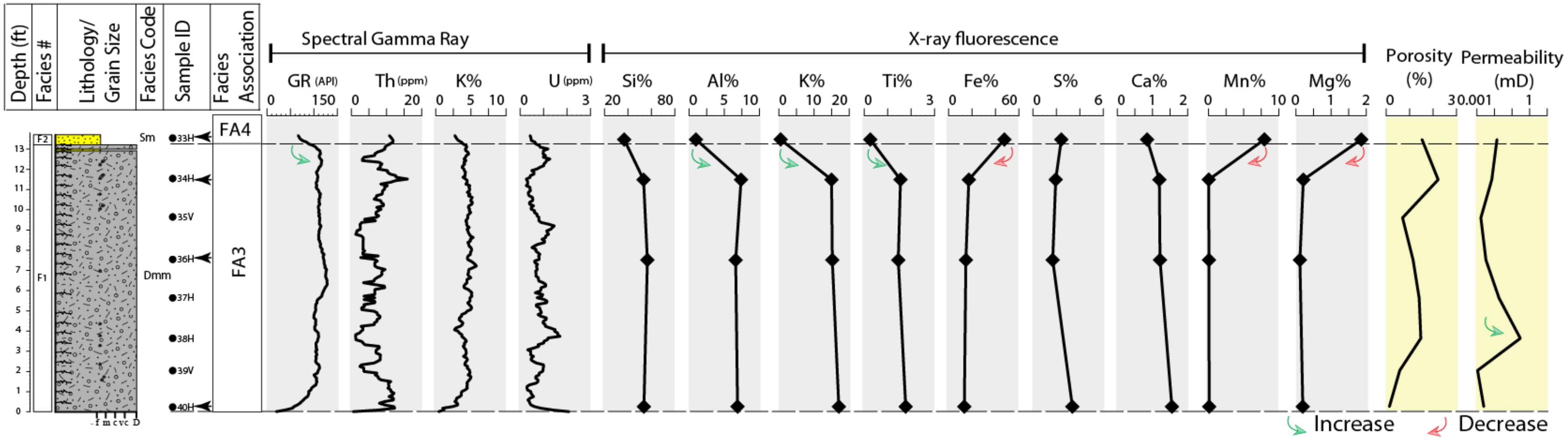

Figure 6.5: Integrated sedimentological, geochemical and petrophysical logs of Well-D. The subglacial lithofacies (FA3) shows low concentrations of Mn, Mg, and Fe and high concentrations of Si, Al, K, and Ti. The high concentration of Mg in the glaciofluvial lithofacies (FA4) is affiliated to Mg-siderite cement.

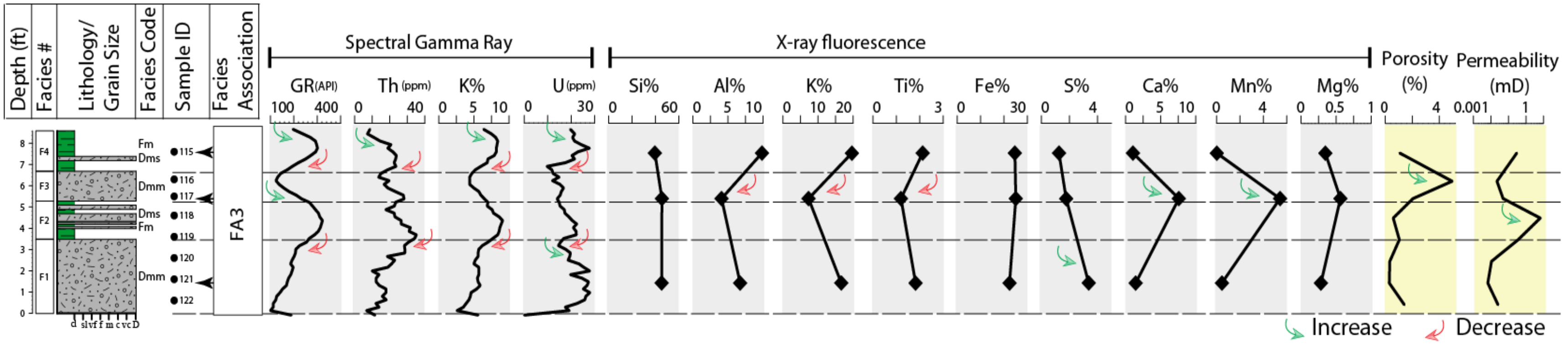

Figure 6.6: Integrated sedimentological, geochemical and petrophysical logs of Well-F. The GR, Th, K and U curves decrease with subglacial lithofacies (FA3) and increase with shale. Porosity and permeability are enhanced by fractures.

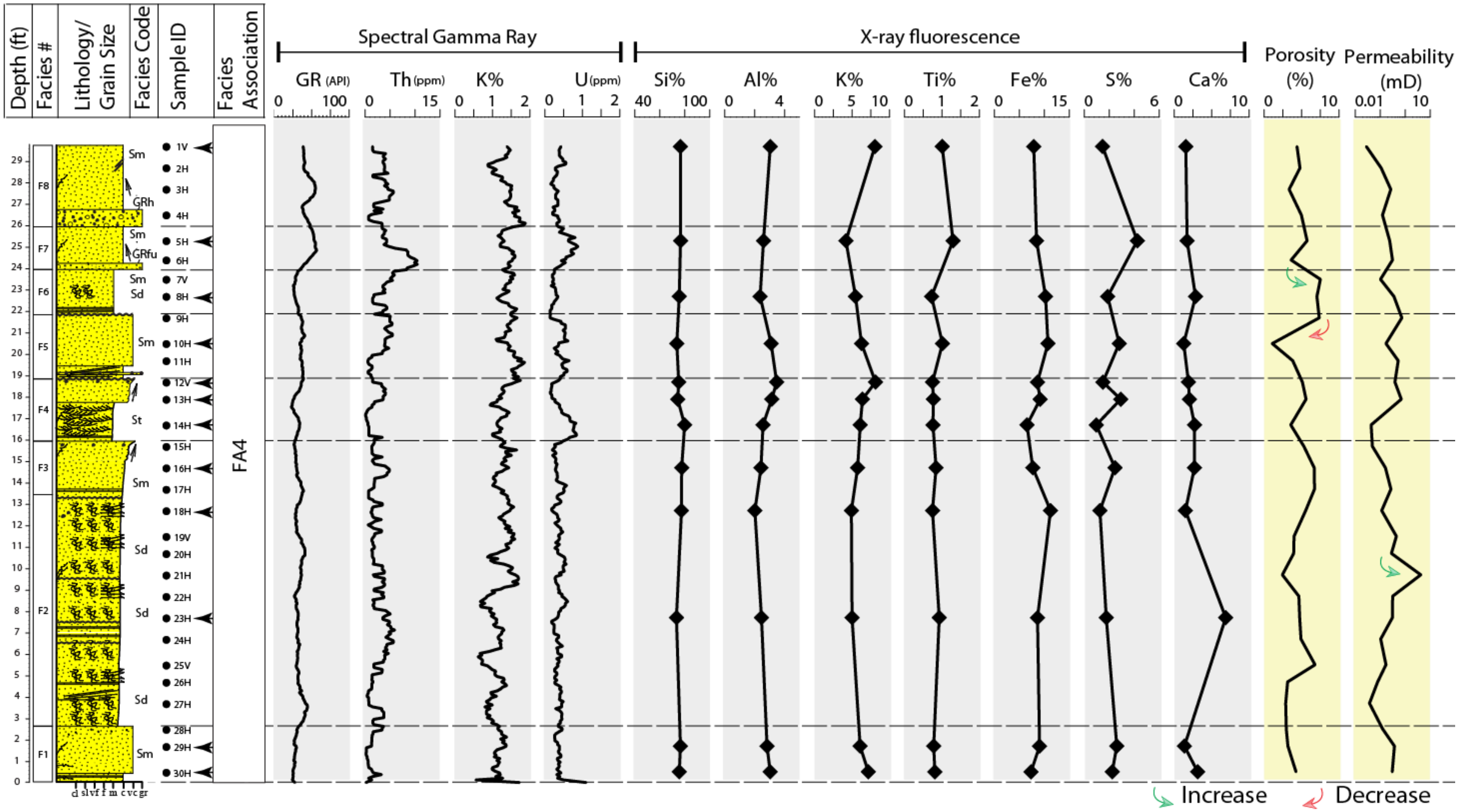

Figure 6.7: Integrated sedimentological, geochemical petrophysical logs of Well-E, glaciofluvial environment (FA4). There is no significant geochemical variation observed in this core. The porosity and permeability might be enhanced by fractures due to the deformation (i.e. F6).

6.4 Biogenic Silica

From lithofacies description, the bioturbation in the nearshore environment is observed (Figure 4.1B,b,e). The Zr element affiliated to the heavy mineral, zircon, is considered to represent a proxy for terrestrial input if it builds a positive linear relationship with SiO_2 (Wright et al., 2010). However, where Zr decreases and SiO_2 increases, this relationship indicates a biogenic source rather than a terrestrial source (Wright et al., 2010). SiO_2 versus Zr plot is applied to recognize biogenic silica within the nearshore environment when compared to the terrestrial input of the subglacial environment (Figure 6.8). The biogenic trend shows a strong negative correlation (r=0.65) while the terrestrial trend shows a strong positive correlation (r=0.63). The correlation strength is based on the absolute value of the coefficient of correlation (r) suggested by Evans (1996).

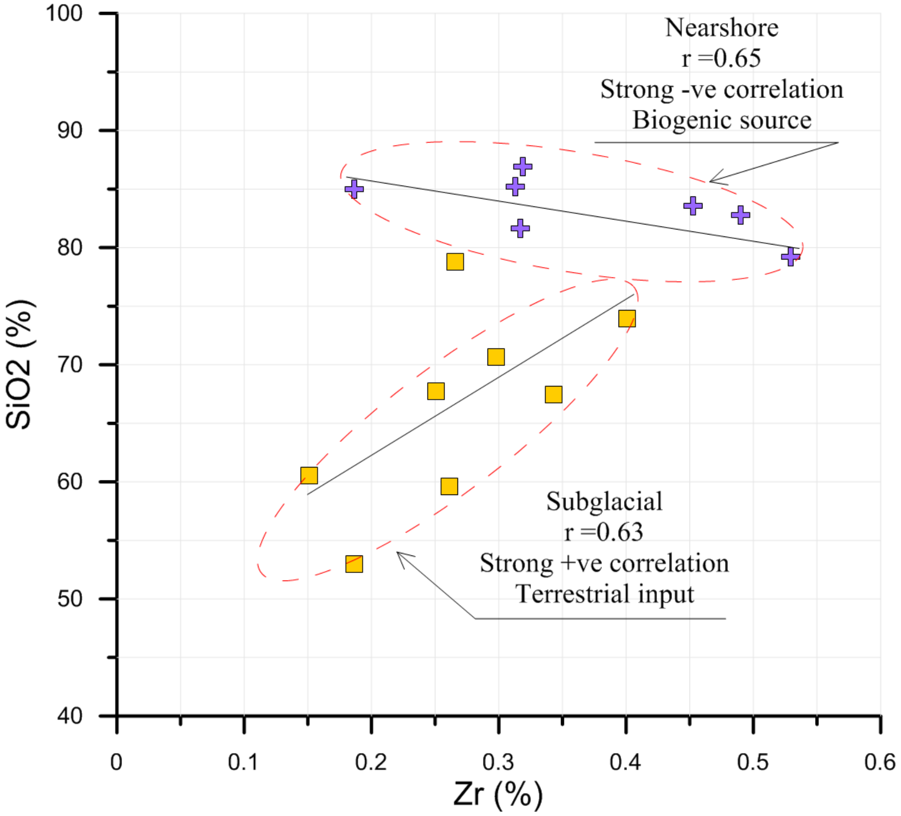

Figure 6.8: The relationship between SiO_2 and Zr differentiates the biogenic quartz of the nearshore from the terrestrial input of the subglacial environment. Note that the absolute value of the coefficient of correlation (r) ranging from 0.60 to 0.79 indicates a strong correlation (Evans, 1996).

6.5 Mineralogical Maturity

There are two types of maturity discussed in this study, the textural maturity, and the mineralogical maturity. The former maturity is based on Folk (1980) maturity classification that is related to the grains shape and the amount of clay content. The latter is reflected by an increase of the quartz content with a decrease of the other detrital grains (Bhatia, 1983). The quartzarenites are composed pure $SiO_{2.,}$ Al_2O_3 coming from clay, K_2O mostly derived from argillaceous rock fragments, CaO from calcite cement (Pettijohn et al., 1987). Harker variation diagram for all the analyzed samples (Figure 6.9) illustrates the abundances of TiO_2, Al_2O_3, Fe_2O_3, MnO, CaO, MgO, SO_3 and K_2O with comparing to SiO_2. The sandstone (G1) which contains high proportions of SiO_2 is more mature than the other groups (Table 6.2). On the contrary, the claystone and/or the argillaceous sandstone (G2) is less mature than the others because they contain low proportions of SiO_2. The diamictites (G4) is located in between these two groups while the calcareous and/or evaporitic sandstone (G3) is characterized by high values of SO_3 and CaO. Based on the depositional environments, the nearshore, and the glaciofluvial lithofacies are relatively more mature than the subglacial and glaciolacustrine delta lithofacies (Figure 6.10).

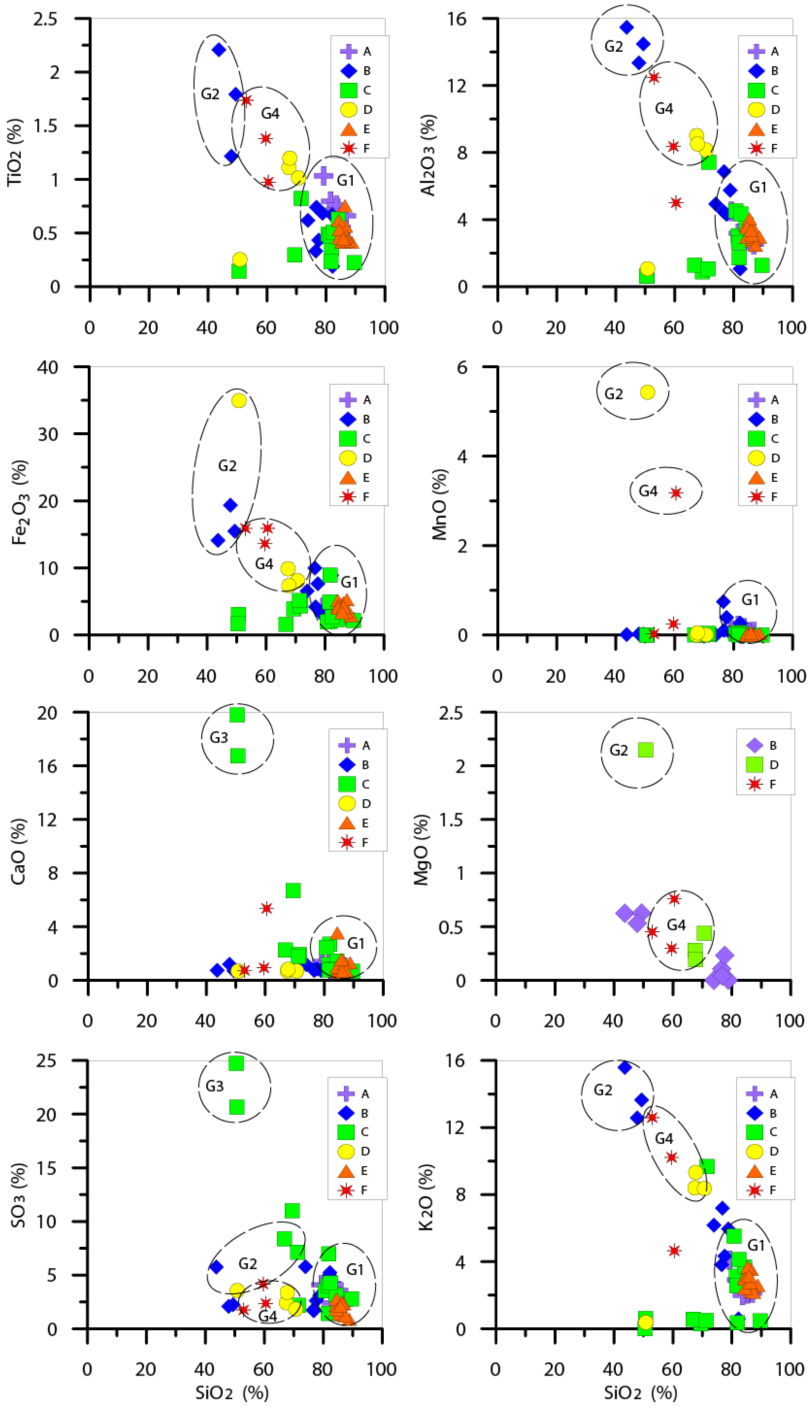

Figure 6.9: Harker variation diagram illustrates the analyzed oxides versus SiO_2 based on the lithological groups. The SiO_2 increases with the increase of quartz content (mature), and decreases with the increase of the other unstable grains (less mature). G1: sandstone, G2: claystone/argillaceous sandstone, G3: calcareous/evaporitic sandstone and G4: diamictites.

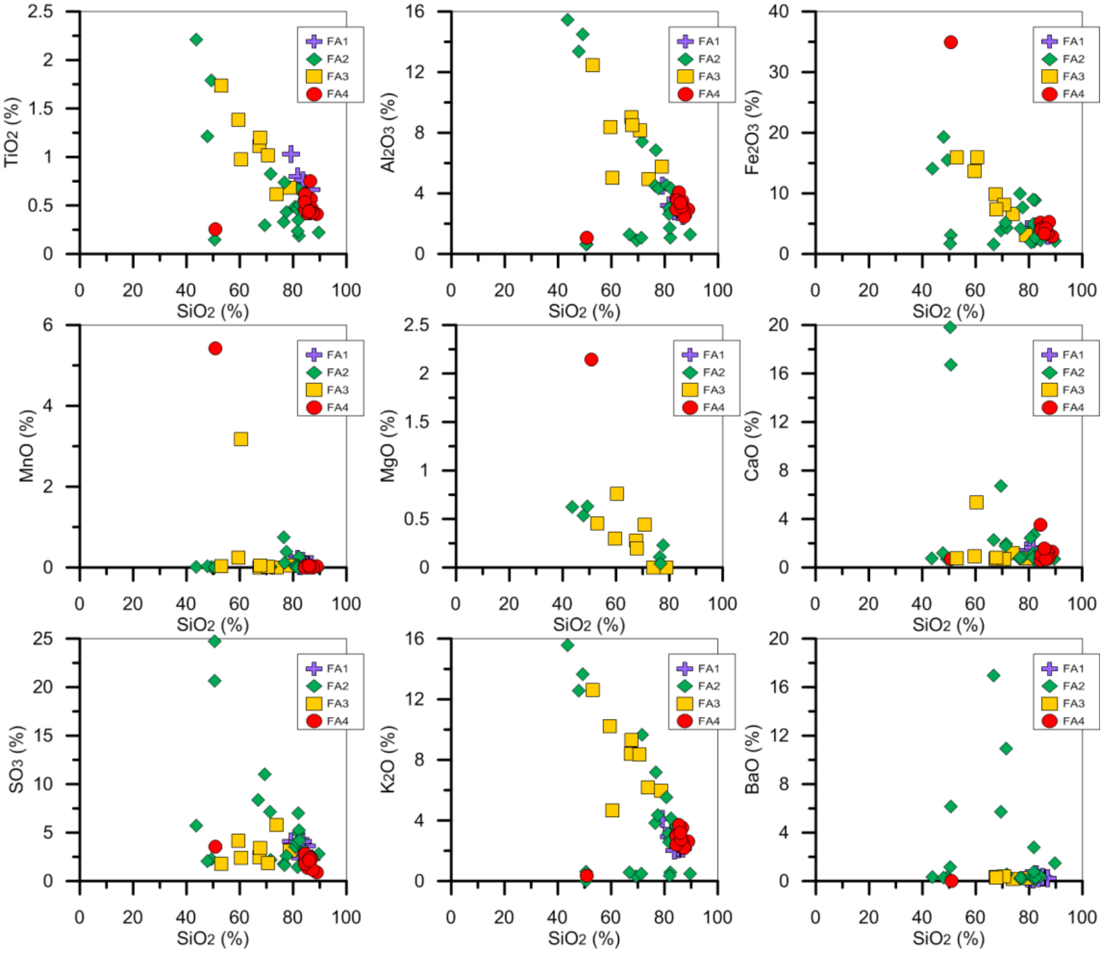

Figure 6.10: Harker variation diagram illustrates the analyzed oxides versus SiO_2 based on the depositional environments. The nearshore (FA1) and the glaciofluvial (FA4) lithofacies are relatively more mature than the subglacial (FA3) and the glaciolacustrine delta (FA2) lithofacies. Note the distribution of each oxide versus SiO_2 in each environment. The more SiO_2, the better mineralogical maturity.

6.6 Sandstone Classification Using Sand Class System

Herron (1988) suggested a Sand Class system from which terrigenous sandstones can be classified by plotting log(Fe_2O_3/K_2O) versus log(SiO_2/Al_2O_3) (Figure 6.11). Accordingly, the core intervals of Well-A (nearshore lithofacies) and Well-E (glaciofluvial lithofacies) are classified as sublitharenite sandstones (Figure 6.12). However, based on the QFL data and following the classification of Folk (1980), the lithofacies from the former depositional environment have been classified as subarkose (Figure 5.1). The chemical classification does not always fit with the petrographic classification (Pettijohn et al., 1987; Rollinson, 1993). This nearshore environment contains zones of biogenic silica as it has been indicated by the SiO_2 vs Zr plot suggested by Wright (2010) (Figure 6.8). Therefore, the difference between the petrographic and the geochemical classification of this environment might be attributed to a diagenetic product such as cement affecting the geochemical analysis of the sandstone or the Sand Class system might not be applicable on the biogenic sandstone.

Although the claystone samples are placed at the shale section in the Sand Class system, the other samples of the Well-B and Well-C are scattered indicating various sandstone types in the glaciolacustrine delta environment (Figure 6.12). The diamictite (subglacial lithofacies) of Well-D is classified as arkose to litharenite while the glaciofluvial argillaceous sandstone of this well is classified as ferruginous sand. The diamictites (subglacial lithofacies) of Well-F is classified as wacke to litharenite.

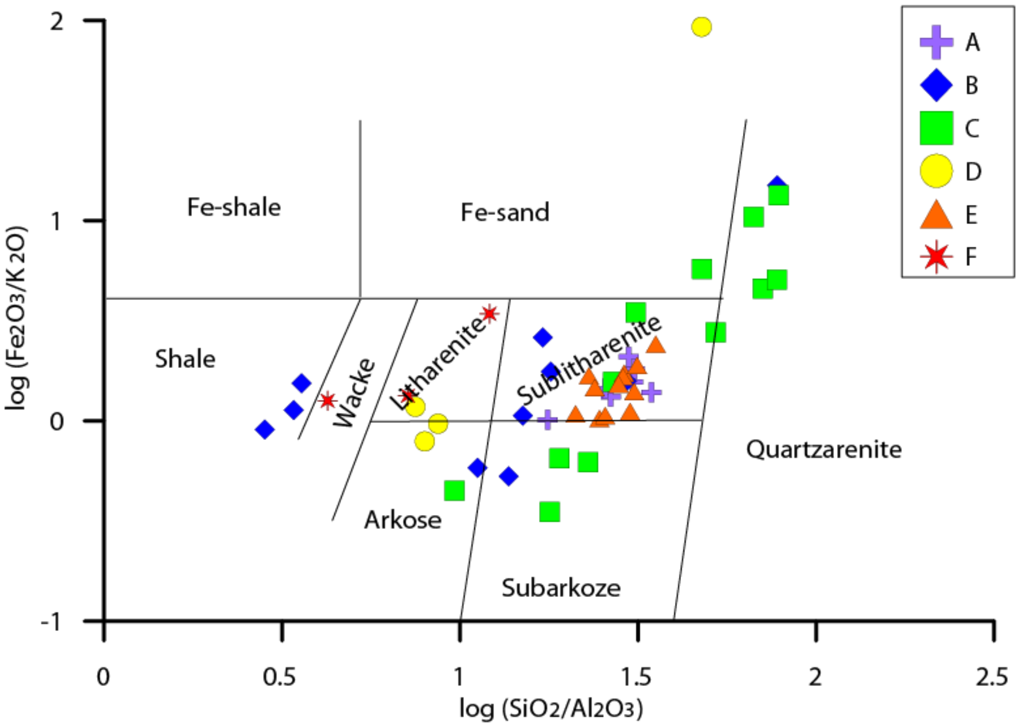

Figure 6.11: Sandstone geochemical classification of all wells (A-F) based on the Sand Class System (Herron, 1988). Samples from Well-A and Well-E are classified as sublitharenite while those from the other wells are variable sandstone classes.

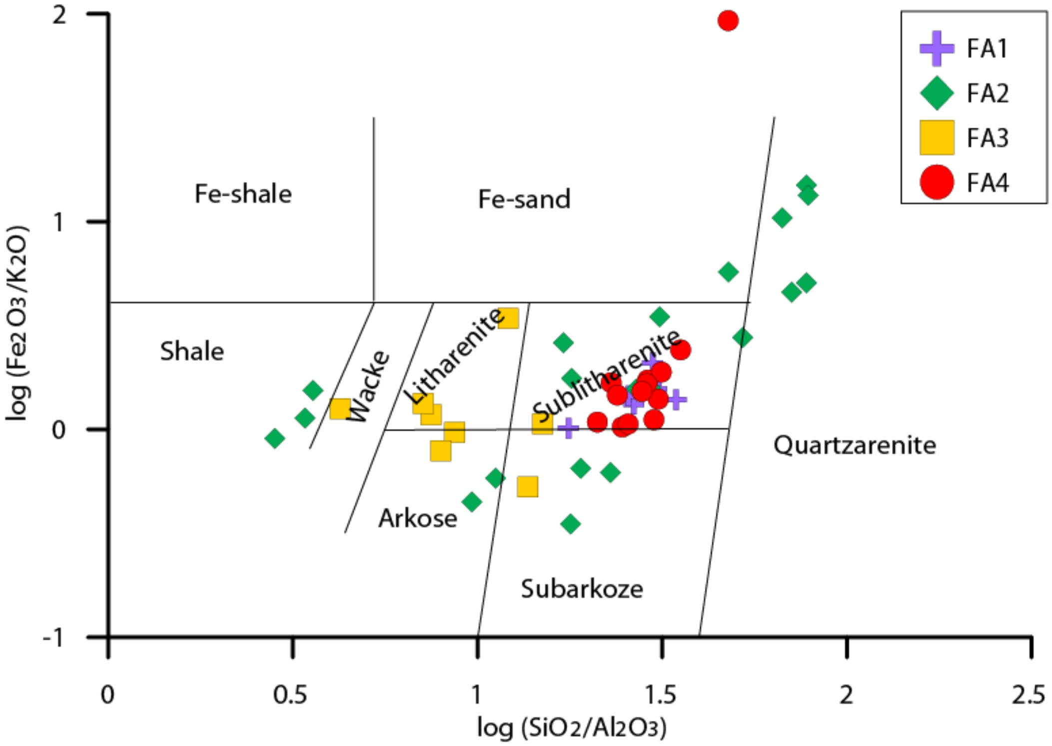

Figure 6.12: Sandstone geochemical classification of the depositional environments based on the Sand Class System (Herron, 1988). The nearshore (FA1) and the glaciofluvial (FA4) lithofacies are classified as sublitharenite while the glaciolacustrine delta (FA2) and the subglacial (FA3) lithofacies are variable.

6.7 Spectral Gamma Ray

Thorium (Th) and uranium (U) are reported in part per million (ppm), whereas potassium (K) is recorded in percentage (%). In sedimentary rocks, Th is exclusively associated with aluminosilicate minerals, K is derived from micas and alkali feldspar, and U element is strongly correlated with organic carbon (Hassan et al., 1976). The Th/K plot can be used to delineate clay types using a plot where Y-axis represents Th ranging from 0 to 25ppm while X-axis contains K values ranging from 0% to 5% (Schlumberger, 2009).

A total of 1717 reading points for Th, K and U have been recorded from the core samples of the six wells. About 7% of them are off-scale of Th/K plot. Particularly in the core interval of Well-F, about 77% of the reading points are off-scale indicating that this core encompasses extreme values of these elements (Table 6.2).

By the contrast, the core intervals of Well-A and Well-E contain the lowest values of these elements. The reading points of Well-D core are greater than those of Well-C core. Each well has been plotted and characterized based on the classified groups (section 6.2). In G1, the Well-A (Figure 6.13) and Well-E (Figure 6.17) exhibit two populations. The first one (Th < 2.5ppm and K< 2%) is dominated by mica and glauconite whereas the second one (2.5 < Th < 10ppm and K<2%) is dominated by montmorillonite and illite.

The plots the Th and K data for the G1 group in Well-B (Figure 6.14) and Well-C (Figure 6.15) are scattered, with Th < 12ppm and K < 4.5%, indicating a diversity in the clay minerals content. The G2 in Well-B is dominated by illite and mica. The G3 exhibits two populations, a population dominated by glauconite, feldspar and potassium evaporites (where Th is less than 2.5ppm) and another population represented by illite (where Th is greater than 2.5ppm, but below 4ppm). In Well-B (Figure 6.14), Well-D (Figure 6.16) and Well-F (Figure 6.18), The G4 shows the abundance of mixed layers, illite, mica, glauconite, and feldspar.

The bivariate plots of Th and K for the depositional environments, the nearshore (FA1) and glaciofluvial (FA4) lithofacies are characterized by lower variation in clay minerals than the glaciolacustrine delta and the subglacial lithofacies (Figure 6.19). The former lithofacies are characterized by montmorillonite, illite, mica and feldspar. On the contrary, the glaciolacustrine delta (FA2) is characterized by various clay minerals reflecting the highest amount of the clay contents among the other environments. In the subglacial lithofacies (FA3), the Th versus K plot is also scattered. The difference between the diamictites types is, however, clearly illustrated in the plot. For instance, the clast-supported and the sandy matrix supported diamictites of Well-B are grouped towards lower clay mineral contents (lower Th and K) while the matrix-supported diamictites of Well-D and Well-F are grouped towards the highest clay mineral contents (higher Th and K).

Table 6.2: Statistical summary of Th, U, and K for all wells. Note that the K is off-scale in the claystone and/or argillaceous sandstone (G2) in Well-B and Well-F, and in the diamictite (G4) of Well-D while the Th is off-scale in G2 of Well-F indicating a higher amount of clay contents.

Wells	SGR	m	SD	CV	Count	Off-Scale
Well-A	Th	2.6	2.7	102%	350	0%
	K	1.0	0.3	29%		0%
	U	0.4	0.1	35%		-
Well-B	Th	6.7	4.6	68%	350	0%
	K	3.2	1.6	49%		15% (G2)
	U	1.0	0.5	48%		-
Well-C	Th	5.4	3.8	70%	444	0%
	K	1.9	0.9	50%		0%
	U	0.7	0.2	37%		-
Well-D	Th	6.9	3.2	46%	165	0%
	K	4.3	0.8	18%		9% (G4)
	U	0.8	0.3	41%		-
Well-E	Th	2.9	1.9	67%	356	0%
	K	1.3	0.2	19%		0%
	U	0.4	0.1	38%		-
Well-F	Th	20.2	7.0	35%	52	23% (G2)
	K	6.3	1.6	25%		23% G4 -53% G2
	U	19.4	5.4	28%		-

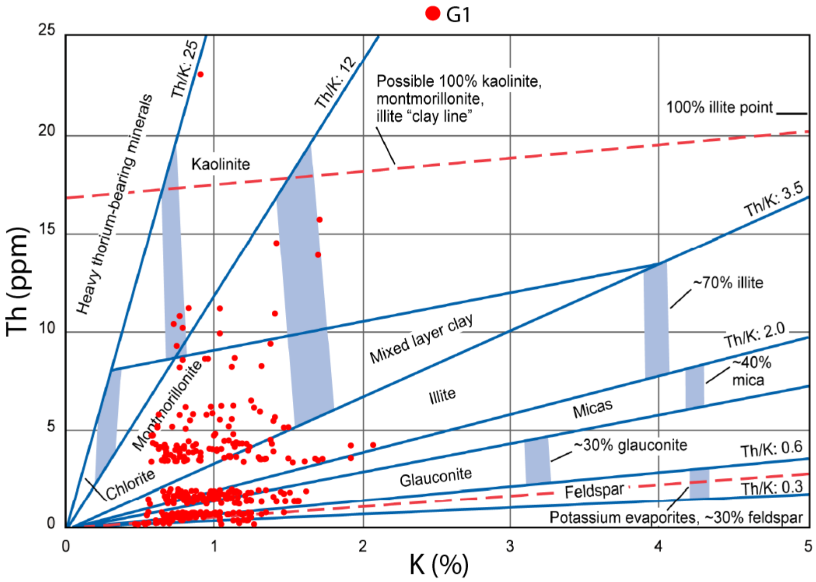

Figure 6.13: Th and K plot for Well-A. Note that the populations of G1 (sandstone) in this figure are two populations, the first likely represent mica, glauconite, and feldspar while the second one likely represents illite and montmorillonite clay minerals. After Schlumberger (2009).

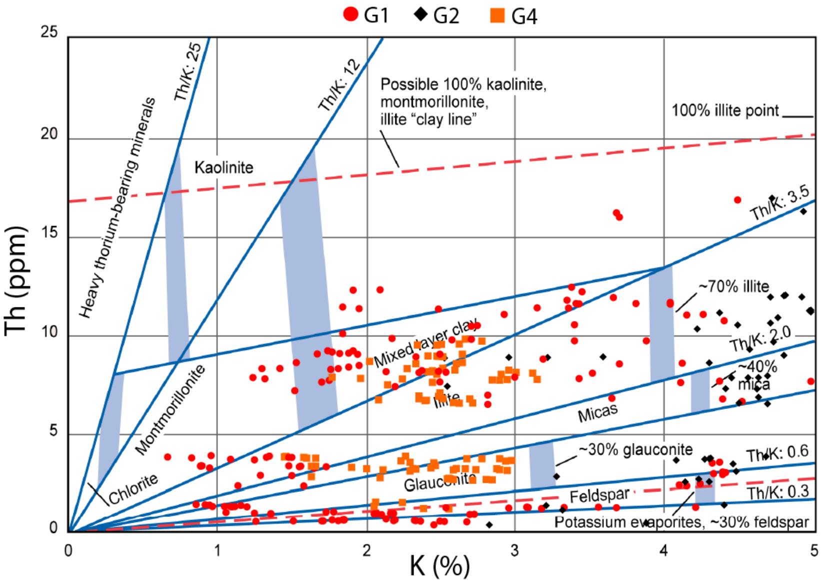

Figure 6.14: Th and K plot for Well-B. Note that the scattering data points of G1 (sandstone), G2 (clay/argillaceous sandstone) and G4 (diamictites) indicate clay minerals variation. After Schlumberger (2009).

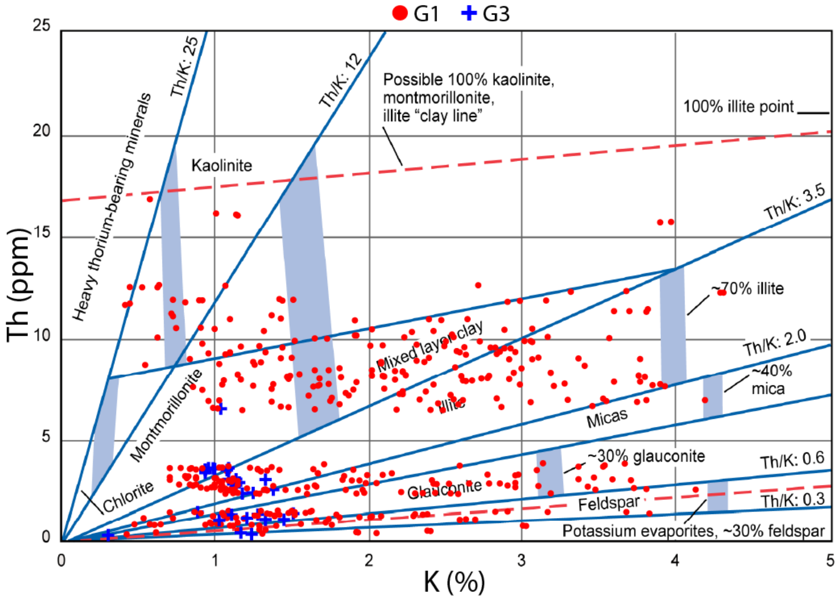

Figure 6.15: Th and K plot for Well-C. Note the scattering data points of G1 (sandstone) and the population of G3 (calcareous/evaporitic sandstone). The latter contains fewer clay minerals variation than the former. This group is characterized by anhydrite cement which is another factor affecting the reservoir quality. After Schlumberger (2009).

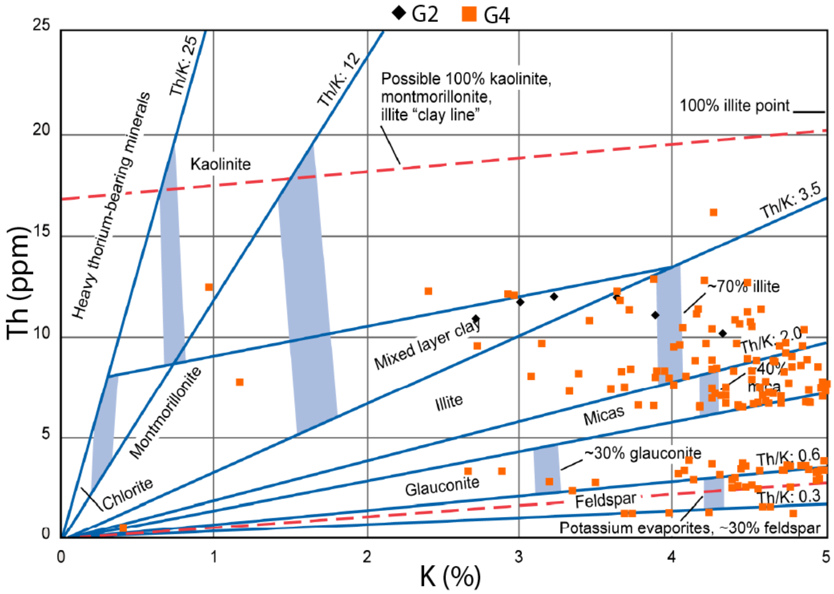

Figure 6.16: Th and K plot for Well-D. Note the data points of the diamictites (G4) and the argillaceous sandstone (G2). The latter is characterized by illite and mixed layer clay. After Schlumberger (2009).

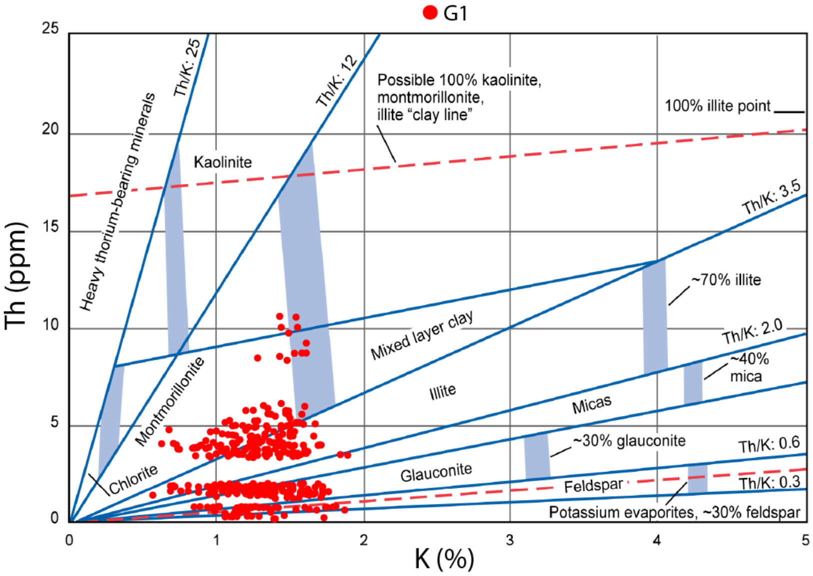

Figure 6.17: Th and K plot for Well-E. Note the populations of G1 (sandstone). In general, this figure shows two populations, the first likely represents mica, glauconite, and feldspar while the second one represents illite and montmorillonite clay minerals. After Schlumberger (2009).

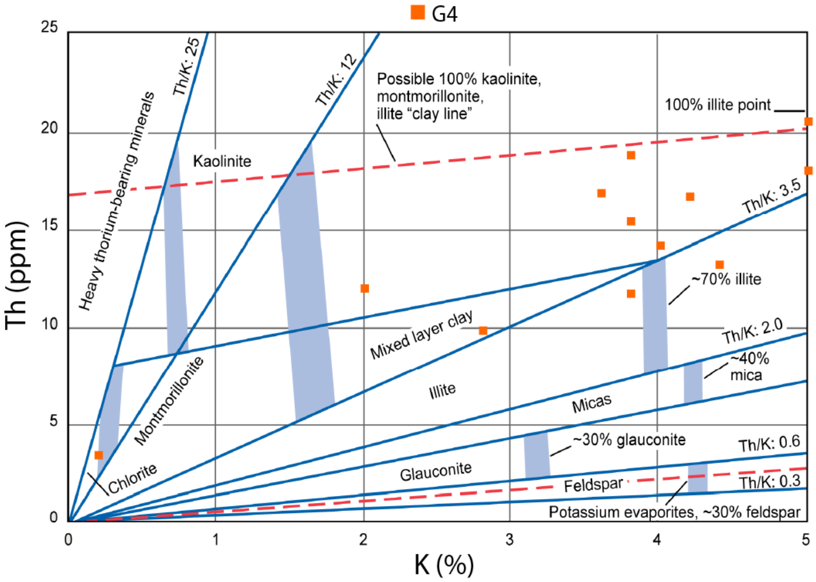

Figure 6.18: Th and K plot for Well-F. Note that about 77% of the reading points are off-scale. However, this well is mainly comprised of matrix supported diamictite intercalated with shale lithofacies. After Schlumberger (2009).

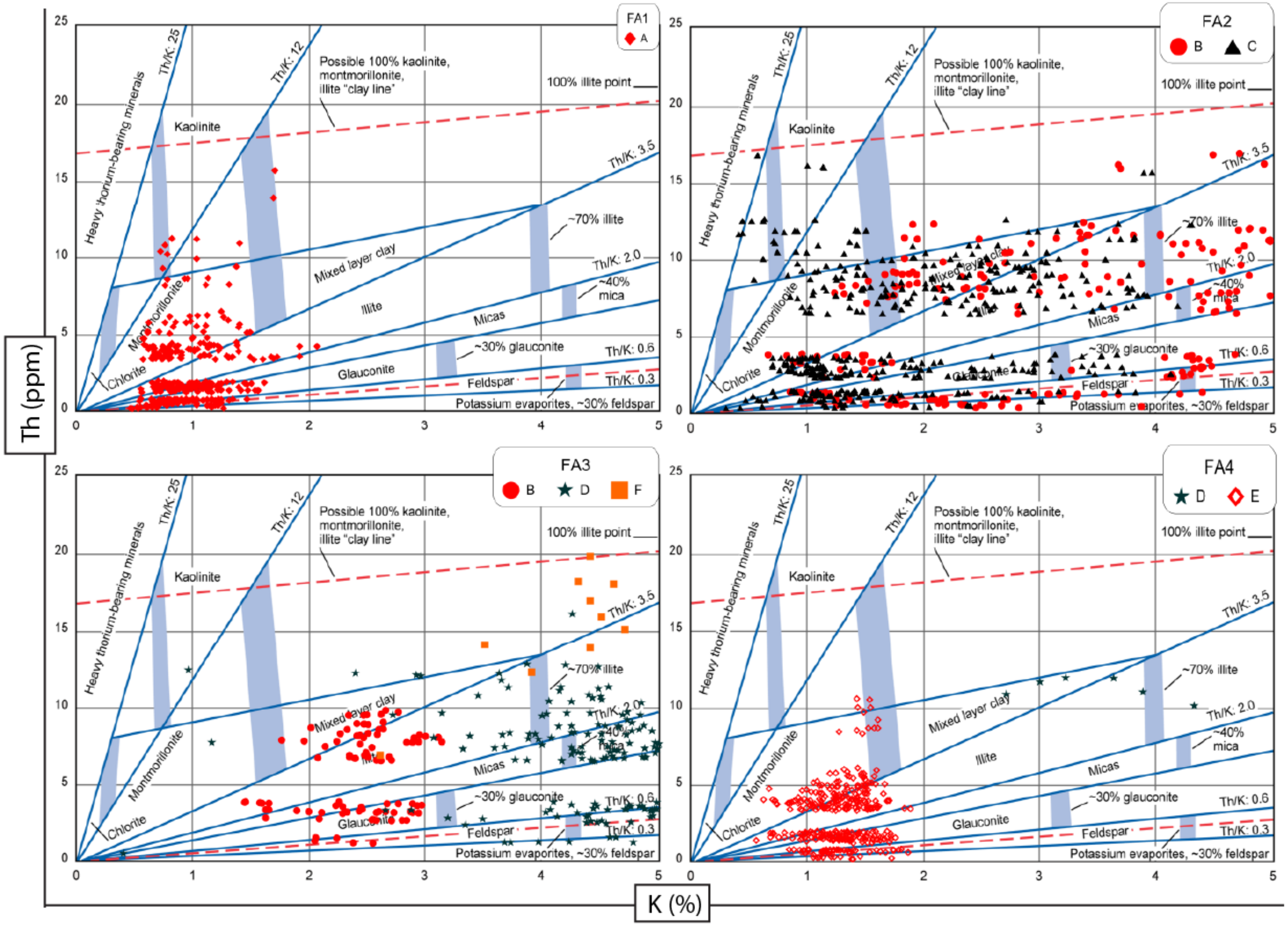

Figure 6.19: Th and K plot for the depositional environments. The nearshore (FA1) and the glaciofluvial (FA4) environments are characterized by lower clay minerals variation than the glaciolacustrine delta (FA2) and subglacial (FA3) environments. A to F are the wells names. In FA3, the matrix-supported diamictites contain higher clay minerals contents (stars and squares). After Schlumberger (2009).

6.8 Interpretation and Discussion

Based on the elemental distribution patterns, the lithofacies were classified into four groups for each well (Table 6.1). These groups are sandstone (G1) containing relatively the highest amount of Si attributed to an increase of quartz mineral content, claystone and/or argillaceous sandstone (G2) containing higher amount of Al, K and Ti associated with an increase of clay contents, calcareous and/or evaporitic sandstone (G3) containing relatively the highest amount of Ca and S attributed to an increase of anhydrite cement, and diamictites (G4) exhibiting higher mineralogical heterogeneity.

There are no significant geochemical variations observed in the nearshore (FA1) (Figure 6.2) and the glaciofluvial (FA4) (Figure 6.7) lithofacies. These lithofacies are geochemically classified as mature (Figure 6.10) sublitharenite (Figure 6.12). The Th and K plots of these environments exhibit almost the same pattern. The plots show that they are both characterized by montmorillonite, illite, mica, glauconite, and feldspar minerals (Figure 6.19 FA1 and FA4).

In contrast, the glaciolacustrine delta (FA2) and the subglacial (FA3) lithofacies show significant geochemical variations (Figure 6.1). In the former environment, the concentrations of S, Ca, and Ba elements increase with decreasing Si concentrations in the sulfate cement interval (Figure 5.11). The increase in the concentrations of Al, K, and Ti and the increase of SGR components in the intervals of these depositional environments are associated with claystone and/or argillaceous sandstone. The glaciolacustrine delta environment is characterized by various clay minerals (Figure 6.19 FA2) and sandstone types (Figure 6.12).

Depending on the diamictite type, the subglacial environment is also characterized by various clay minerals. The matrix-supported diamictites contain higher clay contents than the clast-supported type. Therefore, the Th/K plot can be used to distinguish the matrix-supported diamictites from the clast-supported diamictites (Figure 6.19 FA3). The Sand Class System classification of this environment shows various sandstone types (Figure 6.12). Besides, the environment is characterized by mineralogical heterogeneity indicated by various elemental composition (Figure 6.1).

CHAPTER 7

PETROPHYSICAL CHARACTERIZATION

7.1 Introduction

Porosity, defined as the percentage of pores (void spaces) within a rock (Ulmer-Scholle et al., 2014), can be divided into primary and secondary types. The former was initiated during sediments deposition or rocks formation, whereas the latter was formed after sediments deposition or final rocks formation due to diagenetic processes. Porosity, measured in percentage (%), it is either enhanced or diminished by diagenesis. For instance, in tight sand reservoirs, compacted grains will reduce the number of pores. The pore volume can also be reduced by the amount of the matrix in the pores as in diamictites. In contrast, fractures and/or feldspar dissolution may generate new porosity. The ability of a rock/sediment to transfer liquid and/or gas through it is called permeability (Allaby, 2008) and it is measured in millidarcy (mD). This chapter aims to statistically analyze the original porosity and permeability data and to evaluate the heterogeneity of both parameters after applying outlier's detection using the coefficient of variation. In addition, it also illustrates the factors controlling the development of sweet spots observed from the diagenesis study under the petrographic microscope and the relationships between porosity and permeability for each well and each depositional environment.

In sections 7.2 and 7.3, the original porosity and permeability data are discussed, respectively, for each well in terms of statistical analysis. In section 7.4, the data heterogeneity for both parameters is evaluated using the coefficient of variations. The outlier's detection is demonstrated in section 7.5 while the factors controlling the reservoir quality and the relationships between porosity and permeability are discussed in section 7.6.

7.2 Porosity Data

Porosity data of Well-A (nearshore lithofacies) ranges from 4.5% to 13.5% (CV=19%) representing the highest range amongst the other wells. Compared to the other wells, this well and Well-E (glaciofluvial lithofacies) are characterized by lower porosity variation. Porosity data of Well-E ranges from 1% to 7.5% (CV= 34%) and that of Well-F (subglacial lithofacies) ranges from 0.6% to 5.3% (CV=81%). A summary of the descriptive statistics for porosity data for each well is provided in Table 7.1.

Based on the most frequent class ranges observed from the histograms of the original porosity data for all the wells (Figure 7.1), the core interval of Well-A (nearshore lithofacies) exhibits the highest porosity class range (10%-11%) amongst the other cores whilst the cores of Well-D and Well-F (mostly subglacial lithofacies) exhibit the least porosity class ranges (1% - 1.5% and 0% - 2%, respectively).

Table 7.1: Summary of statistical analysis of the original porosity data (%). Note that the Well-A (nearshore lithofacies) is characterized by the lowest CV (relative to the other wells).

Statistical parameters | Wells	A	B	C	D	E	F
Mean	9.920	3.963	5.501	1.151	4.682	1.871
Median	10.110	3.190	4.370	1.280	4.705	1.462
Standard Deviation	1.912	3.031	3.450	0.656	1.575	1.523
Kurtosis	0.978	1.662	-1.598	-0.209	-0.354	4.737
Skewness	-0.682	1.339	0.081	0.010	0.041	2.076
Range	9.027	12.510	10.450	2.080	6.420	4.654
Minimum	4.521	0.080	0.250	0.140	1.100	0.699
Maximum	13.548	12.590	10.700	2.220	7.520	5.354
Count	29	25	40	8	30	8
Coefficient of Variation	**19%**	**76%**	**63%**	**57%**	**34%**	**81%**
Lower Quartile	8.891	1.965	2.863	0.670	3.583	0.928
Upper Quartile	11.257	4.841	8.858	1.493	5.598	1.971
Interquartile Range	2.367	2.876	5.995	0.823	2.015	1.044

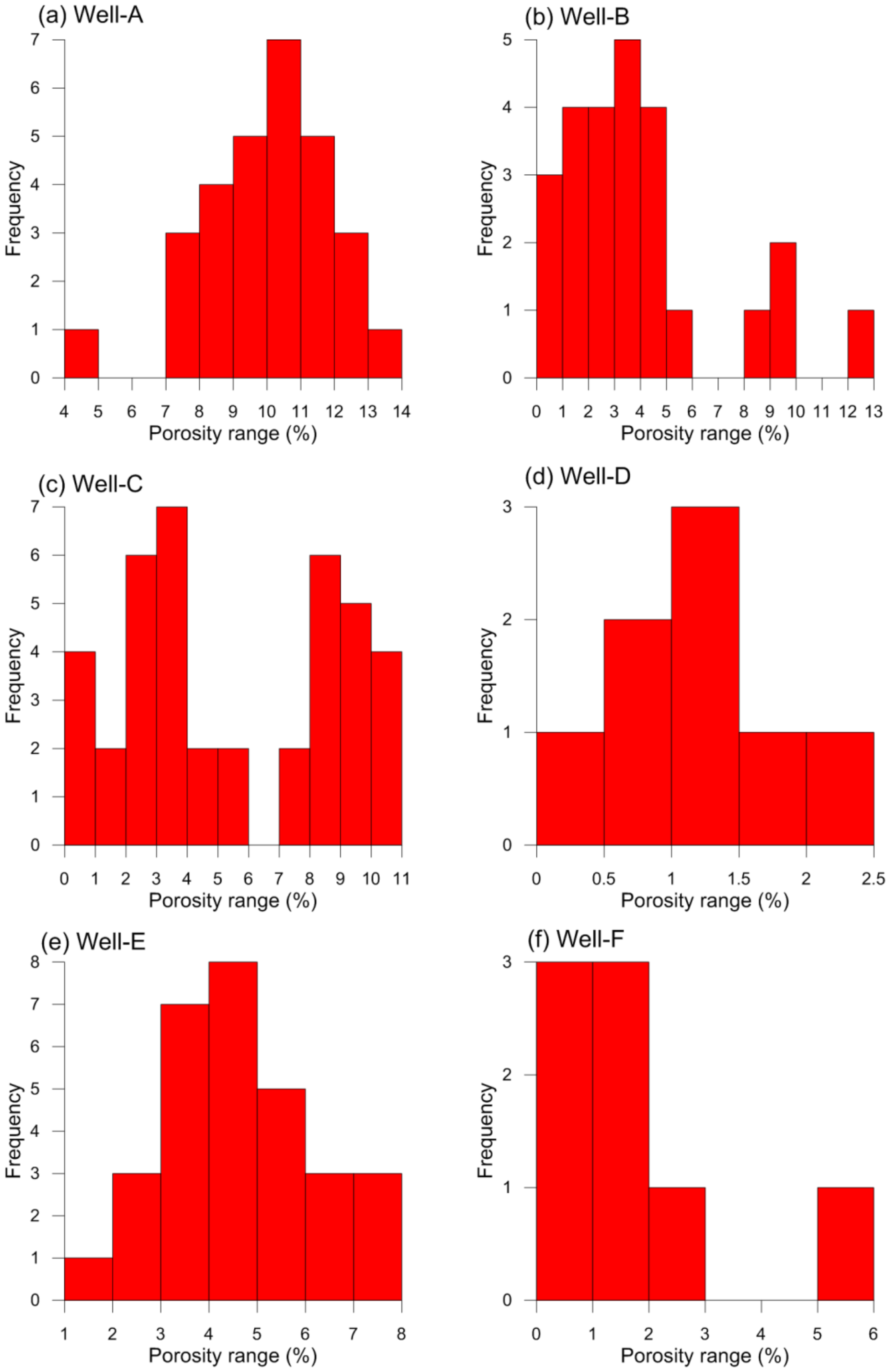

Figure 7.1: Histograms of the original porosity data for all wells. Note that the most frequent porosity ranges are: for Well-A (10 - 11%) (FA1), Well-B and Well-C (3 - 4%), Well-D (1 - 1.5%), Well-E (4 - 5%), and Well-F (0 - 2%).

7.3 Permeability Data

A summary of descriptive statistics for permeability data for each well is provided in Table 7.2. Permeability data is highly variable in each well with CV ranging from 195% in Well-E to 463% in Well-C. It is more variable than porosity data in all wells. Relatively, Well-A (nearshore lithofacies) and Well-E (glaciofluvial lithofacies) are characterized by the lowest permeability variations (CV=196% and 195%, respectively) while Well-C and Well-B (mostly glaciolacustrine delta lithofacies) are characterized by the highest permeability variations (CV=345% and 455%, respectively).

The permeability data histograms (Figure 7.2) illustrate the permeability heterogeneity in each well. The heterogeneity is indicated by high values outliers that are away from the most frequent values. Despite these outliers and based on the most frequent ranges, the highest permeability ranges are observed in Well-A (nearshore lithofacies) while the lowest permeability ranges are observed in Well-D (mostly subglacial lithofacies).

Based on the core description and thin section study, the permeability increases in each well are associated with the presence of natural fractures. Thus, distinguishing natural fractures from the other factors controlling the reservoir quality is suggested to better evaluate the reservoir heterogeneity (section 7.4). For this purpose, outlier detection procedure is performed (see section 7.5).

Table 7.2: Summary of statistical analysis of the original permeability data (mD). Note that the Well-A (nearshore lithofacies) and the Well-E (glaciofluvial lithofacies) are characterized by lower CV (relative to the other wells).

Statistical parameters | Wells	A	B	C	D	E	F
Mean	1.926	0.643	2.150	0.043	0.382	0.917
Median	0.360	0.044	0.047	0.005	0.253	0.038
Standard Deviation	3.782	2.218	9.780	0.103	0.746	2.286
Kurtosis	10.230	20.086	25.722	7.910	26.183	7.909
Skewness	3.053	4.385	4.992	2.808	4.980	2.807
Range	17.415	10.783	56.022	0.296	4.186	6.557
Minimum	0.047	0.000	0.002	0.001	0.028	0.007
Maximum	17.462	10.783	56.024	0.297	4.214	6.564
Count	29	25	40	8	30	8
Coefficient of Variation	**196%**	**345%**	**455%**	**238%**	**195%**	**249%**
Lower Quartile	0.197	0.014	0.021	0.002	0.111	0.019
Upper Quartile	0.990	0.089	0.069	0.015	0.345	0.315
Interquartile Range	0.793	0.076	0.048	0.013	0.235	0.296

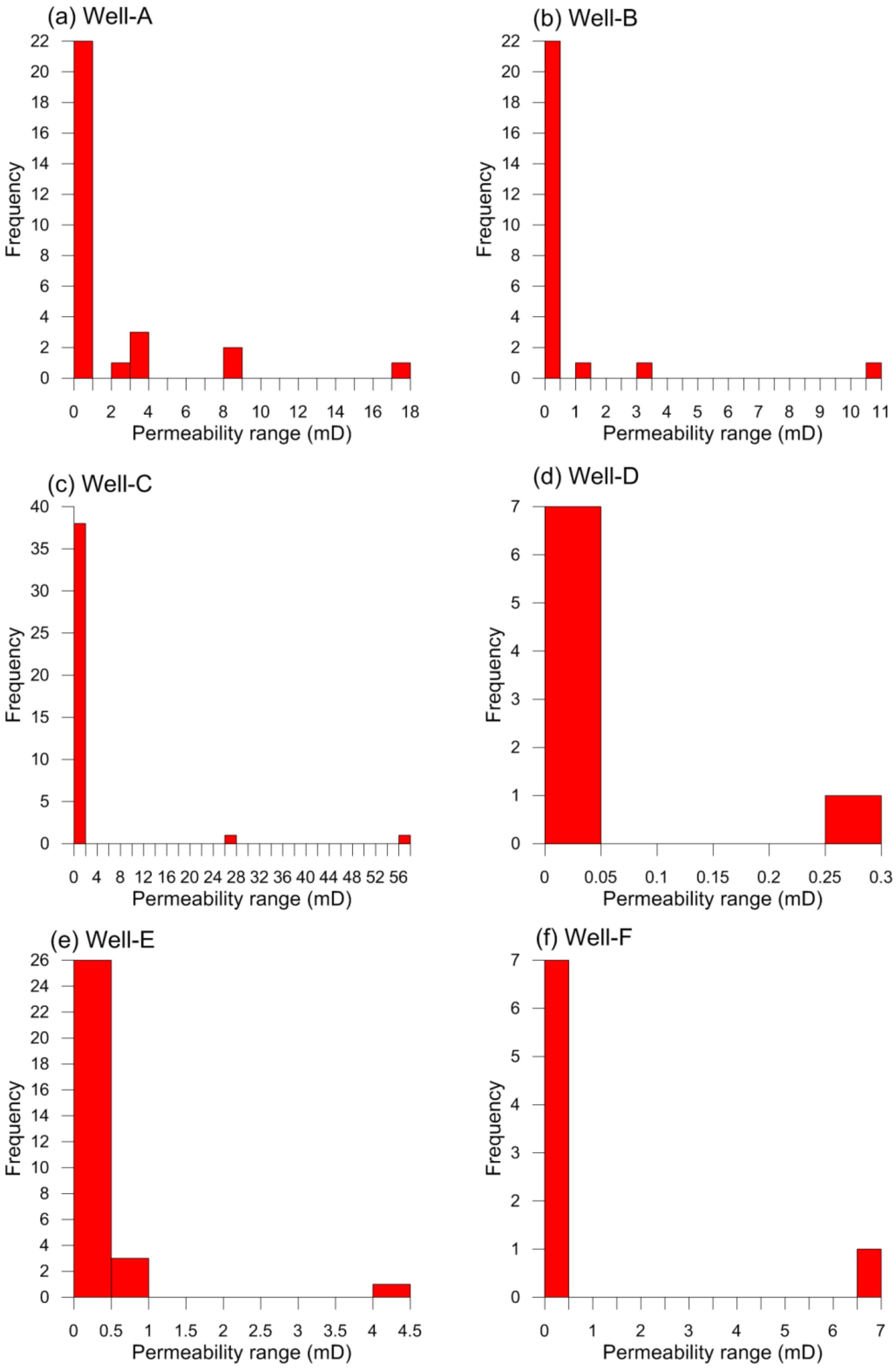

Figure 7.2: Histograms of the original permeability data for all wells. Note that the most frequent permeability ranges are: for Well-A (0 - 1) mD, Well-B (0 – 0.5) mD, Well-C (0 - 2) mD, Well-D (0 – 0.05) mD, Well-E (0 – 0.5) mD, and Well-F (0 – 0.5) mD.

7.4 Data Heterogeneity

Unequal spatial variability in a physical property is defined as heterogeneity (Lake and Jensen, 1989; Allaby, 2008). Geological heterogeneity exhibites as a complexity within a property in three-dimension, rocks/sediments have different ages or different structures, and/or different stratigraphy (Lake and Jensen, 1991; Zhengquan et al., 1998). The ratio of standard deviation to mean, the coefficient of variation (CV), can be utilized to evaluate this heterogeneity (Lake and Jensen, 1989; Corbett and Jensen, 1992; Fitch et al., 2015). The higher CV value reflects more heterogeneity of properties (Lake and Jensen, 1989).

Porosity data of Well-A core interval (nearshore lithofacies) has the lowest variation (CV=19%), while Well-F (subglacial lithofacies) has the highest variation (CV=81%) (Table 7.1). In all wells, the porosity data is less variable than the permeability data (Figure 7.5 & Figure 7.6). The two lowest variations in permeability data are shown in Well-A (nearshore lithofacies, CV=196%) and Well-E (glaciofluvial lithofacies, CV=195%). However, the two highest variations are exhibited in Well-C and Well-B (both are mostly glaciolacustrine lithofacies) with CV=455% and CV=345%, respectively. The heterogeneity within the permeability data is reduced by more than 50% in most of the wells when the outlier’s detection is applied. This indicates that presence of natural fractures within the core samples plays a significant role in increasing the reservoir heterogeneity.

7.5 Data Outlier’s Detection

An abnormally high or low value amongst the same population is called an outlier (Lee, 2008). In the first case where the outliers are having high values, we expect excellent sweet spots where promising reservoir zones occur. In the second case, abnormally low values are expected to represent low or non-reservoir sweet spots. Since we are dealing with tight sand, the average values of air permeability infrequently exceed one millidarcy (Morton-Thompson and Woods, 1993; Hayton et al., 2010).

A simple approach to detect porosity and permeability data-outliers is by using box plot (Lee, 2008), which is also called the box and whisker plot. In this plot, the porosity (Figure 7.3) and permeability (Figure 7.4) values are plotted on a log scale (y-axis). The horizontal bars within the red box indicate the first quartile (lower bar), the median (middle bar), and the third quartile (upper bar). However, the red crossed lines symbols located out of the red box are the outliers recognized by the factor of the interquartile range (IQR). The IQR factor equals 1.5 multiplied by IQR. The outliers with high value are the summation of the third quartile (Q3) and IQR factor whereas the outliers with low value are IQR factor subtracted from the first quartile (Q1). A summary of statistical analysis for both porosity and permeability non-outlier’s data is provided in Table 7.3 and Table 7.4, respectively. The histograms for non-outlier’s data are also provided for both porosity (Figure 7.7) and for permeability data (Figure 7.8).

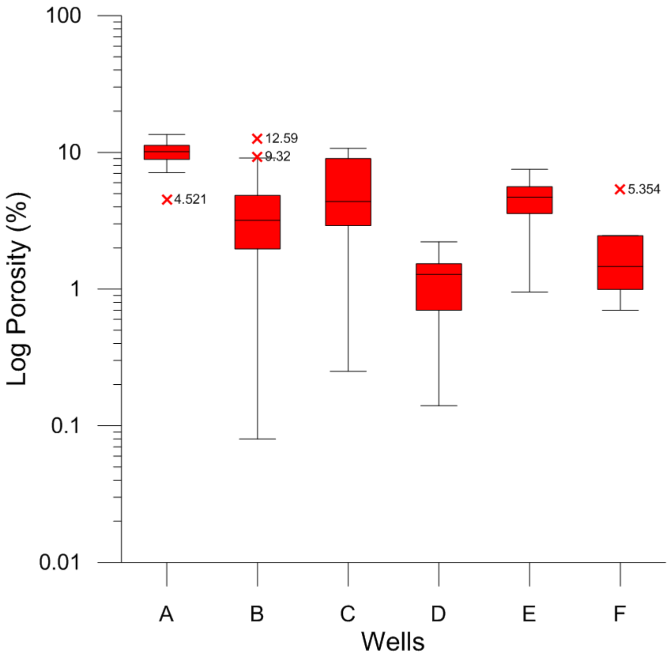

Figure 7.3: Porosity data outliers detection. Note that the crossed lines are the outliers; therefore, the Well-B contains the highest porosity outliers.

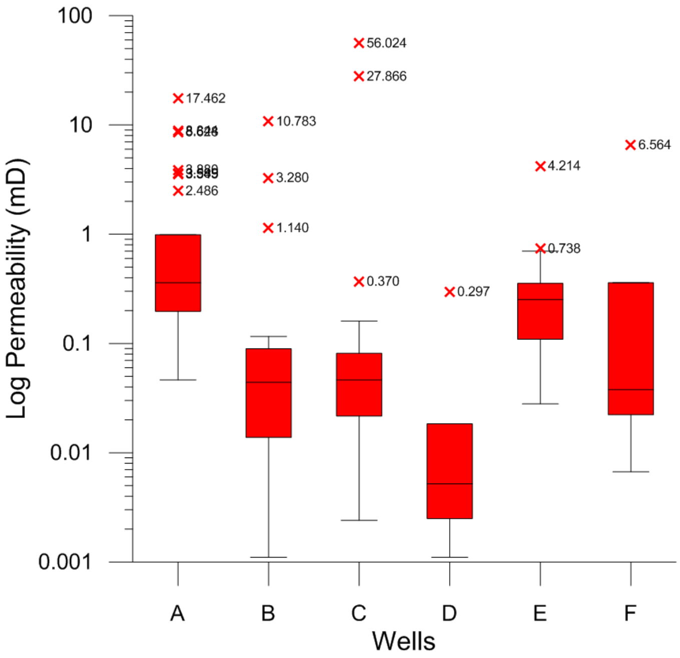

Figure 7.4: Permeability data outliers detection. Note that the crossed lines are the outliers; thus, the Well-A (nearshore lithofacies) contains the highest permeability outliers indicating that it may contain natural fractures more than the other wells.

Table 7.3: Summary of statistical analysis of the non-outlier's porosity data.

Statistical parameters | Wells	A	B	C	D	E	F
Mean	10.11	3.35	5.50	1.15	4.68	1.37
Median	10.12	3.17	4.37	1.28	4.71	1.44
Standard Deviation	1.63	2.22	3.45	0.66	1.57	0.63
Kurtosis	-0.47	1.32	-1.60	-0.21	-0.35	-0.08
Skewness	-0.08	1.04	0.08	0.01	0.04	0.68
Range	6.45	9.02	10.45	2.08	6.42	1.76
Minimum	7.10	0.08	0.25	0.14	1.10	0.70
Maximum	13.55	9.10	10.70	2.22	7.52	2.46
Count	28	23	40	8	30	7
Coefficient of Variation	**16%**	**66%**	**63%**	**57%**	**34%**	**46%**
Lower Quartile	8.99	1.85	2.86	0.67	3.58	0.86
Upper Quartile	11.27	4.47	8.86	1.49	5.60	1.64
Interquartile Range	2.28	2.62	6.00	0.82	2.02	0.78

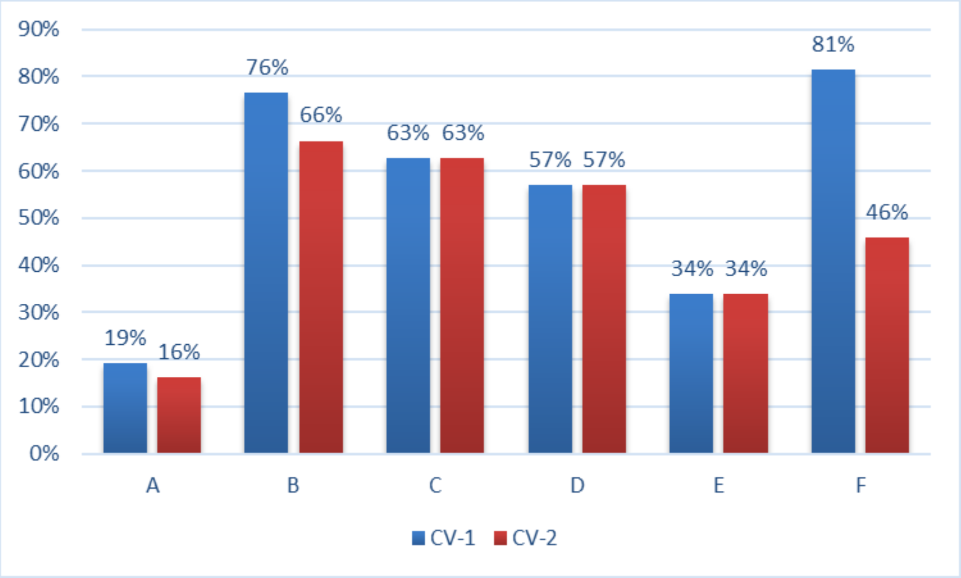

Figure 7.5: Coefficients of variations for porosity data. CV-1: original data, CV-2: non-outlier's data. Note that the highest CV is illustrated in Well-F (subglacial lithofacies).

Table 7.4: Summary of statistical analysis of the non-outlier's permeability data.

Statistical parameters | Wells	A	B	C	D	E	F
Mean	0.338	0.040	0.047	0.007	0.215	0.111
Median	0.261	0.028	0.042	0.003	0.171	0.026
Standard Deviation	0.244	0.035	0.038	0.007	0.136	0.151
Kurtosis	1.177	-0.211	1.816	-0.405	-0.649	-0.525
Skewness	1.204	0.954	1.289	1.075	0.451	1.251
Range	0.944	0.115	0.158	0.017	0.499	0.353
Minimum	0.047	0.001	0.002	0.001	0.028	0.007
Maximum	0.990	0.116	0.161	0.018	0.527	0.360
Count	22	22	37	7	27	7
Coefficient of Variation	**72%**	**88%**	**81%**	**99%**	**63%**	**137%**
Lower Quartile	0.164	0.012	0.019	0.002	0.107	0.017
Upper Quartile	0.465	0.049	0.061	0.011	0.310	0.175
Interquartile Range	0.300	0.037	0.042	0.008	0.203	0.158

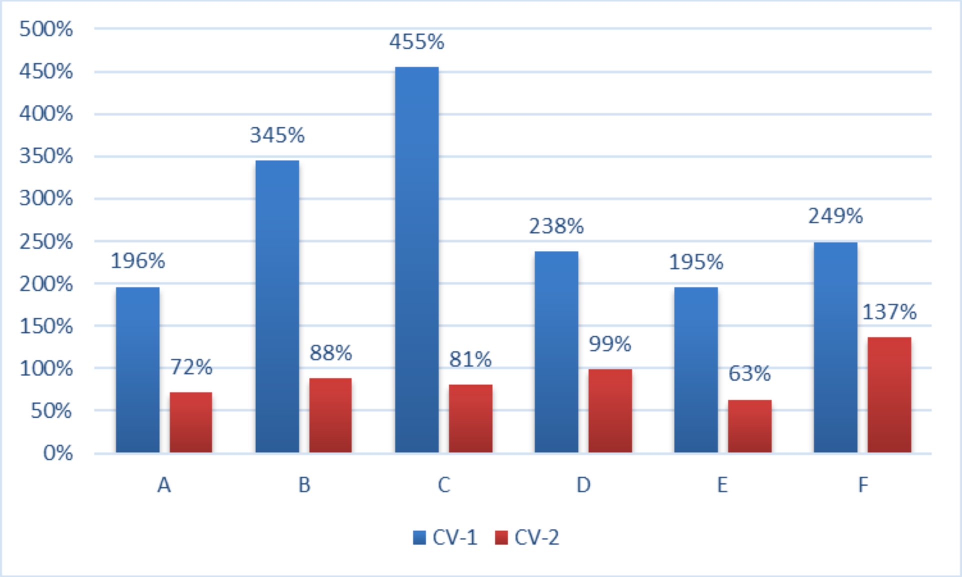

Figure 7.6: Coefficients of variations for permeability data. CV-1: original data, CV-2: non-outlier's data. Note that the highest CV is illustrated in Well-C (glaciolacustrine delta lithofacies).

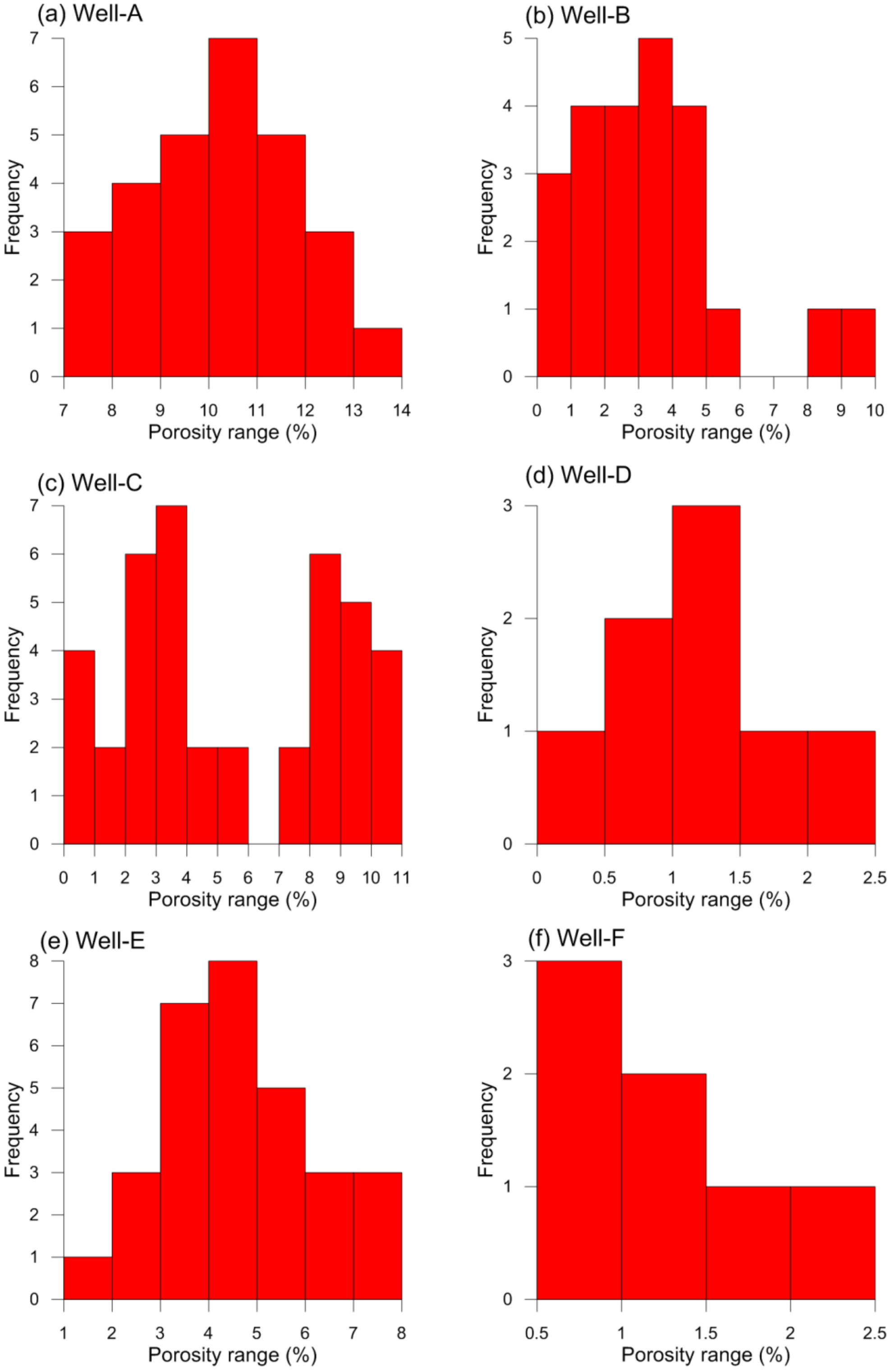

Figure 7.7: Ranges of the non-outlier's porosity data for all wells. Note that the most frequent porosity ranges are: for Well-A (10 - 11) %, Well-B (3 - 4) %, Well-C (3 - 4) %, Well-D (1 - 1.5) %, Well-E (4 - 5) %, and Well-F (0.5 - 1) %.

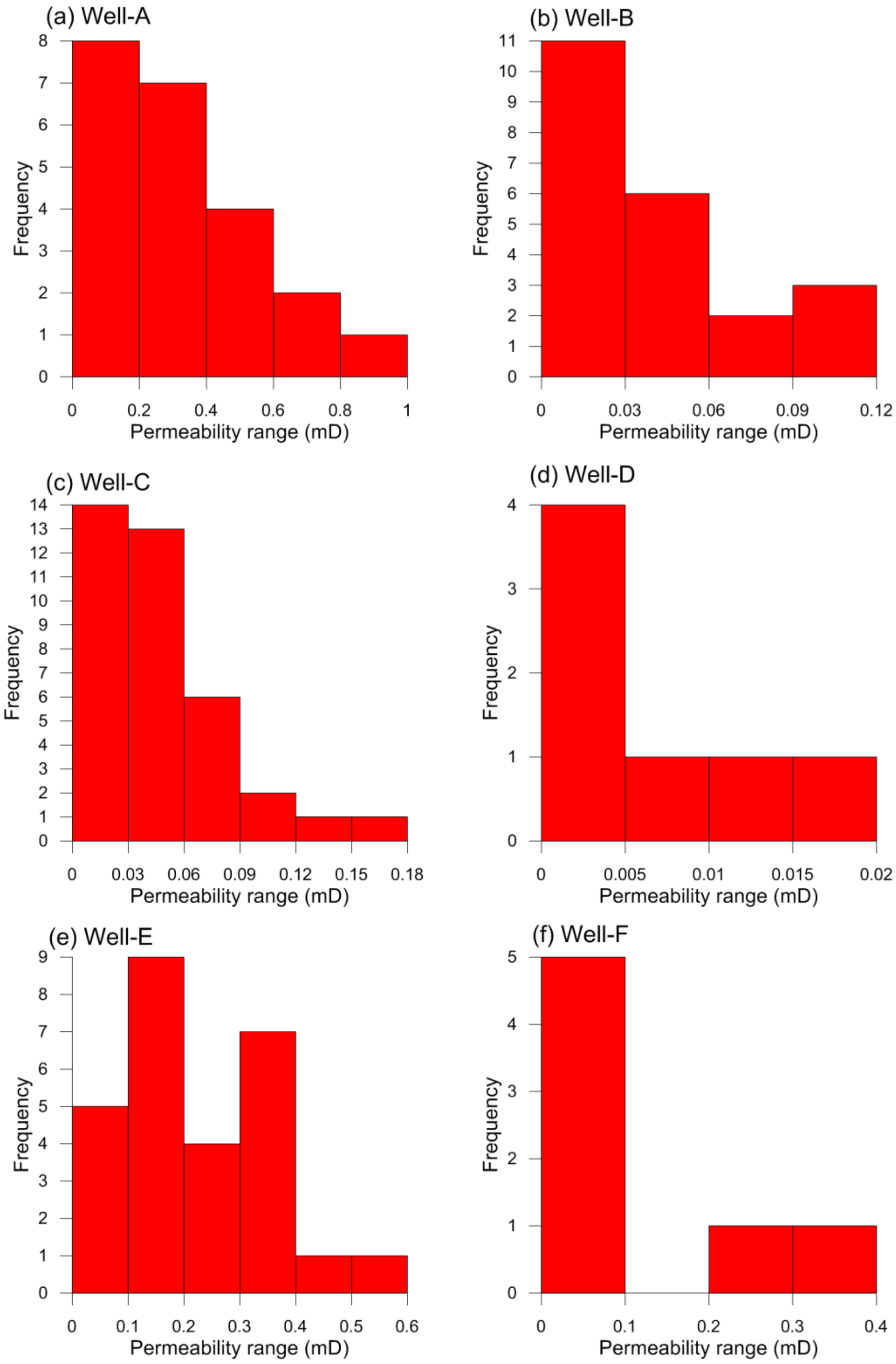

Figure 7.8: Ranges of the non-outlier’s permeability data for all wells. Note that the most frequent permeability ranges are: for Well-A (0 -0.2) mD, Well-B (0 – 0.03) mD, Well-C (0 – 0.03) mD, Well-D (0 – 0.005) mD, Well-E (0.1 – 0.2) mD, and Well-F (0 – 0.1) mD.

7.6 Reservoir Quality

A sweet spot can be defined as a zone where a continuous accumulation can be economically developed (Schenk, 2005) or it is an interval of a well having a relatively higher porosity and permeability (Khalil, 2012; Sahin, 2013). It can also be defined as a zone that is characterized by better reservoir quality (Klimentidis, 2009). Based on one or several factors controlling the development of the sweet spots in the Arabian basin, Khalil (2009 and 2012) suggested three types of sweet spots. These are tectonic (also called structural), sedimentologic and diagenetic sweet spots. Following this author's definition for all the sweet spots types, the tectonic sweet spots are mainly controlled by open fractures resulting from local redistribution of structural stresses. The sedimentologic (also called depositional) sweet spots are recognized in coarser-grained sediments formed by combined effects of sea-level changes and sediments accumulation. Lastly, the diagenetic sweet spots might be formed due to diagenetic processes such as dissolution leading to enhanced permeability.

Natural fractures indicating the tectonic sweet sports are clearly observed in most of the studied core intervals. For instance, the lithofacies description of the cores (Figure 4.1c) and the thin section study (Figure 7.9g) show the presence of natural fracture in the nearshore lithofacies. The effects of stress redistribution may directly and/or indirectly disturb the formation of sweet spots. Stresses can act strata directly by forming open fractures and indirectly by constructing favorable structural settings for sedimentologic and diagenetic sweet spots to be developed (Khalil, 2012). The reservoir permeability will increase along the fractures when the fractures are open. Conversely, it will decrease when the fractures are filled by matrix or cement (Nelson, 2001). The depositional sweet spots are recognized by observing the primary porosity using the thin section investigation (i.e. Figure 7.9h and Figure 7.11h). However, it is affected by an increase in the matrix content as evident in the subglacial lithofacies (Figure 7.12b), and by cementation in the glaciolacustrine delta lithofacies (Figure 7.11a). The diagenetic sweet spots are also recognized using the thin section by the dissolution of the unstable minerals such as feldspar (Figure 7.9i).

The enhancing and reducing factors that controlled the reservoir quality and sweet spots of the studied cores are discussed in subsections **Error! Reference source not found.** and 7.6.2, respectively. The lithofacies heterogeneity and the porosity and permeability relationships are also discussed in subsection 7.6.3.

7.6.1 Reservoir Quality Enhancing Factors

Natural fractures, feldspar dissolution, and primary porosity are the main factors that enhanced the reservoir quality of the studied cores (Enhancing factors, Figure 7.9 to Figure 7.14). The porosity and permeability increases, that were observed in several of the core lithofacies, are associated with fractures (i.e. Figure 6.2 and Figure 6.3). Fractures become significant when they positively affect fluid flow (Nelson, 2001). They are usually associated with highly productive zones (Al-Mahmoud and Al-Ghamdi, 2010) and natural gas accumulation (Sahin, 2013). Total and partial feldspar dissolutions were mostly observed in the nearshore (Well-A) and glaciofluvial lithofacies (Well-E) of the studied cores (i.e. Figure 7.9i). They also occur in the glaciolacustrine delta front lithofacies (Well-B and C) but they are not as much as in the former lithofacies. Overall, in addition to the intergranular porosity observed in some intervals of the cores, natural fractures and feldspar dissolution create secondary porosity (dual porosity) (i.e. Figure 7.11h). These intervals are considered as potential sweet spots for natural gas to be developed in the Sarah Formation.

7.6.2 Reservoir Quality Reducing Factors

Grains compaction, cementation (anhydrite, silica, siderite, iron oxides, barite and clay cements), poor sorting and matrix contents are the main factors that appear to have reduced the reservoir quality of the studied cores (Reducing factors, Figure 7.9 to Figure 7.14). Grains' compaction is observed in free or low cementation zones, mostly, in the nearshore (Well-A, Figure 7.9a), glaciolacustrine delta (Well-B, Figure 7.10a, and Well-C, Figure 7.11a), and glaciofluvial lithofacies (Well-E, Figure 7.13a). Pore spaces and pore connections were hindered by grains compaction resulting in poor reservoir quality lithofacies. In some of the glaciolacustrine lithofacies, the reservoir quality is highly affected by anhydrite, barite (Well-C, Figure 7.11b and Figure 7.11c), iron oxides and clay cements (Well-B, Figure 7.10b and Figure 7.10c). Silica cements are also observed in few samples of the nearshore (Figure 7.9b) and glaciofluvial lithofacies (Figure 7.13c). Siderite cement is also observed in the glaciofluvial lithofacies of Well-D (Figure 7.12a). Poor grain sorting and matrix contents are also other factors that reduced the reservoir quality. These factors are mainly observed in the diamictites lithofacies (subglacial tillites) (i.e. Figure 7.10c and Figure 7.12b).

In addition to a macroscale heterogeneity observed in the sandstone core samples (i.e. diamictites in Well-B (Figure 4.3)), a microscale heterogeneity is also observed in most of the thin sections. The microscale heterogeneity occurs as a mix of reservoir quality enhancing and reducing controls. For instance, feldspar dissolution is associated with grains compaction (i.e. Figure 7.9e), compacted with uncompacted grains (i.e. Figure 7.9f), intergranular porosity and fractures with compaction and cementation (i.e. Figure 7.10e). However, the main inference here is that the reservoir quality of the cores is characterized by multiscale heterogeneity which either positively or negatively affect the reservoir quality of the Sarah Formation.

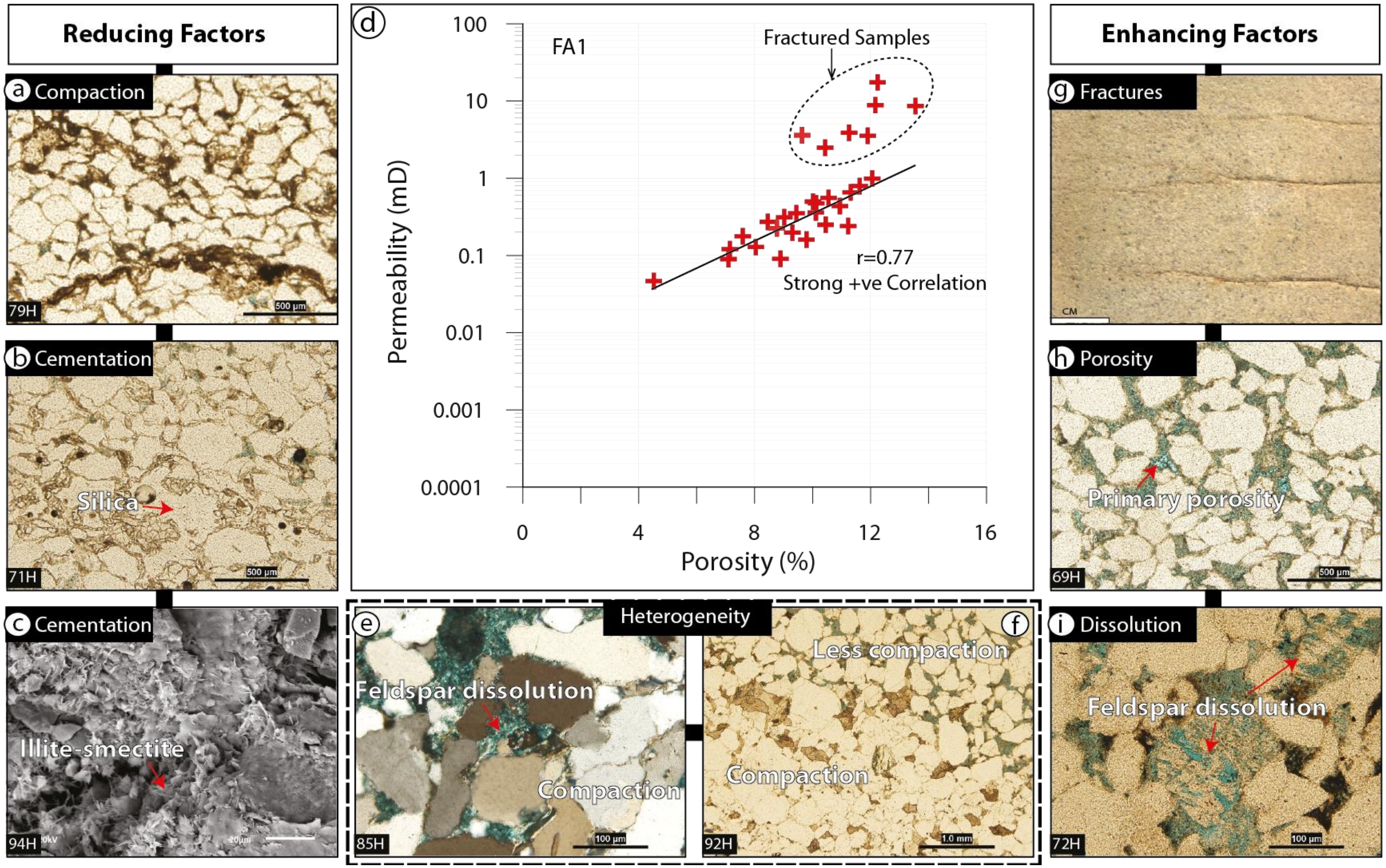

Figure 7.9: Reservoir quality reducing and enhancing factors in Well-A. (a) grains compaction, (b) silica cement, (c) illite-smectite clay mineral, (d) porosity and permeability cross plot for the nearshore environment (FA1). Note, based on this plot, FA1 is dominantly characterized by permeability ranging from 0.05 to 1 mD and porosity ranging from 4.5 to 12%. (e, f) mixed factors, (g) stylolite can be a weak zone for new fracture, (h) intergranular porosity, (i) secondary porosity (feldspar dissolution). Note that fractures increase the permeability up to 17.5 mD and porosity up to 13.55%.

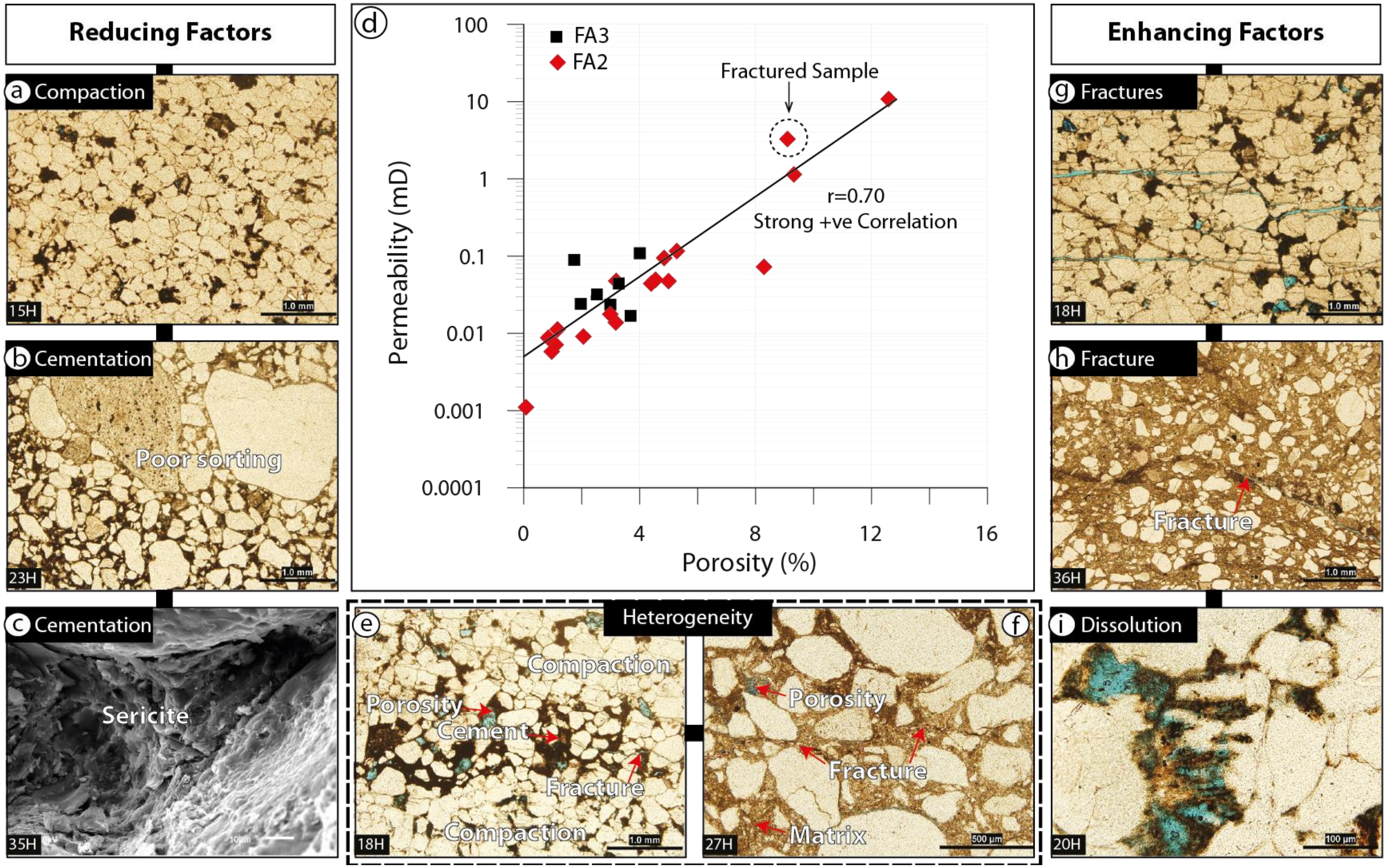

Figure 7.10: Reservoir quality reducing and enhancing factors in Well-B. (a) grains compaction, (b) iron oxide cement, (c) poor sorting grains with iron oxide cement, (d) porosity and permeability cross plot for the glaciolacustrine delta (FA2) and the subglacial (FA3) environments. Based on this plot, both FAs are dominantly characterized by permeability less than 0.1 mD and porosity less than 6%, (e, f) mixed factors, (g) open fractures, (h) a fracture formed by a deformation, (i) secondary porosity (feldspar dissolution) associated with compacted grains.

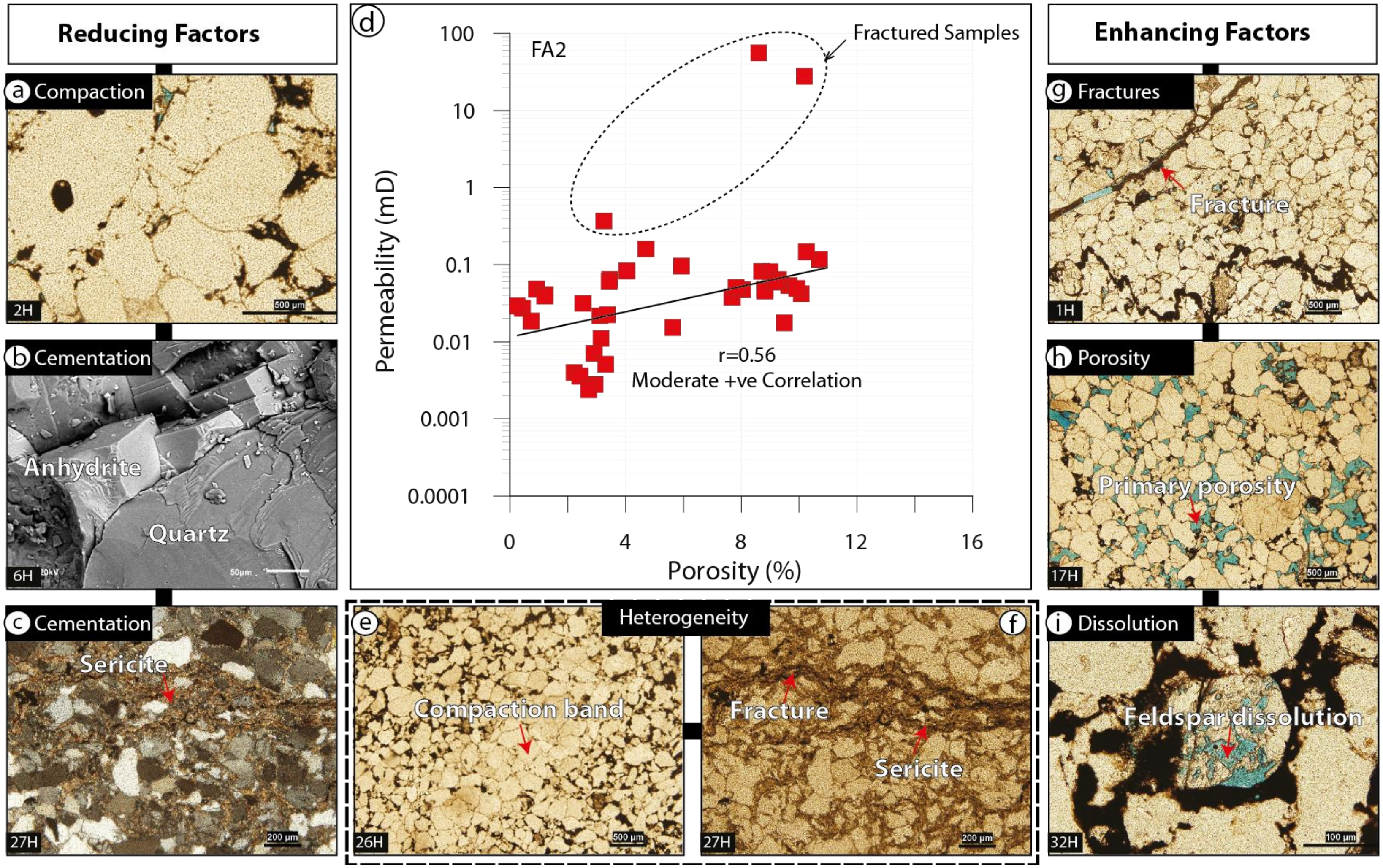

Figure 7.11: Reservoir quality reducing and enhancing factors in Well-C. (a) grains compaction, (b) anhydrite cement, (c) barite cement, (d) porosity and permeability cross plot for the glaciolacustrine delta (FA2). Note, based on this plot, FA2 is dominantly characterized by permeability ranging from 0.002 to 0.16 mD and porosity ranging from 0.25 to 10.7%. (e, f) mixed factors, (g) fracture, (h) intergranular porosity, (i) secondary porosity (feldspar dissolution) associated with iron oxide cement. Natural fractures increase the permeability up to 56 mD.

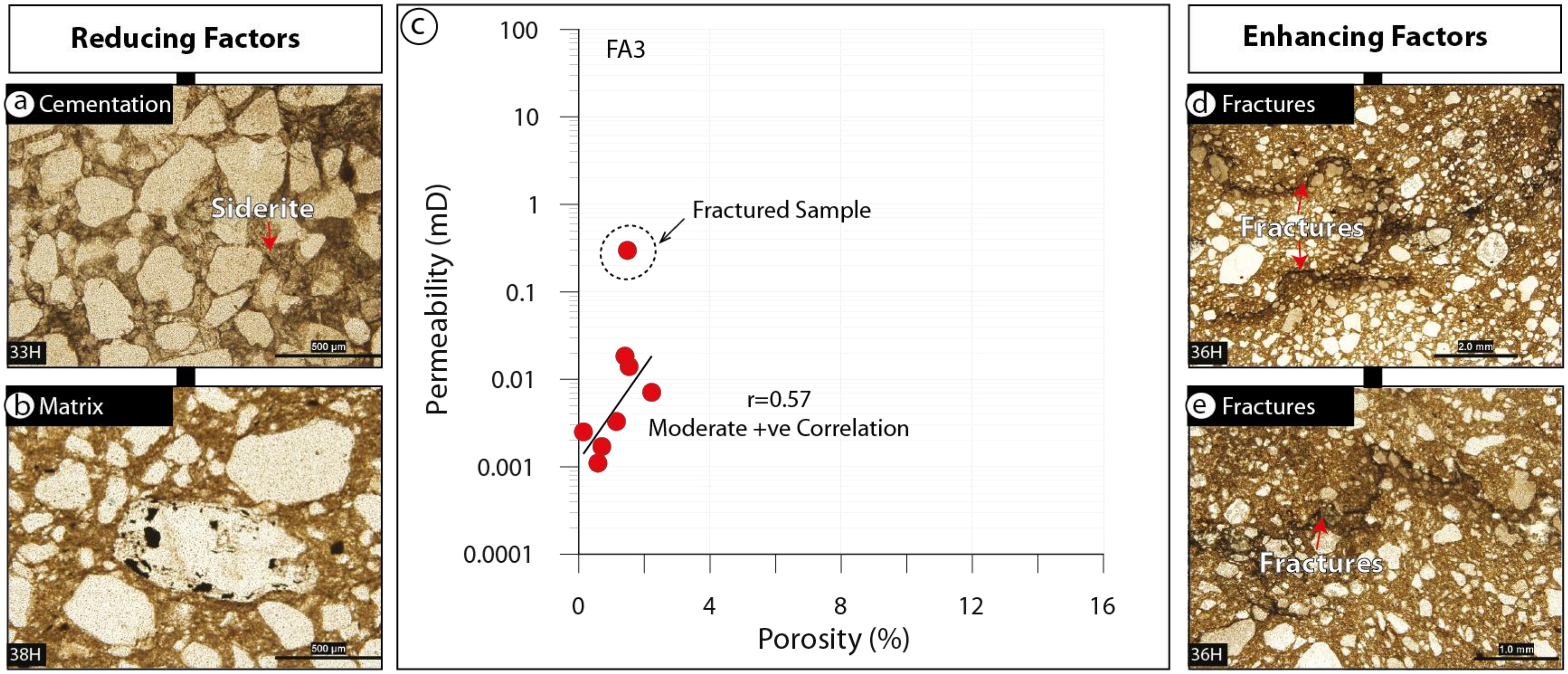

Figure 7.12: Reservoir quality reducing and enhancing factors in Well-D. (a) siderite cement, (b) poor sorting grains associated with matrix, (c) porosity and permeability cross plot for the subglacial environment (FA3). Based on this plot, FA3 is dominantly characterized by permeability ranging from 0.001 to 0.018 mD and porosity ranging from 0.14 to 2.22%. (d, e) fractures formed by deformations. Note that the fracture are the only factors producing sweet spots zones in the subglacial lithofacies (matrix-supported diamictite) with permeability increase up to 0.3 mD.

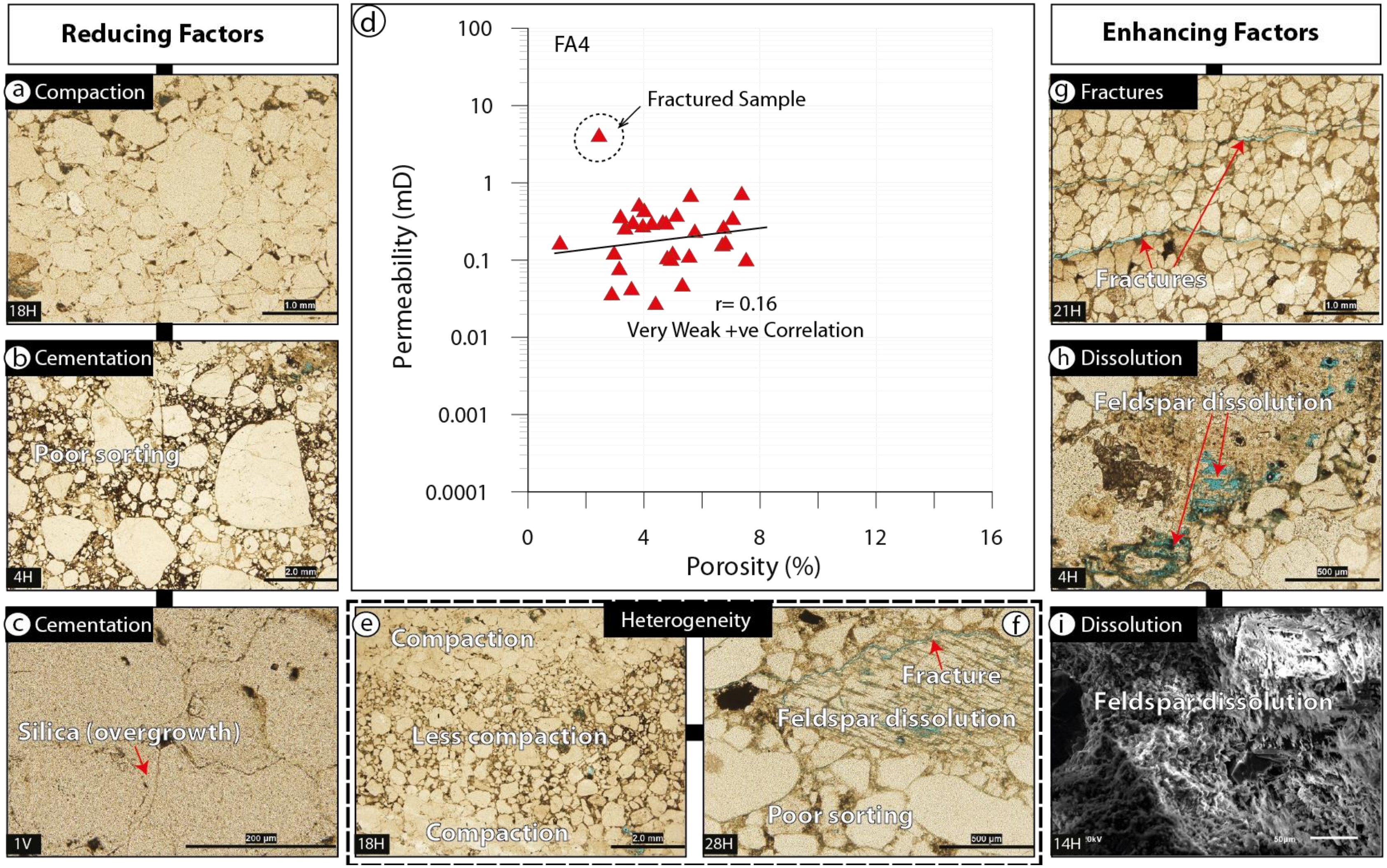

Figure 7.13: Reservoir quality reducing and enhancing factors in Well-E. (a) grains compaction, (b) poor sorting grains associated with iron oxide cement, (c) silica cement, (d) porosity and permeability cross plot for the glaciofluvial environment (FA4). Based on this plot, FA4 is dominantly characterized by permeability ranging from 0.028 to 0.74 mD and porosity ranging from 1.1 to 7.52%. (e, f) mixed factors, (g) open fractures, (h, i) secondary porosity (feldspar dissolutions). Note that natural fractures enhance the permeability up to 4.21 mD.

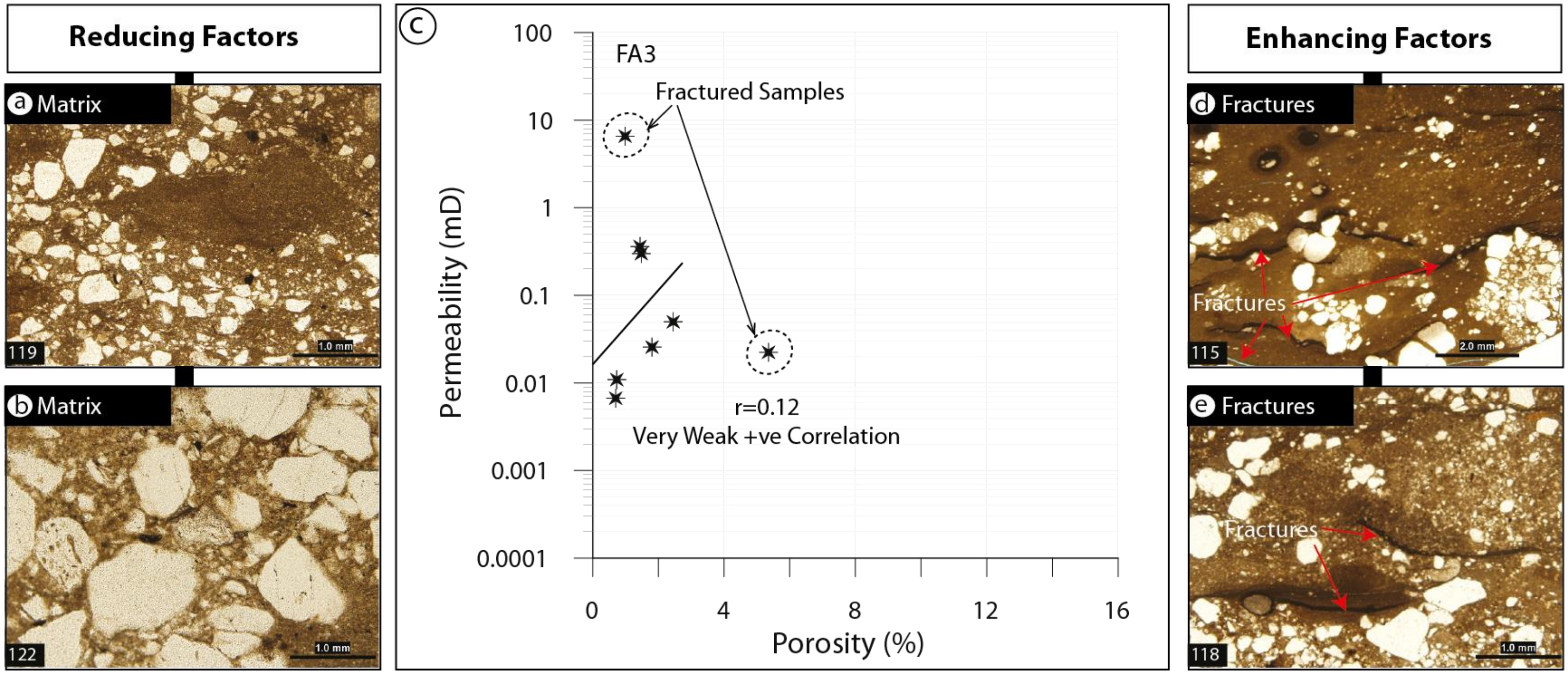

Figure 7.14: Reservoir quality reducing and enhancing factors in Well-F. (a, b) matrix supported diamictite, (c) porosity and permeability cross plot for the subglacial environment (FA3). Based on this plot, FA3 is dominantly characterized by permeability ranging from 0.007 to 0.36 mD and porosity ranging from 0.69 to 2.45%, (d, e) fractures formed by deformations. Note that the fracture are the only factors producing sweet spots zones in the subglacial lithofacies (matrix-supported diamictite) with permeability increase up to 6.56 mD.

7.6.3 Porosity and Permeability Relationship

Porosity and permeability cross plots for each well are illustrated in Figure 7.15. The correlations of these parameters are positive for all wells; however, their coefficients of correlations, and porosity and permeability ranges are different. The cross plots of Wells A and B (Figure 7.15a, b) are characterized by strong correlation while those of Wells F and E (Figure 7.15f, e) are very weak. The cross plots of the Wells C and D (Figure 7.15c, d) exhibit moderate correlations.

Based on the interpreted depositional environments and by excluding the high outliers' data, the nearshore environment is characterized by the strongest positive correlation (Figure 7.16a) with permeability (0.047 – 1 mD) and porosity (4.52-12%). The glaciolacustrine delta (Figure 7.16b) and glaciofluvial environments (Figure 7.16d) are both characterized by weak positive correlations. The former is dominantly characterized by permeability (0.002 - 0.2 mD) and porosity (1 - 11%) while the latter is characterized by permeability (0.015 - 0.17 mD) and porosity (2 - 7.5%). The subglacial environment with permeability (0.001 - 0.014 mD) and porosity (0.1 - 4%) is characterized by a very weak positive correlation.

To understand the linear relationship with lithofacies heterogeneity with porosity and permeability in all environments, three reservoir zones including high, moderate and poor reservoir qualities (Figure 7.17) have been selected. The high reservoir quality with permeability values greater than 1 mD is associated with the massive, fractured and mature sandstone with occasionally intergranular porosity (Figure 7.18). The moderate reservoir quality with permeability (0.1 - 1 mD) is associated with disrupted and heterogeneous lithofacies (Figure 7.19). The poor reservoir quality with permeability values less than 0.1 mD is generally associated with matrix-supported diamictites, claystone and/or argillaceous sandstone (Figure 7.20). The matrix content fills the pores and; therefore, reduces the reservoir quality. In general, the nearshore and glaciofluvial environments are characterized by permeability values that are greater than 0.1 mD while the glaciolacustrine delta and subglacial environments have less than 0.1 mD permeability values.

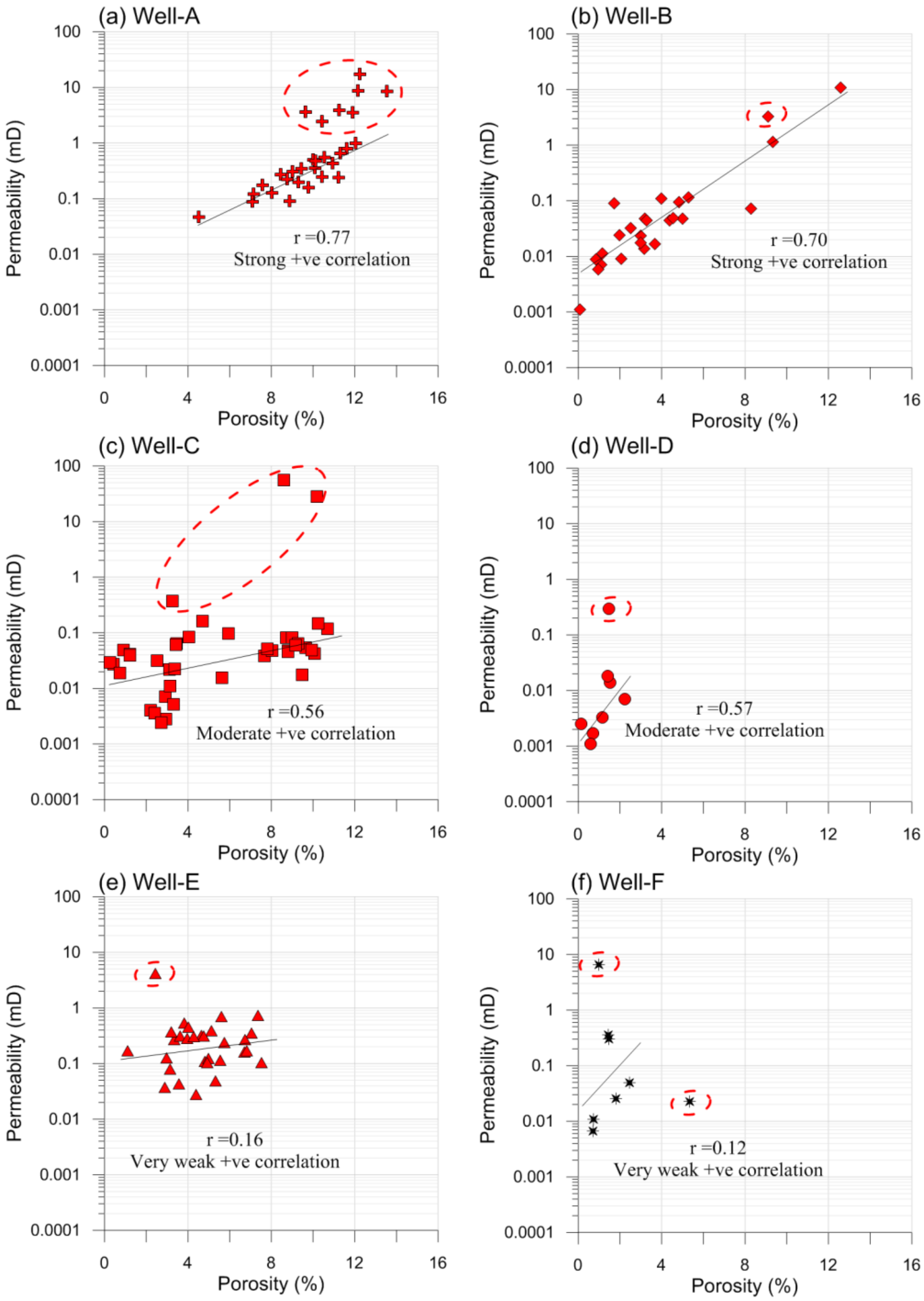

Figure 7.15: Permeability and porosity relationship of all wells. The data outliers are outlined in dashed circles. The absolute value of the coefficient of correlation ranging from 0 to 0.19 indicates a very weak correlation, from 0.2 to 0.39 is weak, from 0.4 to 0.59 is moderate, and from 0.6 to 0.79 is a strong correlation (Evans, 1996).

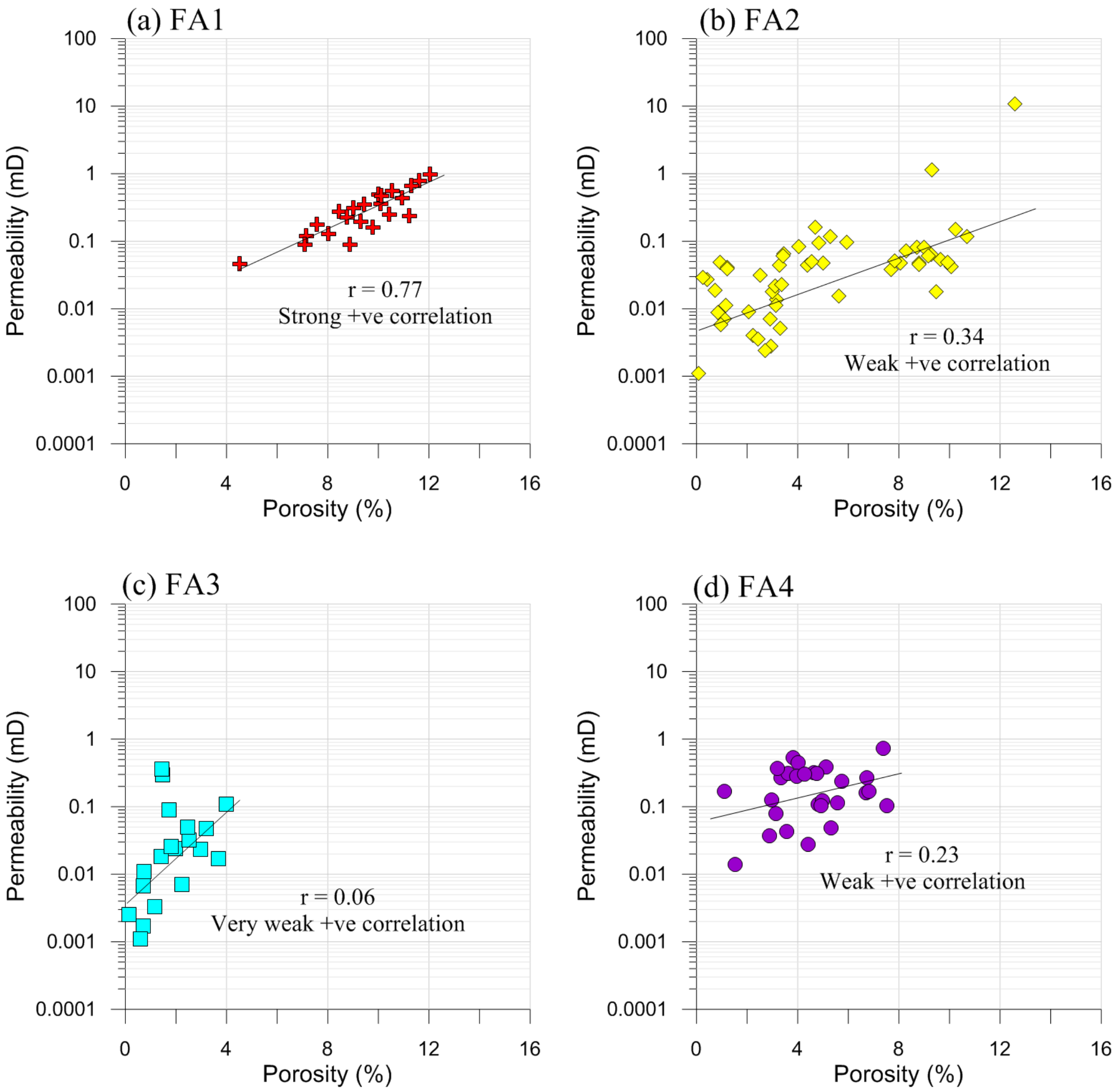

Figure 7.16: Porosity and permeability cross plot for the non-outlier's data for the interpreted depositional environments from all wells. Note that the nearshore environment (FA1) exhibits the strongest correlation while the subglacial environment (FA3) shows the weakest correlation. The glaciolacustrine delta (FA2) and the glaciofluvial (FA4) environments are also characterized by weak correlations but not as weak as the subglacial environment.

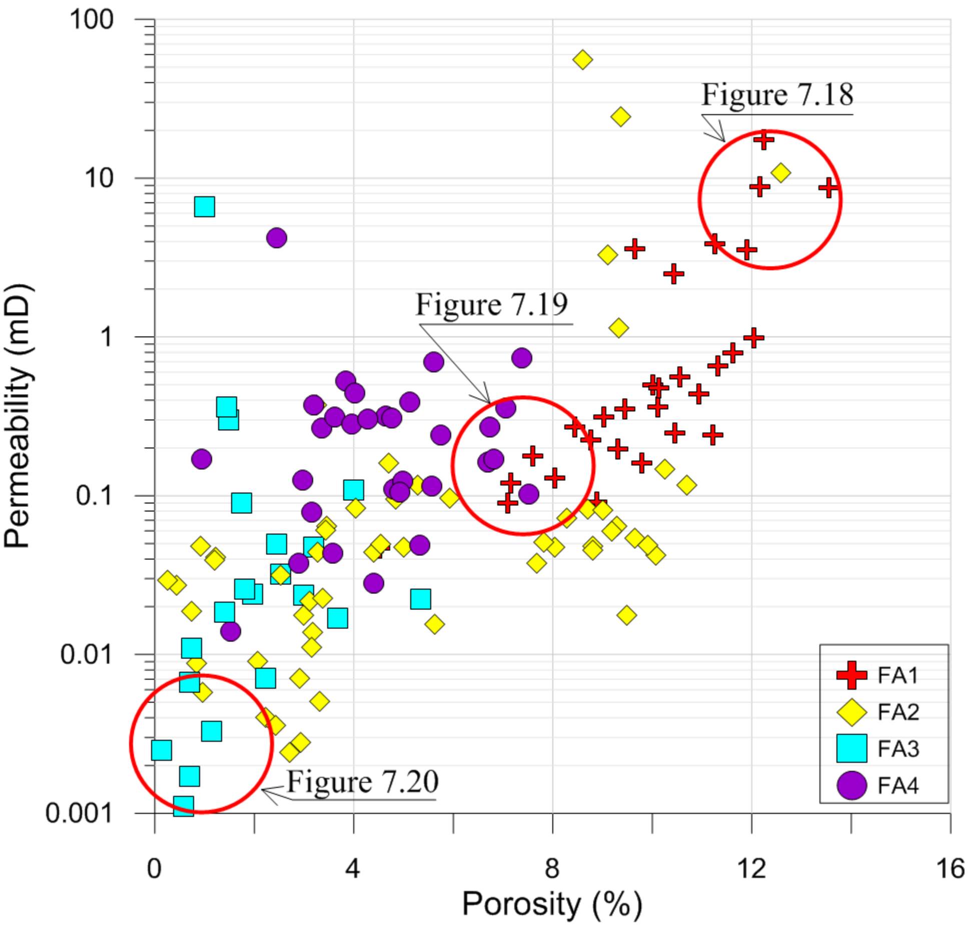

Figure 7.17: Porosity and permeability relationship for the depositional environment. Note that Figure 7.18 represents high reservoir quality with permeability values that are greater than 1 mD. It is associated with massive, fractured and mature sandstone. Figure 7.19 represents moderate reservoir quality. It is characterized by permeability values ranging from 0.1 to 1 mD and it is associated with deformed and heterogeneous lithofacies. Figure 7.20 represents poor reservoir quality characterized by permeability values that are less than 0.1 mD and it is associated with matrix-supported diamictites, claystone and/or argillaceous sandstone. These zones have been established based on the linear relationships between the porosity and permeability values. Generally, the nearshore (FA1) and glaciofluvial (FA4) environments are characterized by permeability values that are greater than 0.1 mD while the glaciolacustrine delta and subglacial (FA3) environments are characterized by permeability values that are less than 0.1 mD. This indicates that the former environments are characterized by better reservoir quality.

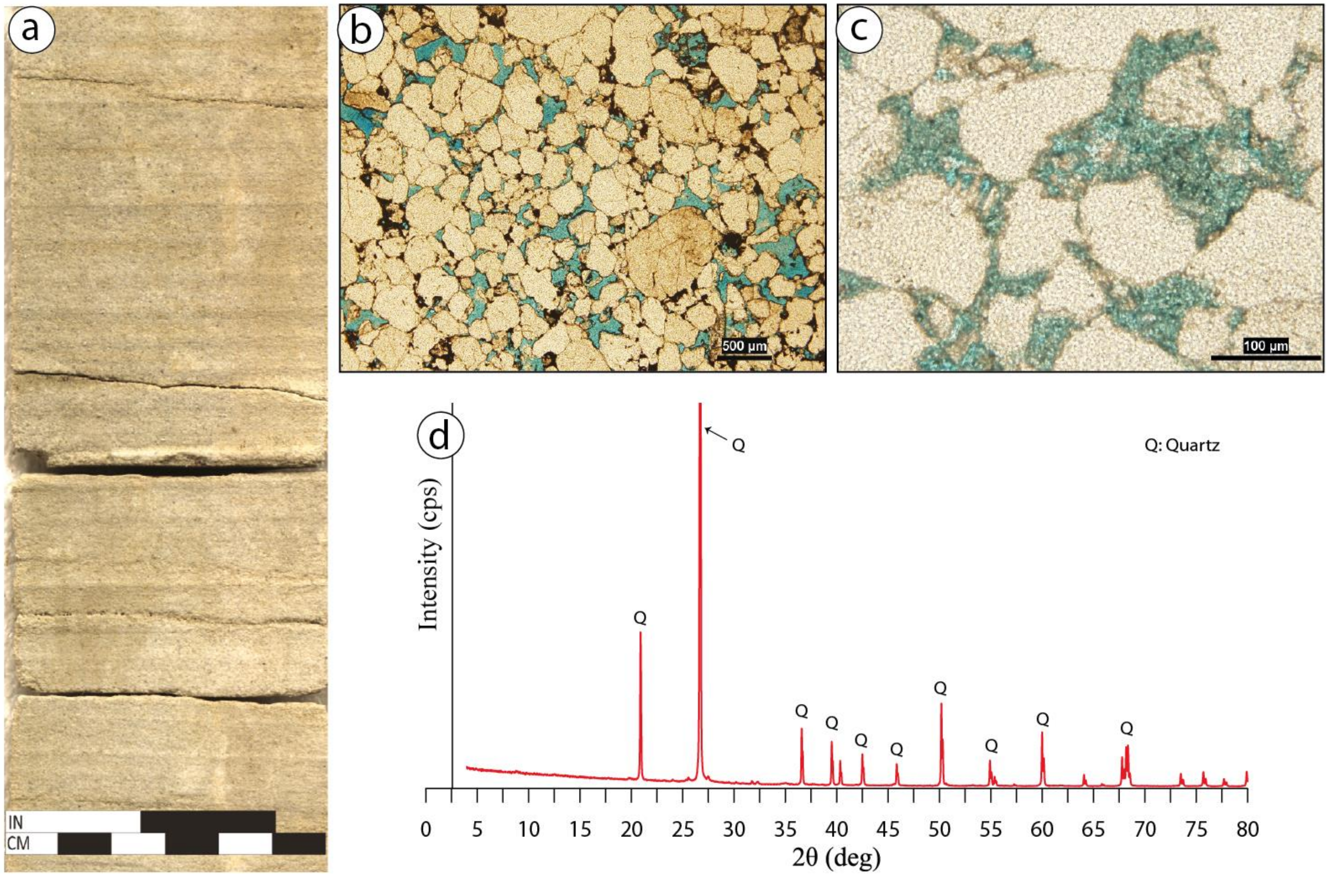

Figure 7.18: Representative lithofacies, thin section, XRD for High reservoir quality with porosity values (9 - 14%) and permeability values that are greater than 1 mD. (a) horizontally fractured massive sandstone, (b) intergranular porosity, (c) total feldspar dissolution, (d) representative XRD analysis showing that all samples are predominated by quartz.

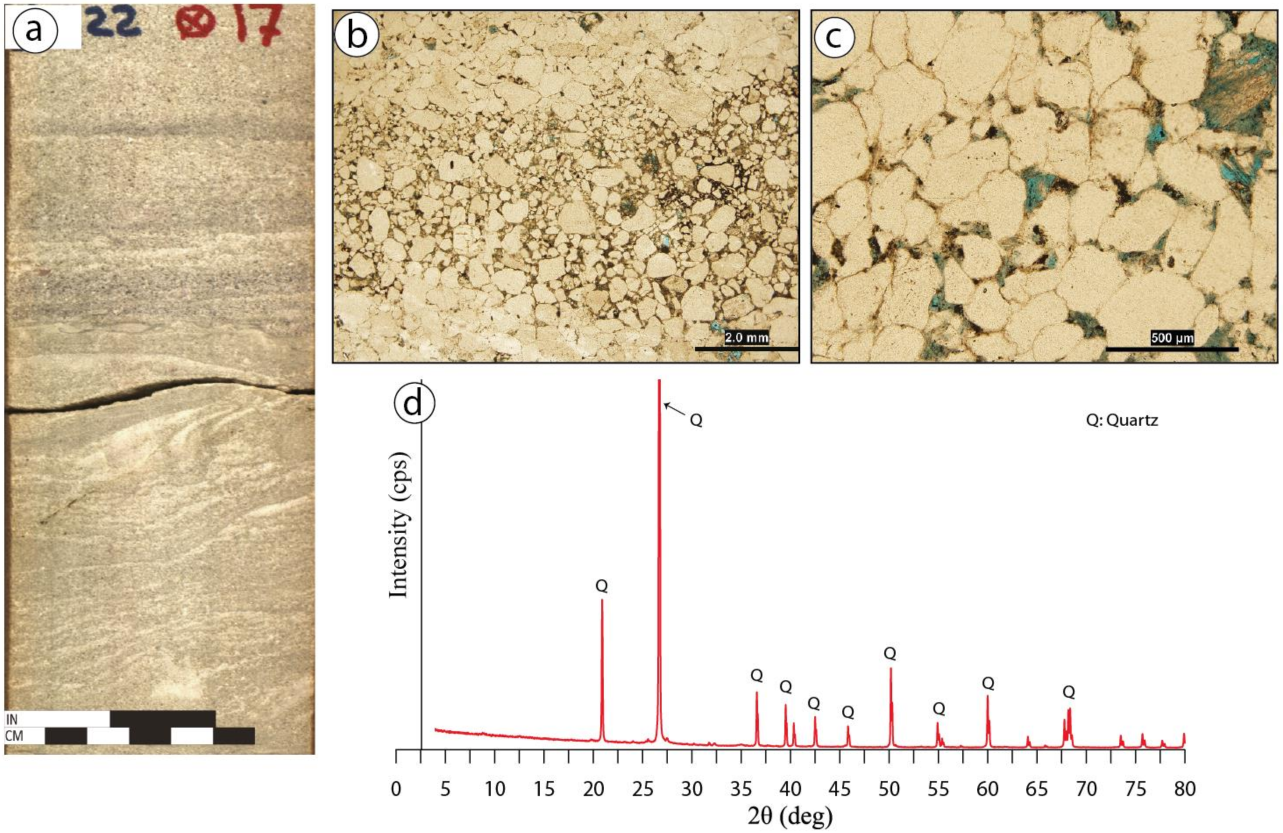

Figure 7.19: Representative lithofacies, thin section and XRD for moderate reservoir quality with porosity values (1 - 12%) and permeability values (0.1 - 1 mD). (a) deformed lithofacies overlain by laminated and massive sandstone, (b) thin section photomicrograph showing uncompacted grains between two compaction bands, (c) compacted grains with feldspar dissolution, (d)) representative XRD analysis showing that all samples are predominated by quartz.

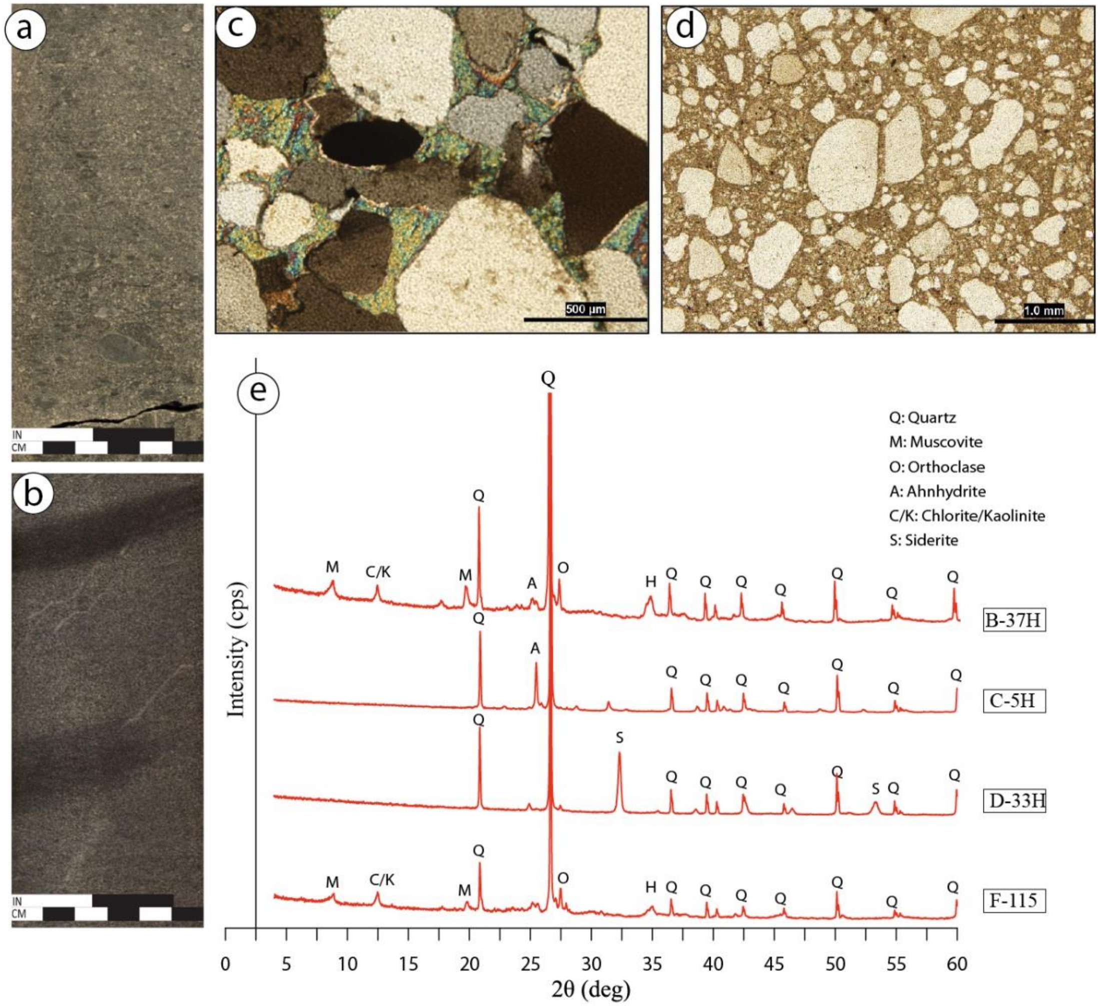

Figure 7.20: Representative lithofacies, thin section, SEM and XRD for poor reservoir quality with porosity values (0% to 11%) and permeability values that are less than 0.1 mD. (a) matrix-supported diamictite, (b) greyish massive sandstone, (c) anhydrite cement (i.e. for cementation), (d) matrix fills the pores, (e) representative XRD analysis showing mineralogical heterogeneity in this reservoir type.

7.7 Discussion

Based on porosity and permeability relationship, three interval zones including high, moderate and poor reservoir qualities have been classified to represent the reservoir quality from the investigated core samples (Figure 7.17). The high reservoir quality is characterized by permeability values that are greater than 1 mD, the moderate is characterized by permeability (0.1 - 1 mD), and the poor is characterized by permeability values that are less than 0.1 mD. The high reservoir quality of the lithofacies (Figure 7.18) is significantly enhanced by fractures, feldspar dissolution and is occasionally associated with primary porosity. The best examples of these lithofacies are observed in the nearshore lithofacies association (Figure 6.2, Well-A: F4) and the glaciolacustrine delta lithofacies association (Figure 6.3, Well-B: F7). Most of the lithofacies in nearshore and glaciofluvial lithofacies association exhibit moderate reservoir quality (Figure 7.19). The quality of these lithofacies occasionally associated with fractures and primary porosity, is enhanced by feldspar dissolution. However, it is reduced by grains compaction, and precipitation of iron oxide, illite/smectite clay and silica cements. The poor reservoir quality lithofacies (Figure 7.20) is mostly associated with glaciolacustrine delta and subglacial lithofacies association. In the glaciolacustrine delta environment, grains compaction (Figure 7.10a), cementation (Figure 7.11b, c) and matrix content (i.e. Figure 7.10f) are the main controls that reduced the reservoir quality. The reduction in the reservoir quality of the subglacial lithofacies appears to be principally controlled by matrix content and poor grain sorting (i.e. Figure 7.14b).

CHAPTER 8

SUMMARY AND CONCLUSION

8.1 Summary

This study investigates the lithofacies of the Sarah Formation from core samples retrieved from six wells (Well-A, Well-B, Well-C, Well-D, Well-E, and Well-F) drilled in the Rub Al-Khali Basin (Empty Quarter). Facies analysis, petrographical, geochemical and petrophysical characterizations have been accomplished. Based on lithofacies analysis; consequently, the core intervals of all cores are classified and assembled to represent four lithofacies associations (FA) including bioturbated massive sandstone (FA1), grayish massive sandstone (FA2), diamictites (FA3), and partially deformed graded to massive sandstone (FA4). Based on the lithofacies associations, four depositional environments comprising of nearshore (FA1), glaciolacustrine-delta (FA2), subglacial tillite (FA3), and glaciofluvial (FA4) environments are interpreted.

Throughout the basin, the Sarah Formation is characterized by a variety of lithofacies reflecting various depositional environments. Proximally, towards the western margin of the basin and close to the Arabian Shield, the Sarah Formation was deposited in the glaciofluvial environment. This environment is characterized by sublitharenite and by relatively moderate reservoir quality. There are no significant geochemical and mineralogical variations observed in this environment.

Distally, toward the eastern margin of the basin, the Sarah Formation was deposited in a nearshore environment. Geochemically, this environment is almost as same as the glaciofluvial environment. However, the nearshore environment is characterized by subarkoze and mature sandstone and by relatively better reservoir quality than the other environments. Natural fractures and feldspar dissolution are the main controls for enhancing reservoir quality in this environment.

Close to the basin center, medially, the Sarah Formation was deposited within glaciolacustrine delta and subglacial environments. These environments exhibit significant geochemical and mineralogical variations reflecting a heterogeneity in their lithofacies. Both environments are characterized by poor reservoir quality. The grains compaction, cementation (anhydrite, barite, clay, and iron oxides) and the matrix content decrease the reservoir quality of the glaciolacustrine environment. However, the reservoir quality of the subglacial lithofacies is mainly reduced by matrix content.

In the subglacial environment, the glaciogenic diamictites exhibit various characteristics including massive matrix-supported, stratified matrix-supported, massive clast-supported, and massive sandy matrix-supported diamictites. They reveal that the advance of the Late Ordovician (Hirnantian) glaciations extended to the Rub' Al-Khali Basin and that the observed deformed lithofacies in the cores might be related to the glacial movements during a period of deglaciation due to a glacial retreat.

8.2 Conclusions

1. Six core intervals retrieved from the Sarah Formation, in the Rub' Al-Khali Basin, Saudi Arabia, are studied and; consequently, the cores have been classified into four lithofacies associations (FA) including massive bioturbated sandstone (FA1), grayish massive sandstone (FA2), diamictites (FA3) and partially deformed, graded to massive sandstone (FA4) lithofacies associations.
2. Based on the lithofacies associations, four depositional environments including nearshore (FA1), glaciolacustrine delta (FA2), subglacial (FA3) and glaciofluvial (FA4) environments are interpreted.
3. The nearshore and glaciofluvial environments were deposited in the eastern and western margins of the basin like, respectively, while the glaciolacustrine and subglacial environments were deposited in graben-like structure closed to the basin center.
4. The observed evidence of the Late Ordovician glaciation in the Rub' Al-Khali Basin are diamictites and glacial deformation.
5. The heterogeneity of the lithofacies is lower at the basin margins with the shallower lithofacies (nearshore and glaciofluvial lithofacies) and higher at the basin center with the deeper lithofacies (glaciolacustrine delta and subglacial lithofacies).
6. The subarkose sandstone of the nearshore lithofacies and the sublitharenite of the glaciofluvial lithofacies are characterized by better reservoir quality than the sublitharenite to quartzarenite of the glaciolacustrine delta and the sublitharenite of the subglacial environments.

7. The main factors that enhance reservoir quality and produce sweet spots intervals are fractures, feldspar dissolution while grains compaction, cementation (anhydrite, barite, siderite, clay, iron oxides), poor sorting grains and matrix content reduce reservoir quality and make non-sweet spots intervals.
8. The nearshore and glaciofluvial lithofacies exhibit no significant geochemical variation when comparing to the glaciolacustrine delta and subglacial lithofacies.
9. Based on porosity and permeability relationships and permeability ranges proposed by this study, some lithofacies observed in the nearshore and glaciolacustrine delta environments are characterized by high reservoir quality. Most of the nearshore and glaciofluvial lithofacies are characterized by moderate reservoir quality. The glaciolacustrine delta and the subglacial lithofacies are characterized by poor reservoir quality.

References

Abu-Ali, M. A., J. L. L. Rudkiewicz, J. G. McGillivray, and F. Behar, 1999, Paleozoic petroleum system of Central Saudi Arabia: GeoArabia, v. 4, no. 3, p. 321–336.

Aguilera, R. F., T. Harding, and F. Krause, 2008, Natural gas production from tight gas formations: a global perspective, *in* Forum 13: Non-conventional gas: World Petroleum Congress.

Al-Harbi, O. A., and M. M. Khan, 2011, Source and origin of glacial paleovalley-fill sediments (Upper Ordovician) of Sarah Formation in central Saudi Arabia: Arabian Journal of Geosciences, v. 4, no. 5–6, p. 825–835.

Al-Mahmoud, M. J., and I. Al-Ghamdi, 2010, An Overview of Tight Gas Reservoirs in Saudi Arabia, *in* Second EAGE Middle East Tight Gas Reservoirs Workshop: EAGE.

Ali, S. a, W. J. Clark, W. R. Moore, and J. R. Dribus, 2010, Diagenesis and Reservoir Quality: Oilfield Review, v. 22, no. 2, Summer, p. 14–27, doi:10.1080/10916466.2012.742542.

Allaby, M., 2008, Dictionary of Earth Sciences: Oxford paperback reference, v. 1, p. 654, doi:10.1036/0071417982.

Babiker, J., 2015, The Relationship between Lithosiratigraphy and Geomechanical Properties of Sarah Formation Outcrop Analogue, central Saudi Arabia: King Fahd University of Petroleum and Minerals, 133 p.

Beretta, E., 2009, Data Collection Strategy for Exploration Wells in Tight Reservoirs, *in* First Workshop on Tight Gas Reservoirs: EAGE.

Bhatia, M. R., 1983, Plate Tectonics and Geochemical Composition of Sandstones: The Journal of Geology, v. 91, no. 6, p. 611–627, doi:10.1086/628922.

Briner, A. P., M. Hulver, A. Azzouni, and C. Harvey, 2010, Regional Reservoir Quality of a Tight Gas Play: the Ordovician Sarah Formation in the Rub'Al Khali Basin of

Southern Saudi Arabia, *in* Second EAGE Middle East.

Clark-Lowes, D. D., 2005, Arabian glacial deposits: recognition of palaeovalleys within the Upper Ordovician Sarah Formation, Al Qasim district, Saudi Arabia: Proceedings of the Geologists' Association, v. 116, no. 3–4, p. 331–347, doi:10.1016/S0016-7878(05)80051-3.

Clark-Lowes, D. D., 1980, Sedimentology and mineralization potential of Saq and Tabuk formations: Imperial college of Science and Technology, London, Open-File Report CRC/IC, v. 7.

Corbett, P. W. M., and J. L. Jensen, 1992, Estimating the mean permeability: how many measurements do you need? First Break, v. 10, no. 3, p. 89–94.

Craigie, N. W., and A. J. Rees, 2016, Chemostratigraphy of glaciomarine sediments in the Sarah Formation, northwest Saudi Arabia: Journal of African Earth Sciences, v. 117, p. 263–284, doi:10.1016/j.jafrearsci.2016.02.006.

Craigie, N. W., A. Rees, K. MacPherson, and S. Berman, 2016, Chemostratigraphy of the Ordovician Sarah Formation, North West Saudi Arabia: An integrated approach to reservoir correlation: Marine and Petroleum Geology, v. 77, p. 1056–1080, doi:10.1016/j.marpetgeo.2016.07.009.

Dickinson, W. R., 1985, Interpreting provenance relations from detrital modes of sandstones, *in* Provenance of Arenites: Springer Netherlands, p. 333–361, doi:10.1007/978-94-017-2809-6_15.

Ejaz, W., 2016, Integration of electrofacies and Geomechanical characteristics of Sarah Formation (Potential Tight Gas Reservoir), Rub' Al-khali Basin, Saudi Arabia: King Fahd University of Petroleum and Minerals.

El-Deek, I. M., 2014, Sedimentological Heterogeneity of the Late Ordovician Glacio-fluvial Sarah Formation, Al-Qaseem Area, Saudi Arabia: Impact on Petrophysical Properties and Reservoir Quality: King Fahd University of Petroleum and Minerals, 206 p.

El-Deek, I., O. Abdullatif, G. Korvin, and K. Al-Ramadan, 2014, Integration of

Sedimentology, Petrophysics and Statistics for Characterizing the Reservoir Heterogeneity of the Late Ordovician Sarah Formation, Central Saudi Arabia, *in* EGU General Assembly Conference Abstracts: EGU, p. 9871.

Evans, J. D., 1996, Straightforward Statistics for the Behavioral Sciences: Brooks/Cole, 122 p.

Evans, D. J. A., and I. D. Benn, 2004, A practical guide to the study of glacial sediments, *in* Edward Arnold: London, p. 266, doi:10.1080/03009480510012962.

Eyles, N., C. Eyles, and A. Miall, 1983, Lithofacies types and vertical profile models; an alternative approach to the description and environmental interpretation of glacial diamict and diamictite sequences: Sedimentology.

Fitch, P. J. R., M. A. Lovell, S. J. Davies, T. Pritchard, and P. K. Harvey, 2015, An integrated and quantitative approach to petrophysical heterogeneity: p. 82–96, doi:10.1016/j.marpetgeo.2015.02.014.

Folk, R. L., 1980, Petrology of Sedimentary Rocks: Austin: Texas, Hemphill Publishing Company, 182 p.

Forsyth, D., N. M. Al Musharfi, and a. M. Al Marzooq, 2011, Tight Gas Petrophysical Challenges in Saudi Aramco: SPE/DGS Saudi Arabia Section Technical Symposium and Exhibition, 15-18 May 2011, Al-Khobar, Saudi Arabia, no. May, p. 15–18.

Fossen, H., R. a. Schultz, Z. K. Shipton, and K. Mair, 2007, Deformation bands in sandstone: a review: Journal of the Geological Society, London, v. 164, no. NA, p. 755–769, doi:10.1144/0016-76492006-036.

El Hajj, H., W. Suzart, M. Al Tammar, T. Al-Ghamdi, and A. Al-Abdullatif, 2015, Significance of Clay Mineralogy for Reservoir Quality Prediction, *in* Third EAGE/AAPG Workshop on Tight Reservoirs in the Middle East: EAGE.

Hardman, D., R. MacDonald, R. Sprague, Y. Meridji, W. Mudjiono, J. Galford, M. Rourke, M. Dix, and M. Kelton, 2011, Using Elemental Geochemistry to Improve Sandstone Reservoir Characterization: a Case Study From the Unayzah A Interval of Saudi Arabia: Petrophysics, v. 52, no. 5, p. 344–356.

Hassan, M., A. Hossin, and A. Combaz, 1976, Fundamentals of the differential gamma ray log-interpretation technique: SPWLA 17th Annual Logging.

Hayton, S., C. Heine, and B. E. Gratto, 2010, Tight Gas Exploration in Saudi Arabia, *in* SPE Deep Gas Conference and Exhibition: Society of Petroleum Engineers.

Le Heron, D. P., J. Craig, and J. L. Etienne, 2009, Ancient glaciations and hydrocarbon accumulations in North Africa and the Middle East: Earth-Science Reviews, v. 93, no. 3, p. 47–76, doi:10.1016/j.earscirev.2009.02.001.

Herron, M. M., 1988, Geochemical classification of terrigenous sands and shales from core or log data: Journal of Sedimentary Research, v. 58, no. 5, p. 820–829, doi:10.1306/212F8E77-2B24-11D7-8648000102C1865D.

Hippler, S. J., J. E. Neal, B. Alramahi, S. Becker, and R. E. Klimentidis, 2013, Advanced Analytical Capabilities for Optimising Exploitation of Unconventional Resources, *in* International Petroleum Technology Conference: International Petroleum Technology Conference.

Holditch, S. A., 2006, Tight gas sands: Journal of Petroleum Technology, v. 58, no. 6, p. 86–93.

Isbell, J. L., 2010, Late Paleozoic Glacial Events and Postglacial Transgressions in Gondwana: Geological Society of America, Geological Society of America Special Papers, 81-100 p., doi:10.1130/2010.2468(03).

Islam, M. R., 2015, Unconventional Gas Reservoirs: 9-69 p., doi:10.1016/B978-0-12-800390-9.00002-5.

Kawata, Y., and K. Fujita, 2001, Some Predictions of Possible Unconventional Hydrocarbons Availability Until 2100: SPE Journal, v. 5, p. 1–10, doi:10.2523/68755-MS.

Khalil, M. H. M., 2012, Reservoir Sweet Spots in the Arabian Petroleum Basin; Types and Controls, *in* GEO 2012.

Khalil, M., 2009, Structural Controls on the Development of Sweet Spots in Tight Reservoirs: First EAGE Workshop on Tight Gas Reservoirs 2009.

Klimentidis, R., 2009, Reservoir Quality Assessment of Tight Gas Reservoirs-Links to Producibility: First EAGE Workshop on Tight Gas Reservoirs 2009.

Konert, G., A. M. Afifi, S. A. Al-Hajri, K. De Groot, A. A. Al Naim, and H. J. Droste, 2001, Paleozoic Stratigraphy and Hydrocarbon Habitat of the Arabian Plate: AAPG Memoir, v. 74, no. 24.

Lake, L. W., and J. L. Jensen, 1991, A review of heterogeneity measures used in reservoir characterization: In Situ, v. 15, no. 4, p. 409–440.

Lake, L. W., and J. L. J. Jensen, 1989, A Review of Heterogeneity Measures Used in Reservoir Characterization: SPE General, v. 53, no. 9, p. 1689–1699, doi:20156-MS.

Lang, J., R. J. Dixon, D. P. Le Heron, and J. Winsemann, 2012, Depositional architecture and sequence stratigraphic correlation of Upper Ordovician glaciogenic deposits, Illizi Basin, Algeria: Geological Society, London, Special Publications, v. 368, no. 1, p. 293–317, doi:10.1144/SP368.1.

Lee, P. J., 2008, Statistical Methods for Estimating Petroleum Resources: International Association for Mathematical Geology: Studies in Mathematical Geology, p. 256.

McClure, H. A., 1978, Early paleozoic glaciation in Arabia: Palaeogeography, Palaeoclimatology, Palaeoecology, v. 25, no. 4, p. 315–326.

McGillivray, and M. I. Husseini, 1992, The Paleozoic Petroleum Geology of Central Arabia (1): AAPG Bulletin, v. 76, no. 10, p. 1473–1490.

Melvin, J., 2015, Lithostratigraphy and depositional history of Upper Ordovician and lowermost Silurian sediments recovered from the Qusaiba-1 shallow core hole, Qasim region, central Saudi Arabia: Review of Palaeobotany and Palynology, v. 212, p. 3–21, doi:10.1016/j.revpalbo.2014.08.014.

Melvin, J., and R. A. Sprague, 2006, Advances in Arabian stratigraphy: Origin and stratigraphic architecture of glaciogenic sediments in Permian-Carboniferous lower Unayzah sandstones, eastern central Saudi Arabia: GeoArabia, v. 11, no. 4, p. 105–152.

Miall, A., 2000, Facies Analysis, *in* Principles of Sedimentary Basin Analysis: Springer

Berlin Heidelberg, p. 141–248.

Miall, A. D., 2015, Stratigraphy: A modern synthesis: 1-454 p., doi:10.1007/978-3-319-24304-7.

Michael, N. A., S. Shammari, D. LePain, A. Abubshait, M. Guy, C. Van Dijk, and R. Zuhlke, 2015, The Sarah Formation: A Glaciogenic Reservoir Analogue in Saudi Arabia, *in* AAPG Annual Convention and Exhibition.

Miller, J., 1996, Glacial Sediments, *in* H. G. Reading, ed., Sedimentary Environments: Processes, Facies and Stratigraphy: Blackwell Publishing, p. 455.

Morton-Thompson, D., and A. M. A. Woods, 1993, Development Geology Reference Manual: AAPG Methods in Exploration Series, No. 10: AAPG, 550 p.

Moscariello, A., P. Spaak, A. Jourdan, and A.-H. Azzouni, 2008, The Ordovician Glaciation in Saudi Arabia—Exploration Challenges Part 1. Geology (Outcrop, Subsurface, Analogues), *in* AAPG International Conference and Exhibition,: Search and Discovery Article #50175.

Nelson, R. a., 2001, Geologic Analysis of Naturally Fractured Reservoirs: 101-124 p., doi:10.1016/B978-088415317-7/50005-1.

Pettijohn, F. J., P. E. Potter, and R. Siever, 1972, Sand and Sandstone: New York, NY, Springer New York, 618 p., doi:10.1007/978-1-4615-9974-6.

Pettijohn, F. J., P. E. Potter, and R. Siever, 1987, Sand and Sandstone: New York, NY, Springer New York, 553 p., doi:10.1007/978-1-4612-1066-5.

Pollastro, R. M., 2003, Total petroleum systems of the Paleozoic and Jurassic, Greater Ghawar Uplift and adjoining provinces of central Saudi Arabia and northern Arabian-Persian Gulf: US Department of the Interior, US Geological Survey, 52 p.

Razzaq, W., 2013, Sedimentological and Petrophysical Characterization of Sarah Formation with the aid of GIS, central Saudi Arabia: King Fahd University of Petroleum and Minerals, 194 p.

Razzaq, W., O. Abdullatif, A. Sahin, and M. Hariri, 2014, Sedimentological and

Petrophysical Heterogeneity of Glaciogenic Paleovalley, Late Ordovician Sarah Formation, Central Saudi Arabia, *in* EGU General Assembly Conference Abstracts: p. 9216.

Reading, H., and J. Collinson, 1996, Clastic coasts, *in* Sedimentary environments: processes, facies and stratigraphy.

Rogner, H.-H., 1997, An Assessment of World Hydrocarbon Resources: Annual Review of Energy and the Environment, v. 22, no. 1, p. 217–262, doi:10.1146/annurev.energy.22.1.217.

Rollinson, H. R. H. R. R., 1993, Using geochemical data :evaluation, presentation, interpretation: Pearson Education Limited, 11-12 p.

Rushing, J. A., K. E. Newsham, and T. A. Blasingame, 2008, Rock Typing-Keys to Understanding Productivity in Tight Gas Sands, *in* SPE Unconventional Reservoirs Conference: doi:10.2118/114164-MS.

Sahin, A., 2013, Unconventional Natural Gas Potential in Saudi Arabia, *in* SPE Middle East Oil and Gas Show and Conference: Society of Petroleum Engineers.

Schenk, C. J. C., 2005, Geologic definition of conventional and continuous accumulations in select US basins—the 2001 approach, *in* AAPG Hedberg Research Conference on Understanding, Exploring and Developing Tight Gas Sands.

Schlumberger, 2009, Log Interpretation Charts: Schlumberger, p. 310.

Scholle, P., and D. Spearing, 1982, Sandstone Depositional Environments: AAPG Memoir 31: AAPG, 410 p.

Schultz, A. W., 1984, Subaerial debris-flow deposition in the Upper Paleozoic Cutler Formation, western Colorado: Journal of Sedimentary Petrology, v. 54:759-772, doi:10.1306/212F84EF-2B24-11D7-8648000102C1865D.

Senalp, M., and A. Al-Duaiji, 2001, Sequence stratigraphy of the Unayzah reservoir in central Saudi Arabia: Saudi Aramco Journal of Technology.

Senalp, M., and A. Al-Laboun, 2000, New evidence on the Late Ordovician glaciation in central Saudi Arabia, JOUR: Saudi Aramco Journal of Technology, Spring, no. Spring, p. 11–40.

Senalp, M., and A. Al-Laboun, 1996, Stratigraphy and Age of the Glacial Deposits in Qasim Region, Central Arabia, *in* 2nd Middle East Geosciences Conference: GeoArabia:, p. 192–193.

Sharland, P., R. Archer, D. Casey, R. Davies, S. Hall, A. Heward, A. Horbury, and M. Simmons, 2001, Arabian plate sequence stratigraphy: GeoArabia, Special Publication 2, v. 18, no. 4, p. 371.

Sohn, Y. K., M. Y. M. Choe, and H. R. H. Jo, 2002, Transition from debris flow to hyperconcentrated flow in a submarine channel (the Cretaceous cerro toro formation, southern Chile): Terra Nova, v. 14, no. 5, p. 405–415, doi:10.1046/j.1365-3121.2002.00440.x.

U.S. Energy Information Administration, 2016, International Energy Outlook 2016 with Projections to 2040: Washington, DC 20585, 276 p.

U.S. Energy Information Administration, 2014, International Energy Statistics: <http://www.eia.gov/beta/international/analysis.cfm?iso=SAU> (accessed December 16, 2016).

Ulmer-Scholle, D. S., P. A. Scholle, J. Schieber, and R. A. Raine, 2014, A Color Guide to the Petrography of Sandstones, Siltstones, Shales and Associated Rocks: The Association of American Petroleum Geologists, 526 p.

Vaslet, D., 1990, Upper Ordovician Glacial Deposits in Saudi-Arabia: Episodes, v. 13, no. 3, p. 147–161.

Vaslet, D., K. S. Kellogg, A. Berthiaux, P. Le Strat, and P. L. Vincent, 1987, Explanatory notes to the geologic map of the Baq’a Quadrangle, Kingdom of Saudi Arabia: Geoscience Map GM-116 C, scale, v. 1, no. 250,000, p. 1–45.

Williams, P. L., D. Vaslet, P. R. Johnson, A. Berthiaux, P. Le Strat, and J. Foumiguet, 1986, Geologic map of the Jabal Habashi quadrangle, sheet 26F: Kingdom of Saudi Arabia: Saudi Arabian Deputy Ministry for Mineral Resources Geoscience Map-

GM-98 A, scale, v. 1, no. 250,000.

Worden, R. H., and S. D. Burley, 2009, Sandstone Diagenesis: The Evolution of Sand to Stone: 1-44 p., doi:10.1002/9781444304459.ch.

Wright, A. M., K. T. Ratcliffe, and D. Spain, 2010, Application of Inorganic Whole Rock Geochemistry to Shale Resource Plays, *in* Canadian Unconventional Resources & International Petroleum Conference: p. 19–21.

Zahid, K., and D. B. Jr, 2011, Constructing sandstone provenance and classification ternary diagrams using an electronic spreadsheet: Journal of Sedimentary ….

Zhang, P., Y. Il Lee, and J. Zhang, 2015, Diagenesis Of Tight-Gas Sandstones In The Lower Cretaceous Denglouku Formation, Songliao Basin, NEChina: Implications For Reservoir Quality: Journal of Petroleum Geology, v. 38, no. 1, p. 99–114.

Zhengquan, W., W. Qingcheng, and C. Quanshe, 1998, Spatial heterogeneity of soil nutrients in old growth forests of Korean pine: Journal of Forestry Research, v. 9, no. 4, p. 240–244, doi:10.1007/BF02912326.

Appendix A: Facies Analysis

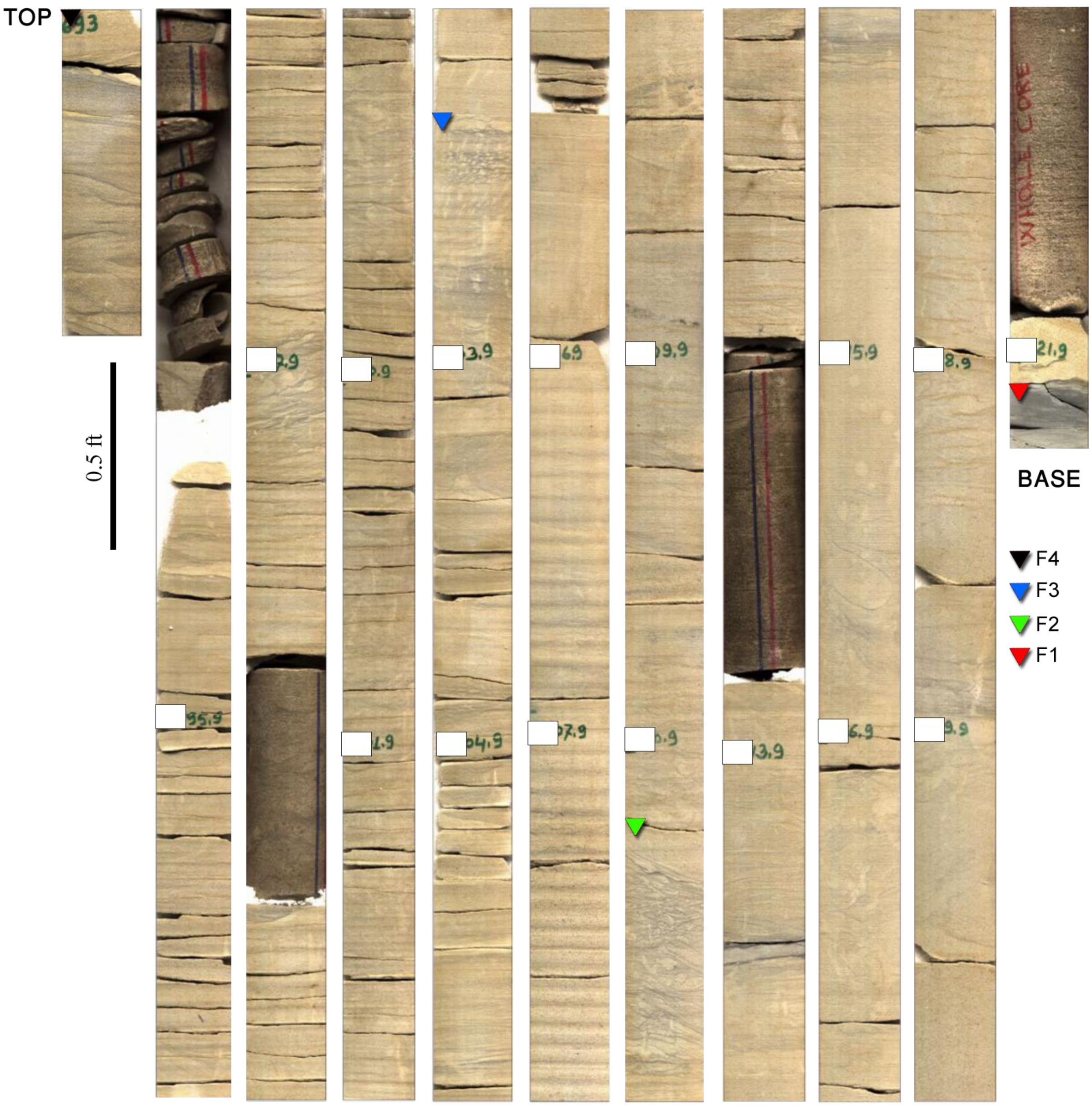

Figure A 1: The core interval of Well-A. Note that the lithofacies classification (F1 to FA4) are based on several criteria including lithology, grains size, grains sorting and bioturbation. This core is interpreted as a nearshore lithofacies.

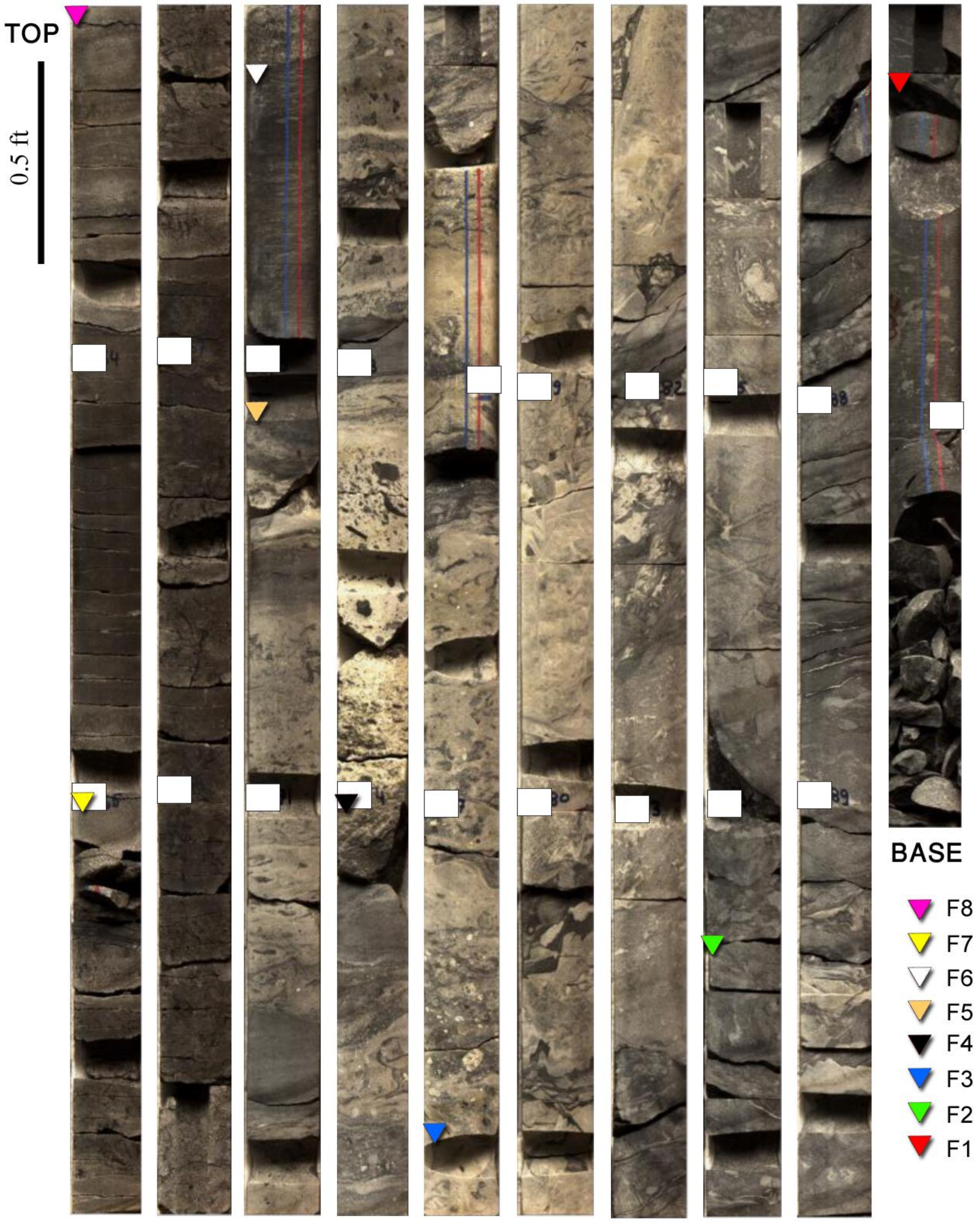

Figure A 2: The core interval of Well-B. Note that the lithofacies classification is based on lithology, grains size, grains sorting, sedimentary structure, and deformation. All the lithofacies of this core are interpreted as glaciolacustrine delta deposits except F4 and F5 that are subglacial lithofacies (diamictites).

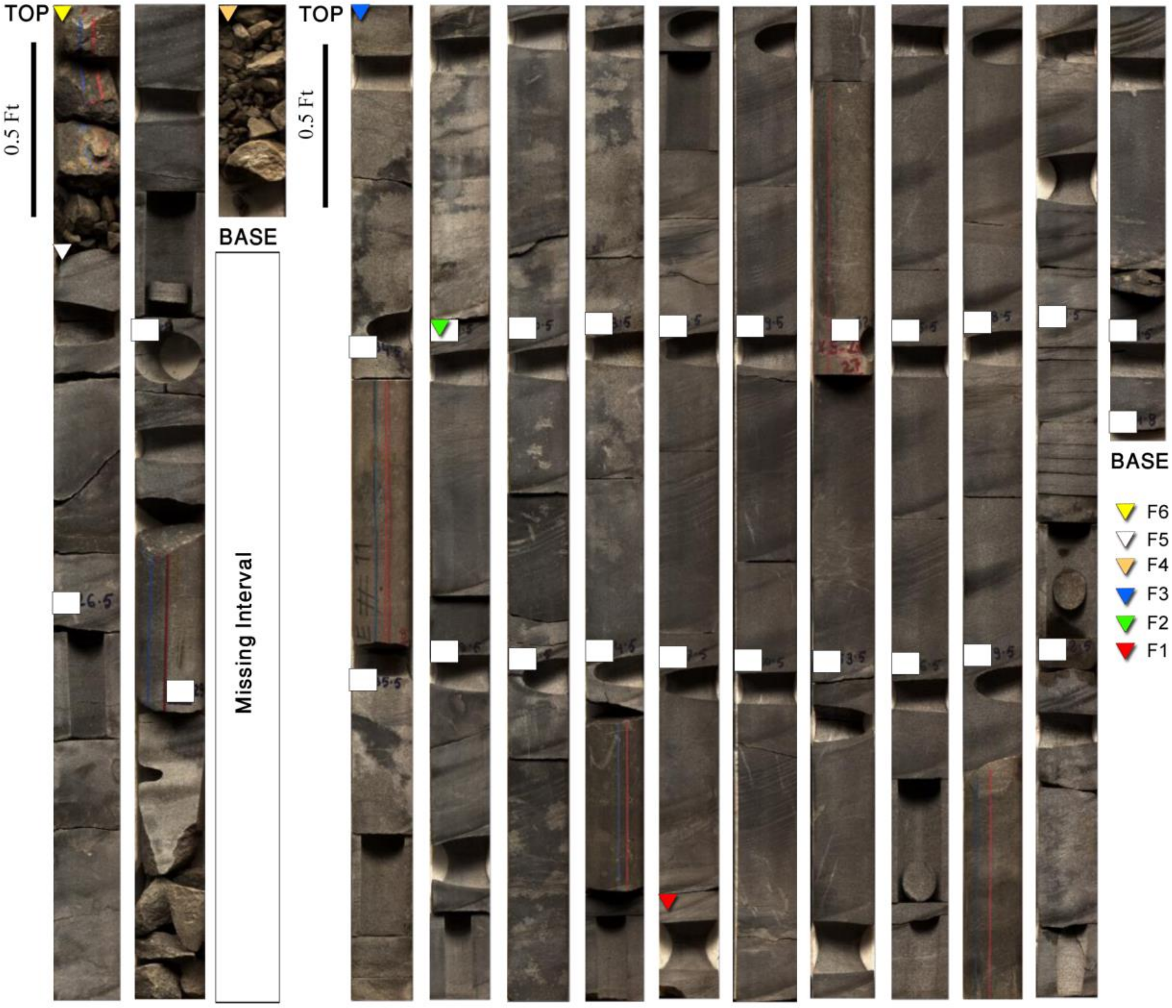

Figure A 3: The core interval of Well-C. Note that the main criteria for lithofacies classification of this core are grains size, grains sorting, erosional surfaces, mud drapes and mud patches. All the lithofacies of this core are interpreted as glaciolacustrine delta deposits.

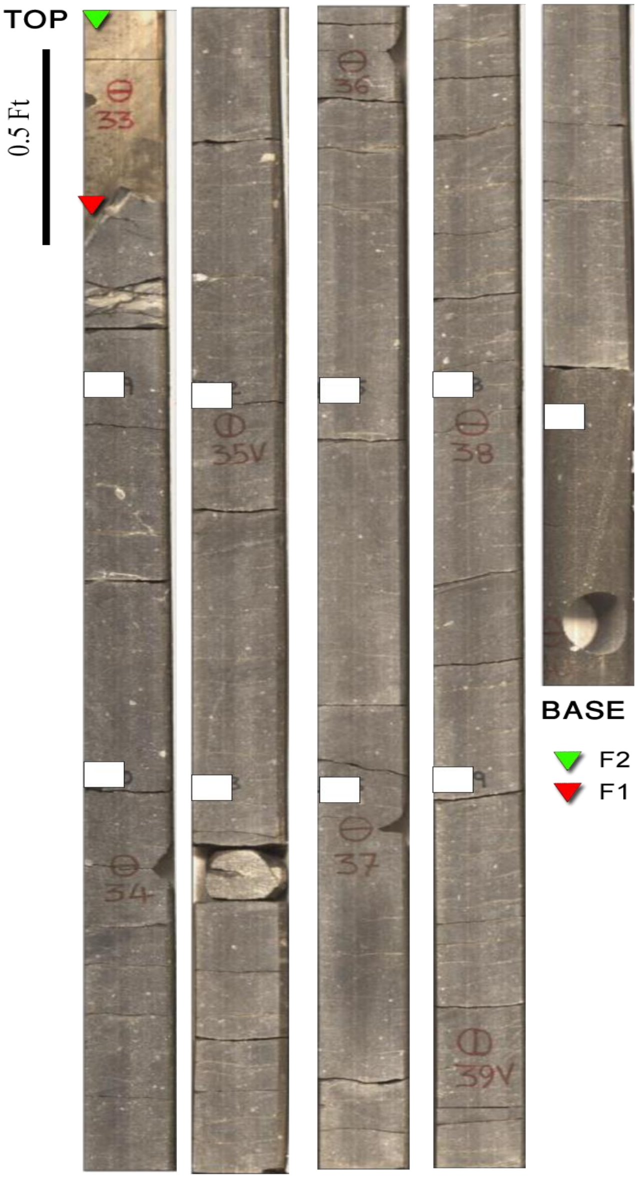

Figure A 4: The core interval of Well-D. Note that the criteria for lithofacies classification are lithology and grain size. These lithofacies are interpreted as subglacial deposits (F1) overlain by glaciofluvial deposits (F2).

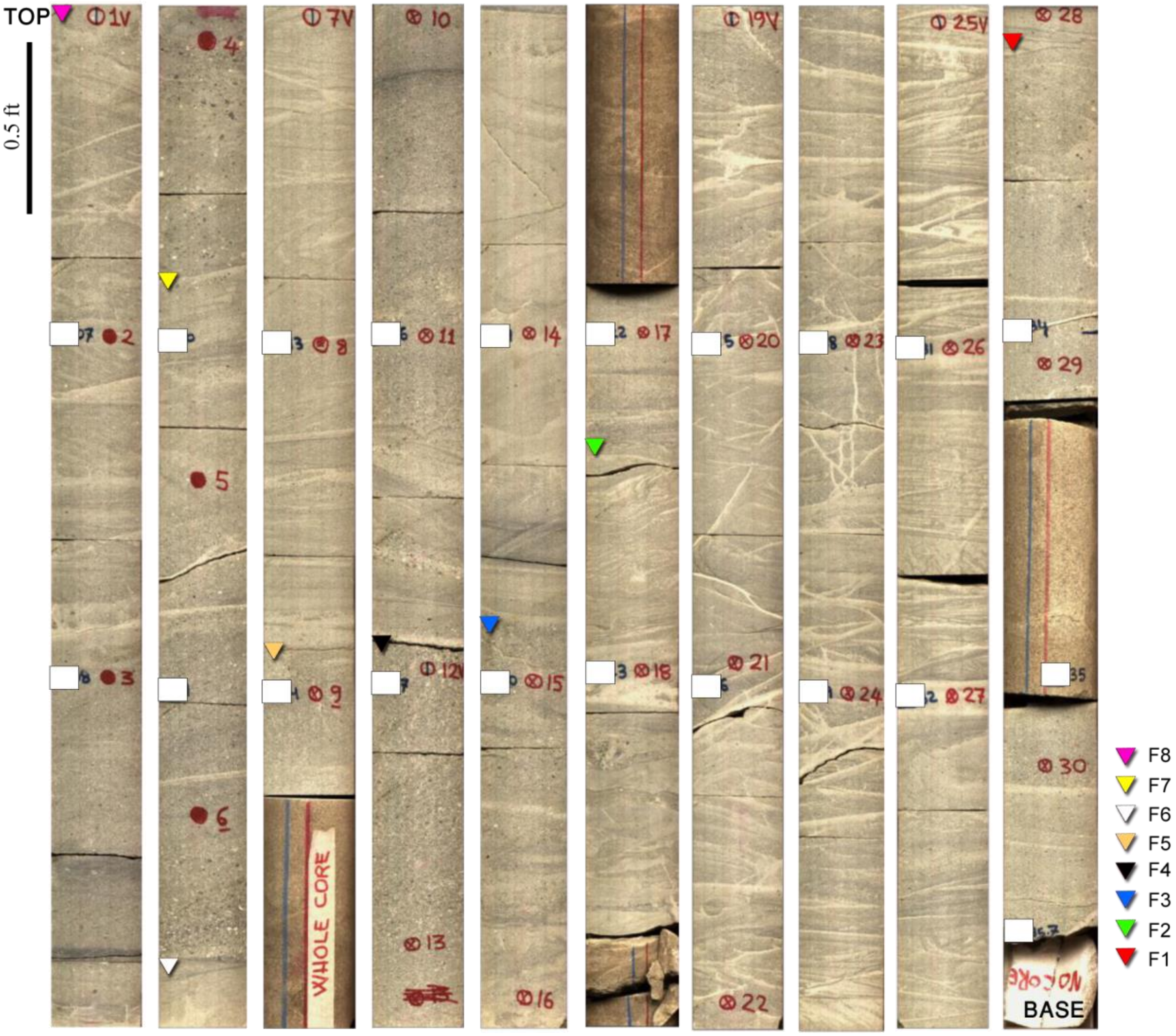

Figure A 5: The core interval of Well-E. Note that the lithofacies classification is based on changes in grain size, sedimentary and deformed structures. This core is interpreted as glaciofluvial lithofacies.

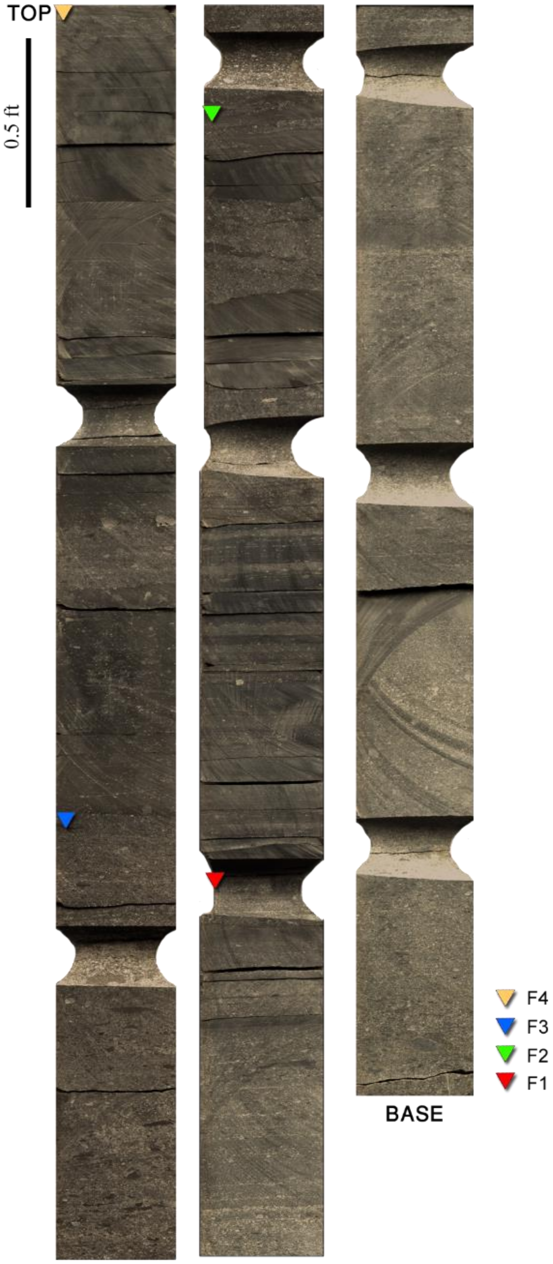

Figure A 6: The core interval of Well-F. Note that the lithofacies classification of this core is based on lithology, sedimentary structure, and diamictite. The diamictites of this core are interpreted as subglacial lithofacies.

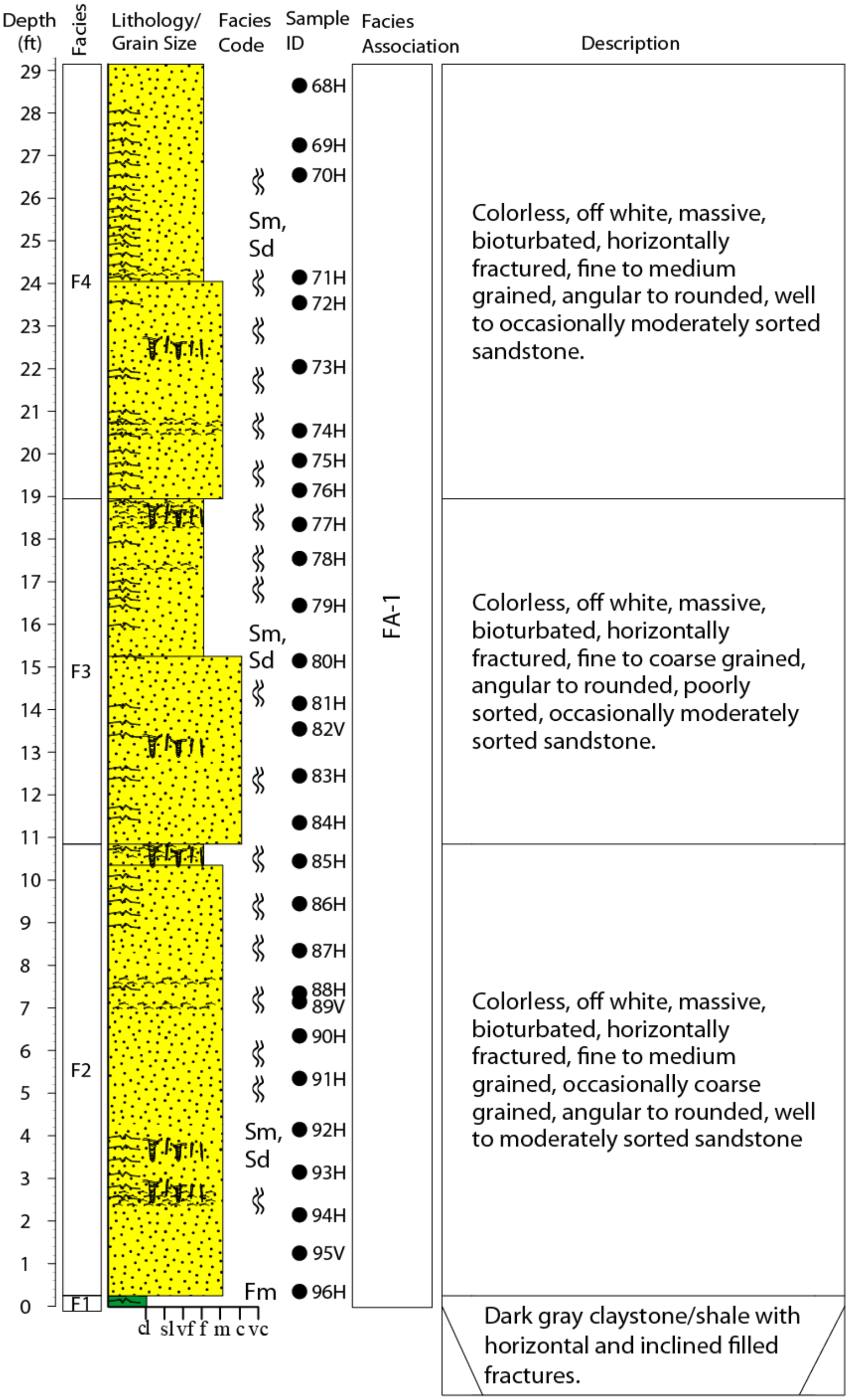

Figure A 7: Sedimentological log of the Well-A core interval. (See Figure 4.2 for the core legend and Table 4.1 for the facies codes).

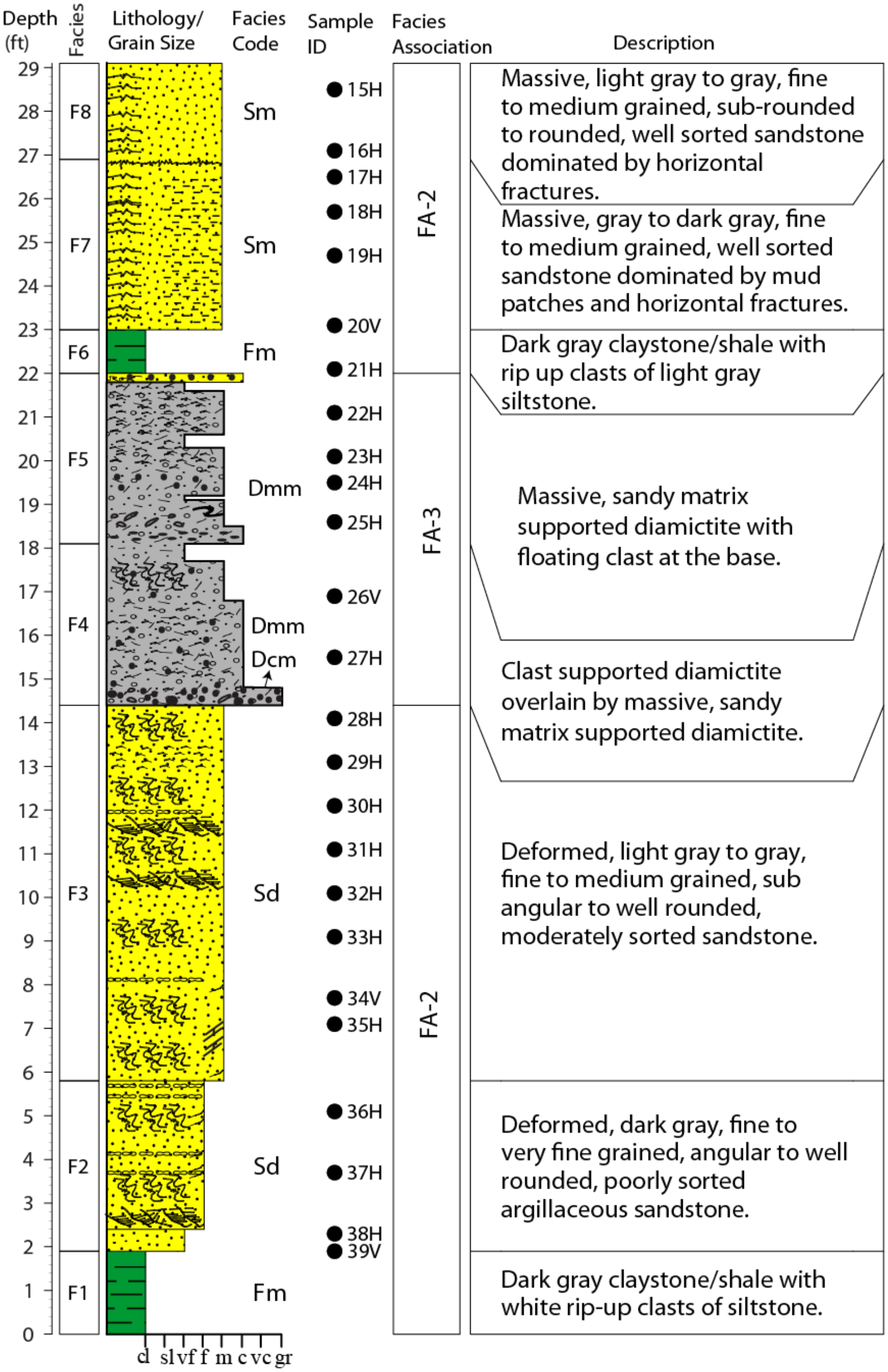

Figure A 8: Sedimentological log of the Well-B core interval. (See Figure 4.2 for the core legend and Table 4.1 for the facies codes).

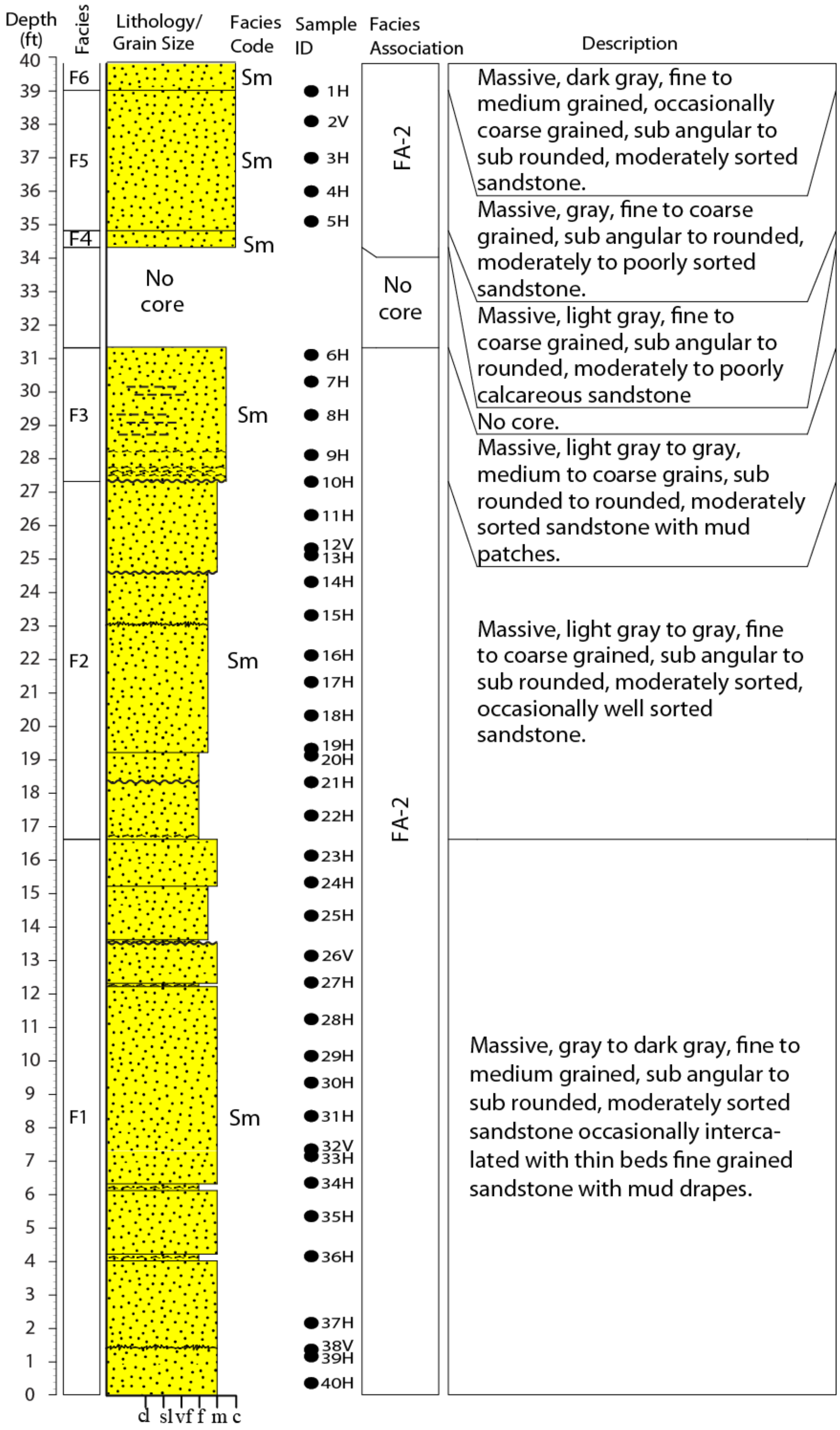

Massive, dark gray, fine to medium grained, occasionally coarse grained, sub angular to sub rounded, moderately sorted sandstone.

Massive, gray, fine to coarse grained, sub angular to rounded, moderately to poorly sorted sandstone.

Massive, light gray, fine to coarse grained, sub angular to rounded, moderately to poorly calcareous sandstone

No core.

Massive, light gray to gray, medium to coarse grains, sub rounded to rounded, moderately sorted sandstone with mud patches.

Massive, light gray to gray, fine to coarse grained, sub angular to sub rounded, moderately sorted, occasionally well sorted sandstone.

Massive, gray to dark gray, fine to medium grained, sub angular to sub rounded, moderately sorted sandstone occasionally intercalated with thin beds fine grained sandstone with mud drapes.

Figure A 9: Sedimentological log of the Well-C core interval. (See Figure 4.2 for the core legend and Table 4.1 for the facies codes).

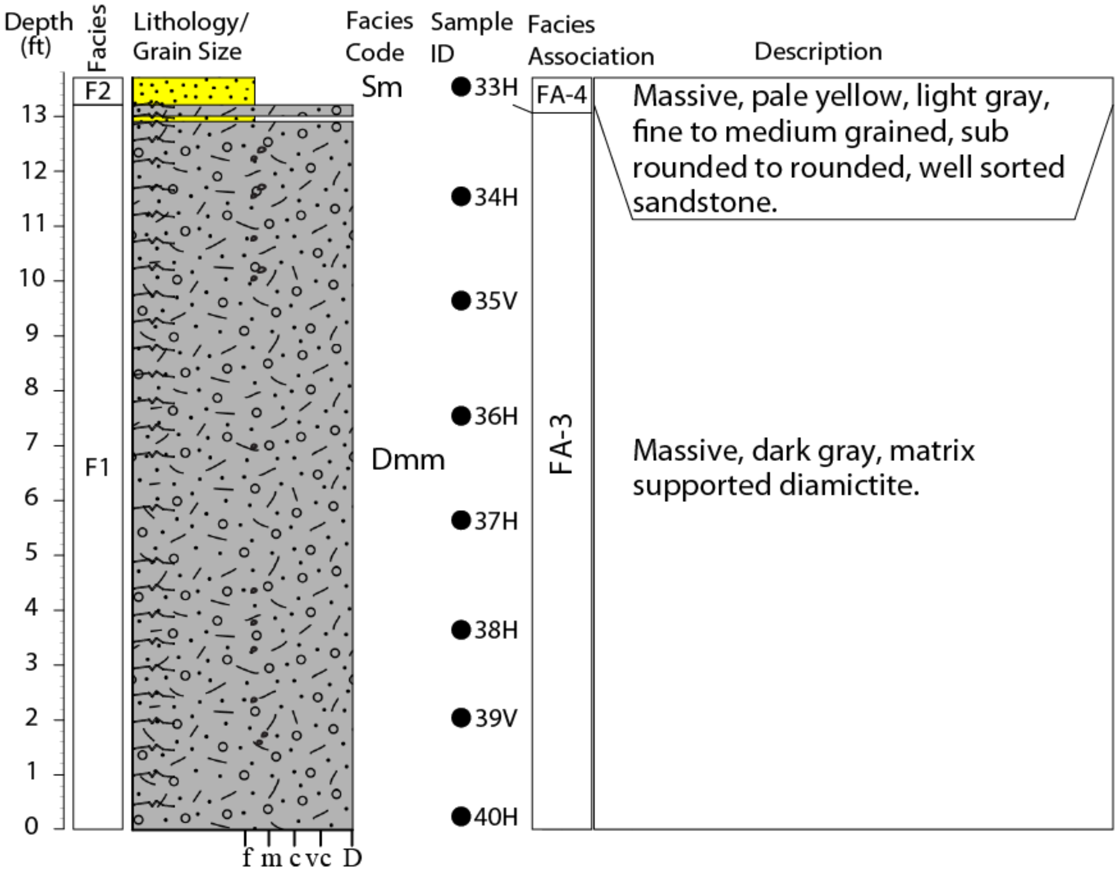

Figure A 10: Sedimentological log of the Well-D core interval. (See Figure 4.2 for the core legend and Table 4.1 for the facies codes).

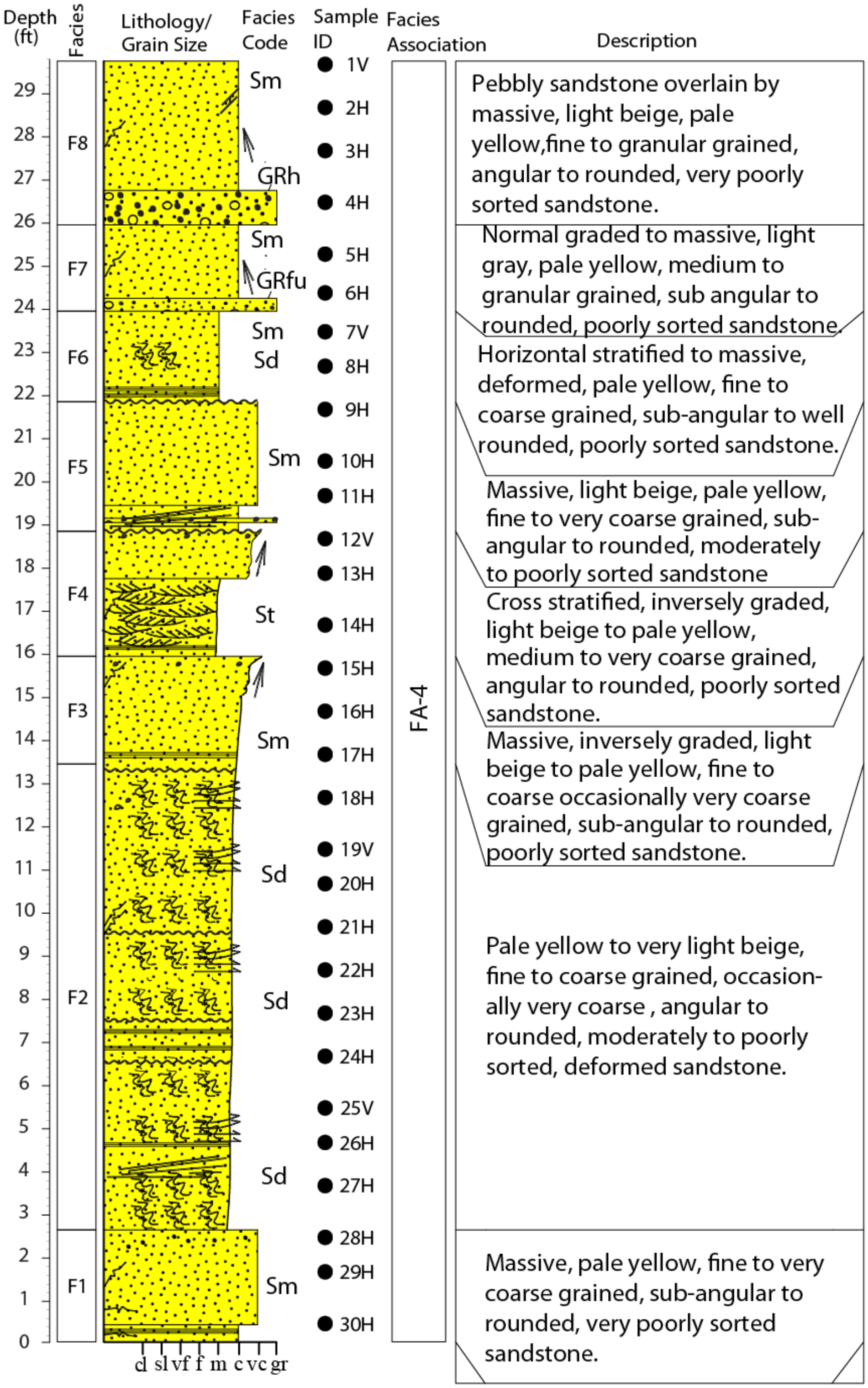

Pebbly sandstone overlain by massive, light beige, pale yellow,fine to granular grained, angular to rounded, very poorly sorted sandstone.

Normal graded to massive, light gray, pale yellow, medium to granular grained, sub angular to rounded, poorly sorted sandstone.

Horizontal stratified to massive, deformed, pale yellow, fine to coarse grained, sub-angular to well rounded, poorly sorted sandstone.

Massive, light beige, pale yellow, fine to very coarse grained, sub-angular to rounded, moderately to poorly sorted sandstone

Cross stratified, inversely graded, light beige to pale yellow, medium to very coarse grained, angular to rounded, poorly sorted sandstone.

Massive, inversely graded, light beige to pale yellow, fine to coarse occasionally very coarse grained, sub-angular to rounded, poorly sorted sandstone.

Pale yellow to very light beige, fine to coarse grained, occasionally very coarse , angular to rounded, moderately to poorly sorted, deformed sandstone.

Massive, pale yellow, fine to very coarse grained, sub-angular to rounded, very poorly sorted sandstone.

Figure A 11: Sedimentological log of the Well-E core interval. (See Figure 4.2 for the core legend and Table 4.1 for the facies codes).

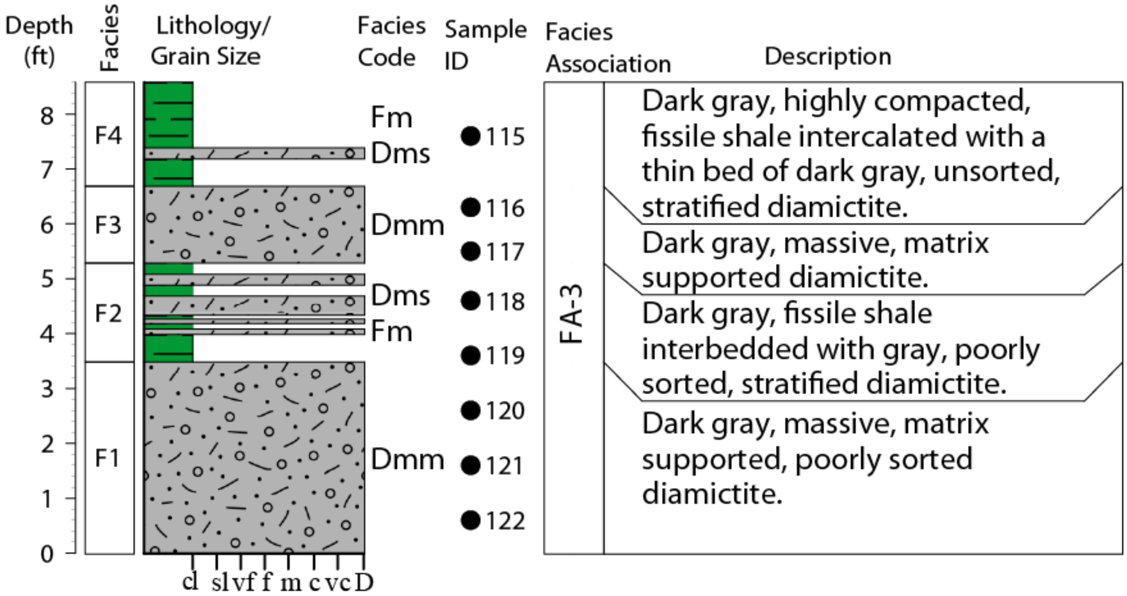

Figure A 12: Sedimentological log of the Well-F core interval. (See Figure 4.2 for the core legend and Table 4.1 for the facies codes).

Appendix B: Petrographical Analysis

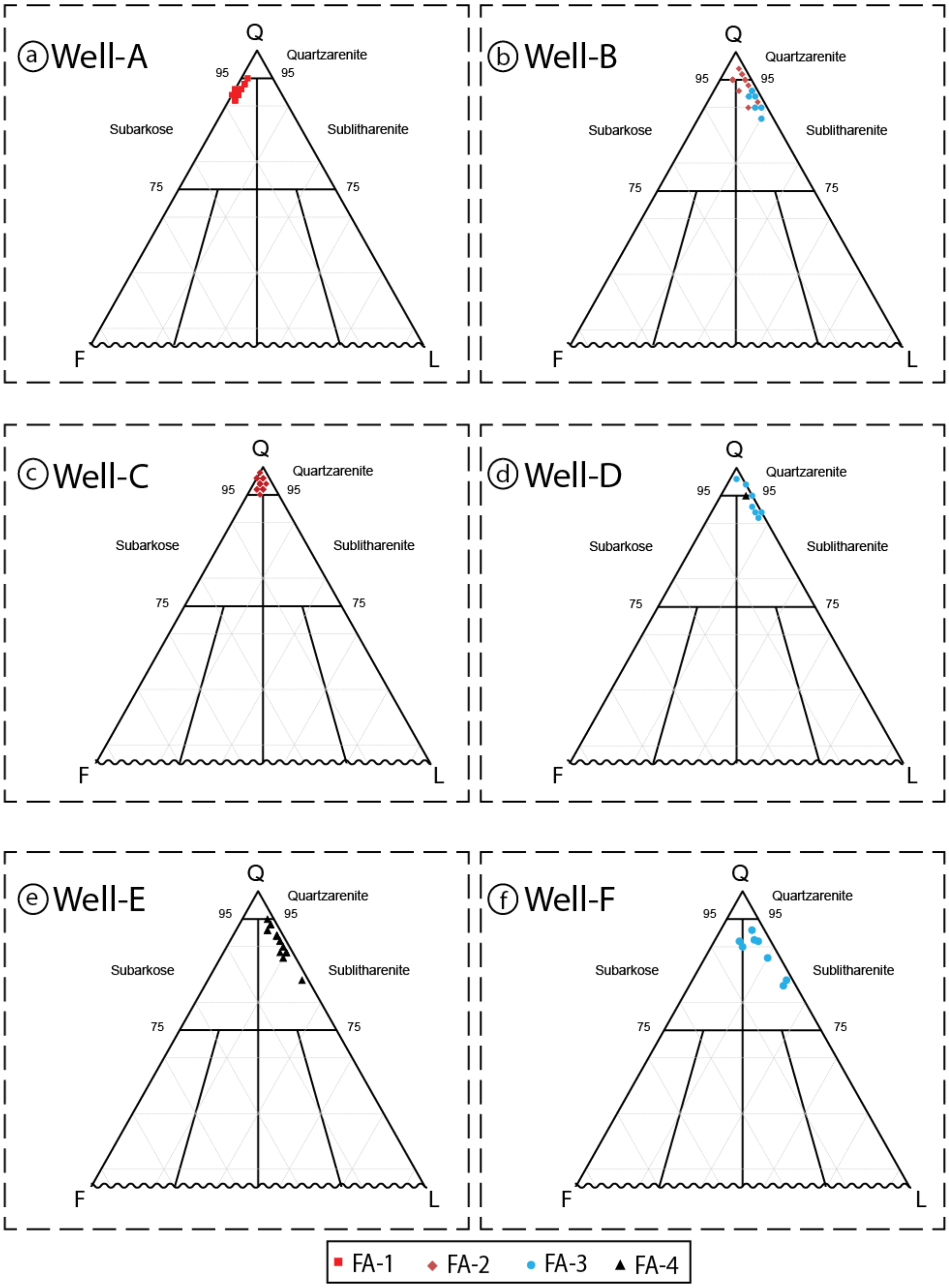

Figure B 1: Sandstone classification for each core interval (Folk, 1980). (FA-1) nearshore, (FA-2) glaciolacustrine delta, (FA-3) subglacial, and (FA-4) glaciofluvial environments.

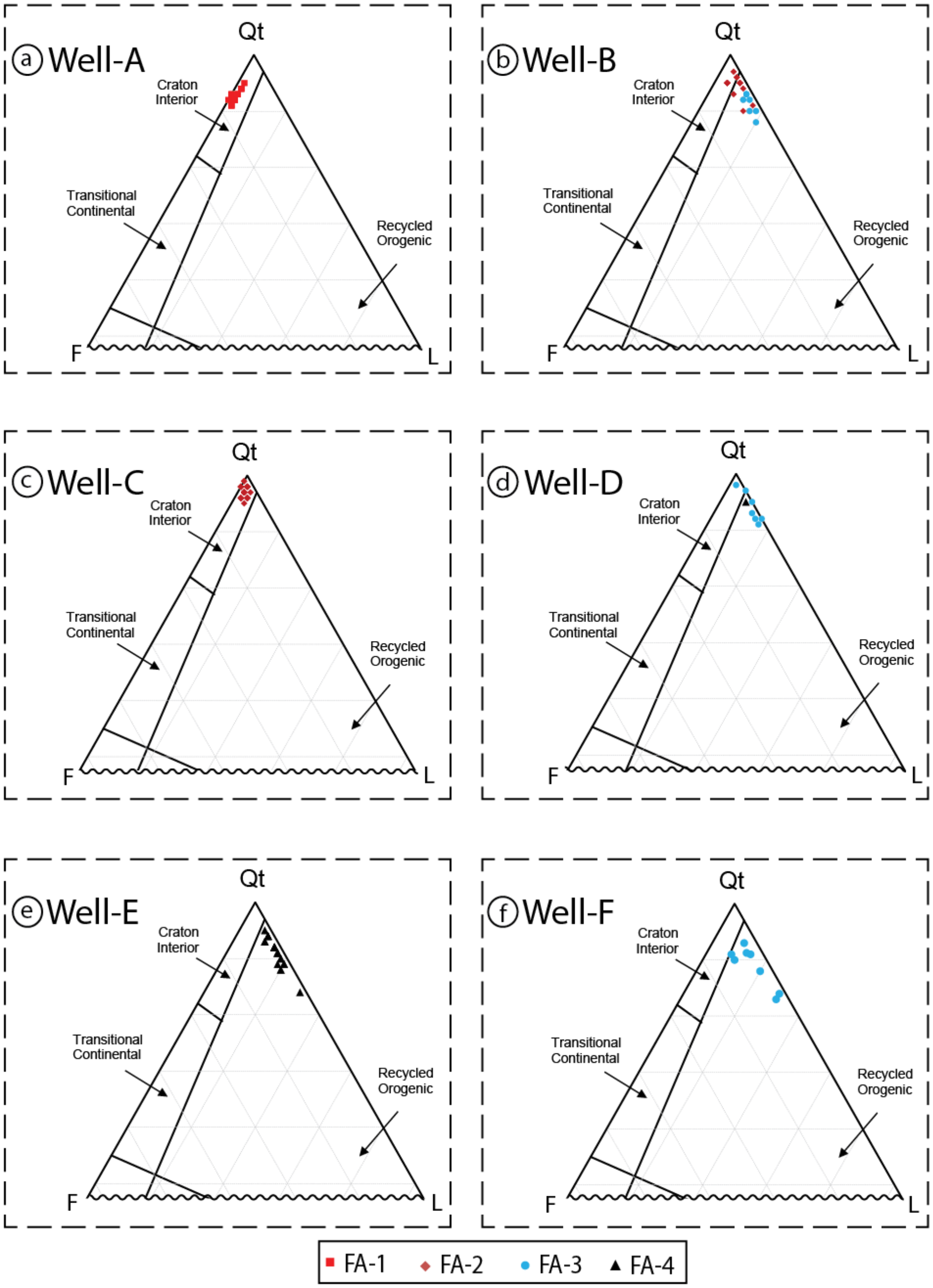

Figure B 2: Sandstone provenance for each core interval (Dickinson, 1985). (FA-1) nearshore, (FA-2) glaciolacustrine delta, (FA-3) subglacial, and (FA-4) glaciofluvial environments.

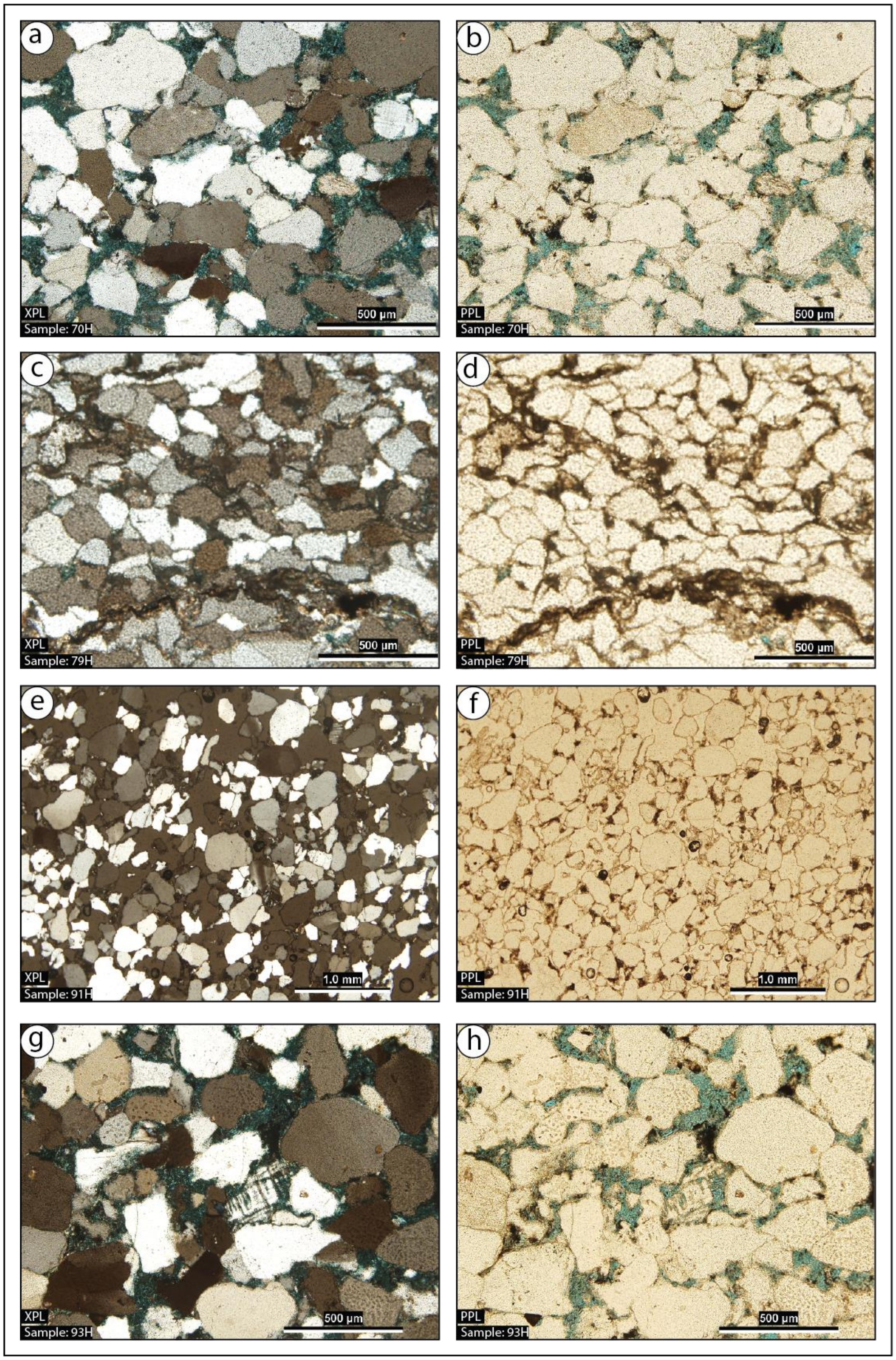

Figure B 3: XPL and PPL extra thin section photomicrographs from Well-A core interval. (a,b) micrographs for medium grains with intergranular porosity, (c,d) compacted grains, (e,f) silica cement, (g,h) partially dissolved microcline within medium grains quartz.

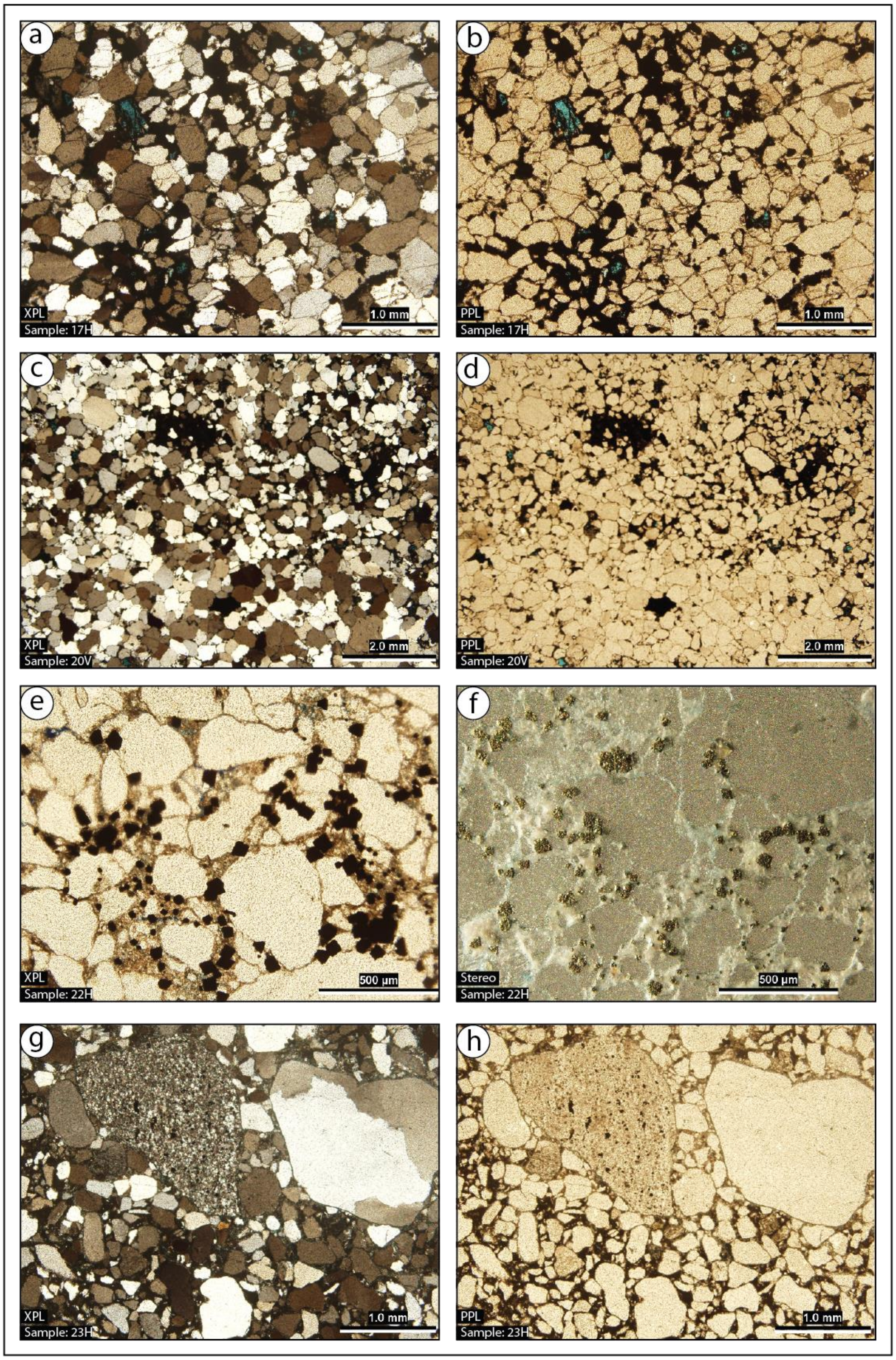

Figure B 4: XPL and PPL extra thin section photomicrographs from Well-B core interval. (a,b,c,d) compacted and uncompacted grains; note pores filled by organic matters, (e,f) pyrite, (g,h) poorly sorted poly- and microcrystalline quartz with lithic rock fragments.

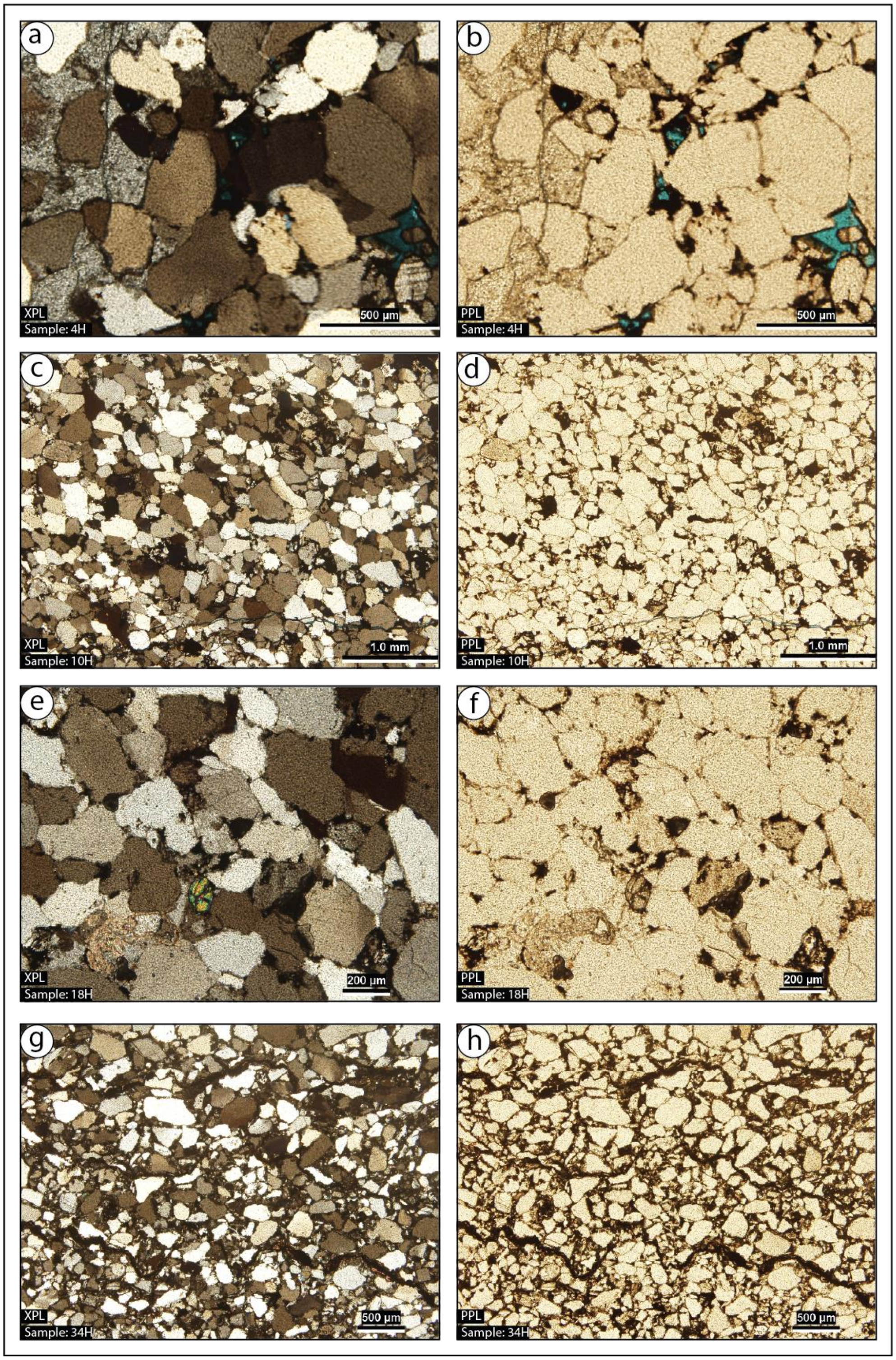

Figure B 5: XPL and PPL extra thin section photomicrographs from Well-C core interval. (a,b) barite cement, (c,d) compacted grains with microfractures, (e,f) compacted grains, (g,h) stylolite with fine to medium grains.

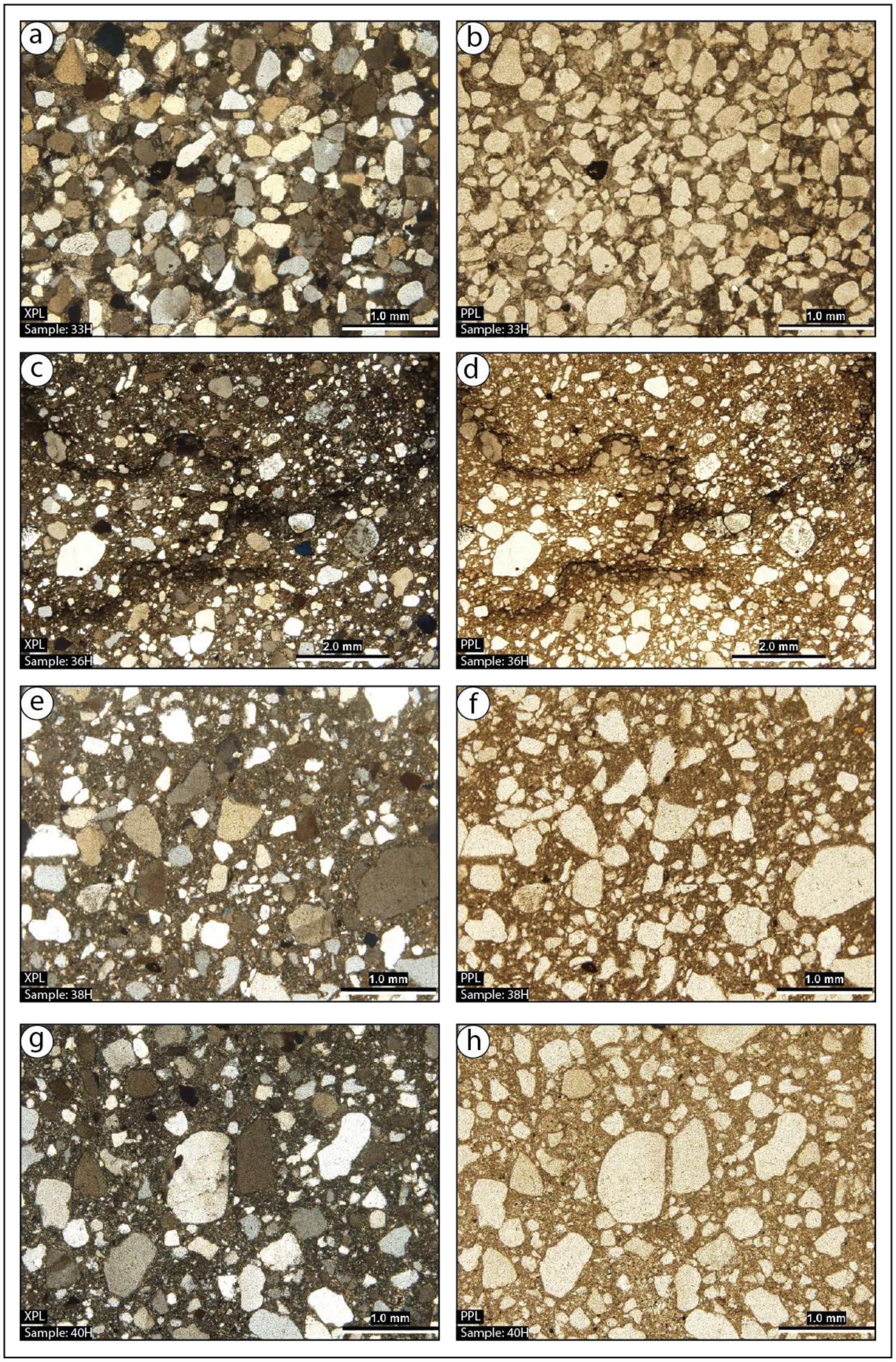

Figure B 6: XPL and PPL extra thin section photomicrographs from Well-D core interval. (a,b) siderite cement and fine grains of microcrystalline quartz, (c,d) deformed matrix supported diamictite, (e,f,g,h) undeformed matrix supported diamictite.

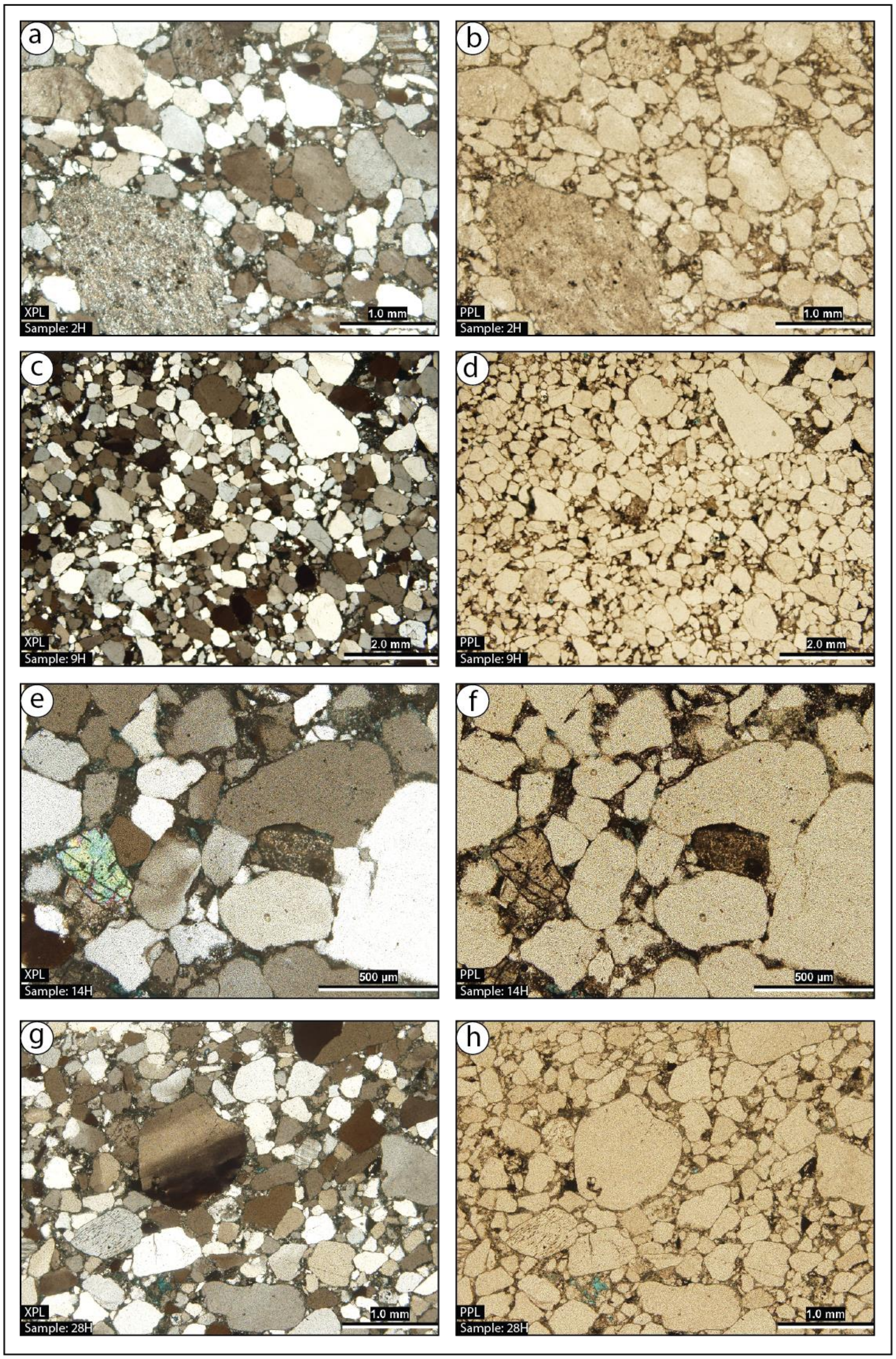

Figure B 7: XPL and PPL extra thin section photomicrographs from Well-E core interval. (a,b) poorly sorted quartz grains with lithic rock fragment, (c,d,e,f,g,h) compacted and poorly sorted grains.

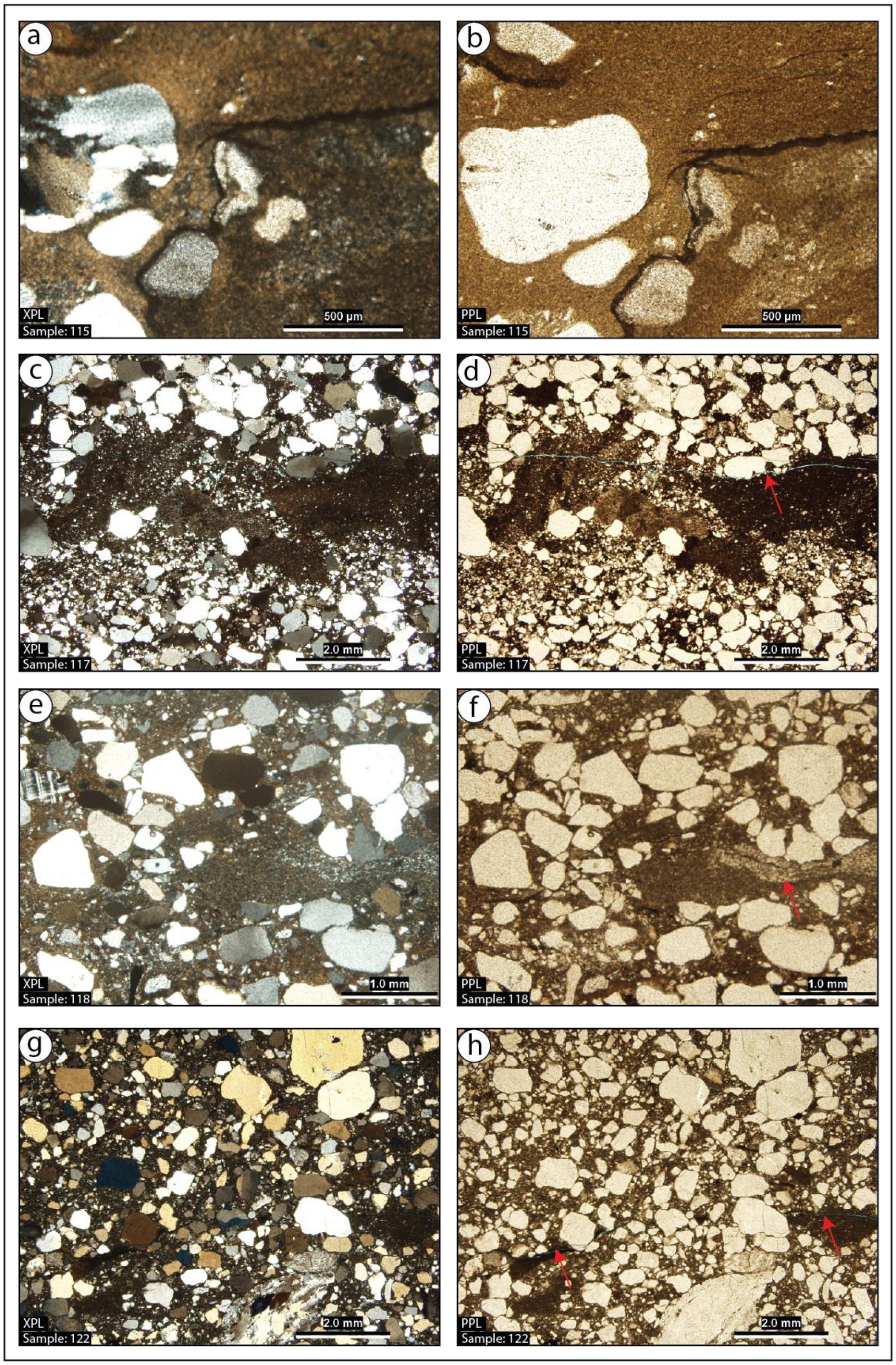

Figure B 8: XPL and PPL extra thin section photomicrographs from Well-F core interval. (a,b) deformed matrix supported diamictite, (c,d) stratified matrix supported diamictite, (e,f,g,h) matrix supported diamictite. Note fractures are indicated by red arrows.

Appendix C: Geochemical Analysis

Table C 1: Showing the values of all analyzed elements used in this study. Note that all elements are measured in weight percent (wt%). (W) Well, (ID) sample number of each well.

W	ID	Si	Al	Fe	K	S	Ca	Ti	Mn	P	Mg	Cr	Sr	V	Zn	Zr	Ni	Ba
A	70H	72.0	2.8	9.3	6.9	3.5	2.0	1.2	0.0			0.5	0.1	0.1	0.0	0.5		1.2
A	71H	76.4	2.3	7.3	4.9	4.0	2.1	1.0	0.2			0.4	0.1	0.2	0.0	0.3		0.8
A	76H	75.1	2.6	8.5	5.0	2.9	2.4	0.9	0.1	1.1		0.3	0.1	0.1	0.0	0.2		0.8
A	81H	77.9	2.3	6.5	4.9	2.5	2.1	1.1	0.2	1.1		0.2	0.1	0.1	0.0	0.3		0.7
A	85H	68.3	4.0	8.6	8.7	4.1	2.6	1.7	0.3			0.4	0.1	0.2	0.0	0.5		0.5
A	90H	70.9	2.7	8.9	6.5	4.0	3.1	1.3	0.5	0.8		0.4	0.1	0.2	0.1	0.3		0.3
A	94H	73.8	2.2	9.0	4.5	4.3	2.0	1.3	0.3	0.7		0.4	0.1	0.2	0.0	0.5		0.6
B	15H	71.5	2.4	9.5	6.2	5.0	1.2	1.1	0.2	0.9		0.5	0.0	0.2	0.0	0.5		0.6
B	18H	71.3	0.9	17.6	1.2	5.2	1.0	0.3	0.6			1.2	0.0	0.2	0.0	0.3		0.3
B	21H	32.1	11.9	21.7	23.9	4.0	1.0	2.7	0.0	0.7	0.4	0.1	0.2	0.1	0.0	0.4		0.6
B	23H	61.3	4.3	12.7	11.8	5.3	2.0	0.9	0.0			0.8	0.1		0.0	0.4		0.4
B	27H	67.5	4.9	6.6	12.5	3.0	1.5	1.2	0.1	1.0		0.4	0.1	0.3	0.0	0.3		0.6
B	28H	63.7	3.7	18.4	7.2	1.5	1.2	0.5	1.5	1.0	0.2	0.2	0.1	0.0	0.0	0.2		0.5
B	31H	65.1	3.7	14.8	8.6	2.3	1.6	0.6	0.8	0.8	0.1	0.6	0.1	0.1	0.0	0.3		0.5
B	35H	64.5	5.7	8.4	14.3	1.6	1.5	1.1	0.2	1.1	0.1	0.2	0.1	0.0	0.0	0.3		0.7
B	37H	36.6	11.3	23.7	20.9	1.8	1.1	2.2	0.0	0.6	0.5	0.2	0.2	0.1	0.0	0.2		0.5
B	38H	33.8	9.6	30.0	19.0	1.7	1.7	1.5	0.0	0.9	0.3	0.2	0.2	0.2	0.0	0.2		0.6
C	3H	81.8	1.1	5.0	1.2	3.2	1.5	0.4	0.0	1.2		0.3	0.1	0.1	0.0	0.2	0.0	4.0
C	5H	38.2	0.5	5.3	1.0	15.5	25.2			0.9		0.3	0.2			0.1	0.0	12.8
C	7H	38.9	0.4	3.2		20.0	32.8	0.2	0.0	0.8		0.3	0.4	0.1	0.0	0.1	0.0	2.7
C	10H	56.2	0.7	7.3	0.5	9.3	10.8	0.5	0.0	0.8		0.5	0.7	0.0	0.0	0.4	0.0	12.2
C	15H	72.0	1.4	4.4	0.7	7.2	5.2	0.5	0.1			0.6	0.4	0.2	0.0	0.2	0.0	7.0
C	17H	50.6	1.1	2.4	0.9	6.2	3.2		0.0	0.6		0.1	3.8		0.0	0.2	0.0	30.9
C	20H	57.5	6.1	8.2	18.2	2.0	3.4	1.3		0.8		0.6	0.1	0.1	0.0	0.3	0.0	1.3
C	22H	68.4	4.0	4.1	11.7	3.5	5.0	0.8	0.0	0.8		0.4	0.1	0.1	0.0	0.2	0.0	0.8
C	27H	70.4	2.7	10.2	6.7	4.1	2.4	0.8	0.1	0.6		0.9	0.1	0.1	0.0	0.4	0.0	0.7
C	31H	74.0	3.2	5.1	8.2	3.2	3.0	1.1	0.0			0.4	0.0	0.2	0.0	0.4	0.1	1.0
C	34H	72.2	3.8	5.8	9.2	4.5	1.7	0.8	0.0			0.6	0.0	0.2	0.0	0.3	0.0	0.7
C	35H	68.8	2.3	17.2	5.0	1.4	1.4	0.3				1.3	0.2		0.0	0.2	0.1	1.7
C	37H	56.1	0.9	8.7	0.8	5.5	2.6		0.1			0.6	3.4		0.0	0.2	0.1	21.1
D	33H	36.7	1.0	47.6	0.5	2.4	0.8	0.3	8.0	0.2	1.9	0.3	0.0	0.1	0.0	0.2		0.1
D	34H	53.2	7.4	17.3	15.0	1.9	1.2	1.5	0.0	0.8	0.2	0.2	0.1	0.1	0.0	0.3		0.6
D	36H	56.5	6.6	14.8	15.2	1.7	1.2	1.5	0.1	0.9	0.1	0.2	0.1	0.1	0.0	0.3		0.8
D	40H	53.6	6.9	13.5	17.1	3.4	1.6	1.8	0.1	0.6	0.2	0.3	0.2	0.2	0.1	0.3		0.6
E	1V	76.6	3.0	7.9	8.1	1.5	1.6	1.0				0.1	0.1		0.0	0.2		
E	5H	76.7	2.6	8.5	4.2	4.2	1.7	1.3	0.0			0.3	0.1	0.1	0.0	0.3		
E	8H	75.7	2.4	10.3	5.5	1.9	2.9	0.7	0.1			0.4	0.1		0.0	0.2		
E	10H	73.7	3.1	10.7	6.3	2.8	1.3	1.0	0.0			0.5	0.1	0.2	0.0	0.3		
E	12V	75.3	3.5	8.6	8.1	1.5	1.9	0.8				0.1	0.1		0.0	0.1		
E	13H	74.4	3.1	9.2	6.4	2.9	2.0	0.8	0.1			0.3	0.1	0.0	0.4	0.1		
E	14H	80.0	2.6	6.5	6.1	1.0	2.7	0.8	0.1			0.1	0.1			0.1		
E	16H	77.6	2.4	7.7	5.8	2.5	2.7	0.8	0.0			0.2	0.1		0.0	0.1		
E	18H	77.5	2.0	11.3	4.9	1.3	1.5	0.7				0.5	0.1		0.0	0.2		
E	23H	73.4	2.5	8.6	5.0	1.8	6.9	0.9	0.5			0.1	0.1		0.0	0.2		
E	29H	76.6	2.8	9.1	6.1	2.6	1.4	0.8				0.3	0.1	0.0	0.0	0.2		
E	30H	75.7	3.0	7.4	7.2	2.2	3.1	0.8	0.1			0.2	0.1		0.0	0.1		
F	115	39.7	9.9	24.7	19.6	1.3	1.1	2.1	0.0	0.7	0.3	0.1	0.2	0.0	0.0	0.2		
F	117	45.6	4.1	25.1	7.3	1.8	7.6	1.2	5.4	0.8	0.6	0.2	0.2	0.0	0.0	0.2		
F	121	45.4	6.8	22.4	16.6	3.4	1.4	1.8	0.5	0.4	0.3	0.4	0.3	0.1	0.0	0.3		

Table C 2: Showing the values of all analyzed elemental oxides used in this study. Note that all oxides are measured in weight percent (wt%). (W) Well, (ID) sample number of each well.

W	ID	SiO2	Al2O3	Fe2O3	K2O	SO3	CaO	TiO2	MnO	P2O5	MgO	Cr2O3	SrO	V2O5	ZnO	ZrO2	NiO	BaO
A	70H	82.8	3.1	4.5	3.4	2.4	1.0	0.7	0.0	1.0		0.2	0.0	0.1	0.0	0.2		0.5
A	71H	85.2	2.8	3.3	2.1	3.6	1.0	0.6	0.1	0.7		0.2	0.0	0.1	0.0	0.1		0.3
A	76H	85.0	2.7	4.0	2.2	2.8	1.2	0.5	0.1	1.0		0.1	0.0	0.0	0.0	0.1		0.3
A	81H	86.9	2.5	3.0	2.1	2.3	1.0	0.7	0.1	0.9		0.1	0.0	0.0	0.0	0.1		0.2
A	85H	79.2	4.5	4.1	4.1	4.1	1.4	1.0	0.1	0.6		0.2	0.0	0.1	0.0	0.2		0.2
A	90H	81.6	3.2	4.2	2.9	4.0	1.6	0.8	0.2	0.9		0.2	0.0	0.1	0.0	0.1		0.1
A	94H	83.6	2.8	4.2	2.0	4.1	1.0	0.8	0.2	0.6		0.2	0.0	0.2	0.0	0.2		0.2
B	15H	82.1	2.8	4.4	2.8	5.0	0.6	0.7	0.1	0.7		0.2	0.0	0.1	0.0	0.2		0.2
B	18H	82.2	1.1	8.9	0.6	5.2	0.6	0.2	0.3			0.7	0.0	0.1	0.0	0.1		0.1
B	21H	43.7	15.5	14.1	15.6	5.7	0.7	2.2	0.0	1.0	0.6	0.1	0.1	0.1	0.0	0.2		0.3
B	23H	73.9	4.9	6.6	6.2	5.8	1.2	0.6	0.0		0.0	0.4	0.0		0.0	0.2		0.2
B	27H	78.8	5.8	3.1	5.9	3.1	0.7	0.7	0.1	1.0	0.0	0.2	0.0	0.2	0.0	0.1		0.2
B	28H	76.5	4.5	10.0	3.8	1.8	0.7	0.3	0.7	1.0	0.1	0.1	0.0	0.0	0.0	0.1		0.2
B	31H	77.6	4.3	7.6	4.3	2.6	0.9	0.4	0.4	0.8	0.2	0.3	0.0	0.1	0.0	0.1		0.2
B	35H	76.8	6.9	4.2	7.2	1.7	0.8	0.7	0.1	1.0	0.0	0.1	0.0		0.0	0.1		0.3
B	37H	49.4	14.5	15.5	13.6	2.2	0.7	1.8	0.0	0.9	0.6	0.2	0.1	0.1	0.0	0.1		0.3
B	38H	47.9	13.4	19.3	12.6	2.1	1.2	1.2	0.0	1.1	0.5	0.1	0.1	0.1	0.0	0.1		0.3
C	3H	89.6	1.3	2.2	0.5	2.8	0.7	0.2	0.0	1.0		0.2	0.0	0.0	0.0	0.1	0.0	1.5
C	5H	50.7	0.7	3.1	0.6	20.7	16.7		0.0	1.1		0.2	0.1		0.0	0.1	0.0	6.1
C	7H	50.5	0.6	1.7	0.0	24.7	19.8	0.1	0.0	0.9		0.1	0.2	0.1	0.0	0.0	0.0	1.1
C	10H	69.5	0.9	3.9	0.3	11.0	6.7	0.3	0.0	0.9		0.3	0.3	0.1	0.0	0.2	0.0	5.7
C	15H	81.9	1.7	2.1	0.4	7.0	2.7	0.4	0.1	0.5		0.3	0.1	0.1		0.1	0.0	2.8
C	17H	66.8	1.3	1.6	0.6	8.4	2.3		0.0			0.0	1.9		0.0	0.1	0.0	17.0
C	20H	71.6	7.4	4.3	9.7	2.2	1.9	0.8	0.0	0.9		0.3	0.1	0.0	0.0	0.2	0.0	0.6
C	22H	80.8	4.5	1.9	5.5	3.5	2.5	0.5	0.0			0.2	0.0	0.1	0.0	0.1	0.0	0.4
C	27H	81.6	3.0	4.9	3.1	4.0	1.2	0.5	0.0	0.6		0.5	0.0	0.1	0.0	0.1	0.0	0.3
C	31H	84.3	3.7	2.3	3.7	3.1	1.5	0.6	0.0			0.2	0.0	0.1	0.0	0.2	0.0	0.4
C	34H	82.4	4.3	2.7	4.1	4.2	0.8	0.5	0.0			0.3	0.0	0.1	0.0	0.1	0.0	0.3
C	35H	81.7	2.6	8.9	2.6	1.4	0.8	0.2	0.0			0.8	0.1			0.1	0.0	0.8
C	37H	71.3	1.1	5.1	0.5	7.1	1.8		0.0			0.4	1.6		0.0	0.1	0.0	10.9
D	33H	50.8	1.1	34.9	0.4	3.6	0.7	0.3	5.4	0.2	2.1	0.2	0.0	0.1	0.0	0.1		0.0
D	34H	67.5	9.0	9.9	8.4	2.4	0.7	1.1	0.0		0.3	0.1	0.1	0.1	0.0	0.2		0.3
D	36H	70.7	8.1	8.1	8.4	1.8	0.7	1.0	0.0		0.4	0.1	0.1	0.1	0.0	0.1		0.4
D	40H	67.7	8.5	7.4	9.3	3.4	0.8	1.2	0.0	0.7	0.2	0.1	0.1	0.1	0.0	0.1		0.3
E	1V	86.6	3.5	3.6	3.5	1.3	0.7	0.6	0.0			0.0	0.0		0.0	0.1		
E	5H	86.5	3.0	3.9	2.3	2.5	0.9	0.8	0.0			0.1	0.0	0.1	0.0	0.1		
E	8H	86.3	2.7	4.8	2.5	1.5	1.4	0.4	0.0			0.2	0.0		0.0	0.1		
E	10H	84.3	3.7	5.1	3.1	2.2	0.6	0.6	0.0			0.2	0.0	0.0	0.0	0.1		
E	12V	85.4	4.0	4.0	3.7	1.4	0.9	0.4	0.0			0.0	0.0		0.0	0.0		
E	13H	84.5	3.5	4.3	3.0	2.8	1.0	0.5	0.0			0.1	0.0	0.0	0.2	0.0		
E	14H	88.8	3.0	2.9	2.6	0.9	1.3	0.4	0.0			0.0	0.0		0.0	0.0		
E	16H	87.0	2.8	3.5	2.5	2.3	1.3	0.5	0.0			0.1	0.0		0.0	0.1		
E	18H	87.4	2.5	5.3	2.2	1.2	0.7	0.4	0.0			0.3	0.0		0.0	0.1		
E	23H	84.4	2.9	4.0	2.4	1.8	3.5	0.5	0.0			0.1	0.0	0.0		0.1		
E	29H	86.2	3.1	4.2	2.8	2.4	0.7	0.4	0.0			0.2	0.0		0.0	0.1		
E	30H	85.8	3.4	3.4	3.2	2.1	1.6	0.4	0.0			0.1	0.0		0.0	0.0		
F	115	53.0	12.5	15.9	12.6	1.8	0.7	1.7	0.0	1.0	0.5	0.1	0.1	0.0	0.0	0.1		
F	117	60.5	5.0	15.9	4.6	2.4	5.4	1.0	3.2	1.0	0.8	0.1	0.1		0.0	0.1		
F	121	59.6	8.4	13.6	10.2	4.2	0.9	1.4	0.2	0.6	0.3	0.2	0.1	0.1	0.0	0.1		

Appendix D: Petrophysical Analysis

Table D 1: Porosity and permeability data of Well-A core interval. Note that FA-1 stands for the nearshore environment.

FAs	Wells	Samples	Porosity (%)	Permeability (mD)	Facies
FA-1	A	68H	8.042	0.129	F4
FA-1	A	69H	13.548	8.628	F4
FA-1	A	70H	12.244	17.462	F4
FA-1	A	71H	7.150	0.121	F4
FA-1	A	72H	11.625	0.793	F4
FA-1	A	73H	9.021	0.312	F4
FA-1	A	74H	11.257	3.880	F4
FA-1	A	75H	11.228	0.240	F4
FA-1	A	76H	12.165	8.844	F4
FA-1	A	77H	7.589	0.177	F3
FA-1	A	78H	10.554	0.557	F3
FA-1	A	79H	7.098	0.089	F3
FA-1	A	80H	10.110	0.360	F3
FA-1	A	81H	8.453	0.272	F3
FA-1	A	82V	10.015	0.498	F3
FA-1	A	83H	12.054	0.990	F3
FA-1	A	84H	10.941	0.436	F3
FA-1	A	85H	9.639	3.589	F2
FA-1	A	86H	11.903	3.545	F2
FA-1	A	87H	9.305	0.197	F2
FA-1	A	88H	9.788	0.160	F2
FA-1	A	89V	4.521	0.047	F2
FA-1	A	90H	10.125	0.474	F2
FA-1	A	91H	9.444	0.352	F2
FA-1	A	92H	10.434	2.486	F2
FA-1	A	93H	11.316	0.657	F2
FA-1	A	94H	8.766	0.225	F2
FA-1	A	95V	10.453	0.249	F2
FA-1	A	96H	8.891	0.091	F2

Table D 2: Porosity and permeability data of Well-B core interval. Note that FA-2 stands for the glaciolacustrine delta environment while FA-3 stands for the subglacial environment.

FAs	Wells	Samples	Porosity (%)	Permeability (mD)	Facies
FA-2	B	15H	4.995	0.048	F8
FA-2	B	16H	4.392	0.044	F8
FA-2	B	17H	9.096	3.280	F7
FA-2	B	18H	12.590	10.783	F7
FA-2	B	19H	9.320	1.140	F7
FA-2	B	20V	8.291	0.073	F7
FA-2	B	21H	0.080	0.001	F6
FA-3	B	22H	3.190	0.048	F6
FA-3	B	23H	3.996	0.109	F5
FA-3	B	24H	2.987	0.024	F5
FA-3	B	25H	1.965	0.024	F5
FA-3	B	26V	2.520	0.032	F4
FA-3	B	27H	1.739	0.089	F4
FA-3	B	28H	3.680	0.017	F3
FA-2	B	29H	4.841	0.095	F3
FA-2	B	30H	5.283	0.116	F3
FA-2	B	31H	4.544	0.049	F3
FA-2	B	32H	3.277	0.044	F3
FA-2	B	33H	3.171	0.014	F3
FA-2	B	34V	2.058	0.009	F3
FA-2	B	35H	2.985	0.018	F3
FA-2	B	36H	1.163	0.011	F2
FA-2	B	37H	1.101	0.007	F2
FA-2	B	38H	0.840	0.009	F2
FA-2	B	39V	0.961	0.006	F2

Table D 3: Porosity and permeability data of Well-C core interval. Note that FA-2 stands for the glaciolacustrine delta environment.

FAs	Wells	Samples	Porosity (%)	Permeability (mD)	Facies
FA-2	C	1H	3.250	0.370	F6
FA-2	C	2V	2.910	0.007	F5
FA-2	C	3H	3.450	0.065	F5
FA-2	C	4H	4.040	0.084	F5
FA-2	C	5H	0.430	0.027	F5
FA-2	C	6H	0.250	0.029	F3
FA-2	C	7H	0.920	0.048	F3
FA-2	C	8H	1.220	0.041	F3
FA-2	C	9H	0.740	0.019	F3
FA-2	C	10H	3.150	0.011	F3
FA-2	C	11H	2.220	0.004	F2
FA-2	C	12V	2.940	0.003	F2
FA-2	C	13H	2.420	0.004	F2
FA-2	C	14H	3.310	0.005	F2
FA-2	C	15H	2.520	0.032	F2
FA-2	C	16H	3.430	0.061	F2
FA-2	C	17H	10.177	27.866	F2
FA-2	C	18H	2.720	0.002	F2
FA-2	C	19V	10.070	0.042	F2
FA-2	C	20H	10.700	0.117	F2
FA-2	C	21H	8.710	0.082	F2
FA-2	C	22H	10.250	0.148	F2
FA-2	C	23H	7.680	0.038	F1
FA-2	C	24H	9.000	0.081	F1
FA-2	C	25H	8.810	0.048	F1
FA-2	C	26V	8.810	0.046	F1
FA-2	C	27H	1.210	0.039	F1
FA-2	C	28H	8.050	0.048	F1
FA-2	C	29H	9.640	0.054	F1
FA-2	C	30H	9.280	0.064	F1
FA-2	C	31H	9.180	0.060	F1
FA-2	C	32V	9.490	0.018	F1
FA-2	C	33H	9.920	0.049	F1
FA-2	C	34H	5.630	0.015	F1
FA-2	C	35H	7.820	0.051	F1
FA-2	C	36H	3.110	0.022	F1
FA-2	C	37H	8.600	56.024	F1
FA-2	C	38V	3.370	0.023	F1
FA-2	C	39H	5.930	0.096	F1
FA-2	C	40H	4.700	0.161	F1

Table D 4: Porosity and permeability data of Well-D core interval. Note that FA-3 stands for the subglacial environment while FA-4 stands for the glaciofluvial environment.

FAs	Wells	Samples	Porosity (%)	Permeability (mD)	Facies
FA-4	D	33	1.530	0.014	F2
FA-3	D	34	2.220	0.007	F1
FA-3	D	35	0.700	0.002	F1
FA-3	D	36	1.150	0.003	F1
FA-3	D	37	1.410	0.018	F1
FA-3	D	38	1.480	0.297	F1
FA-3	D	39	0.580	0.001	F1
FA-3	D	40	0.140	0.003	F1

Table D 5: Porosity and permeability data of Well-F core interval. Note that FA-3 stands for the subglacial environment.

FAs	Wells	Samples	Porosity (%)	Permeability (mD)	Facies
FA-3	F	115	1.480	0.300	F4
FA-3	F	116	5.354	0.022	F3
FA-3	F	117	2.456	0.050	F3
FA-3	F	118	0.992	6.564	F2
FA-3	F	119	1.444	0.360	F2
FA-3	F	120	0.735	0.011	F1
FA-3	F	121	0.699	0.007	F1
FA-3	F	122	1.810	0.026	F1

Table D 6: Porosity and permeability data of Well-E core interval. Note that FA-4 stands for the glaciofluvial environment.

FAs	Wells	Samples	Porosity (%)	Permeability (mD)	Facies
FA-4	E	1V	4.400	0.028	F8
FA-4	E	2H	4.800	0.110	F8
FA-4	E	3H	3.350	0.266	F8
FA-4	E	4H	4.990	0.124	F8
FA-4	E	5H	5.750	0.240	F7
FA-4	E	6H	3.620	0.311	F7
FA-4	E	7V	7.520	0.103	F6
FA-4	E	8H	7.060	0.355	F6
FA-4	E	9H	7.370	0.738	F5
FA-4	E	10H	1.100	0.171	F5
FA-4	E	11H	3.830	0.527	F5
FA-4	E	12V	5.120	0.390	F4
FA-4	E	13H	5.610	0.700	F4
FA-4	E	14H	3.570	0.043	F4
FA-4	E	15H	5.320	0.049	F3
FA-4	E	16H	6.700	0.162	F3
FA-4	E	17H	6.740	0.270	F3
FA-4	E	18H	5.560	0.115	F2
FA-4	E	19V	4.010	0.446	F2
FA-4	E	20H	3.960	0.282	F2
FA-4	E	21H	2.450	4.214	F2
FA-4	E	22H	4.650	0.316	F2
FA-4	E	23H	4.760	0.309	F2
FA-4	E	24H	4.930	0.105	F2
FA-4	E	25V	6.810	0.171	F2
FA-4	E	26H	3.150	0.079	F2
FA-4	E	27H	2.890	0.037	F2
FA-4	E	28H	2.970	0.126	F1
FA-4	E	29H	3.190	0.372	F1
FA-4	E	30H	4.270	0.304	F1

Vitae

Name : Abdullah Mohammed Saleh Alqubalee

Nationality : Yemeni

Date of Birth :11/11/1983

Email : qubalee@live.com

Address : Qerbah, Alzahir, Albaida, Yemen

Academic Background :BSc in Engineering Geology from College of Oil and Minerals, University of Aden, Yemen (2007).

Accepted Conference / Workshop Papers

Alqubalee, A. Abdullatif, O. Babalola, L., 2017, Application of Spectral Gamma Ray for Lithofacies and Paleo-environmental Interpretation: A Case Study from The Late Ordovician Glaciogenic Deposits, Saudi Arabia, in: EGU General Assembly 2017, Vienna, Austria.

Alqubalee, A. Abdullatif, O. Babalola, L. Makkawi, M., 2017, Diagenetic Controls on Reservoir Quality: Insight into the Late Ordovician Sarah Tight Sand, Rub' Al-Khali Basin, Saudi Arabia, in: Siliciclastic Reservoir of the Middle East workshop, AAPG, Amman, Jordan.

Alqubalee, A. Abdullatif, O. Babalola, L. Makkawi, M., 2017, Lithofacies and Depositional Environments of the Late Ordovician Sarah Formation in the Subsurface of Rub' Al-Khali Basin, Saudi Arabia, in: Siliciclastic Reservoir of the Middle East workshop, AAPG, Amman, Jordan.

Alqubalee, A. Abdullatif, O. Babalola, L. Makkawi, M., 2017, Reservoir Characterization of Tight Gas Sand: Integration of lithofacies and Petrophysical Properties, Subsurface, Saudi Arabia, in: 79th EAGE Conference & Exhibition 2017, Paris, France.

Alqubalee, A. Abdullatif, O. Babalola, L., Sahin, A., 2017, Lithofacies and Paleoenvironments of the Late Ordovician Sarah Tight Sand, Subsurface of the Rub' Al-

Khali Basin, Saudi Arabia, in: AAPG/SEG International Conference & Exhibition, London, England.

Submitted Conference / Workshop Papers

Alqubalee, A. Abdullatif, O. Babalola, L. Makkawi, M., 2017, Multi-Scale Reservoir Characterization of Tight Gas Sand: A Case Study from the Paleozoic Glaciogenic Sarah Formation, Rub' Al-Khali Basin, Saudi Arabia., in: 4th EAGE Workshop on Rock Physics, Abu Dhabi, United Arab Emirates.

Alqubalee, A. Abdullatif, O. Babalola, L. Makkawi, M., 2017, Geochemical Characterization of the Late Ordovician Glaciogenic Deposits, Saudi Arabia, in: KFUPM 8th Students Forum, Dhahran, Saudi Arabia.

Journal Manuscripts (Under preparation)

Alqubalee, A. Abdullatif, O. Babalola, L. Makkawi, M., 2017, Lithofacies and Paleoenvironments of the Late Ordovician Sarah Tight Sand, Subsurface of the Rub' Al-Khali Basin, Saudi Arabia.

Alqubalee, A. Abdullatif, O. Babalola, L. Makkawi, M., 2017, Reservoir Properties of the Late Ordovician Glaciogenic Tight Sand Reservoir, Rub' Al-Khali Basin, Saudi Arabia.